



# Politecnico di Bari

Repository Istituzionale dei Prodotti della Ricerca del Politecnico di Bari

Development of compact and innovative optical sensors for trace gas detection

This is a PhD Thesis

*Original Citation:*

Development of compact and innovative optical sensors for trace gas detection / Menduni, Giansergio. -  
ELETTRONICO. - (2021). [10.60576/poliba/iris/menduni-giansergio\_phd2021]

*Availability:*

This version is available at <http://hdl.handle.net/11589/226323> since: 2021-05-24

*Published version*

<http://hdl.handle.net/11589/226323>  
DOI: 10.60576/poliba/iris/menduni-giansergio\_phd2021

*Terms of use:*

Altro tipo di accesso

(Article begins on next page)



Politecnico  
di Bari

Department of Electrical and Information Engineering  
Electrical and Information Engineering  
Ph.D. Program  
SSD: ING-INF/01–Electronics

**Final Dissertation**

---

# Development of compact and innovative optical sensors for trace gas detection

---

by  
Menduni Giansergio:

Supervisors:

Prof. Vittorio M.N. Passaro

Eng. Leonardo Chieco

Verena Mackowiak,  
Head of Spectroscopy,  
Thorlabs GmbH

*Coordinator of Ph.D. Program:*  
*Prof. Luigi Alfredo Grieco*

---

*Course n°33, 27/01/2018-26/03/2021*



LIBERATORIA PER L'ARCHIVIAZIONE DELLA TESI DI DOTTORATO

Al Magnifico Rettore  
del Politecnico di Bari

Il/la sottoscritto/a Giansergio Menduni nato/a a Corato (BA) il 12/11/93

residente a Corato (BA) in via Vico Sanza, 4 e-mail giansergio.menduni@poliba.it

iscritto al 3° anno di Corso di Dottorato di Ricerca in Ingegneria Elettrica e dell'Informazione ciclo 33

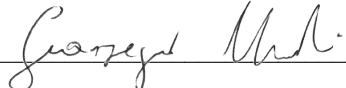
ed essendo stato ammesso a sostenere l'esame finale con la prevista discussione della tesi dal titolo:

Development of compact and innovative optical sensors for trace gas detection

**DICHIARA**

- 1) di essere consapevole che, ai sensi del D.P.R. n. 445 del 28.12.2000, le dichiarazioni mendaci, la falsità negli atti e l'uso di atti falsi sono puniti ai sensi del codice penale e delle Leggi speciali in materia, e che nel caso ricorressero dette ipotesi, decade fin dall'inizio e senza necessità di nessuna formalità dai benefici conseguenti al provvedimento emanato sulla base di tali dichiarazioni;
- 2) di essere iscritto al Corso di Dottorato di ricerca Ingegneria Elettrica e dell'Informazione ciclo 33, corso attivato ai sensi del "Regolamento dei Corsi di Dottorato di ricerca del Politecnico di Bari", emanato con D.R. n.286 del 01.07.2013;
- 3) di essere pienamente a conoscenza delle disposizioni contenute nel predetto Regolamento in merito alla procedura di deposito, pubblicazione e autoarchiviazione della tesi di dottorato nell'Archivio Istituzionale ad accesso aperto alla letteratura scientifica;
- 4) di essere consapevole che attraverso l'autoarchiviazione delle tesi nell'Archivio Istituzionale ad accesso aperto alla letteratura scientifica del Politecnico di Bari (IRIS-POLIBA), l'Ateneo archiverà e renderà consultabile in rete (nel rispetto della Policy di Ateneo di cui al D.R. 642 del 13.11.2015) il testo completo della tesi di dottorato, fatta salva la possibilità di sottoscrizione di apposite licenze per le relative condizioni di utilizzo (di cui al sito <http://www.creativecommons.it/Licenze>), e fatte salve, altresì, le eventuali esigenze di "embargo", legate a strette considerazioni sulla tutelabilità e sfruttamento industriale/commerciale dei contenuti della tesi, da rappresentarsi mediante compilazione e sottoscrizione del modulo in calce (Richiesta di embargo);
- 5) che la tesi da depositare in IRIS-POLIBA, in formato digitale (PDF/A) sarà del tutto identica a quelle **consegnate**/inviata/da inviarsi ai componenti della commissione per l'esame finale e a qualsiasi altra copia depositata presso gli Uffici del Politecnico di Bari in forma cartacea o digitale, ovvero a quella da discutere in sede di esame finale, a quella da depositare, a cura dell'Ateneo, presso le Biblioteche Nazionali Centrali di Roma e Firenze e presso tutti gli Uffici competenti per legge al momento del deposito stesso, e che di conseguenza va esclusa qualsiasi responsabilità del Politecnico di Bari per quanto riguarda eventuali errori, imprecisioni o omissioni nei contenuti della tesi;
- 6) che il contenuto e l'organizzazione della tesi è opera originale realizzata dal sottoscritto e non compromette in alcun modo i diritti di terzi, ivi compresi quelli relativi alla sicurezza dei dati personali; che pertanto il Politecnico di Bari ed i suoi funzionari sono in ogni caso esenti da responsabilità di qualsivoglia natura: civile, amministrativa e penale e saranno dal sottoscritto tenuti indenni da qualsiasi richiesta o rivendicazione da parte di terzi;
- 7) che il contenuto della tesi non infrange in alcun modo il diritto d'Autore né gli obblighi connessi alla salvaguardia di diritti morali od economici di altri autori o di altri aventi diritto, sia per testi, immagini, foto, tabelle, o altre parti di cui la tesi è composta.

Luogo e data Bari, 21/05/2021

Firma 

Il/La sottoscritto, con l'autoarchiviazione della propria tesi di dottorato nell'Archivio Istituzionale ad accesso aperto del Politecnico di Bari (POLIBA-IRIS), pur mantenendo su di essa tutti i diritti d'autore, morali ed economici, ai sensi della normativa vigente (Legge 633/1941 e ss.mm.ii.),

**CONCEDE**

- al Politecnico di Bari il permesso di trasferire l'opera su qualsiasi supporto e di convertirla in qualsiasi formato al fine di una corretta conservazione nel tempo. Il Politecnico di Bari garantisce che non verrà effettuata alcuna modifica al contenuto e alla struttura dell'opera.
- al Politecnico di Bari la possibilità di riprodurre l'opera in più di una copia per fini di sicurezza, back-up e conservazione.

Luogo e data Bari, 21/05/2021

Firma 



Politecnico  
di Bari

Department of Electrical and Information Engineering  
Electrical and Information Engineering  
Ph.D. Program  
SSD: ING-INF/01–Electronics

Final Dissertation

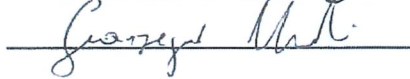
---

Development of compact and  
innovative optical sensors for trace  
gas detection

---

by

Menduni Giansergio:



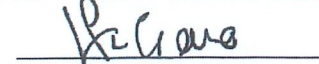
Referees:

Prof. William Whelan-Curtin

Prof. Tomasz Starecki

Supervisors:

Prof. Vittorio M.N. Passaro



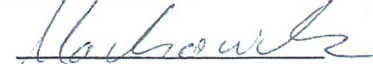
Eng. Leonardo Chieco



Verena Mackowiak

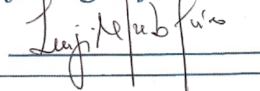
Head of Spectroscopy,

Thorlabs GmbH



Coordinator of Ph.D Program:

Prof. Luigi Alfredo Grieco



---

Course n°33, 27/01/2018-26/03/2021



List of acronyms.....	4
Abstract .....	5
Introduction .....	6
Thesis organization .....	9
Chapter 1: Quartz Enhanced Photoacoustic Spectroscopy.....	12
1.1 Fundamentals of Quartz Enhanced Photoacoustic Spectroscopy.....	12
1.1.1 Fiber-based QEPAS .....	16
1.1.2 Intracavity QEPAS.....	17
1.1.3 QEPAS configuration based on dual micro-resonators and dual quartz tuning forks (QTFs).....	19
1.2 QEPAS with custom QTFs .....	22
1.2.1 QTF modeling .....	23
1.2.2 Custom QTFs design and characterization.....	25
1.2.3 QEPAS with QTF operating in the first overtone flexural mode.....	29
1.2.4 Single-tube micro-resonator coupled with QTF operating at the first overtone flexural mode.....	35
1.2.5 Double antinode excited quartz-enhanced photoacoustic spectrophone.....	36
1.2.6 Simultaneous dual-gas detection.....	39
1.2.7 Energy relaxation dynamics in gas mixtures.....	41
1.3 Resonator Tubes.....	43
1.3.1 Open-end correction in resonator tubes.....	43
1.3.2 Experimental Setup .....	45
1.3.3 Results and Discussion.....	47
1.4 Loss Mechanisms .....	52
1.4.1 Tuning fork design for QEPAS .....	53
1.4.2 Measurement of Resonance Properties .....	54
1.5 Front-End Electronics Architecture .....	59
1.5.1 Front-end electronics.....	59
1.5.2 Measurements of QEPAS Sensor performance.....	62
1.5.3 Results and Discussion.....	64
Chapter 2: QEPAS sensors for real world applications .....	67
2.1 Dual-gas QEPAS sensor.....	68
2.1.1 Dual-gas spectrophone design.....	68
2.1.2 Architecture of dual-gas QEPAS sensor .....	71
2.1.3 Simultaneous QEPAS detection of CH <sub>4</sub> and H <sub>2</sub> O .....	72
2.1.4 Simultaneous QEPAS detection of N <sub>2</sub> O and H <sub>2</sub> O.....	76
2.2 QEPAS sensor for CH <sub>4</sub> environmental monitoring.....	78
2.2.1 QEPAS apparatus for CH <sub>4</sub> environmental monitoring.....	78

2.2.3 Measurements of CH <sub>4</sub> and H <sub>2</sub> O in Air .....	80
2.3 Leak detector .....	89
2.3.1 SF <sub>6</sub> QEPAS sensor architecture .....	90
2.3.2 SF <sub>6</sub> calibration .....	92
2.3.3 SF <sub>6</sub> QEPAS sensor for leak detection .....	94
Chapter 3: Multi-gas detection .....	98
3.1 Trace gas detection of non-interfering absorbers .....	99
3.1.1 Fiber-Coupled QEPAS sensor for CH <sub>4</sub> and C <sub>2</sub> H <sub>6</sub> monitoring .....	99
3.1.2 Detection of methane isotopes .....	109
3.2 Trace gas detection of overlapping absorbers .....	113
3.2.1 CH <sub>4</sub> , C <sub>2</sub> H <sub>6</sub> and C <sub>3</sub> H <sub>8</sub> detection using a QEPAS sensor and an ICL .....	113
3.2.2 Broadband detection of CH <sub>4</sub> and N <sub>2</sub> O using a DFB QCL array .....	125
3.2.3 PLSR as a tool to retrieve gas concentrations in mixtures detected using QEPAS.....	136
3.3 High concentration QEPAS measurements.....	150
3.3.1 CH <sub>4</sub> and C <sub>2</sub> H <sub>6</sub> high concentration detection.....	150
Chapter 4: Integration of QEPAS sensors .....	154
4.1 Modeling and Design of a Semi-Integrated QEPAS Sensor .....	154
4.1.1 Modeling and Design of a Semi-Integrated QEPAS Sensor .....	155
4.1.2 Performance comparison: FS-QEPAS vs SI-QEPAS .....	158
4.1.3 Performances comparison with microresonators: MR-QEPAS vs MRSI-QEPAS .....	160
4.1.4 Optical resonant enhancement: OMRSI-QEPAS .....	162
Conclusions and perspectives.....	166
Bibliography.....	168
List of publications.....	178
Publications on international journal.....	178
Proceeding of international conferences .....	180

## List of acronyms

<b>ADM</b>	Acoustic Detection Module
<b>AM</b>	Amplitude Modulation
<b>C1</b>	Methane
<b>C2</b>	Ethane
<b>C3</b>	Propane
<b>CEU</b>	Control Electronics Unit
<b>CUT</b>	Component Under Test
<b>DAQ</b>	Data AcQuisition
<b>DFB</b>	Distributed FeedBack
<b>FWHM</b>	Full Width at Half Maximum
<b>ICL</b>	Interband Cascade Laser
<b>LAS</b>	Laser Absorption Spectroscopy
<b>MDL</b>	Minimum Detection Limit
<b>MLR</b>	MultiLinear Regression
<b>MVA</b>	MultiVariate Analysis
<b>NNEA</b>	Normalized Noise Equivalent Absorption
<b>OEC</b>	Open-End Correction
<b>PAS</b>	PhotoAcoustic Spectroscopy
<b>PLSR</b>	Partial Least Squares Regression
<b>QCL</b>	Quantum Cascade Laser
<b>QEPAS</b>	Quartz Enhanced PhotoAcoustic Spectroscopy
<b>QTF</b>	Quartz Tuning Fork
<b>RH</b>	Relative Humidity
<b>SCCM</b>	Standard Cubic Centimeter per Minute
<b>SNR</b>	Signal-to-Noise Ratio
<b>TEC</b>	Thermo-Electric Cooler
<b>UAV</b>	Unmanned Aerial Vehicle
<b>WMDM</b>	Wavelength-Modulation Division Multiplexing
<b>WM</b>	Wavelength Modulation

# Abstract

Trace gas sensing is crucial in several application fields. In this thesis, Quartz Enhanced Photoacoustic Spectroscopy (QEPAS)-based sensors were studied, designed and employed to detect gas traces. Quartz Tuning Forks (QTFs) are employed as transducers in this sensing technique. Studies of electrical, mechanical and resonance characteristics of QTFs allowed improvements of QEPAS sensors performances. These innovative sensors were employed to both monitor the presence of pollutants in air and control the quality of mechanical components. Different detection strategies to detect multiple gas traces in mixtures were investigated. Finally, the design of a Semi-Integrated QEPAS sensor is described.

The research activity related to the Industrial Ph.D. Program and presented in this thesis was carried out within the framework of PON RI 2014-2020 “Dottorato di Ricerca a Caratterizzazione Industriale” (DOT130W083), and in collaboration with two industries, i.e., MASMEC S.p.a. (Italy) and THORLABS GmbH (Germany).

# Introduction

Trace gas sensing is crucial in several application fields. In air quality monitoring, the concentration of pollutant substances can reach level lower than part-per-million (ppm) range, thereby this kind of application requires high sensitivity sensors to accurately detect pollutants. For example, methane ( $\text{CH}_4$  or C1) concentration in atmosphere can reach level as low as 1.87 ppm [1]. The accurate C1 detection is critical because of its effect on global warming and climate change. Carbon monoxide (CO) is another marker of atmospheric pollution and it is mainly released from burning of fossil fuels and biomass. Its typical concentration in atmosphere is about 80 part-per-billion (ppb) [2]. Together with high sensitivity sensors, safety monitoring applications require wide concentration range detection, real-time and in-situ monitoring of hazardous gases. For example, high concentration of  $\text{CH}_4$  is transported in pipelines employed in oil and gas industries [3] - [4]. Leakages could occur in pipes; thus, methane could be highly diluted with surrounding air. Trace gas sensors need to be capable to detect a slight increase in the atmospheric C1 concentration and pinpoint the leakage position, following the gradient concentration. Methane can reach percentage-range level close to the leakage spot. Another example is represented by hydrogen sulfide ( $\text{H}_2\text{S}$ ), which is produced in many oil fields. Its concentration can range from ppm to percentage levels [5]. The Occupational Safety and Health Administration (U.S. Department of Labor) lists the acceptable concentration limit for exposure to  $\text{H}_2\text{S}$  at 20 ppm for an eight-hour period, with the maximum peak exposure at 50 ppm for 10 min [6]. Higher concentration levels can cause instant death [7]. In several industrial fields, trace gas sensors can be also employed to test and control the quality of products requiring hermetically closed areas, vessels, and tubes conveying pressurized gases or liquids. Leaks in devices produced by automotive, mechatronics or biotechnology industries (e.g., injectors, artificial heart valves) are a serious threat to the reliability of more complex systems. The test of these devices in a production line requires compact, high stability and short response time sensors. The above listed requirements are also needed in petrochemical applications. In this field, the further capability to detect multiple gas traces is crucial since the monitoring of hydrocarbons such as methane, ethane ( $\text{C}_2\text{H}_6$  or C2) and propane ( $\text{C}_3\text{H}_8$  or C3) represents one of the most efficient ways to predict production outputs, estimate reserves and assess raw material quality of source rocks and reservoirs [8].

Laser absorption spectroscopy (LAS)-based sensors are devices capable to fulfill the abovementioned requirements. Compared with other techniques [9]-[13], LAS allow the realization of sensors characterized by response time lower than 1s, minimal drift, high gas specificity and sensitivity, real time and in situ monitoring without disturbing the gas sample (important in process control). Optical gas sensors are mainly based on light absorption, ruled by the Lambert-Beer's law. Among the LAS techniques [9]-[10], photoacoustic spectroscopy (PAS) is one of the most innovative and sensitive optical scheme, employable to realize trace gas sensors. PAS is based on the detection of acoustic waves, which results from the absorption of modulated light in a specific targeted gas. Light absorbed excites a fraction of the ground-state molecular population into higher energy levels. These excited states subsequently relax through a combination of radiative and non-radiative pathways. The non-radiative component ultimately generates heat in the localized region of the excitation light beam and pressure waves propagate from the source, and then detected by a microphone. The targeted gas is enclosed inside a resonant acoustic cell. The quality factor Q and the resonance frequency of those cells typically fall in the ranges of 40 - 200 and 1 - 4 kHz, respectively. Photoacoustic detection is unique since it is a direct monitor of the non-radiative relaxation channel and, hence, complements absorption spectroscopic techniques. Furthermore, PAS does not require an optical detector and is wavelength independent. Other advantages include small size, large linear dynamic range (from few % to part-per-trillion concentration range), and long-term stability [14]. These advantages make the PAS technology competitive with, and in many cases, preferred to, other trace gas sensing methods. A significant improvement of the PAS technique was made by replacing the microphone with a high-Q factor piezoelectric quartz tuning fork (QTF) with a resonance frequency close to 32.7 kHz. This frequency refers to the plane flexural mode in which the QTF prongs move in opposite directions. This mode is piezoelectrically active (symmetric mode) and has a Q-value of 100 000 or higher when it is encapsulated in vacuum and >10 000 at normal atmospheric pressure. QTF-based PAS is referred to as quartz-enhanced photoacoustic spectroscopy or QEPAS.

The 32.7 kHz QTF were designed for timing application, thus they are not optimized for trace gas sensing. Since 2013, custom QTFs were designed and optimized to be employed in QEPAS sensors [14].

For these reasons, I decided to focus the research activities of my Industrial Ph.D. on design and implementation of innovative and beyond state-of-the-art QEPAS-based

sensing systems. The Ph.D. program was conceived within the framework of PON RI 2014-2020 “Dottorato di Ricerca a Caratterizzazione Industriale” (DOT130W083) and the research goals were pursued in collaboration with two industries, i.e., MASMEC S.p.a. (Italy) and THORLABS GmbH (Germany).

Firstly, as described in section **1.3**, my efforts were focused on the study of the acoustic properties of custom QTFs coupled with resonator tubes. The investigation of loss-mechanisms in QTFs was carried out in section **1.4**, with the aim of identifying design rules for resonators based on i) their figures of merit (i.e., resonance frequency and quality factor) and ii) the required characteristics for the final application, such as expected detection limits, operating conditions, complexity of the gas mixtures. Together with the acousto-mechanical analysis, an investigation of the electrical properties of the quartz resonators was also carried out in section **1.5**. These studies allowed the realization of an efficient front-end amplifier for piezoelectric transducers with a subsequent evaluation of its performance in a QEPAS apparatus.

The technological development of the sensitive element above described set the basis for the implementation of specific sensing architectures devoted to real world applications, reported in **Chapter 2**. In this context, I was directly involved in designing and implementing a dual-gas QEPAS sensing configuration. In this architecture, two vibrational modes of a custom QTF were excited with two laser sources to simultaneously detect environmental pollutants, such as methane or nitrous oxide, and water vapor concentrations in atmosphere. This configuration, reported in section **2.1**, can only be implemented by employing custom QTFs having i) a first overtone mode frequency below 40 kHz and ii) its vibrational antinodes, separated enough to allow an easy alignment of the two laser beams. T-shaped custom QTFs were implemented in a QEPAS sensor aimed at monitoring the part-per-million-level of methane in atmosphere. For this application, described in section **2.2**, I was directly involved in the development of this state-of-art sensor to detect low concentrations of environmental methane while compensating the water vapor effect on methane QEPAS signal, in terms of energy relaxation promotion. For this sensing system, I demonstrated that a commercial hygrometer is reliable enough to be employed in a QEPAS sensor and enable methane signal compensation. This configuration avoids the simultaneous QEPAS detection of both gas ( $\text{CH}_4$  and  $\text{H}_2\text{O}$ ) and keeps the detection scheme and sensor architecture relatively simple. As a further implementation of QEPAS sensors into the industrial world, I designed and realized a compact QEPAS leak

detector to be potentially integrated into production chains of mechatronic components. As reported in section **2.3**, a first validation of the sensor consisted in the evaluation of the sealing of innovative 3D printed vacuum chambers, aimed at replacing the current acoustic detection modules made of stainless steel.

As described in **Chapter 3**, a major topic of my Ph.D. research has been represented by multi-gas detection of hydrocarbons, which is one of the main challenges in the oil and gas field for natural gas analysis. The estimation of production output plays a key role in guiding the exploration and minimizing the environmental impact. The scientific problem consists in a comprehensive detection of the lightest alkanes while the gas matrix can significantly change. In environmental monitoring, the signals due to absorption from multiple gas can overlap in QEPAS spectra, thus making the detection of each gas nontrivial. Therefore, I was strongly involved in the development of different strategies to accurately measure the concentration of gas traces in mixtures.

Finally, as a future perspective, I was involved in the design and modeling of a semi-integrated QEPAS architecture, capable of replacing free-space optics guiding the laser beam and thus improving the sensor robustness. This study, reported in **Chapter 4**, represents a solid starting point for the implementation of a new generation of sensors for environmental monitoring empowered by Unmanned Aerial Vehicles (UAVs) technology and machine learning methods.

## **Thesis organization**

**Chapter 1:** In this chapter, the basic principles and configurations of the Quartz Enhanced Photoacoustic Spectroscopy technique are described. The design and the performance measurements of custom Quartz Tuning Forks are illustrated. Finally, the improvements of QEPAS sensor performances thanks to the modeling of acoustic and mechanical resonators and the design of a voltage front-end amplifier, instead of the commonly used transimpedance amplifier, are discussed.

**Chapter 2:** The employment of QEPAS sensors for real world applications is discussed in this chapter. The first QEPAS sensor described is aimed to the simultaneous monitoring of methane or nitrous oxide and water vapor. Then, a system capable to monitor the presence of methane in atmosphere using the QEPAS technique and simultaneously monitor the

presence of water vapor using an electronic hygrometer is illustrated. Finally, a sulfur hexafluoride (SF<sub>6</sub>) QEPAS sensor employed as leak detector is described.

**Chapter 3:** This chapter is focused on the detection strategies of multiple gases in complex mixtures. In the first QEPAS sensor, two laser diodes capable to independently detect methane and ethane were employed. Then, a quantum cascade laser (QCL) allowed the detection of methane isotopes. In the third QEPAS sensor, a single interband cascade laser (ICL), emitting in a spectral range where absorption features of methane, ethane and propane overlap, was employed to detect the three hydrocarbons. Methane and nitrous oxide detection employing an innovative laser source, composed of a QCL array, in a QEPAS sensor is illustrated. Partial least squares regression (PLSR) was demonstrated to be more efficient than multi linear regression (MLR) when employed in a QEPAS sensor aimed to detect two or three components in a mixture. PLSR proved to be an efficient method even when dealing with nonlinear QEPAS signal related to high concentrations of hydrocarbon in mixture.

**Chapter 4:** The compactness and the robustness of QEPAS sensor can be improved thanks to the integration of the laser beam delivery system. In this chapter, a Semi-Integrated QEPAS sensor is compared to state-of-art QEPAS sensors. The simulated pressure waves generated in both QEPAS sensor versions are comparable, thus implying the feasibility of an integrated QEPAS sensor.



# Chapter 1: Quartz Enhanced Photoacoustic Spectroscopy

The first part of this chapter describes the working principles of Quartz-Enhanced Photoacoustic Spectroscopy (QEPAS) and explains the impact of custom Quartz Tuning Forks (QTF), designed on purpose for spectroscopy, on the latest developments of this technique. In the last three sections, my contributions to the improvements of custom resonators and front-end amplifiers are illustrated.

Starting from the acoustics of 1-D resonators, the geometrical dimensions of the resonator tubes, which are employed as sound amplification system in QEPAS sensor, were analytically derived. Experiments and theory proved to be in good agreement.

The investigations on loss-mechanisms in quartz transducers allowed defining the design rules for QTFs, with the aim of better fitting the resonator characteristics with the target gas features, operating pressure and gas matrix composition.

Finally, a new front-end amplifier was developed and tested in a standard QEPAS sensor, demonstrating an enhanced minimum detection limit for the sensor.

## 1.1 Fundamentals of Quartz Enhanced Photoacoustic Spectroscopy

Quartz-Enhanced Photoacoustic Spectroscopy (QEPAS) represents an alternative approach of traditional photoacoustic detection of gas traces. The basic idea of QEPAS is to accumulate the acoustic energy in a sharply resonant acoustic transducer, avoiding the use of traditional gas-filled photoacoustic cells, thereby removing restrictions imposed on the gas cell design by the acoustic resonance conditions [15]. The transducer is positioned in the acoustic near-field zone of the laser excitation beam and the cell only serves to separate the target sample from the surrounding environment and fix and control its pressure. Conventional microphones are designed to have flat frequency response, whereas QTFs are perfect candidates to detect weak photoacoustic excitation, since they are characterized by a sharp resonant acoustic profile. QTFs operating in the few kHz range can be used, since the energy transfer processes in gases occur on a  $\mu\text{s}$  time scale [16] and the PAS

signal decreases at higher frequencies. The most convenient is the QTF used in electronic timing devices, such as clocks and smartphones as frequency standards, with a resonance frequency of 32 768 Hz in vacuum. A 32 kHz-QTF has been the only QTF employed in QEPAS sensor systems for the first ten years after the invention of this technique in 2002 [17]. Merits of QEPAS include a simple design, no requirement for a spectrally selective optical component, applicability over a wide range of pressure, including atmospheric pressure, capability to analyze trace-gas samples as low as few cm<sup>3</sup> in volume, and immunity to external acoustic noise. A QTF has an acoustic quadrupole geometry, providing good environmental noise immunity. The only way to cause QTF to vibrate via the photoacoustic effect is to produce sound waves from an acoustic source located between the two QTF prongs. The standard way to realize such a condition is to focus the excitation laser beam through the gap between the prongs on the QTF crystal plane. Similar to PAS based sensing systems, the detection sensitivity of QEPAS sensor systems are proportional to the exciting laser optical power [10], [17], [18]. The detected photoacoustic signal can be expressed in the same way as for PAS [15]

$$S \propto \frac{Q \cdot P_L \cdot \alpha}{f} \quad \text{Eq.1.1}$$

where  $f$  is the QTF resonance frequency,  $Q$  its quality factor,  $\alpha$  is the gas target absorption coefficient, and  $P_L$  is the laser power. Thus, the performance of QEPAS-based sensors can benefit from the consistently improved output powers of commercially available near infrared, mid-infrared and far infrared lasers due to the technology developments by the semiconductor industry.

Significant enhancements of the QEPAS signal-to-noise ratio have also been obtained as a result of the implementation of micro-resonators (mR). A mR is formed by one or two thin tubes and the QTF is positioned either between (on-beam QEPAS [19]-[22], [25]) or adjacent to the tube(s) (off-beam QEPAS [23], [24], [26]-[29]) to probe the acoustic vibration excited in the gas contained inside the tubes. A subsystem composed of the QTF and the mR is called a spectrophone or acoustic detection module (ADM). In both on-beam or off-beam sensor configurations, it is critical that the photoacoustic exciting radiation does not hit the ADM, as otherwise an undesirable background that can be several times larger than the QTF thermal noise level arises, with a shifting fringe-like interference

pattern shape, which limits the detection sensitivity [30], [31]. A schematic of a typical QEPAS setup, as used in most reported QEPAS sensor systems, is shown in **Figure 1.1**.

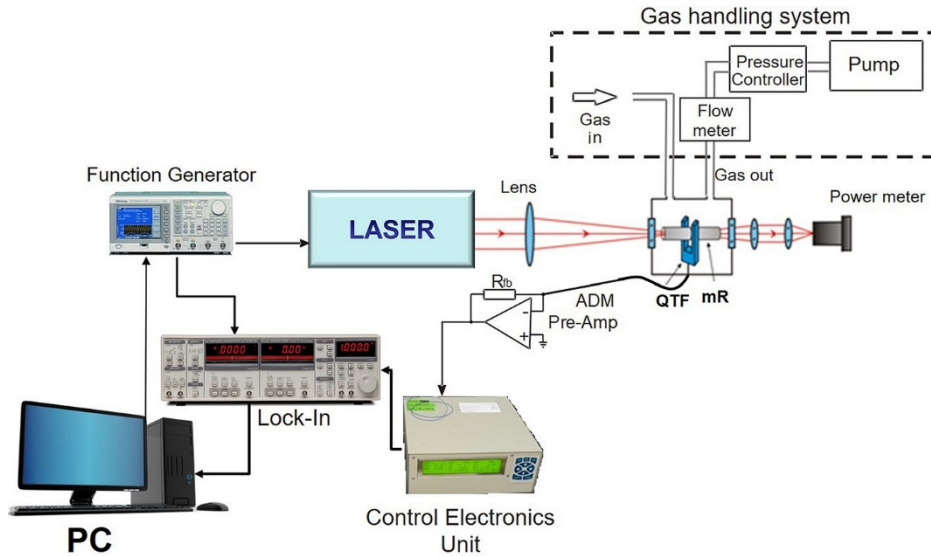


**Figure 1.1** Schematic of a typical QEPAS sensor setup. QTF, quartz tuning fork; mR, acoustic micro-resonator; ADM, acoustic detection module; PC, personal computer [14].

A laser source, typically a quantum cascade laser (QCL) or an interband cascade laser (ICL), serves as the excitation source for generating the QEPAS signal. The ADM is mounted inside a vacuum-tight cell equipped with optical windows. The laser beam is focused by a lens between the QTF prongs and it passes through the ADM. A power meter is used for monitoring the laser power as well as for optical alignment. A function generator is used to sinusoidally modulate either the laser current at the QTF resonance frequency or one of its subharmonics.

The flow rate and pressure of the sample gas passing through the ADM can be controlled and maintained by using a flow meter and pressure controller, respectively. A control electronics unit (CEU) is used to determine the main QTF parameters: dynamic resistance  $R$ , quality factor  $Q$ , and resonant frequency  $f$ . The CEU is also designed to pass on the amplified signal from a transimpedance preamplifier (Pre-Amp) to the lock-in amplifier to demodulate the QEPAS signal. A picture of the commercial ADM developed through a collaboration between THORLABS and PolySense joint-research Lab is shown in **Figure 1.2**.



**Figure 1.2** Picture of the commercial Thorlabs ADM. An optical window and the gas inlet and outlet connectors are also visible [32].

QEPAS based sensor systems are usually operated with a wavelength modulation (WM) and  $2f$  detection configuration in order to suppress background noise originating from spectrally non-selective absorbers (such as the mR, QTF, and the optical windows of the ADM). One important advantage of WM is that only the noise centered within the detection bandwidth will affect trace-gas measurements. In WM, the laser beam is wavelength modulated at  $f/2$  frequency and the lock-in amplifier demodulates the QTF response at  $f$ .

Spectral data can be acquired when the laser wavelength is scanned. For broadband gas species with unresolved rotational spectral structure, the WM approach is not usable since the laser source cannot be wavelength modulated with a sufficient spectral tuning coverage. Thus, the only possibility is to operate in an amplitude modulation (AM) configuration, where the laser is modulated at  $f$  and the QEPAS signals are detected by the lock-in amplifier at the same  $f$  frequency. Unlike WM QEPAS, AM QEPAS is not background free. Residual absorption of laser radiation by the cell windows as well as scattered radiation absorbed inside the gas cell produce a sound at the QTF resonance frequency, thus generating a coherent background. However, this AM QEPAS background can be stable over several hours and hence allows background subtraction [33] - [35].

In the following sections, I introduce several QEPAS configurations employed. The use of fiber-based beam delivery system allowed compacting the system sensor architecture while guaranteeing the state-of-art detection performances. The evanescent wave generated in tapered fibers can be exploited to excite the QTF. This configuration optimize the sensor compactness and robustness, but the reachable minimum detection limits are lower than

those obtained in standard experiments because of the confinement factor of the exponentially decreasing electric field leaking out from the core of the fiber, which results in a lower available optical power between the QTF prongs. The use of optical cavities to realize QEPAS sensors is also described. A possible configuration for building-up the power consists in the use of optical resonators, but the implementation of cavities in free space optics requires a high space occupancy and high reflectivity mirrors to be employed. In Chapter 4, a semi-integrated QEPAS approach consisting in i) beam-delivery based on waveguides and ii) optical build-up obtained by coupling the waveguide with a ring resonator system via evanescent wave is proposed. This approach paves the way for an innovative QEPAS sensing, highly deployable and reliable. Finally, the simultaneous monitoring of two gases is achievable exciting two QTF vibrational modes. The dual micro-resonator configuration is designed to accomplish this task.

### **1.1.1 Fiber-based QEPAS**

One of the critical issues of a QEPAS sensing system is the optical alignment. Different approaches, starting from a standard solution based on focusing lenses, have been implemented to focus the laser light between the QTF prongs and through the mR, with particular care in avoiding that the laser beam illuminates the ADM. This condition is more easily fulfilled if the laser beam power distribution resembles a Gaussian  $TEM_{00}$  profile, as otherwise the use of a pinhole to filter out beam tails becomes necessary. Spatial filters reduce the optical power focused through the QTF and consequently reduce the QEPAS signal. An effective solution for improving the mid-IR laser beam profile is the use of single-mode optical fibers. Both hollow- [39] and solid-core [40] - [42] fibers have been demonstrated to be very efficient for both near-IR diode lasers as well as mid-IR ICL and QCL beam spatial cleaning and can cover the 2  $\mu\text{m}$  - 12  $\mu\text{m}$  spectral range. A schematic of the optical coupling between laser excitation source and the ADM via an optical fiber is shown in **Figure 1.3(a)**.

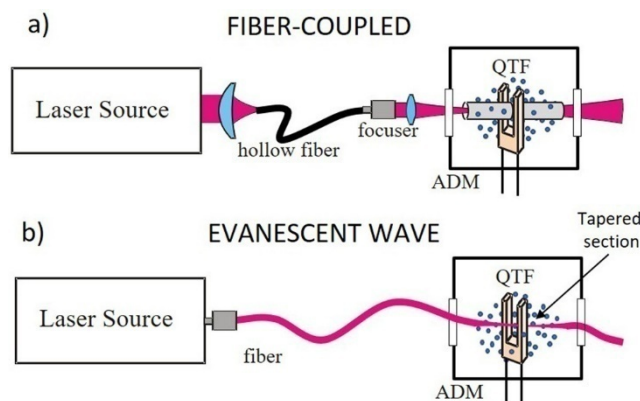


**Figure 1.3 (a)** Schematic of the single-mode fiber-coupling between the laser source and the ADM and **(b)** evanescent-wave approach to excite a gas sample (blue dots) [14].

A laser output focuser is mounted at the fiber exit in order to provide a focusing distance of several centimeters and produce laser beam shaping of the light exiting from the fiber and to be transmitted through the ADM without hitting it. Several QEPAS sensors exploiting single mode mid-IR fibers providing enhanced versatility in terms of flexible laser beam guidance and compactness have been demonstrated [21], [29], [43] - [46]. Another way to guide the laser light through the QTF and generate pressure waves between the prongs is the exploitation of the evanescent wave effect in optical fibers [47] - [49]. This approach has been demonstrated in the near-IR spectral range and is based on fiber tapering. A portion of the tapered fiber is positioned in the gap between the two prongs of the QTF. The laser radiation is guided along the fiber with a very small beam size and the light coming out from the tapered portion of the fiber interacts with the gas sample via the evanescent wave effect. A schematic of the evanescent-wave approach to excite the gas sample is shown in **Figure 1.3(b)**.

The evanescent field generated in the tapered section positioned between the QTF prongs can be absorbed by the target gas molecules surrounding the fiber, thereby generating acoustic pressure waves that are detected by the QTF.

### 1.1.2 Intracavity QEPAS

The QEPAS technique is characterized by direct proportionality between the signal amplitude and the laser power available for gas excitation. An increase of the optical power focused between the QTF prongs improves the minimum detection limit of a QEPAS sensor. Approaches like multi-pass and/or cavity optical build up are used to

increase the interaction length of the laser beam in the gas sample. The first demonstration of a QEPAS sensor exploiting a build-up cavity with high finesse for laser optical power enhancement was reported in [50] and [51]. This novel QEPAS approach combines QEPAS with cavity enhanced absorption spectroscopy (CEAS) and is called intra-cavity QEPAS (I-QEPAS). Using this configuration, CO<sub>2</sub> detection sensitivities in part-per-trillion (ppt) concentration range were achieved [50]. A schematic of the I-QEPAS configuration is shown in **Figure 1.4**.

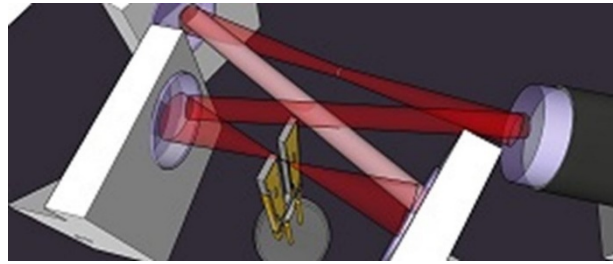


**Figure 1.4** Schematic of the I-QEPAS configuration [14].

In the first I-QEPAS demonstration, a bow-tie resonator system configuration composed by two concave mirrors and two plane mirrors was implemented. The quartz tuning fork (QTF) was positioned at the cavity waist between the two concave mirrors. In I-QEPAS experiments, it is crucial to lock the resonance frequency of the cavity to the laser during the slow linear scan time in order to retrieve a spectral scan of a selected gas absorption line. The simplest way is to adjust the cavity length by using a piezoelectric actuator attached to one of the cavity mirrors mounts. The improvement in terms of sensitivity with respect to conventional QEPAS setup (operating under the same conditions of molecular linewidth, pressure and laser output power) is equal to the power enhancement factor occurring in the optical resonator ( $\sim 240$  in [50] and [51]). Recently, novel compact bow-tie cavities capable to reach power enhancement factors over 300 have been realized [52], [53], promising even further improvements in detection sensitivity. Since to-date a bare QTF was used in I-QEPAS based sensors. Additional improvements are expected by adding a mR to the photoacoustic detection module, potentially leading to the realization of sensors with a part-per-quadrillion (ppq) detection limit. However, a useful figure of merit to compare different types of QEPAS sensors is the normalized noise equivalent absorption (NNEA). The minimum detectable absorption coefficient ( $\alpha_{\min}$ ) can be normalized with the laser power  $P_L$  and the detection bandwidth  $\Delta f_B$  to determine NNEA, defined as  $NNEA = P_L \cdot (\alpha_{\min}) / (\Delta f_B)^{1/2}$ . Typical NNEA values reached with mid-IR QEPAS

sensors fall in the range of  $10^{-8}$ - $10^{-9}$   $\text{W}\cdot\text{cm}^{-1}\cdot\text{Hz}^{-1/2}$  with an integration time of 1 s and assuming typical optical powers of a few tens of milliwatt [14]. Taking advantage from the optical power build-up enhancement factor occurring in the cavity, I-QEPAS experiences a reduction of the  $\alpha_{\min}$  with respect to the QEPAS technique when the same laser source is used (which means the same  $P_L$  value), corresponding to a reduction of the NNEA value to the  $10^{-12}$   $\text{W}\cdot\text{cm}^{-1}\cdot\text{Hz}^{-1/2}$  range, which is compatible with the optical power build-up enhancement factor due to the cavity finesse.

### **1.1.3 QEPAS configuration based on dual micro-resonators and dual quartz tuning forks (QTFs)**

A simplified model, which considers the total momentum of a pressure force acting on the two prongs of the QTF due to a point-source sound wave positioned between the QTF prongs, has allowed calculating the optimal laser beam focus position with respect to the vertical axis for a bare QTF [14]. The results agree with a more detailed theoretical model of a QEPAS sensor proposed by Petra et al. [54] and show a very good agreement with experimental results [14]. For example, for a standard QTF operating at 32 kHz, the optimal vertical position is located at 0.33 mm below the QTF opening and centered between its tines [14]. However, the presence of a mR and its interaction with the QTF alter the acoustic characteristics of the ADM, and the optimal focus position has to be experimental determined. An experimental investigation of the mR position effects was reported in [55] and [56] and demonstrated that the QEPAS signal-to-noise plot as a function of the mR vertical position shows a maximum centered on a nearly flat curve. This flat curve region is sufficiently wide that it allows the positioning of two mRs in a QTF, as shown in **Figure 1.5**. This novel QEPAS configuration has been referred to as “double mR QEPAS.”

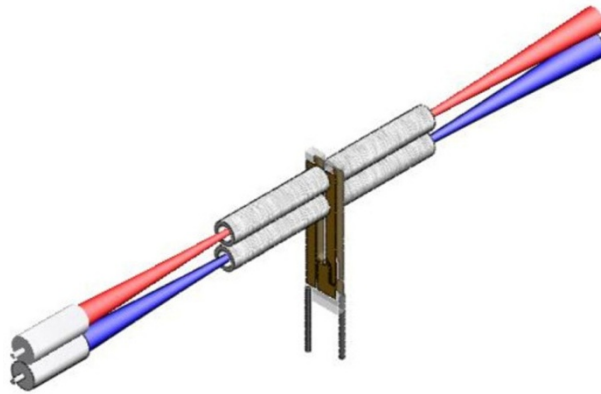


**Figure 1.5** Schematic of double mRs QEPAS [14].

The lowering of the ADM Q-factor due to the acoustic coupling of the QTF with the two mRs leads to an ADM response time 20 times faster compared with a bare QTF and to a wider response bandwidth. Hence, the signal amplitude and phase of the double mR spectrophone become insensitive to small drifts of the resonant frequency compared to the high-Q bare QTF and to the single mR spectrophone. Such a double mR configuration can provide two advantages: (1) two laser excitation sources from different optical wavelength scans perform the optical signal addition or cancellation by means of the spectrophone, avoiding laser beam combination as required by Modulation Cancellation Method or MOCAM [57]-[59] and (2) the spectrophone can implement ultrafast two-gas measurements by switching between two detection channels. Performing a two spectra signal cancellation with the line-locked mode of two lasers at a specific concentration ratio of two target gases, the double mR spectrophone is able to measure directly the deviation of the concentration ratio. The deviation can then be used as a feedback to control gas valves to maintain a specific gas mixing ratio, which is important for controlling gas chemical reactions, gas mixtures or optimizing combustion processes.

Another configuration relies on the use of two QTFs in a single ADM [60]. In this multi-quartz-enhanced photoacoustic spectroscopy (M-QEPAS) sensor system, the acoustic wave signal is detected by multiple QTFs simultaneously and the electrical signals generated by the QTFs is added in order to increase the effective signal amplitude. A schematic of the M-QEPAS configuration is shown in **Figure 1.6**.

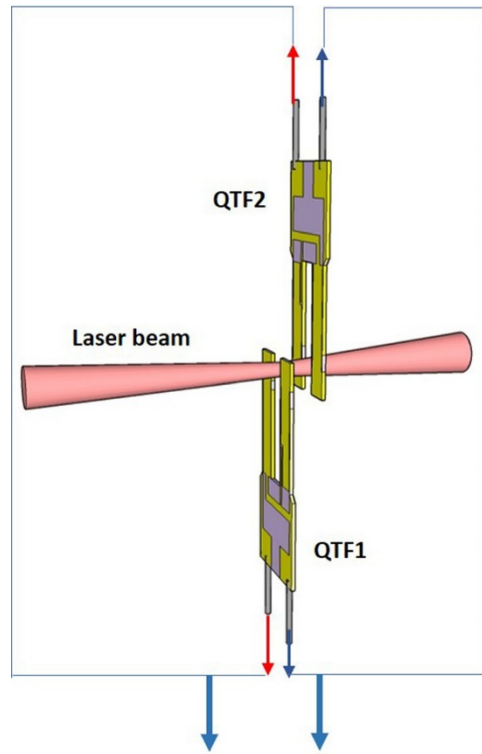


**Figure 1.6** Schematic of M-QEPAS with two QTFs [14].

The results reported in [56], showed that, compared with QEPAS sensor using a bare single QTF, M-QEPAS employing two bare QTFs provided a signal enhancement of 1.7 times for the same operating conditions. Further improvement in detection sensitivity of the M-QEPAS configuration was achieved by employing acoustic micro-resonator tubes for both QTFs, as demonstrated in [61]. Two kinds of multi-QTF based “on-beam” QEPAS spectrophones were realized. Schematics of these two configurations are shown in Figure 1.7.

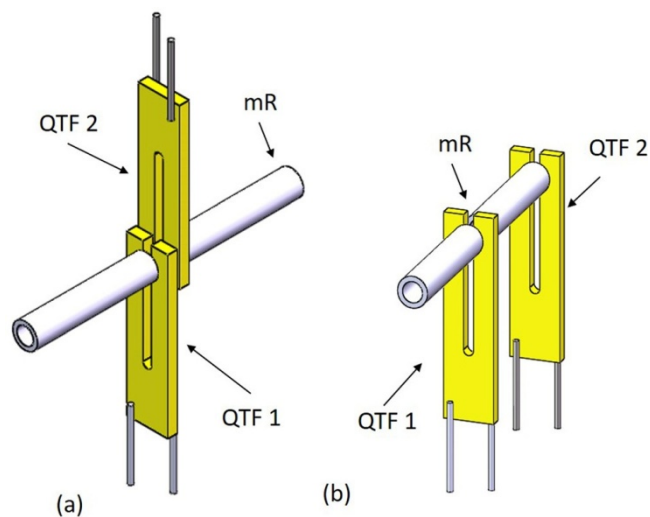


**Figure 1.7 (a) and (b)** Two kinds of multi-QTF based “on-beam” spectrophones [14].

When two QTFs were placed close to each other and in parallel and coupled with two mRs, as shown in **Figure 1.7(a)**, the Q-factor of the multi-QTFs system becomes higher than that of each QTF in a “standard” on-beam configuration using the same mR system. This configuration yielded a 1.4 times enhancement compared to the traditional single QTF based “on-beam” spectrophone and a 33 times enhancement compared to the single bare QTF based spectrophone. For the configuration shown in **Figure 1.7(b)** with the two QTFs spaced by one of the mR tubes, the Q-factor increases with respect to the two QTFs in a “standard” on-beam configuration, but the QEPAS signal is 1.6 times higher than that of the traditional single QTF based “on-beam” spectrophones signal and 36 times higher than that of the single bare QTF based spectrophone. The signal enhancement can be further improved by using a phase shifter to adjust the phase difference among multi-QTFs and a capacitance in series with one of the QTFs to perfectly match the resonance frequencies.

## 1.2 QEPAS with custom QTFs

Prior to 2013, QEPAS sensors reported in literature employed commercial standard QTFs operating at the fundamental in-plane flexural resonant mode, with a frequency of 32.7 kHz. However, as mentioned before, the standard QTFs structure and its operating frequency were optimized for timing purposes and not for spectroscopic applications. Two main factors pose limitations to the use of standard QTFs for QEPAS sensing. First, the QEPAS signal depends strongly on the energy relaxation rates associated with the targeted gas species. The relaxation time constant  $\tau_T$  depends on the specific molecule and on the specific gas carrier (typically either air or  $N_2$ ) and intermolecular interactions. For gases, vibrational-translational (V-T) time constants  $\tau_T$  fall typically in the  $\mu s$  temporal range [62]. To ensure that the energy transfer occurs efficiently for a fast modulation  $f$  of the incident laser radiation, it is necessary to satisfy the condition  $f \ll 0.5 \cdot \pi \cdot \tau_T$  [63]. Therefore, QEPAS is more sensitive to the energy relaxation rate compared to the conventional PAS, which is commonly performed at  $f < 4$  kHz [15], [64]. For gas species with a slow relaxation rate (such as CO,  $CO_2$  and NO), the thermal waves in the gas cannot follow fast changes of the laser induced molecular vibration excitation. Thus, the generated photoacoustic wave is weaker than it would be in case of fast V-T energy equilibration

[10]. Second, standard 32 kHz-QTFs are characterized by a small volume between their prongs ( $\sim 0.3 \times 0.3 \times 3 \text{ mm}^3$ ). Hence, the use of light sources with a limited beam quality, like LED, a fiber amplified laser, or a laser emitting in the THz spectral region ( $\lambda > 30 \text{ }\mu\text{m}$ ), is precluded, since they do not allow adequate focalization of the excitation beam between the prongs spaced by  $300 \text{ }\mu\text{m}$ . The best method to circumvent these limitations is to employ QTFs with larger prongs spacing and operation frequencies possibly  $< 20 \text{ kHz}$  to approach gas relaxation rates, but typically a decrease in  $f$  leads to a decrease of the resonance Q-factor [65], so that a trade-off optimization of the above parameters must be found.

### 1.2.1 QTF modeling

A QTF can be considered as two identical cantilevers coupled by a low-loss quartz bridge. A schematic of a QTF is shown in **Figure 1.8**.

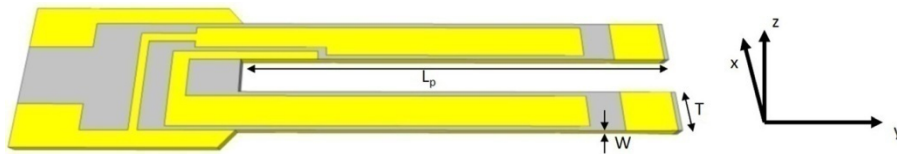


**Figure 1.8** Schematic of a custom QTF with a gold contact pattern. The coordinate system with the y-axis parallel to the beam axis of the prong is depicted. In this way, the prongs bending for in-plane flexural modes occur in the xy-plane [14].

The in-plane flexural vibrations modes of the two prongs can be classified as in phase (symmetric) and out of phase (antisymmetric). The flexural antisymmetric modes, in which the two prongs oscillate in antiphase, are the only vibrational modes employed in QEPAS based sensor systems [66]. The resonance frequencies of the QTF can be calculated in the approximation of an independent cantilever vibrating in in-plane modes. Each prong of the tuning fork can be treated as a clamped beam. In this approximation, the frequencies of the vibrational modes are obtained by including a free-motion condition on one boundary of the prong and a clamped condition on the other (clamped-free boundary condition) and then solving for the propagation of a shear acoustic wave. Assuming that an elastic Young modulus  $E$  of the QTF material, a moment of inertia  $I$  of the prong, and a cross-sectional area  $A = T \cdot W$  are constant along the prong length for small amplitude oscillations, the

motion of each prong can be described using a one-dimensional model and the resonance frequencies in vacuum are given by [67]

$$f_{n,vac} = \frac{\pi T}{8\sqrt{12}L_p^2} \sqrt{\frac{E}{\rho}} v_n^2 \quad \text{Eq. 1.2}$$

where  $\rho = 2650 \text{ kg/m}^3$  is the quartz density,  $E = 72 \text{ GPa}$  is the component of the quartz Young's modulus in the vibrating plane of the QTF.  $L_p$  and  $T$  are the tuning prong length and thickness, as depicted in **Figure 1.8**. The first two eigenmodes values are obtained for  $v_{n=0} = 1.194$  (fundamental mode) and for  $v_{n=1} = 2.988$ , (first overtone mode). Let us consider a QTF vibrating in a fluid medium. The vibration will induce a motion of the fluid and thus the QTF will experience an energy loss (part of the energy is transferred to the fluid or to the bulk) and additional inertia. Therefore, this situation can be modeled by adding a reaction force of the fluid consisting of two terms: a resistive term (which leads to energy dissipation by acoustic loss) and a reactive term (which leads to the additional inertia of the QTF). Taking into account both effects, the Euler-Bernoulli equation expresses the vibrational profile of the single prong results [68]

$$\frac{\partial^4 y}{\partial x^4} + C_d \frac{\partial y}{\partial t} + (\rho A + u) \frac{\partial^2 y}{\partial t^2} = 0 \quad \text{Eq. 1.3}$$

where  $C_d$  is the damping parameter, which accounts for energy loss and  $u$  is the added mass per unit length,  $t$  is the time, and  $x$  and  $y$  directions are represented in **Figure 1.8**. If the damping parameter is negligible, the extra mass term causes a variation of the resonant frequencies of the QTF flexural modes, which now can be calculated as

$$f'_n = \frac{\pi}{8L^2} \sqrt{\frac{EI}{(\rho A + u)}} v_n^2. \quad \text{Eq. 1.4}$$

If the relation  $u \ll \rho A$  is verified, then is possible to calculate the frequency shift  $\Delta f$  due to gas as

$$\Delta f = \frac{f_n - f'_n}{f'_n} = -\frac{1}{2} \frac{u}{\rho A} \quad \text{Eq. 1.5}$$

The added mass is proportional to the density  $\rho_0$  of the fluid medium. Since the relationship between the pressure  $P$  and the density  $\rho_0$  in a gas is  $P \propto \rho_0$ ,  $\Delta f$  varies linearly with the gas pressure and it is possible to rewrite previous equation as

$$f_n(p) = f_{n,vac} - k_{p,n}P \quad \text{Eq. 1.6}$$

where  $k_{p,n} = f_{n,vac} \cdot u / (2\rho WT)$ . The energy dissipation due to acoustic losses in the fluid leads to a reduction of the Q-factor of the flexural mode resonance. A fluid damping parameter can be introduced, which is proportional to the density  $\rho_0$  and the viscosity  $\eta$  of the fluid. Assuming that  $P \propto \rho_0$  and  $\eta$  does not noticeably change with  $P$ , the influence of the fluid damping on Q can be expressed in terms of the energy loss  $1/Q(P)$  at the gas pressure, and considering the damping parameter in the form  $C_d = a \cdot (P)^{1/2}$  [69], where  $a$  is a parameter specific of the tuning fork, the dependence of the Q-factor from the pressure results in

$$Q(P) = \frac{Q_0}{1 + Q_0 a \sqrt{P}} \quad \text{Eq. 1.7}$$

where  $Q_0$  is the Q-factor under vacuum conditions. This analysis describes the behavior of a cantilever beam. Therefore, it is feasible to use a single quartz cantilever beam of the size of the fork's prong as a photoacoustic transducer. In this case, a tuning fork is a system of two coupled cantilevers oscillating in opposition. The result is that, in spite of its arms' motion, the center of mass remains fixed in position. In contrast, a resonating single cantilever beam has an oscillating center of mass. This motion dissipates energy, while this energy dissipation channel is not present in a well-balanced QTF. In a cantilever, the losses due to the center of mass motion are generally large and lead to a reduction of the Q by several orders of magnitude. This explains why only QTFs are used for QEPAS applications.

## 1.2.2 Custom QTFs design and characterization

While the resonance frequencies  $f_{n,vac}$  can be estimated using Eq. 1.2, a prediction of the QTF Q-factor via an analytical method is not possible, since too many extrinsic and intrinsic losses mechanisms contribute to its value. Extrinsic losses mechanisms are due to interactions with the surrounding medium, while the intrinsic losses mechanisms include support losses (interactions with its support structure) as well as thermo-elastic losses. In addition, less predictable factors such as processing anisotropy, crystal quality, and gold patterning contribute to the final Q-factor value. In [66] and [70], a set of QTFs with different values of prong spacing, lengths, and thicknesses as well as crystal thickness were

designed, fabricated, and evaluated, leading to a determination of the dependence of the QTF parameters and performance on their relevant dimensions. The investigated QTF samples' dimensions are listed in **Table 1.1**, while **Figure 1.9** shows the schematic of the seven different QTF designs.

**Table 1.1** Dimensions of standard and custom tuning forks studied in [66] and [70]:  $L_p$  (QTF prong length),  $T$  (thickness of the prong),  $W$  (thickness of the quartz crystal) [14].

Parameters	QTF standard	QTF #1	QTF #2	QTF #3	QTF #4	QTF #5	QTF #6
<b>L (mm)</b>	3.0	3.5	10.0	10.0	11.0	17.0	16.8
<b>W (mm)</b>	0.34	0.25	0.25	0.5	0.25	0.25	0.8
<b>T (mm)</b>	0.35	0.2	0.9	1.0	0.5	1.0	1.4
<b>Prong spacing (mm)</b>	0.3	0.4	0.8	0.5	0.6	0.7	1.0

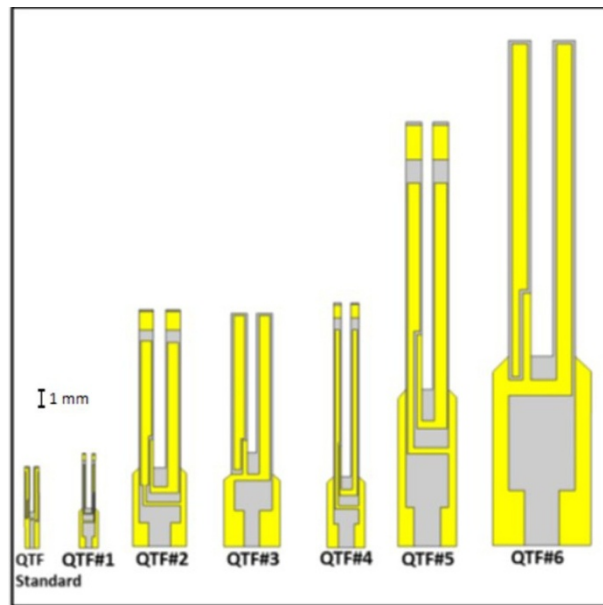


**Figure 1.9** x-z plane view of standard and custom designed tuning forks. The size scale is indicated on the left side. The grey areas represent uncovered quartz, while the gold-yellow area represents gold electrode patterns [14].

The QTFs were realized starting from a z-cut quartz wafer with a  $2^\circ$  rotation along the x-axis. The z-cut is the dominant low frequency (up to 50 kHz) crystal-cut, which provides thermally stable flexural vibrational modes frequencies. Standard photolithographic techniques were used to etch the QTFs. Cr and Au patterns are deposited on both sides of the wafer. The main QTF parameters (resonance frequencies, related Q-factors, and

electrical resistance) were determined by electrically exciting the QTF with a sinusoidal voltage signal generated by an arbitrary function generator (AFG). The current signal is collected and converted into a voltage signal by a transimpedance amplifier and sent to a lock-in amplifier, which demodulates the signal at the same angular frequency set by the AFG. A schematic of the setup used for these measurements is shown in **Figure 1.10**.

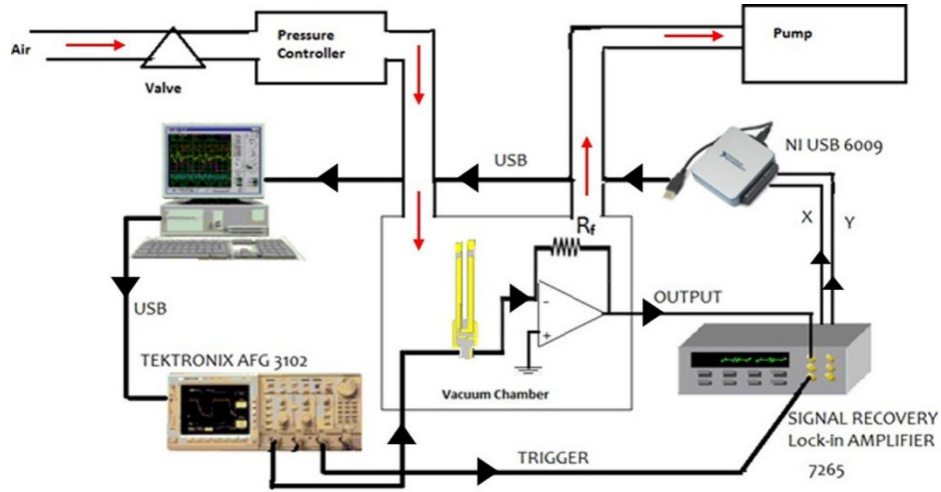


**Figure 1.10** Schematic of a setup used for electrical characterization of QTFs. The excitation sine voltage is supplied by a high-resolution arbitrary function generator (AFG), which also provides the reference TTL signal for the lock-in amplifier. The QTF current output is converted to a voltage by means of a transimpedance amplifier. The QTF is mounted inside a vacuum chamber to perform low gas pressure measurements. Red arrows mimic the gas flux direction [14].

The extracted resonance frequency of the fundamental  $f_{0(exp)}$  flexural mode and the related  $Q_0$ -factors under vacuum conditions are compared in **Table 1.2**, together with the theoretical  $f_{0,vac}$ , calculated using **Eq. 1.4**. In **Table 1.2**, the electrical resistances  $R$  and the  $Q$ -factor ( $Q_{atm}$ ) measured at atmospheric pressure are also listed.

**Table 1.2** Experimental and calculated physical parameters for the QTFs: resonance frequencies of the fundamental mode  $f_{0,vac}$  (calculated) and  $f_{0(exp)}$  (measured) and related quality factor  $Q_0$ . The electrical resistances  $R$  and the  $Q$ -factor ( $Q_{Atm}$ ) measured at atmospheric pressure are also listed [14].

QTF type	$f_{0,vac}$ (Hz)	$f_{0(exp)}$ (Hz)	$Q_0$	$Q_{Atm}$	$R$ (k $\Omega$ )
QTF standard	32743.61	32762.84	88719	13690	94.6

<b>QTF #1</b>	13746.59	14049.20	10862	3980	1913.3
<b>QTF #2</b>	7577.81	7230.27	36564	8400	301.7
<b>QTF #3</b>	8419.79	8439.51	47020	13150	455.6
<b>QTF #4</b>	3479.25	3456.69	23282	3880	990.2
<b>QTF #5</b>	2913.42	2869.07	34800	5210	810.1
<b>QTF #6</b>	4176.48	4250.01	50130	17850	194.1

The small discrepancies (< 5%) between experimental and theoretical values are due to additional weight of the electrode gold layers, dependence of the elasticity modulus of quartz on the crystallographic axes orientation, and deviations in geometry between the modeled and the actual QTFs.

In **Figure 1.11**, the results obtained by plotting the QTFs resistances and Q-factors measured for the QTFs fundamental vibrational mode at atmospheric pressure (see **Table 1.2**) versus the geometrical parameters of the QTFs are shown.

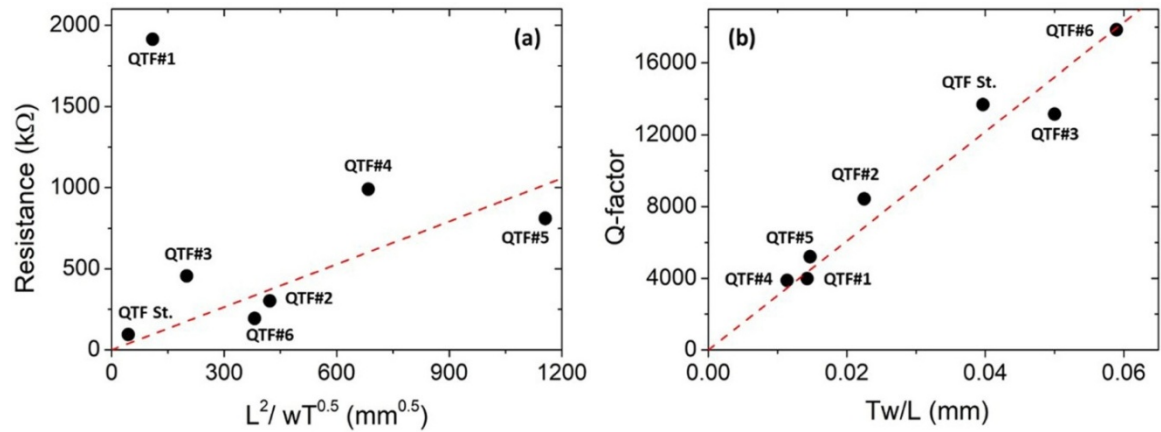


**Figure 1.11** (a) Dependence of the QTFs resistances versus ( $\bullet$  symbols) versus the ratio  $(L_p)^2/W \cdot T^{1/2}$ . QTF St. is the standard QTF. The solid curve is the best linear fit considering only the standard QTF (QTF St.) and QTF#2,3,5,6, using the function  $R = n \cdot (L_p)^2/W \cdot T^{1/2}$ , with  $n = 0.346 \text{ k}\Omega/(\text{mm})^{1/2}$ . (b) quality factor  $Q$  ( $\bullet$  symbols) versus  $WT/L_p$ . The red dashed line is the best linear fit, using the function  $Q = m \cdot WT/L_p$ , with  $m = 3.04 \cdot 10^5 \text{ mm}^{-1}$ . All measurements have been performed at atmospheric pressure [14].

Theoretically,  $R$  is related to geometrical parameters since  $R \sim (L_p)^2/W \cdot T^{1/2}$  [67]. A linear correlation is observed between resistances and  $(L_p)^2/W \cdot T^{1/2}$  values, except for QTF#1 and QTF#4 where the discrepancy is due to the different charge collection efficiency determined by the gold contacts QTF patterns. Noteworthy is the linearity between Q-

factors versus  $W \cdot T/L_p$  values, see **Figure 1.11(b)**. This result allows the empirical prediction of the trend of the Q-factor from the prongs size. For QEPAS applications,  $R$  should be kept low and the  $Q$  as high as possible. Both conditions can be obtained by increasing  $W$  and the ratio  $T/L_p$ . However, the resonance frequency  $f$  increases with  $T/(L_p)^2$  and  $f$  should not exceed 40 kHz since the thermal waves in the gas cannot follow rapid changes of the laser induced molecular vibration excitation. Hence, custom QTFs have been used for QEPAS sensing applications and led to new approaches in QEPAS based sensor technology.

### 1.2.3 QEPAS with QTF operating in the first overtone flexural mode

In QEPAS sensing, the resonance frequency of the QTF must be limited below 40 kHz to ensure that the transfer of the excess energy absorbed by the target gas follows efficiently the fast modulation  $f$  of the incident laser radiation [14]. As already mentioned, for gases with slow energy relaxation rates, the energy transfer does not efficiently follow the laser modulation at 32 kHz [30], [31]. Hence, relaxation promoters (typically H<sub>2</sub>O or SF<sub>6</sub>) are added to the gas sample mixture in order to increase the energy relaxation process.

Using this approach, enhancements of two orders of magnitude in the QEPAS signal have been reported [10], [14], [17], [31], [71], [72]. This requires accurate measurements of the promoter concentration and additional sensor calibration. A reduction of the operational frequency fulfills the  $f \ll 1/2\pi\tau_T$  condition for slow-relaxing gases and was one of the main motivations that guided the realization of custom QTFs. However, the first overtone modes frequencies are also reduced with a decrease of the fundamental resonance frequency to  $\sim 3$  kHz. This opened the way to the implementation of QTF overtone flexural modes for QEPAS trace gas sensing. By using **Eq. 1.4**, it can be verified that the first overtone mode frequency is 6.2 times higher than the fundamental mode. For a 32 kHz-QTF, the first overtone mode falls at frequencies 200 kHz [73] and cannot be implemented in a QEPAS based sensor system. The first demonstration of QEPAS system exploiting a QTF operating on the first overtone flexural mode is reported in [74]. In this case, QTF#5 (having a fundamental resonance frequency at 2.8 kHz and a first overtone mode at 17 kHz) was implemented in a QEPAS based sensor system operating in the near-IR spectral range. The selected target gas was water vapor and allowed a comparison of the QEPAS signal using both the fundamental and first overtone QTF flexural modes. The fundamental

and the overtone mode exhibit different quality factors because the loss mechanisms depend on both the resonance frequency and on the vibrational dynamics of the resonance mode. The dominant loss mechanism is vibration damping due to the medium surrounding the vibrating QTF. A resonating QTF prong in a medium can be physically treated as a solid body immersed in an airflow with a small Reynolds number (i.e., in case of laminar flow). The damping dynamics are derived from the Navier-Stokes equation and the continuity equation for incompressible fluids. When the prongs are oscillating at the  $n$ -th natural flexural frequency, the quality factor associated with air damping  $Q_{air}$  can be assumed to be proportional to [75]

$$Q_{air} \propto \frac{4\pi\rho TW^2 f_n}{3\pi\mu W + \frac{3}{4}\pi W^2 \sqrt{4\pi\rho_a\mu f_n}}, \quad \text{Eq. 1.8}$$

where  $\rho_a$  is the air density,  $\mu$  is the air viscosity.  $Q_{air}$  increases with the resonance frequency, since the air damping effect decreases with an increasing overtone mode order  $n$ . If

$$3/4\pi W^2 \sqrt{4\pi\rho_a\mu f_n} \gg 3\pi\mu W, \quad \text{Eq. 1.9}$$

the  $Q_{air}$  factor can be considered to be quasi-independent of the crystal width  $W$ , which implies that  $f_n \gg 4\mu/(\pi\rho_a W^2)$ . In standard QTF operating conditions (room temperature and pressure in the range 10-760 Torr), this approximation is valid for overtone modes and leads to the following simplified dependence for the  $Q_{air}$ , overtone based on its geometrical parameters:

$$Q_{air, overtone} \propto \frac{8\rho T \sqrt{f_n}}{3\sqrt{\pi\rho_a\mu}} \propto \frac{T^{3/2}}{L_P} \quad \text{Eq. 1.10}$$

For a QTF, the air damping mechanisms are strongly reduced when the QTF vibrates at the overtone mode with respect to the fundamental mode. A second loss mechanism to be considered for a vibrating QTF is support losses. Support losses are due to dissipation of the prong vibrational energy through its support. Hence, support losses are influenced by the vibrational dynamics of the resonance mode. In terms of the Q-factor, the contributions of extrinsic and intrinsic loss mechanisms depend on the vibrational dynamics of the selected resonance mode since each vibrational mode can be characterized by different distributions of its effective mass [76]. The fundamental in-plane flexural mode can be

represented by a single point-mass on the prong tip, while the first overtone can be considered as a system of two-coupled point-mass subsystems, located at two antinodes. The different distribution of the effective mass affects mainly the support losses. Since the dimensions of the support are assumed to be much larger than those of the prong, flexural vibrations can be treated using the single cantilever beam theory. The contribution of the quality factor due to support losses is given by [77]

$$Q_{sup} \propto \frac{1}{k_n^2} \left( \frac{L_p}{T} \right)^3, \quad \text{Eq. 1.11}$$

where  $k_n$  is a constant that increases as the mode number increases. Hence,  $Q_{sup}$  is mainly influenced by the ratio between the prong length and its thickness and decreases for higher order modes. For overtone modes, the higher the  $L_p/T$  ratio, the lower will be the mechanical stress onto the QTF support. The total losses can be evaluated by considering the sum of the different factors causing energy dissipation and hence the overall quality factor for a QTF operating in air can be expressed as

$$\frac{1}{Q} = \frac{1}{K_0} \left( \frac{1}{Q_{sup}} + \frac{1}{Q_{air}} \right). \quad \text{Eq. 1.12}$$

The factor  $K_0$  takes into account the fraction of the collected piezoelectric charge with respect to the total generated charge due to the partial coverage of the QTF surface by electric contacts. To reduce the support losses of the overtone modes, the factor  $(L_p/T)^3$  should be increased, according to **Eq. 1.8**, leading to an increase of the air damping losses, negatively affecting the overall quality factor. Thus, even if the support losses increase with the mode number [77], it is possible to obtain a larger Q-factor for overtone modes with respect to the fundamental mode by optimizing the QTF prongs dimensions in order to strongly reduce the air damping mechanisms, which is the dominant loss mechanism.

The first overtone flexural mode can be modeled as 2-coupled point-masses, each one positioned at an antinode and oscillating in counter-phase. The two antinodes identify the position of the maximum vibration amplitudes along the prong. A typical calculated vibration profiles of the QTF prongs at the first overtone flexural mode for maxima displacements conditions is shown in **Figure 1.12** (for QTF#5) as a function of the distance from the support base for the first overtone mode.

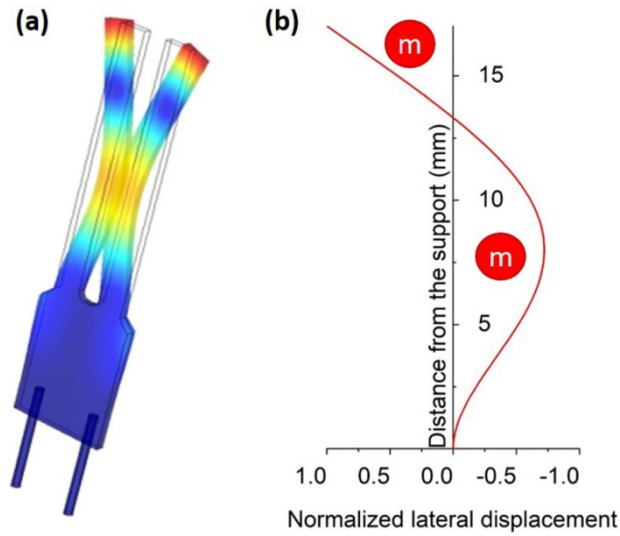


**Figure 1.12** Deformation of the QTF prongs **(a)** and normalized lateral displacement for the QTF#5 first overtone mode calculated as a function of distance from the support and normalized with respect to the maximum value occurring at 17 mm **(b)**. Blue circles represent the point-mass subsystems. Both deformation and vibration profiles have been calculated using COMSOL Multiphysics software [14].

The vibrational profile was calculated assuming standing waves propagating along the two QTF prongs. The QEPAS signal is strongly dependent on the position of the laser focusing point along the QTF symmetry axis. When the focusing spot is located at the antinodes points of the vibration profile, where the maximum vibration amplitude is allowed, the QEPAS signal is maximized. The optimum laser focusing position along the QTF symmetry axis must be identified for each QTF design by measuring the correlated QEPAS peak signals obtained by slowly scanning step by step the laser focusing position along the QTF symmetry axis. A representative first overtone flexural mode QEPAS scan, obtained for QTF#4, is shown in **Figure1.13**.

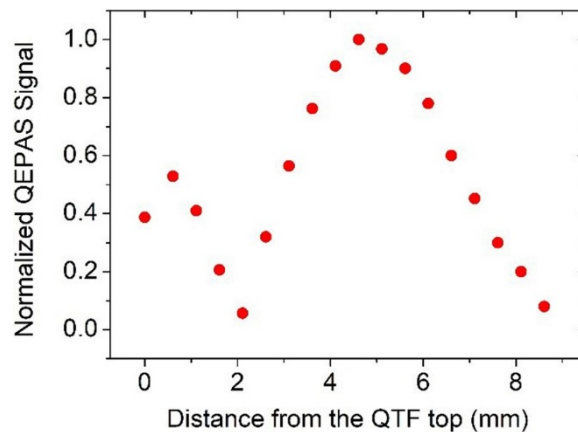


**Figure 1.13** Normalized QEPAS signal as a function of the beam distance from the QTF support measured for the first overtone mode of QTF#4 at atmospheric pressure. The laser beam position was scanned along the symmetry axis of the QTF. All data are normalized to the QEPAS highest signal, measured for the first overtone mode at  $d = 4.7$  mm [14].

The discrepancy between the QEPAS signal at two antinodes results from the spherical symmetry of the exciting acoustic wave. The closer to the prong top is the vertical position of the acoustic source, the larger is the fraction of the pressure wave not hitting the QTF prong. This effect downshifts at 0.8 mm the optimum vertical position of the laser spot for the antinode at the prongs top [10] and do not influence the lower antinode at 4.7 mm that becomes the more efficient one. A similar behavior was observed for other QTFs. More detailed investigations of custom QTFs operating in the overtone flexural modes are reported in [74]. The resonance frequencies for the overtone mode ( $f_i$ ) and related Q-factors ( $Q_i$ ) are reported in **Table 1.4**.

**Table 1.4** Experimental and calculated QTFs physical parameters: resonance frequencies of the first overtone flexural mode  $f_{i,vac}$  (calculated) and  $f_{i(exp)}$  (measured) and related quality factor  $Q_i$ . The operating pressures are also listed [14].

QTF type	$f_{i,vac}$ (Hz)	$f_{i(exp)}$ (Hz)	$Q_1$	P (Torr)
QTF standard	200263.1	191784.66	8500.0	vacuum
QTF #1	86088.96	86574.40	9464.2	760
QTF #2	47456.56	41075.90	10770.3	75
QTF #3	52729.52	51009.13	15895.2	760
QTF #4	21789.04	21497.23	24533.8	75
QTF #5	18245.50	17788.95	31373.8	75
QTF #6	25786.05	25413.10	9800.0	760

A selection of six custom QTFs were investigated to compare QEPAS signals obtained operating at the QTFs fundamental and first overtone flexural modes. QTF#2 and QTF#5 were implemented in QEPAS sensor systems employing a single-mode diode laser as an excitation source, targeting a water absorption line at  $7299.43 \text{ cm}^{-1}$  with a linestrength of  $1.01 \cdot 10^{-20} \text{ cm/mol}$  [78], whereas QTF#4 and QTF#6 were tested using a QCL emitting at  $1296.49 \text{ cm}^{-1}$ , in resonance with a water absorption line having a linestrength of  $1.70 \cdot 10^{-22} \text{ cm/mol}$  [74]. In all cases, the gas samples consisted of air containing a fixed concentration of 1.7% of water vapor. The focused laser spot was positioned between the two prongs at

the vertical positions maximizing the QEPAS signal. In particular, when operating at the QTFs first overtone mode, the lower antinode point was selected. The operating gas pressure and laser modulation amplitude were optimized for each QTF fundamental or first overtone modes. A comparison between the QEPAS spectral scans measured for the two vibrational modes of the investigated QTFs are shown in **Figure 1.14**.

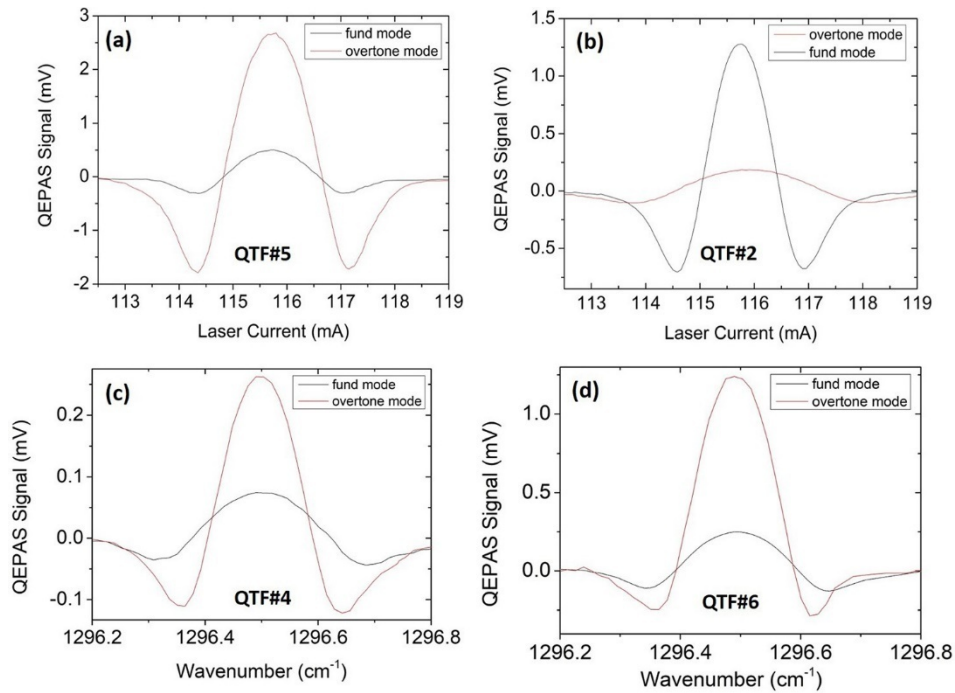


**Figure 1.14** QEPAS spectral scans of a gas mixture containing air with a 1.7% water concentration for the fundamental mode (black solid line) and for the first overtone one (red solid line) of the QTF#5 (a), QTF#2 (b), QTF#4 (c), and QTF#6 (d). QTF#2 and QTF#5 were operated at 75 Torr, while QTF#4 and QTF#6 were operated at atmospheric pressure [14].

For QTF#4, QTF#5, and QTF#6, the QEPAS peak signal acquired when operating at the QTFs overtone mode is higher than the corresponding one measured using the fundamental mode. These results confirmed that, by optimizing the QTF design, it is possible to favor the first overtone flexural mode operation with respect to the fundamental mode one in terms of QEPAS signal.

The design of custom QTFs opened up the possibility to excite the first two flexural in-plane modes for QEPAS experiments. This solution can be implemented to detect simultaneously two different gases with two laser sources. The possibility of exciting the

same gas at different frequencies can be also used to study its relaxation dynamics. In conclusion, the possibility to choose a specific resonator among a large set of custom QTF allows a perfect match between application and sensing apparatus, based on i) the laser source(s) characteristics, ii) relaxation rates of the gas target in a given matrix and iii) overall dimensions and weight required of the sensor for the specific application.

#### **1.2.4 Single-tube micro-resonator coupled with QTF operating at the first overtone flexural mode**

With respect to the standard 32 kHz-QTF, the realization of QTFs with lower resonance frequency and larger prongs spacing is advantageous in terms of gas target relaxation rates and optical sensor alignment. However, implementing dual-tube or single-tube mR for QTFs having resonance frequency  $< 10$  kHz becomes challenging. The length of the mR is correlated with the sound wavelength, given by  $\lambda = v/f$ , where  $v$  is the sound speed (343 m/s in air). As an example, for an  $f$  as low as 10 kHz,  $\lambda = 3.43$  cm. The optimal mR length falls between  $\lambda/2$  and  $\lambda$ , because of the mR acoustic coupling with the QTF, closer to  $\lambda$  for dual-tube mR [19], while closer to  $\lambda/2$  for a single-tube mR [79]. For QTFs operating at frequencies  $< 10$  kHz, the optimal length of the mR system is several centimeters. This makes optical alignment challenging when operating with mid-IR and inhibits operations with a THz laser or excitation sources with limited beam profiles. For example, for QTF#6 operating at 4.2 kHz and implemented in the first demonstration of a THz QEPAS sensor system [80], the optimal single-tube mR length is  $\sim 8$  cm. For QTF#2 operating at 7.2 kHz, this length is reduced to  $\sim 3.8$  cm, still more than 4 times larger than the length of the dual-tube mR used for the commercial 32 kHz-QTF ( $\sim 9$  mm). Since the first overtone frequency is 6.2 times higher than the fundamental one, operating at the first overtone will require a significantly reduced mR length, combined with a higher mode quality factor, when the prong sizes are appropriately chosen. The first demonstration of a QEPAS system implementing a QTF operating at the first overtone flexural mode and coupled with a single-tube mR is reported in [81]. A schematic of the employed setup is shown in **Figure 1.15**.

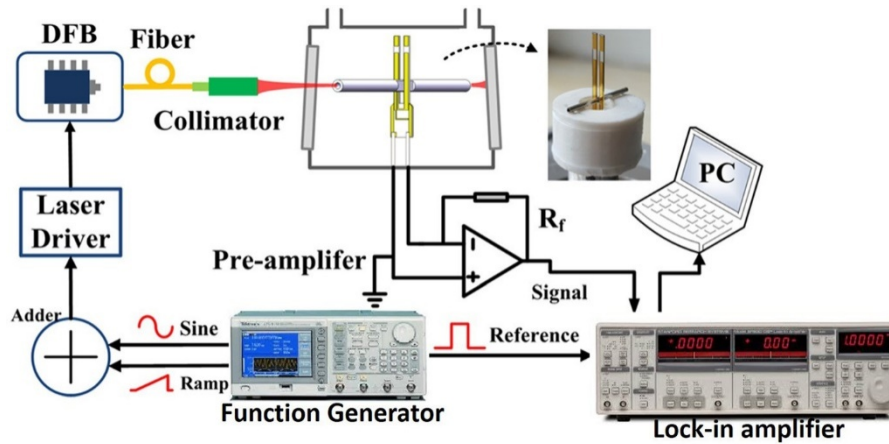


**Figure 1.15** Schematic of the experimental setup. DFB: distributed feedback laser; PC: personal computer;  $R_f$ : feedback resistance [14].

A single-mode continuous-wave distributed feedback (DFB) laser emitting at  $1.37 \mu\text{m}$  was employed as the excitation source to generate photoacoustic signals, targeting a water vapor absorption line. QTF#5 was implemented for this demonstration and the support losses were significantly reduced due to the optimization of geometrical ratio  $L_p/T$ , providing a more than 2 times higher Q-factor for the overtone mode with respect to the fundamental mode [74]. The maximum signal amplitude was obtained for a single-tube length of 14.5 mm, larger than  $\lambda/2$  (9.5 mm), proving that the first harmonic acoustic standing waves in the mR were partially distorted by the two slits present in the resonator. The highest signal amplitude obtained is 50 times larger than that measured using a bare QTF operating in the first overtone resonance mode and 380 times higher than that obtained with the bare QTF operating in fundamental resonance mode. The achieved sensitivity enhancement factor is  $\sim 13$  times higher than that attained by a conventional QEPAS spectrophone based on a commercial 32 kHz-QTF [19].

### 1.2.5 Double antinode excited quartz-enhanced photoacoustic spectrophone

Different from a fundamental flexural mode, the first overtone mode oscillation shows two antinodes, oscillating in counter-phase. Hence, it is possible to excite two resonance antinode points simultaneously by using two laser beams if their phase shift is properly adjusted. The first demonstration of a double-antinode excited quartz-enhanced photoacoustic spectroscopy (DAE-QEPAS) system was reported in [82], implementing

QTF#5 and a dual-tube mR system. The schematic of the double antinode excited QEPAS (DAE-QEPAS) spectrophone is depicted in **Figure 1.16**.

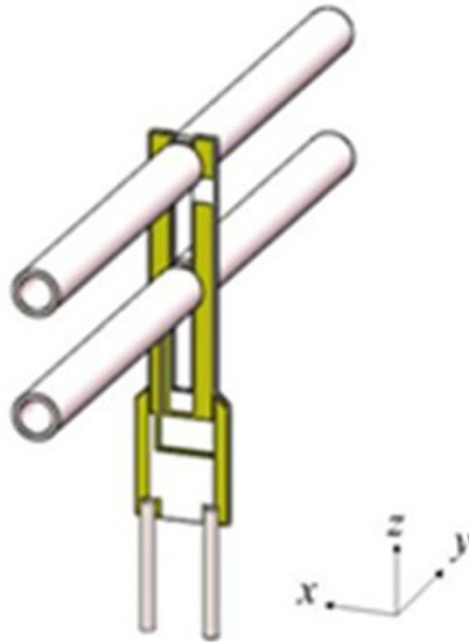


**Figure 1.16** Schematic of the DAE-QEPAS spectrophone [14].

The QTF is positioned between the two mRs tubes to probe the acoustic vibration excited in the gas contained inside the tubes and the two mRs are positioned at heights corresponding to the lower and higher QTF first overtone resonance antinode points. The schematic of the DAE- QEPAS setup is shown in **Figure 1.17**.

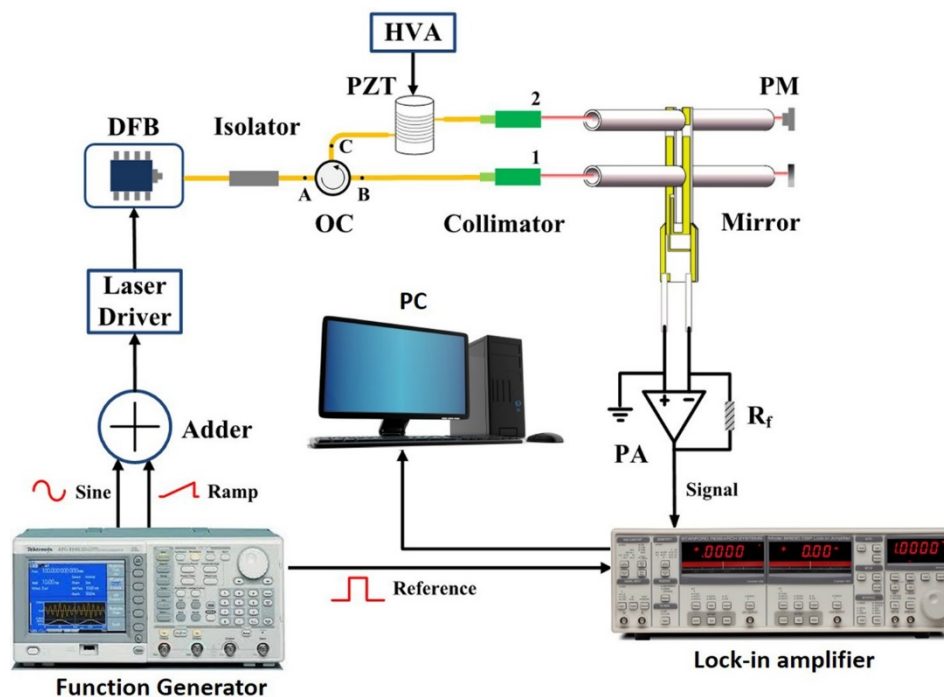


**Figure 1.17** Schematic of the DAE-QEPAS setup. DFB: distributed feed- back diode laser; OC: optical circulator; PZT: piezoelectric transducer; HVA: high voltage amplifier; PM: power meter; PA: pre-amplifier; PC: personal computer; R<sub>f</sub>: feedback resistance [14].

A pigtailed distributed feedback (DFB) laser emitting at 1.37  $\mu\text{m}$  was employed to generate the photoacoustic signal, by exciting a water vapor absorption line located at  $7306.75\text{ cm}^{-1}$  with a line intensity of  $1.8 \cdot 10^{-20}\text{ cm/mol}$ . The PZT phase compensator was used to adjust the phase between the two laser beams passing through the two mRs in order to maximize the QEPAS signal. The phase shift between the two antinode points is  $\sim 180^\circ$ . The laser beam passed twice through the lower mR and once through the upper mR, exciting the two QTF resonance antinodes simultaneously with a compensated phase. The largest QEPAS SNR was obtained employing 8.5 mm-long tubes for the two mRs. The achieved signal amplitude was  $\sim 3$  times higher than that obtained with standard on-beam QEPAS,  $\sim 100$  times higher than that obtained with a bare QTF operating at the first overtone mode and  $\sim 500$  times higher when operating at the fundamental flexural mode resonance. A comparison of the best results achieved with the different on-beam spectrophone configuration reported to date is shown in **Table 1.5**.

**Table 1.5** Comparison of on-beam QEPAS spectrophone configurations. OD: outer tube diameter and ID: inner tube diameter [14].

QTF	Configuration	QTF #	OD (mm)	ID (mm)	mR length (mm)	Gain factor
<b>Custom</b>	<b>Bare QTF</b>	2				1
	<b>Two-tubes</b>	2	1.5	1.3	46	40
	<b>Single-tube</b>	2	0.9	0.65	38	130
	<b>Single-tube + overtone</b>	2	0.98	0.62	14.5	380
	<b>Double antinode + overtone (dual-tube)</b>	5	1.58	1.3	19	500
<b>Standard</b>	<b>Bare QTF</b>	Stand.				1
	<b>On-beam</b>	Stand.	1.24	0.8	10.0	30

The minimum mR length for custom QTFs demonstrated so far is 14.5 mm comparable with the standard 32 kHz-QTF mR length (~10 mm). Further improvement of the SNR gain factor can be achieved either by assembling two single-tube mRs exploiting the on-beam QEPAS spectrophone configuration or by designing and implementing an octupole configuration for the QTF gold pattern in order to increase the charge collection efficiency of the first overtone flexural mode resonance. The possibility to increase the space between the prongs, potentially up to few mm will allow to employ mR tubes with a large ID, thereby simplifying optical alignment and making the QEPAS spectrophone less sensitive to external vibrations in future field applications such as sensing on trains or on-drones.

### 1.2.6 Simultaneous dual-gas detection

Multi-gas on-line detection is a topic of considerable interest in recent years because of its important applications in environmental monitoring, medical diagnosis, industrial process control, agriculture and food industries, and pollution monitoring. In several cases, like isotope concentration ratios, to retrieve the actual ratio value, the concentration measurements of two isotopes must be performed simultaneously. This is also the case when it is required to control the relative concentration of two different gas target in a matrix that rapidly changes with time, as in agricultural applications or from sample to sample, as in breath analysis (e.g., NO and H<sub>2</sub>O). With a standard QEPAS approach, simultaneous gas detection is not feasible since the force sensing based QTF cannot recognize the molecular source of an induced acoustic wave. Even when a single laser source is able to separate two absorption features referred to two different gas species, there is a delay in time in the measurements of two different target gas concentrations,

since the laser source has to be tuned from one absorption line to the other absorption line. However, due to the reduction in the fundamental resonance frequency achieved with custom QTFs, the first overtone flexural mode becomes available for QEPAS operation, allowing the simultaneous excitation of the QTF both on the fundamental and first overtone modes, using the same or two different laser sources. Recently, this approach was employed in the first demonstration of simultaneous dual-gas sensing, based on a QTF frequency division multiplexing (FDM) technique [83]. The QTF in a dual-gas QEPAS sensor is excited simultaneously at the fundamental and first overtone flexural modes by two independently modulated lasers. The two target gases are detected via demodulation of the custom QTF piezoelectric signal at the fundamental frequency  $f_0$  and the first overtone frequency  $f_1$ , respectively, by means of two lock-in amplifiers. The schematic of the developed dual-gas QEPAS system is shown in **Figure 1.18**.

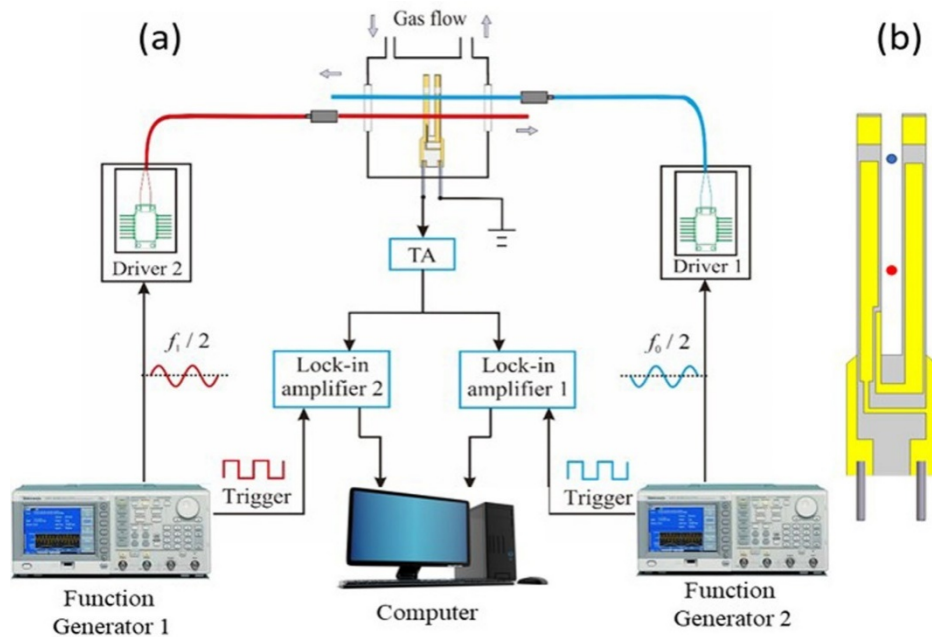


**Figure 1.18 (a)** Schematic of a dual-gas QEPAS sensor system based on a QTF combined vibration at fundamental and first overtone modes. TA: transimpedance amplifier. **(b)** QTF#5 with two focused laser beam spots represented by the red and blue dots [14].

QTF#5 was enclosed inside a gas cell and two laser beams were focused on the QTF plane. The focused beams were positioned near to the antinode point for the fundamental flexural mode (blue dot in **Figure 1.18(b)**) and close to the first overtone flexural mode lower antinode point (red dot in **Figure 1.18(b)**), respectively. The QTF was connected to a custom transimpedance amplifier, which delivered the amplified signal to two lock-in

amplifiers for wavelength modulation detection. A preliminary test with both laser sources tuned to the same wavelength at 1368.6 nm, resonant with a H<sub>2</sub>O absorption line was performed to verify that there are no cross-talking effects between the fundamental and the first overtone flexural mode QEPAS signals, when the QTF was operated in the combined vibrations. No interference effects and no excess noise were observed when the QTF operates in combined vibrational motion with respect to the pure fundamental or first overtone flexural mode. The capability of the QEPAS sensor to perform simultaneous dual-gas spectral detection was demonstrated by implementing a DFB laser source targeting an acetylene (C<sub>2</sub>H<sub>2</sub>) absorption line located at 6541.96 cm<sup>-1</sup> with a linestrength of 3.5·10<sup>-20</sup> cm·mol<sup>-1</sup> [78] and a diode laser targeting a H<sub>2</sub>O absorption line. The QEPAS spectra of both H<sub>2</sub>O and C<sub>2</sub>H<sub>2</sub> were acquired continuously without signal cross-talking. The sensor performance in terms of NNEA coefficient for water vapor and C<sub>2</sub>H<sub>2</sub> are 9.12·10<sup>-7</sup> cm<sup>-1</sup>·W/(Hz)<sup>1/2</sup> and 1.51·10<sup>-7</sup> cm<sup>-1</sup>·W/(Hz)<sup>1/2</sup>, respectively. The difference in performance is due to the different QEPAS response of QTF#5 for the fundamental vibrational mode with respect to the first overtone mode, which is ~6 times higher for the latter. This difference can be adjusted by optimizing the QTF prongs geometry. Applications of a dual-gas QEPAS system include detection of gases with slow energy relaxation rates (such as NO, CO, and CH<sub>4</sub>). As mentioned previously, to enhance the QEPAS signal, relaxation promoters (typically H<sub>2</sub>O or SF<sub>6</sub>) are added to the gas mixture and are crucial to control their concentration levels. Thereby, the additional detection channel can be devoted to monitoring the relaxation promoter concentration and using this information to normalize the slow-relaxing gas QEPAS signal amplitude [84]. Further improvements of dual-gas QEPAS sensors performances can be achieved by adding dual- or single-tube acoustic micro-resonators to enhance the generated photoacoustic wave intensity.

### 1.2.7 Energy relaxation dynamics in gas mixtures

A crucial aspect in QEPAS detection is the dependence of the QEPAS signal on the radiation-to-sound conversion efficiency  $\varepsilon$ , which affects the sound wave generation within the gas. When the light is periodically absorbed by the gas, the excess energy is mainly dissipated through non-radiative relaxation processes, involving vibrational and rotational excited states. Sound waves are then generated via energy transfer from excited states to translational degrees of freedom (V-T relaxation) [85]. With respect to the standard QTF

resonance frequency of 32.7 kHz, gas species can be categorized in two groups, fast and slow relaxing gases, usually referring to relatively low concentrations (ppm range or lower) of the absorbing analyte in a matrix of inert gas, typically N<sub>2</sub>. For slow relaxing gases, the 32.7 kHz laser modulation frequency is significantly higher than the effective analyte relaxation rate in the gas matrix, not allowing a complete release of the absorbed energy during each oscillation period. Thereby, the realization of custom QTFs with resonance frequencies < 32.7 kHz paved the way to the efficient detection of slow-relaxing molecules concentration and leading to improved sensitivity levels [14]. Conversely, for fast relaxing gas species, the relaxation rate is significantly faster than the optical modulation frequency and an efficient energy transfer occurs between absorbing molecules and surrounding gas matrix during each oscillation period [86]. However, the effective relaxation rate of a target gas depends on the surrounding matrix composition. Therefore, fast relaxing gases (such as H<sub>2</sub>O) can be added in the gas matrix to act as relaxation promoters, thereby enhancing the target analyte relaxation rate and the QEPAS detection sensitivity [87]. In this case, the excited target molecules can relax in different channels through collisions with the different types of molecules composing the matrix, including both the buffer and the promoter. The relaxation rate is then given by the sum of the relaxation rate constants  $k_i$  related to collisions with the different types of neighbor molecules, weighted by the concentration  $C_i$  of each species in the mixture [88]. The influence of V-T relaxation rate on photoacoustic signal was first investigated in 1996 by Repond and Sigrist [89], studying its dependence on fundamental thermodynamic parameters, namely the pressure and the temperature. In 2006, Wysocki et al. [90] studied the vibrational relaxation rate on a QEPAS sensor employing a 32.7 kHz-QTF. In this work, the amplitude and phase of the QEPAS signal of CO<sub>2</sub> at a fixed concentration were analyzed as a function of the concentration of H<sub>2</sub>O vapor, acting as V-T promoter. The obtained results highlighted the possibility of estimating absolute relaxation rate, which is the relaxation time of a molecule on itself, starting from known concentrations of the molecules in the mixture. However, a QTF frequency as high as 32.7 kHz is not appropriate for a slow relaxing gas like CO<sub>2</sub>. In general, an accurate estimation of the gases vibrational relaxation rate can only be performed by exploiting different quartz tuning forks having resonance frequencies in a wide frequency range, in order to comprehensively investigate both slow and fast relaxing gases with high accuracy. With this aim, Dello Russo et al. employed custom QTFs with resonance frequencies ranging from 3 kHz to 45

kHz, to measure the effective relaxation time of a relatively slow relaxing analyte like methane, and a fast one like water vapor. For each QTF and respective resonance mode, the CH<sub>4</sub> and H<sub>2</sub>O QEPAS signals, as well as the quality factor of the QTFs were measured as a function of pressure. The radiation-to-sound conversion efficiency was then reconstructed as a function of pressure, for different acoustic frequencies, leading to an accurate estimation of the effective relaxation rates for both gas species. In particular, relaxation times of 3.2 ms·Torr and 0.25 ms·Torr were estimated for CH<sub>4</sub> and H<sub>2</sub>O, respectively, in excellent agreement with values reported in literature [88].

### 1.3 Resonator Tubes

In QEPAS sensors, QTFs are not used as a standalone sound wave detector: they are acoustically coupled with a pair (or a single) of resonator tubes located on both sides (or between the prongs) of the QTF [14], [19]. Resonator tubes act as an organ pipe acoustic resonator and can enhance the intensity of the acoustic field between the QTF prongs up to 60 times [91]. The QTF coupled with a pair of resonator tubes constitutes the QEPAS spectrophone and represents the detection unit of sound waves in a gas. The impact of the spectrophone design parameters on QEPAS performance was investigated in different experimental studies [14], [19]. For a selected QTF, the geometric parameters influencing the sensor performance are the internal diameter (ID) and the length of the two tubes  $l$ . The length of the two tubes is correlated with the sound wavelength  $\lambda = v_s/f_0$ , where  $v_s$  is the sound speed in the sample gas mixture air. If the gap between the tubes is neglected, each tube forms a half-wave resonator with the QTF placed on the antinode point of the sound field. In this section, a theoretical model capable of predicting both the optimal internal diameter and length of the tubes of a QEPAS spectrophone as a function of the QTF prongs geometry and spacing is described.

#### 1.3.1 Open-end correction in resonator tubes

A resonator tube is an open-ended, rigid circular pipe with a negligible wall thickness. When a sound wave generated by a source located close to one end of the resonators propagates through a resonator tube, a standing wave vibrational pattern is created within the resonator when multiple reflected waves from the ends of the resonator constructively interfere with the incident wave, in a way that makes specific points along the resonator appear to be standing. If the resonator tube diameter is small compared to the sound

wavelength, the excited sound field varies only along the resonator length, resulting in a one-dimensional acoustic field. Hence, a resonator tube can be considered as a one-dimensional acoustic resonator. In this approximation, a nearly complete reflection of a dominant mode sound wave occurs at the open end of the resonator. Hence, the standing wave pattern's antinodes should correspond to the open ends of microresonator. Actually, the antinode of a standing sound wave in a resonator with an open end is located slightly outside the end point, at a distance called the open-end correction (OEC). The OEC can be explained by considering the effect of the air surrounding the resonator on the pressure field inside the tube. The mismatch between the one-dimensional acoustic field inside the resonator and the three-dimensional field radiated by the open end outside the resonator causes the pressure field outside the tube to oscillate with the one inside. Therefore, differing from the free-edge boundary conditions, the air inside the tube is affected by the reaction force from the air outside. As a result, the antinode appears a little away from the end of the tube. Ogawa and Kaneko [92] estimated the open-end correction value  $\Delta l$  as being:

$$\Delta l = \frac{8a}{3\pi} \quad \text{Eq. 1.13}$$

where  $a$  is the radius of the acoustic resonator. The OEC should be added to the length of the tube. Therefore, an open-end resonator should have resonances when the sum of the resonator length and the OEC is equal to an integer multiple half the wavelength. Thereby, the corresponding resonance frequencies can be obtained from the following expression:

$$f_n = \frac{n \cdot v_s}{2(l + \Delta l)} \quad \text{Eq. 1.14}$$

where  $n = 1, 2, 3, \dots$  identifies the mode orders of standing waves,  $v_s$  is the sound velocity, and a factor of 2 has been taken into account to consider the two openings of each resonator. By using **Eq. 1.13** and **Eq. 1.14**, the effective length of the resonators for the dominant mode ( $n = 1$ ) can be estimated as:

$$l = \frac{v_s}{2f_0} - \frac{16a}{3\pi} \quad \text{Eq. 1.15}$$

When the propagating waves approach the resonator end, part of the incident waves is back-reflected into the resonator, while the transmitted wave propagates outside the resonator. Levine, H.; Schwinger [93] determined the amplitude and phase of the back-

reflected wave and the amplitude of the diverging spherical wave at a large distance from the resonator end. By choosing the end of the resonator as a reference plane, the distribution of the sound emitted by an isotropically radiating point source at an angle  $\theta$  measured from the axis of the resonator,  $G(ka, \theta)$ , is described using the function:

$$G(ka, \theta) = \frac{4}{\pi \sin^2 \theta} \frac{J_1(ka \sin \theta)}{\sqrt{J_1^2(ka \sin \theta) + [N_1(ka \sin \theta)]^2}} \frac{|R|}{1 - |R|^2} \exp \left\{ \frac{2ka \cos \theta}{\pi} P \int_0^{ka} \frac{x \tan^{-1} \left[ -\frac{J_1(x)}{N_1(x)} \right]}{[x^2 - (ka \sin \theta)^2] \sqrt{[x^2 + (ka)^2]}} dx \right\} \quad \text{Eq. 1.16}$$

where  $|R|$  is the reflection coefficient of the dominant mode, given by:

$$|R| = \exp \left\{ -\frac{2ka}{\pi} \int_0^{ka} \frac{\tan^{-1} \left[ -\frac{J_1(x)}{N_1(x)} \right]}{x \sqrt{[(ka)^2 - x^2]}} dx \right\} \quad \text{Eq. 1.17}$$

$J_1$  and  $N_1$  are the first-order cylinder functions,  $k = 2\pi/\lambda$  is the propagation constant of sound waves in free space, and  $P$  is the notation used to indicate the Cauchy principal value.

### 1.3.2 Experimental Setup

In the on-beam spectrophone configuration, the QTF is positioned between the tubes. The geometrical parameters of the tubes must be properly chosen in order to ensure a sound amplification that is as high as possible. A custom-made QTF with  $s = 1.5$  mm, having a prong length of 9.4 mm and a prong thickness of 2.0 mm, similar to the QTF-S15 presented in Patimisco et al. [91], has been employed. This QTF exhibits a resonance frequency of 15 801.6 Hz and a quality factor of 15 400 in air at atmospheric pressure. This QTF was implemented in the QEPAS setup that is schematically depicted in **Figure 1.19**.

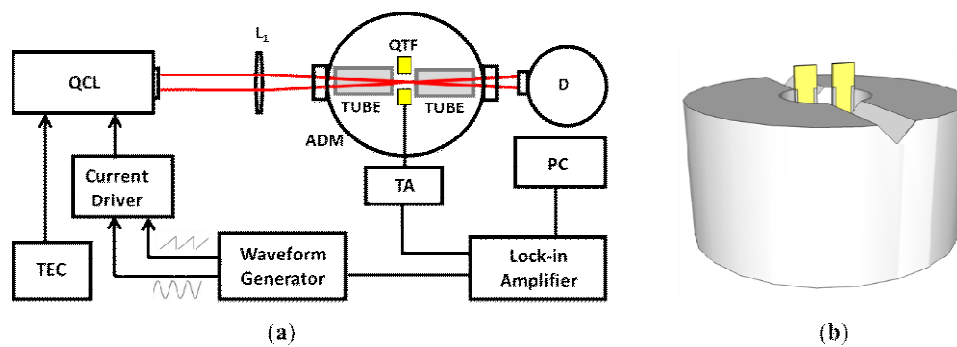


**Figure 1.19 (a)** Schematic of the quartz-enhanced photoacoustic spectroscopy (QEPAS) trace gas sensor system used. The laser beam is focused on the acoustic detection module (ADM) by means of a lens L1. TEC: temperature controller. PC: personal computer. TA: transimpedance amplifier. D: optical detector. **(b)** Sketch of the hollow metallic cylinder: the quartz tuning fork (QTF) is positioned in the center and tubes (not shown in the picture) are located on the V-groove [94].

A single-mode, continuous-wave quantum cascade laser (QCL) emitting at  $7.8 \mu\text{m}$  was employed as the excitation source to generate pressure waves via the photoacoustic effect, targeting a water vapor absorption line at  $1297.19 \text{ cm}^{-1}$  with a linestrength of  $3.6 \cdot 10^{-22} \text{ cm/molecule}$  [78]. At atmospheric pressure, the selected water vapor line is well isolated from other spectral lines of molecules present in standard air. The laser beam was focused between the QTF prongs, 2 mm below the prongs top, using a ZnSe lens with a focal length of 50 mm. The QTF was soldered in an acoustic cell and positioned in the center of a hollow metallic cylinder with a V-groove on the top, properly designed to easily accommodate and fix resonator tubes with different lengths and diameters (see **Figure 1.19(b)**). The gas cell was filled with standard air at atmospheric pressure. The water vapor concentration was kept fixed at 1.7% using a Nafion humidifier and monitored by an external hygrometer. The QCL scanned the selected  $\text{H}_2\text{O}$  absorption line using a slow ramp applied to the current driver. The sensor operated using wavelength modulation and 2f-detection: the laser current was modulated at half of the QTF resonance frequency and the QTF signal was demodulated using a lock-in amplifier at the resonance frequency. Once the spectral scan was recorded, the peak value of the QTF signal corresponding to the water absorption peak was extracted.

### 1.3.3 Results and Discussion

In an on-beam QEPAS spectrophone, each tube is located close to the QTF, perpendicular to its surface, and their dimensions are correlated with the sound wavelength: this results in tubes with lengths in the millimeter range separated by much less than 1 mm. Hence, the tubes can be considered acoustically coupled to each other and the QTF as a probe for the acoustic vibration excited inside the tubes. In other words, the point-sized sound waves source (generated by the photoacoustic effect in the gas) is located between the tubes: the sound wave isotropically propagates inside the two tubes, becomes reflected at one end, and then propagates back to the other end of tube, where one part is returned inside the tube in reflected waves and one part propagates in the other tube until a standing wave pattern is formed. The tubes' geometrical parameters influencing the optical coupling are the internal diameter ID and the length of the two tubes together with the spacing between the tube and the QTF. Due to the ease of processing, low cost, and high quality of the inner surface, metal microresonator tubes have been chosen for this work. Six different tubes with internal diameters ID = 1.36 mm, 1.41 mm, 1.59 mm, 1.83 mm, 2.06 mm, 2.31 mm, and 2.41 mm were investigated at different lengths. By using OEC, the optimal tube length could be estimated. The OEC has been applied to all QTFs used so far for QEPAS sensing to predict the optimal tube length  $l_{th}$  maximizing the sensor performance. In **Table 1.6**, the tube lengths predicted using **Eq. 1.15** were compared with those experimentally found to maximize the QTF signal ( $l_{exp}$ ).

**Table 1.6** Best geometry parameters of dual-tube spectrophones realized for four different QTFs operating at different frequencies: the prongs' spacing ( $s$ ), the internal diameter of the tube (ID), the sound half wavelength ( $\lambda/2$ ), and the theoretical ( $l_{th}$ ) and experimental ( $l_{exp}$ ) optimal tube lengths [94].

QTF frequency (kHz)	Prongs spacing (mm)	ID (mm)	$\lambda/2$ (mm)	$l_{th}$ (mm)	$l_{exp}$ (mm)
32.7	0.3	0.60	5.25	4.7	4.4
7.2	0.8	1.30	23.9	22.8	23.0
25.4	1.0	1.52	6.8	5.5	5.3
12.4	0.8	1.59	13.8	12.4	12.4

From this comparison, it is evident that the OEC predicts the optimal tube length well with an uncertainty of less than 10%. Based on **Eq. 1.15**, the optimal tube length for the QTF

used in this work should linearly decrease from 9.8 mm to 9.0 mm when the tube diameter ranges from 1.3 mm to 2.4 mm.

In **Figure 1.20(a)–(c)**, the QTF peak signal measured with the setup shown in **Figure 1.19(a)** is plotted as a function of the tube length for three representative tube diameters. In all cases, the tubes were placed 150  $\mu\text{m}$  away from the QTF surface. Each point is the mean value of peak values found using at least 20 spectral scans. The fluctuations of the peak value are comparable to a 1- $\sigma$  off-resonance noise value ( $\sigma$ -standard deviation), estimated by tuning the laser far from the water absorption peak.

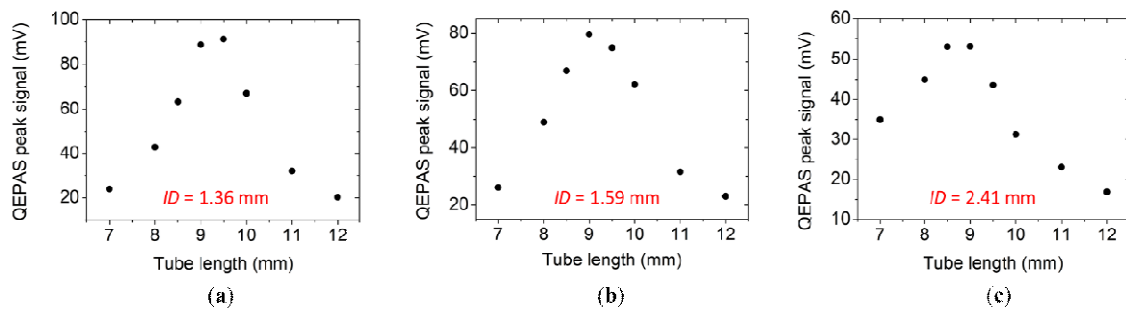


**Figure 1.20** QEPAS peak signals measured with three different spectrophones employing acoustic resonator tubes with an ID = 1.41 mm (a), 1.59 mm (b), and 2.06 mm (c) as a function of the tube length [94].

A  $l_{\text{exp}}$  of 9.5 mm was measured for ID = 1.36 mm and ID = 1.41 mm, while a  $l_{\text{exp}} = 9.00$  mm was found for larger diameters. These results show that the optimal tube length weakly varied with the internal diameter and were in good agreement with the values predicted by the theoretical model, considering the precision on the tubes cut to 500  $\mu\text{m}$ .

The second geometric parameter to be optimized was the distance between the two tubes, which was much smaller than their length. For this reason, the two tubes can be considered as a 1D single resonator. According to the theoretical model proposed, the optimal distance between the tubes is the one maximizing the sound energy transfer from one tube to the other. Geometrically, the transferred energy corresponds to the energy propagating within the cone having a vertex in the center of the open end of one tube and a base at the outer section of the opposite tube, as shown in **Figure 1.21**.

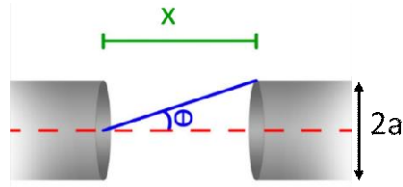


**Figure 1.21** Schematic of two tubes separated by a distance  $x$ . The sound field included within the cone having height  $x$ , vertex angle  $\theta$ , and base  $4\pi a^2$  is supposed to couple with the opposite tube [94].

With a fixed tube diameter  $2a$ , the vertex angle of the cone scales with the tube distance  $x$  is given as  $\theta(x) = \tan^{-1}(a/x)$ . Hence, the amount of transmitted energy can be estimated by integrating Eq. 1.16 from 0 to  $\theta(x)$ . With tubes having a length of 9.5 mm and internal diameter of 1.59 mm, the experimental results and theoretical data are plotted in Figure 1.22 as a function of the distance  $x$ . To compare the two trends, each set of data has been divided by the respective value obtained at  $x = 550 \mu\text{m}$ , which corresponds to the maximum of the experimental data.

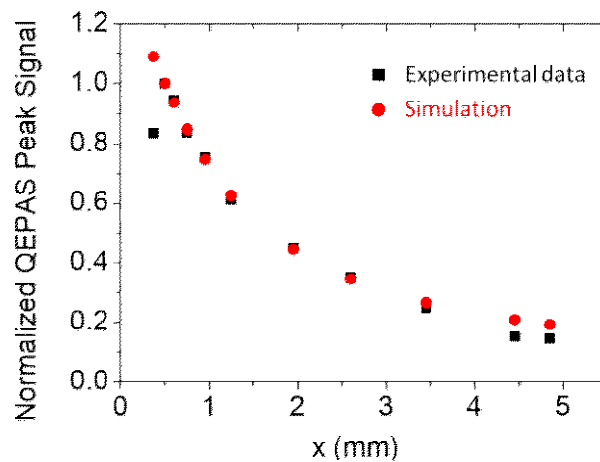


**Figure 1.22** Normalized QEPAS Peak signal as a function of the distance between the two tubes (■), together with the theoretical simulation (●). Both experimental and theoretical values are normalized to the respective value measured at  $x = 550 \mu\text{m}$  [94].

For  $550 \mu\text{m} \leq x \leq 4.8$  mm, the theoretical model matched the experimental data, proving that the QTF acted as a perfect probe for the acoustic field intensity measurement in the area between the two tubes. The highest intensity QEPAS signal occurred at  $x = 550 \mu\text{m}$ , which corresponds to an optimal distance between the QTF surface and the tubes of 150

$\mu\text{m}$ , considering a  $250 \mu\text{m}$  crystal thickness. For a shorter distance,  $x = 400 \mu\text{m}$ , the QTF signal was reduced. This drop was not predicted by the theoretical model but can be explained by considering that when tubes are too close to the QTF, they generate a damping of QTF vibrations, causing an overall quality factor decreasing that negatively affects the QTF signal [95]. At distances larger than  $5 \text{ mm}$ , the sound energy transfer between the tubes was highly reduced; therefore, these distances are not feasible for QEPAS sensing. The theoretical model can also be used to predict the optimal tube radius that maximizes the QTF signal. Placing both tubes at a distance of  $150 \mu\text{m}$  away from the QTF, the vertex angle of the cone will scale according to  $\theta(a) = \tan^{-1}(a/0.55)$  as a function of the tube radius  $a$  (in millimeters). However, if the prong spacing becomes lower than the tube diameter, part of the sound field exiting from the tube will be shielded by the QTF surface. As a consequence, the effective angle  $\theta$  will become  $s/0.55$ , for all  $a \geq s/2$ . The amount of energy transfer can be estimated as:

$$C(ka, \vartheta) = 2 \int_0^{\theta(a)} G(ka, \theta) d\vartheta \quad \text{Eq. 1.18}$$

considering the shielding effect due to the prong's surface when  $a \geq s/2$ . The results of the simulation are shown in **Figure 1.23** for the QTF under investigation and for the standard 32.7-kHz QTF (each curve has been normalized to the related highest value). The model proposed by Levine et al. [93] requires that  $ka \ll 1$ . For a 15.8-kHz QTF,  $ka = 0.22$ , while for the standard 32.7-kHz QTF, it is equal to 0.18. Hence, it is safe to use the theoretical model for both QTFs.

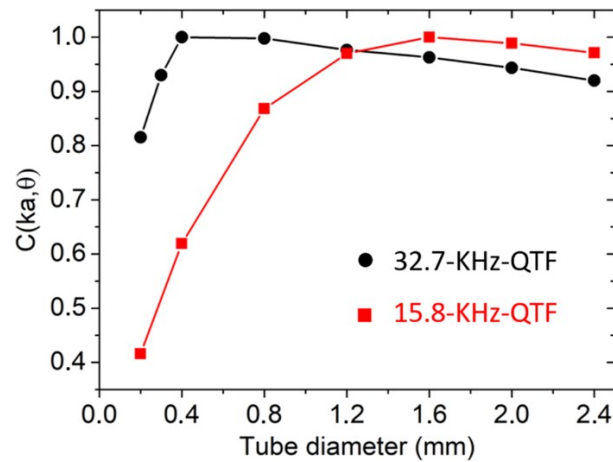


**Figure 1.23** Normalized  $C(ka, \theta)$  calculated as a function of tube diameter by using **Eq. 1.16** and **Eq. 1.18**, for the 15.8-kHz QTF and the standard 32.7-kHz QTF [94].

As predicted, the optimal tube diameter depends on the sound wavelength and the prong spacing. For a standard 32.7-kHz QTF, the model predicted optical tube diameters in the range 400 - 800  $\mu\text{m}$ , in agreement with the values found in Dong et al. [19]. Moving to 15.8 kHz and increasing the prong spacing up to 1.5 mm, the theoretical optical tube diameter fell in the range  $1.4 \text{ mm} \leq a \leq 1.8 \text{ mm}$ . In **Figure 1.24(a)**, the QEPAS peak signal enhancement with respect to the bare QTF is reported as a function of the internal diameter for tubes having  $l_{\text{exp}} = 9.5 \text{ mm}$  for  $\text{ID} = 1.36 \text{ mm}$  and  $1.41 \text{ mm}$  and  $l_{\text{exp}} = 9.0 \text{ mm}$  for all other IDs.

The experimental results show that the largest signal enhancement was obtained for a tube diameter of 1.41 mm, in agreement with the theoretical prediction. Differently from the simulation, the QTF signal decreased rapidly when tubes with diameters greater than the optimal one were used.

The model failed to predict the experimental trend when  $a \gg s/2$ , since in this case, in addition to pressure wave shielding, the prongs' surfaces distort the standing wave pattern, thereby altering the resonance conditions and the sound waves enhancement. Tube diameters lower than 1.38 mm cannot be used to validate the theoretical model since photothermal noise on the QTF signal arises due to a portion of the laser beam touching parts of the spectrophone. The QEPAS scan of the water absorption line measured with the optimal spectrophone ( $l = 9.0 \text{ mm}$  and  $\text{ID} = 1.41 \text{ mm}$ ) is shown in **Figure 1.24 (b)**, together with the QEPAS scan acquired with the bare QTF. The QEPAS peak signal was 93.6 mV, corresponding to a signal enhancement of 26 with respect to the bare QTF, with a comparable noise level, demonstrating that good sound amplification levels can also be achieved with a QTF with a large prong spacing that is comparable to the best result obtained with the standard 32.7-kHz QTF [19], with the advantage of having halved the resonant frequency and exploited a prong spacing that was 5 times larger.

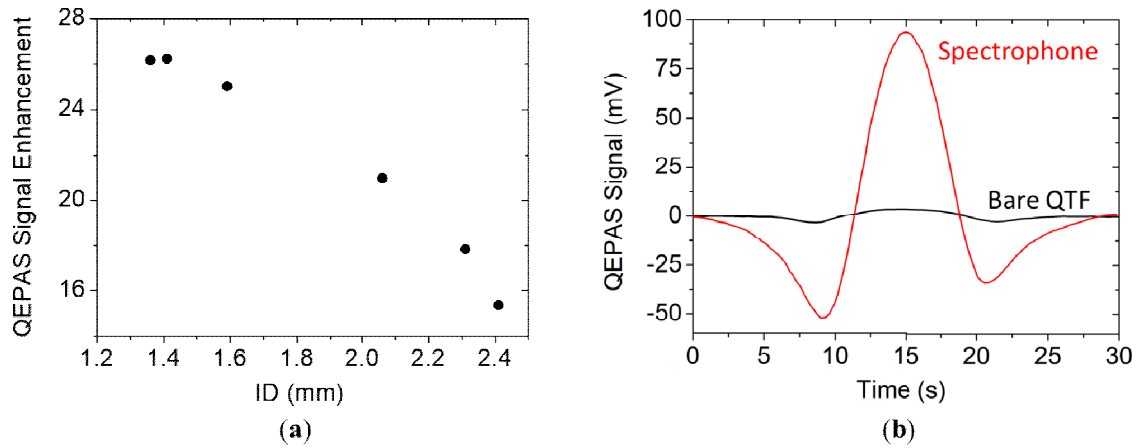


**Figure 1.24** (a) Signal enhancement of the spectrophone signal with respect to the bare QTF signal as a function of the tubes' internal diameter when the optimal tube length was used for each ID. (b) QEPAS spectral scan of water absorption line acquired with the bare QTF (black solid line) and with a spectrophone composed of the QTF and a pair of resonator tubes having a length of 9.5 mm and internal diameter of 1.41 mm, both positioned 150  $\mu\text{m}$  away from the QTF surface (red solid line) [94].

## 1.4 Loss Mechanisms

In QEPAS operation, the tuning fork is used as acoustic transducer to convert sound waves produced by an absorbing gas in an electrical signal. The sound wave generation efficiency is strictly related to the capability of the gas to completely relax the excess of energy before the succeeding light absorption process occurs [74], [90], [96]. This means that the sound wave generation efficiency is mainly determined by the resonance frequency of the vibrating QTF mode. In QEPAS, the operating frequency should not exceed 40 kHz to ensure that the transfer of the excess energy absorbed by the target gas follows efficiently the fast modulation of the incident laser radiation [14]. It was also demonstrated that lowering the resonance frequency is beneficial for QEPAS sensing [97]. This establishes the main constraint in the realization of QTFs to be used as acoustic transducer in QEPAS both at fundamental and first overtone flexural mode. In this section, the measurements of the resonance frequency and quality factor of in-plane flexural fundamental and first overtone resonance modes allow the study of the dependence of main loss mechanisms on the geometry of piezoelectric QTFs.

For this investigation, the first overtone resonance frequency is fixed to 20 kHz: in this way, by using the Euler-Bernoulli equation, the fundamental mode resonance falls at 3 kHz. Lowering the operating frequency at values  $< 3$  kHz is not recommended in QEPAS since the sensor system would be more influenced by the environmental acoustic noise.

### 1.4.1 Tuning fork design for QEPAS

According to **Eq. 1.2**, the constraint on the resonance frequency leads to the length and the thickness of the prongs to be fixed by the relation  $T/L^2 \approx 3.8 \cdot 10^{-3} \text{ mm}^{-1}$ . This condition must be combined with practical requirements. When the QTF is excited both at the fundamental and the first overtone mode in QEPAS, one laser beam is focused close to the antinode point of the fundamental mode, which is located at the top of the QTF, while the second laser beam is focused close to the second antinode point of the overtone mode, located close to the middle of prong [98]. Hence, for practical use, the prong length should be not less than 0.5 cm. In addition, a constraint can be fixed also on the prong thickness  $T$ : QTFs are realized via standard chemical etching and when  $T < 300 \text{ mm}$  imperfections can affect both the geometry and the symmetry of two prongs. All combinations of prong thickness and length satisfying these requirements were simulated. A precision of 1.0 and 0.1 mm was assumed for the prong length and thickness, respectively.  $Q_{air}$  and  $Q_{supp}$  values were calculated by using **Eq. 1.8**, **Eq. 1.10** and **Eq. 1.11**, respectively, assuming a crystal thickness of 0.25 mm. The results are reported in **Table 1.8**.

**Table 1.8** Calculated  $f_0$ ,  $f_1$ , and related  $Q_{air}$  and  $Q_{supp}$  values for QTFs having prong length  $L$  spanning from 10 and 19 mm with related prong thickness  $T$  properly chosen to ensure a fundamental mode resonance frequency  $3.2 \text{ kHz} < f_0 < 3.5 \text{ kHz}$  and first overtone resonance frequency  $19 \text{ kHz} < f_1 < 22 \text{ kHz}$ , estimated by using **Eq. 1.19**.  $Q_{air}$  and  $Q_{supp}$  are calculated by using **Eq. 1.21** and **Eq. 1.22**, respectively [98].

L (mm)	T (mm)	Fundamental mode			First overtone mode		
		$f_0$ (Hz)	$Q_{air}$	$Q_{supp}$	$f_1$ (Hz)	$Q_{air}$	$Q_{supp}$
10	0.4	3367.91	10 894	56 187	19 529.44	31 820	4671
11	0.5	3479.25	15 232	32516	21 091.79	44 277	2703
12	0.6	3508.24	19 425	22158	21 789.04	56 352	1842
13	0.7	3487.48	23 429	16648	21 970.62	67 933	1384
14	0.8	3436.65	27 234	13329	21 840.62	78 996	1108

15	0.9	3367.91	30 845	11153	21 522.24	89 550	927
16	1.0	3288.98	34 272	9634	21 091.79	99 624	801
17	1.0	3204.76	37 527	8524	20 597.46	109 248	709
18	1.2	3378.31	40 624	7681	20 070.05	118 456	639
19	1.4	3265.29	49 598	5524	21 156.89	144 147	459
20	1.6	3367.91	52 304	5202	20 449.11	152 336	432

For both the fundamental and the first overtone mode, the air damping strongly decreases at longer prongs while the support loss increases. Theoretical models describe each loss mechanism as standalone. To investigate which loss mechanism dominates, two different QTF geometries from **Table 1.8** were selected: the first having  $L = 11$  mm,  $T = 0.5$  mm (named hereafter as QTF#1) and the second with a longer prong length,  $L = 17$  mm,  $T = 1$  mm (named hereafter as QTF#2), both with a crystal thickness  $w = 0.25$  mm. A schematic of these QTFs is shown in **Figure 1.25**. Both QTFs were realized starting from a z-cut quartz wafer with a  $2^\circ$  rotation along the x-axis. The geometry was generated by chemical etching and electrodes, consisting of chromium (50 Å thick) and gold (250 Å thick) patterns, were applied photolithographically by means of shadow masks defined on both sides of the wafer. The electrode pattern was designed to enhance the fundamental flexural mode but allowing also the excitation of the first overtone mode [95], [98].

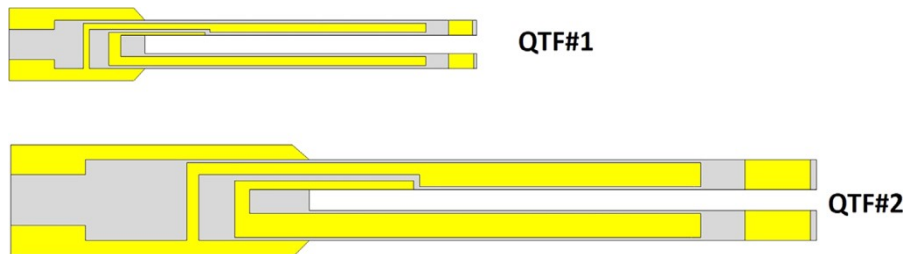


**Figure 1.25** Schematic view of the realized QTFs labelled as QTF#1 and QTF#2 [98].

### 1.4.2 Measurement of Resonance Properties

The properties of a QTF, namely the resonance frequency and the quality factor, can be measured by exciting it electrically. A sketch of the experimental setup is depicted in **Figure 1.26**.

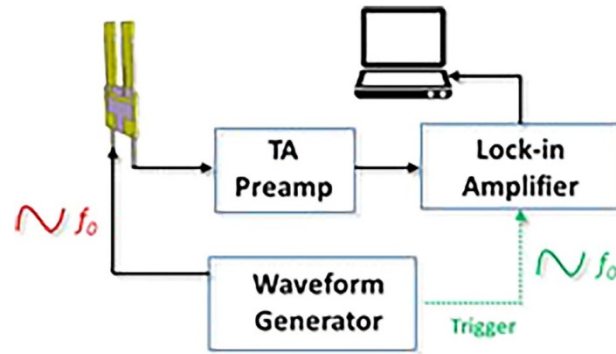


**Figure 1.26** Schematic view of the experimental setup employed to electrically excite QTFs and acquire their frequency spectral response. TA – trans-impedance amplifier [98].

A sinusoidal voltage excitation results in a piezoelectric charge distribution across the QTF prongs. This piezoelectric current is then converted to a voltage signal by means of a transimpedance preamplifier. The voltage signal is then fed to a lock-in amplifier to be demodulated at the same frequency of the signal excitation. The QTF was mounted in a vacuum chamber, connected with a pressure controller and an oil-free pump in order to keep fixed the working pressure. The QTF response curves were acquired by performing a wide frequency scan of the excitation voltage. Since the air damping losses are dependent on the air pressure surrounding the QTF, the QTF response curves were acquired both at atmospheric pressure and at 25 Torr. The resonance curves measured for QTF#1 and QTF#2 at atmospheric pressure, both for the fundamental and overtone mode are shown in **Figure 1.27**.

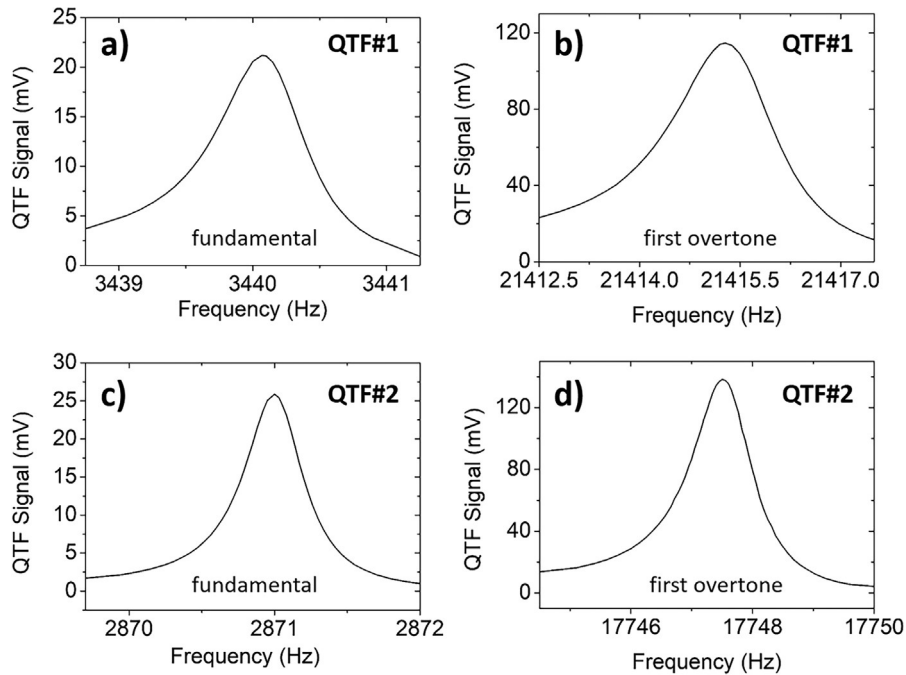


**Figure 1.27** QTFs resonance curves measured at atmospheric pressure in standard air for QTF#1 fundamental (a) and first overtone mode (b), and for QTF#2 fundamental (c) and first overtone mode (d) [98].

Each spectral response was fitted by using a Lorentzian function to determine the resonance frequency, that is, the peak frequency value  $f$  of the Lorentzian fit function, and the full-width-half-maximum (FWHM). The FWHM value allow determining the quality factor as  $Q = f/FWHM$  for the fundamental and overtone mode. In **Table 1.9**, the resonance frequencies and quality factors are reported for both resonance modes, at atmospheric pressure.

**Table 1.9** Resonance frequencies and related quality factor values extracted from **Figure 1.27** for QTF#1 and QTF#2 fundamental and overtone modes, at atmospheric pressure [98].

	Fundamental mode		Overtone mode	
	$f_0$ (Hz)	Q-factor	$f_1$ (Hz)	Q-factor
QTF #1	3440.03	4400	21 415.19	11 370
QTF #2	2870.98	5860	17 747.47	14 570

Discrepancies between the calculated and measured resonance frequency can be mainly ascribed to: 1) gas damping; 2) additional weight of the electrode gold layers; 3) dependence of the elasticity modulus of quartz on the crystallographic axes orientation; 4)

deviations in geometry between the modeled and the real QTFs; and 5) motion of prong support junction that cannot be assumed completely fixed [99]. The results clearly show that moving from the fundamental to the overtone mode, the quality factor increases for both QTF#1 and QTF#2. It can be concluded that air damping is the main losses mechanism affecting the vibrating tuning fork. According to Hosaka's model [75],  $Q_{air, overt}/Q_{air, fund} \approx 2.91$  is expected for both QTFs (see **Table 1.8**), while an increase of the quality factor for the overtone mode of 2.58 and 2.48 with respect to the fundamental mode for QTF#1 and QTF#2 was respectively measured. Hence, it can be supposed that while the air damping effect decreases, the support loss mechanism starts to grow. In addition, QTF#1 exhibits an increase of the quality factor higher than that measured for QTF#2, in agreement with the support losses predicted by Hao's model (see **Table 1.8**) [77]. Since the dissipation mechanisms are assumed independent of each other and the resonator quality factor is proportional to the inverse of total energy dissipated, the overall Q-factor can be calculated as a reciprocal sum of the two independent dissipative contributions (**Eq. 1.12**). By using  $Q_{supp}$  and  $Q_{air}$  values listed in **Table 1.7** for QTF#1 and QTF#2, the estimated quality factor values are: 10373 (QTF#1, fundamental mode), 2547 (QTF#1, first overtone mode), 6946 (QTF#2, fundamental mode), and 704 (QTF#2, first overtone mode). The combination of the Hosaka's and Hao's model predicts a reduction of the overall quality factor by a factor of 4.1 and 9.8 for QTF#1 and QTF#2, respectively, when moving from the fundamental to the first overtone mode. This is in contrast with measurements. However,  $Q_{air}$  is supposed to increase when the first overtone mode is excited, as confirmed by the trend observed for the measured overall quality factors, for both QTFs. In order to reduce the contribution from air damping, the same analysis was performed at 25 Torr. The obtained response curves are shown in **Figure 1.28** and the obtained results are listed in **Table 1.10**.

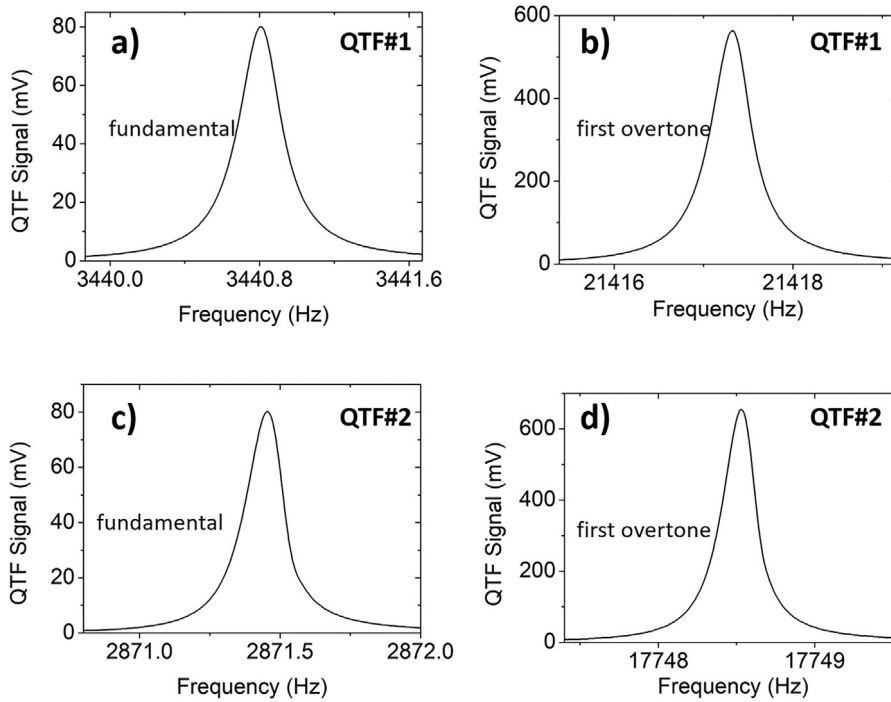


**Figure 1.28** QTFs resonance curves measured at air pressure of 25 Torr for QTF#1 fundamental (a) and first overtone mode (b), and for QTF#2 fundamental (c) and first overtone mode (d) [98].

**Table 1.10** Measured resonance frequencies and related quality factor values for QTF#1 and QTF#2 fundamental and overtone modes at a pressure of 25 Torr [98].

	Fundamental mode		Overtone mode	
	$f_0$ (Hz)	Q-factor	$f_1$ (Hz)	Q-factor
QTF #1	3440.81	11 820	21 419.14	44 680
QTF #2	2871.56	21 340	17 749.53	65 730

The overall quality factors are significantly higher with respect to those measured at atmospheric pressure, for both flexural modes. This further confirms that the vibrating prongs mainly suffer from air damping. Conversely, the model due to Hao predicts a huge contribution of support losses to the overall quality factor. At the first overtone mode, support losses are expected to increase more than one order of magnitude with respect to the fundamental mode, leading to a negligible contribution of  $Q_{\text{air}}$  in the overall quality factor estimation. This disagrees with measurements, allowing affirming that while the Hao’s model well predicts the trend of the support losses as a function of the prong geometry, it overestimates the actual values. Indeed, for QTF #2 overtone mode, the estimated Q - factor is 704, while the observed value is  $Q = 14570$  at atmospheric pressure

and 65730 at 25 Torr. With respect to the fundamental mode, QTF#1 exhibits a quality factor 3.78 times higher at the first overtone mode, while for QTF#2 this factor is 3.08. The discrepancy between these two factors is increased when the pressure is reduced, meaning that the support losses are not negligible. This effect is more evident in the QTF design showing the highest support loss value (QTF#1). Despite that, QTF#2 showed quality factors higher than those obtained for QTF#1, at both modes and pressure values, meaning that for the realization of QTFs with high Q- factors the air damping losses must be minimized. The effect of support losses can become remarkable at pressures much lower than 25 Torr, which is a pressure range typically not feasible for QEPAS operation.

## 1.5 Front-End Electronics Architecture

The collection of transducer signals is crucial to optimize the final sensor performance. Starting from the model of the signal source, several topologies can be implemented to amplify and filter the generated signal. In this section, the investigation on representing a quartz tuning fork as a current or a voltage source aims to enhance the performance of the front-end electronics in terms of the collected signal, thus improving QEPAS sensors final detection limits.

### 1.5.1 Front-end electronics

The most common amplifier architecture employed in QEPAS sensors has a single-ended input configuration, where the voltage signal is referred to ground, as shown in **Figure 1.29(a)**. The noise affecting the QTF signal is a combination of the common-mode and differential-mode noise. This last type of noise is related to the characteristics of the sensitive element (e.g., thermal noise, shot noise) [100]. Once each noise source is characterized, a differential-mode contribution can be lowered by an analog filter. The common-mode noise is mainly related to electromagnetic interferences [101], [102] and their contribution can be lowered by using a differential input amplifier (**Figure 1.29(b)**) [103].

In a typical QEPAS set-up, the amplified QTF signal is further demodulated by a lock-in amplifier. An improvement of the SNR can be achieved by employing a differential demodulation of the QTF signal. In this case, an amplifier architecture with a differential output configuration is required. The two outputs of the amplifier are fed into the lock-in

amplifier for differential demodulation, as shown in **Figure 1.29(c)**. By combining the advantages provided by a differential input and a differential output configuration, a fully differential amplifier, as depicted in **Figure 1.29(d)**, is expected to yield the highest SNR.

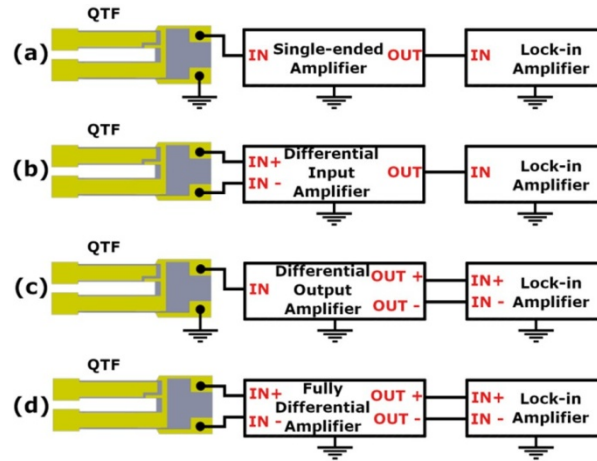


**Figure 1.29** Schematic of the quartz tuning fork (QTF)/front-end amplifier/lock-in connection for four input/output amplifier configurations: **(a)** single-ended, **(b)** differential input, **(c)** differential output and **(d)** fully differential [104].

Among the eight possible amplifier architectures obtained by alternating between a transimpedance and voltage amplifier, combined with the four input/output configurations shown in **Figure 1.29**, the performances of the four amplifier architectures were investigated and compared: a single-ended transimpedance amplifier, a differential output transimpedance amplifier, a differential input voltage amplifier, and a fully differential voltage amplifier. Circuit diagrams of the tested QTF amplifiers are depicted in **Figure 1.30**.

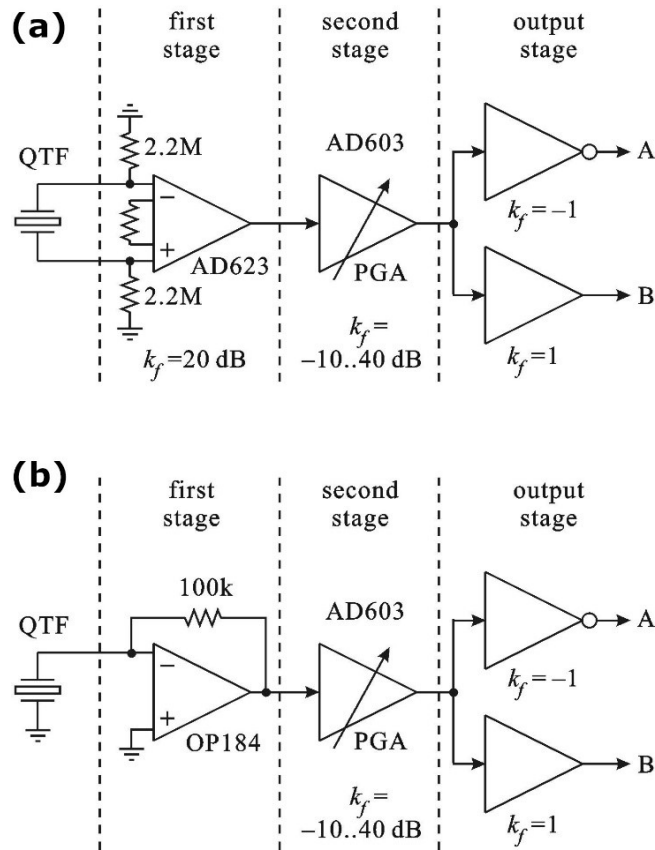


**Figure 1.30** Simplified circuit diagrams of the tested QTF signal amplifiers with: **(a)** voltage amplifier input, **(b)** transimpedance amplifier input [104].

In both cases, the amplifier consists of three stages. The first one contains an input circuit working in a voltage (**Figure 1.30(a)**) or transimpedance (**Figure 1.30(b)**) mode. The use of an instrumentational amplifier (AD623) in the voltage input amplifier (**Figure 1.30(a)**) allows for the implementation of a fully differential input, in which the QTF is placed between the inverting and non-inverting inputs of the amplifier and none of these inputs are tied to the local signal ground of the signal amplifier (the 2.2 MOhm resistors are used only in order to supply the minimum necessary bias current to both inputs). The separation of both inputs from the ground of the measurement apparatus set-up reduces the influence of the noise (such as electromagnetic parasitic interferences from the environment) that may be induced on the ground plane in the case of a non-differential configuration. The transimpedance input (**Figure 1.30(b)**) is implemented in a standard way. The remaining two stages shown in **Figure 1.30(a)-(b)** are identical in both amplifiers. The second stage is a programmable gain amplifier (PGA) based on an AD603 voltage gain amplifier (VGA), in which the gain was adjustable with a potentiometer. A PGA was used instead of

a fixed gain amplifier to easily adjust the gain, depending on the level of photoacoustic signal obtained in the experiments. The third stage consists of two fixed gain amplifiers which produce the output signals in counter-phase. As a result, a single-ended output (if only one of the output channels: A or B is used) or a differential output (in such a case both outputs, A and B must be used) is obtained. Obviously, with such an implementation, the amplitude of the differential output signal was twice the single-ended output signal amplitude.

### 1.5.2 Measurements of QEPAS Sensor performance

The QEPAS sensor setup employed to investigate the performance of the proposed amplifiers is depicted in **Figure 1.31**.

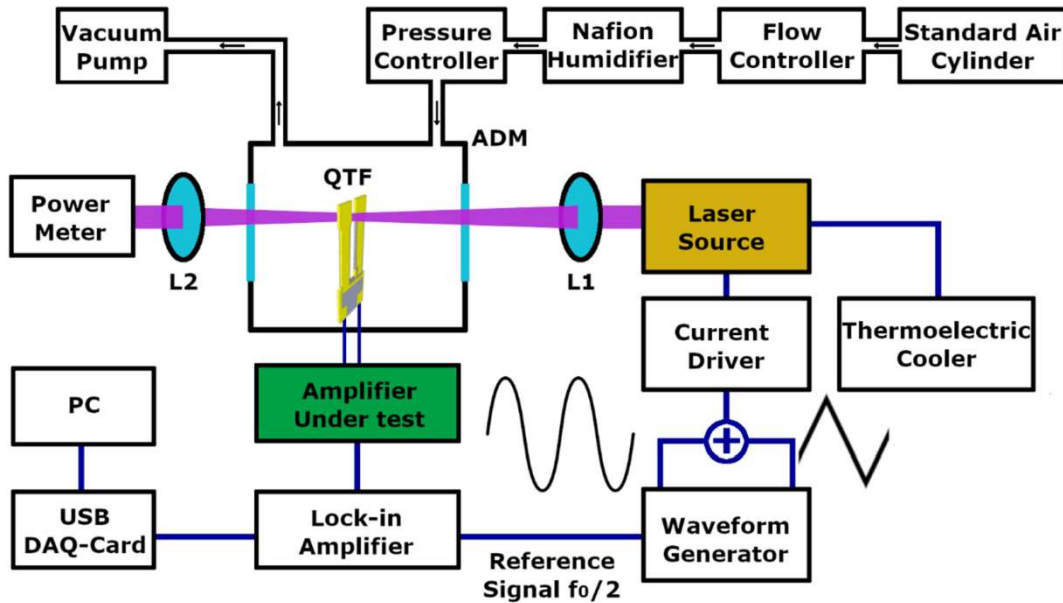


**Figure 1.31** Schematic of the experimental apparatus. ADM-acoustic detection module, QTF-quartz tuning fork, L1, L2-lenses, PC-personal computer [104].

A single-mode continuous-wave distributed-feedback QCL with a central emission at 7.72  $\mu\text{m}$  was used as the light source. The QCL operates in the 20–30  $^{\circ}\text{C}$  temperature range and in the 140–280 mA injected current range. The laser beam was focused between the prongs of the QTF by using a ZnSe lens with a focal length of 75 mm (L1 in **Figure 1.31**). Its transmittance is 95% at the laser wavelength. The employed QTF has prongs spaced by 800  $\mu\text{m}$  in order to minimize possible optical noise due to the light hitting the QTF prongs [105]. The frequency of the fundamental resonance mode is  $f_0 = 12456.16$  Hz at

atmospheric pressure. The QTF is mounted in an acoustic detection module (ADM) equipped with two ZnSe windows for the laser beam entrance and exit. Beyond the ADM, a ZnSe lens (L2 in **Figure 1.31**) collects the light on the sensitive element of a power meter for optical alignment. A standard air cylinder and a Nafion humidifier were used to generate a gas mixture with a constant water vapor concentration of 2%. A gas flow controller was used to fix the mixture flow to 30 sccm, while a vacuum pump and a pressure controller were used to fix the gas pressure to 760 Torr. Wavelength modulation spectroscopy with second harmonic demodulation was employed as a detection scheme [30]. Laser wavelength modulation was achieved by dithering the current driver with a sinusoidal wave with a frequency of  $f = f_0/2$ . A ramp with a frequency of 5 mHz was added to the laser current driver in order to scan the wavelength emission across the absorption line. Both the fast modulation and the ramp were provided by a waveform generator (Tektronix AFG102). The QEPAS sensor architecture allowed for an easy interchange of the QTF front-end amplifiers, without altering the experimental conditions. A National Instrument Data Acquisition (DAQ) card (NI USB-6008) was used to acquire the QTF signal demodulated by a PerkinElmer 7265 lock-in amplifier. The lock-in integration time was set to 100 ms and the signal acquisition time to 300 ms. The reference signal for the lock-in amplifier was provided by the TTL output channel of the waveform generator.

At a laser operating temperature of 20 °C within its current dynamic range, the wavelength emission of the QCL ranges from 1296 to 1298  $\text{cm}^{-1}$ . In this spectral range, the HITRAN database was used to simulate the absorption cross-section spectrum of standard air [78] as shown in **Figure 1.32**.

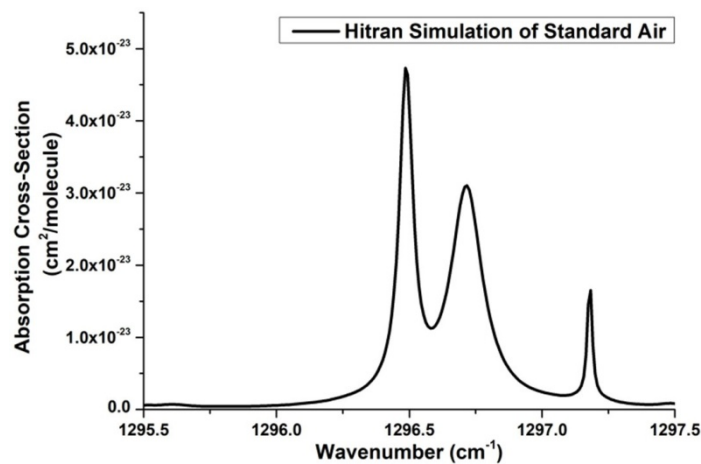


**Figure 1.32** Absorption cross-section of standard air at 760 Torr [104].

For our investigation, we selected the two highest water vapor absorption features, which peaked at 1296.48 and 1296.71  $\text{cm}^{-1}$  with absorption cross-sections of  $4.7 \cdot 10^{-23}$  and  $3.1 \cdot 10^{-23} \text{ cm}^2/\text{molecule}$ , respectively.

### 1.5.3 Results and Discussion

The performances of the four amplifiers were evaluated and compared by acquiring the QEPAS spectral scans of the water absorption features, as shown in **Figure 1.32**. The QEPAS signal was recorded while varying the laser current, i.e., the laser wavenumber. In **Figure 1.33**, the normalized QEPAS spectral scans obtained by using the four different architecture amplifiers are reported. Normalization was performed to allow for an easy comparison of the SNRs. Measurements were performed by switching the amplifiers and maintaining the experimental conditions, namely the gas pressure, flow and concentration, as well as the optical alignment and lock-in integration time being fixed. For each spectral scan a current modulation depth of 24 mA was used, thereby maximizing the two QEPAS peaks' signals.

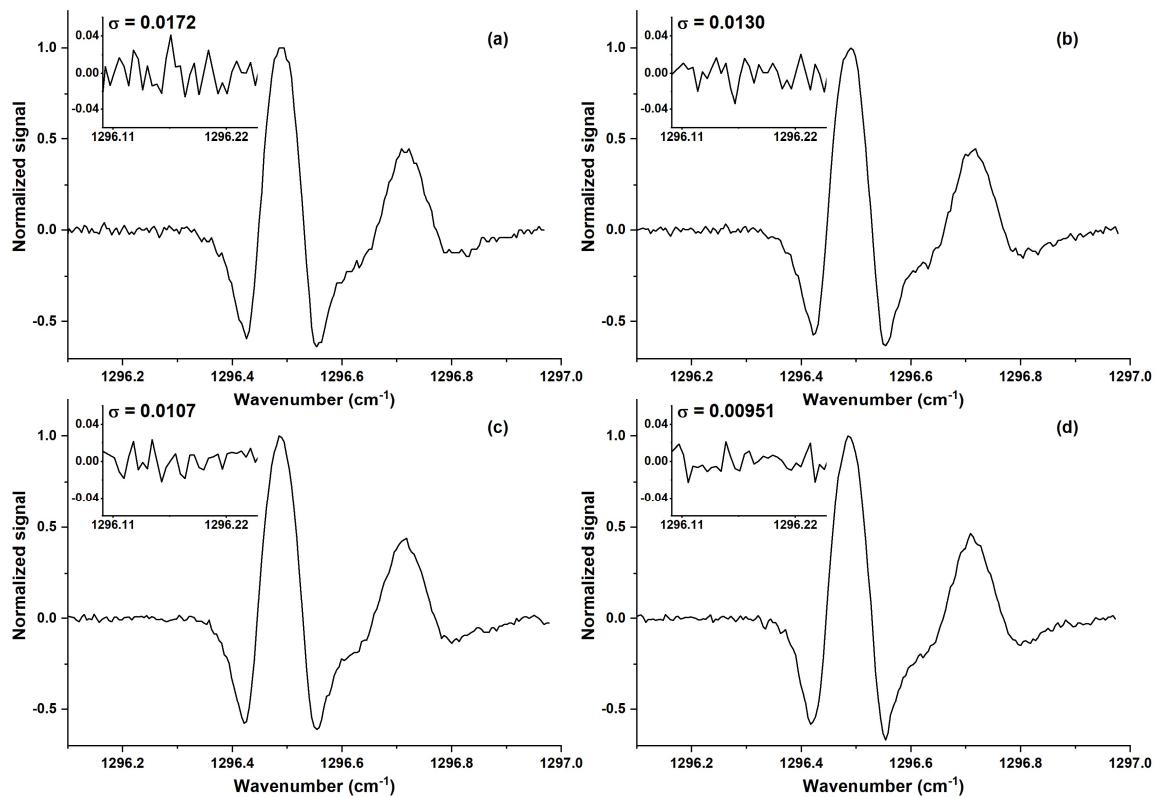


**Figure 1.33** Normalized 2f-QEPAS signals of a mixture containing 2% of water vapor acquired with (a) single-ended transimpedance amplifier, (b) differential output

transimpedance amplifier, (c) differential input voltage amplifier and (d) fully differential voltage amplifier. In the insets the enlarged views of the normalized noise fluctuations are shown [104].

In each spectral scan, the two water vapor absorption peaks are clearly distinguishable with a small overlap between the negative lobes of the 2f-waveforms. The range between  $1296.1 \text{ cm}^{-1}$  and  $1296.25 \text{ cm}^{-1}$  is free from any absorption feature as also shown by a HITRAN simulation in **Figure 1.33**. Hence, this range is suitable for the estimation of the  $1\sigma$  noise level for the amplifiers under test. Starting from these values, the SNR of the two peaks was calculated for each employed amplifier as the performance parameter to be compared. The noise levels and SNRs for both water vapor peaks are summarized in **Table 1.11** for the four amplifier architectures.

**Table 1.11** Quartz-enhanced photoacoustic spectroscopy (QEPAS)  $1\sigma$  noise and signal-to-noise ratio calculated for water vapor absorption features falling at  $1296.48 \text{ cm}^{-1}$  and  $1296.71 \text{ cm}^{-1}$  when implementing the four different amplifier architectures [104].

Amplifier Architecture	Normalized Noise ( $\sigma$ )	SNR @ $1296.48 \text{ cm}^{-1}$	SNR @ $1296.71 \text{ cm}^{-1}$
Single-Ended Transimpedance	0.0172	58	26
Differential Output Transimpedance	0.0130	77	34
Differential Input Voltage	0.0107	93	41
Fully-Differential Voltage	0.00951	105	49

By using a single-ended transimpedance amplifier (**Figure 1.33(a)**), the measured noise is 0.0172, with an SNRST of the strongest water vapor peak of 58. With the differential output transimpedance amplifier (**Figure 1.33(b)**), the QEPAS noise measured is 0.0130 with an SNRDT of 77 for the same water vapor absorption line, 1.3 times higher than the value obtained with the single-ended architecture.

This result confirms that the SNR can be enhanced when a differential design is selected. The noise level measured by using a differential input voltage amplifier is 0.0107 (**Figure 1.33(c)**). The calculated SNRDIV is 93, 1.6 times greater than SNRST and 1.22 times

greater than SNRDT, suggesting that a voltage amplifier architecture improves the QTF front-end electronics performance. This result is confirmed by the measurements made by using the fully differential voltage amplifier architecture. For a QEPAS noise of 0.00951 (**Figure 1.33(d)**), the achieved SNRFDV for the peak at  $1296.48\text{ cm}^{-1}$  is 105. Combined with a differential output configuration, the voltage amplifier architecture leads to an overall SNR enhancement of nearly double, with respect to the most used single-ended transimpedance amplifier. This demonstrates that a QTF can be more efficiently schematized as a voltage generator rather than a current generator. Similar results have been obtained for the SNRs measured for the water vapor peak falling at  $1296.71\text{ cm}^{-1}$ .

## Chapter 2: QEPAS sensors for real world applications

The studies illustrated in the previous chapter on the basic components of a QEPAS sensitive element, i.e. the spectrophone and the amplifier, served as a starting point for the employment of custom QTFs in QEPAS sensors devoted to trace gas sensing for the real world applications.

The first sensor was designed to simultaneously monitor water vapor and methane or nitrous oxide concentrations in mixtures. As introduced in the previous chapter, QEPAS signals depends on the radiation-to-sound conversion efficiency  $\varepsilon$ , which depends in turn on the relaxation rates of the target molecule through each relaxation channel weighted by the concentration of the collisional partners. Water vapor can be considered a fast relaxing gas which acts as relaxation promoters for many molecules. The high and variable H<sub>2</sub>O concentration in standard air-like mixtures strongly affects the energy relaxation process of slow relaxing molecules, such as CH<sub>4</sub>, CO, CO<sub>2</sub>. For this reason, H<sub>2</sub>O monitoring is crucial for accurately determining the concentration of other components in mixtures. In this sensor, two laser sources were focused at the fundamental and the overtone mode antinodes of a custom QTF to simultaneously detect water vapor and methane or nitrous oxide concentrations.

As alternative to the dual gas detection, a QEPAS sensor specifically designed to monitor the CH<sub>4</sub> ppm-level concentration in atmosphere and mounting a commercial humidity sensor for water vapor continuous measurement, is also described in this chapter. Methane concentration monitoring is fundamental in environmental monitoring applications, being CH<sub>4</sub> one of the most relevant marker of the pollution level. This second sensor demonstrated that a simplified architecture employing a commercial humidity hygrometer is capable of effectively perform a real-time compensation of the water vapor effect on methane detection and provide a continuous on-peak measurement of the CH<sub>4</sub> concentration in air.

Finally, a SF<sub>6</sub> QEPAS sensor was employed as leak detector. The high sensitivity of the sensor allows the identification and quantification of small leaks in mechatronics components. This sensor was firstly tested to evaluate the sealing of innovative 3D printed

vacuum chambers, aimed at replacing acoustic detection modules currently made of stainless steel.

## **2.1 Dual-gas QEPAS sensor**

QTF response depends only on the sound waves intensity and not on the wavelength of the exciting laser used, which makes it suitable for coupling multiple sources emitting at different wavelengths for multi gas detection. Many gas sensing applications require simultaneous detection and quantification of different components in a gas mixture, such as detection of isotopes concentration ratio, environmental monitoring of greenhouse gases, monitoring of different biomarkers in human breath and study of molecular relaxation dynamics. A straightforward way to guarantee simultaneous detection is developing a wavelength-modulation division multiplexing (WMDM) scheme. Different laser sources are independently modulated, one for each gas species to be detected and then combined using a single detector. The recorded signal is then demodulated at different modulation frequencies. The development of custom QTFs opened the way to exploit QEPAS technique in WMDM configuration [91]. If the QTF frequency of the in-plane flexural mode is decreased to a few kHz, the frequency of the in-plane first overtone mode, which is  $\sim 6.2$  times higher than the fundamental one, becomes accessible for QEPAS operation. In this section, a dual-gas QEPAS sensor aimed at simultaneous detection of methane or nitrous oxide and water vapor is described.

### **2.1.1 Dual-gas spectrophone design**

Simultaneous dual-gas detection with QEPAS technique can be obtained only by exciting at the same time two different flexural vibrational modes of a QTF, that is, the fundamental and the first overtone mode. The related resonance frequencies can be chosen at the design phase by properly selecting the prongs length and thickness and making both modes suitable for QEPAS operation. In [106], three different QTF designs were proposed and tested, having both the fundamental and the first overtone mode frequencies lower than 40 kHz. Among them, we selected the QTF labeled as QTF#1 since it showed the highest quality factor value and consequently the best QEPAS performance, for both fundamental and first overtone modes. QTF#1 has two rectangular prongs with length of 17 mm, thickness of 1 mm and a quartz crystal width of 0.25 mm. These QTF geometrical parameters leads to a fundamental frequency as low as 2.88 kHz, while the first overtone

mode resonates at  $\sim 17.78$  kHz. The spacing between the two prongs is 0.7 mm. The fundamental mode has an antinode point on the top of the QTF while the first overtone mode has two antinode points, one coincident to that of the fundamental mode and the other one close to the middle of the prong (at 9 mm from the QTF#1 top). Two pairs of microresonator tubes were employed to simultaneously enhance the fundamental and the overtone mode vibrations. One pair was located at 2 mm from the top of the prongs for the fundamental mode and the other pair at 9.5 mm from the top of the prongs for the first overtone mode, as discussed in [106]. The length and internal diameter of tubes must be accurately selected to optimize the QEPAS performance of the spectrophone [94]. The length of the tubes is correlated to the sound wavelength by the relation  $\lambda_s = v/f$ , where  $v$  is the sound speed and  $f$  is the QTF resonance frequency [70], [107]. The optimal tube length was experimentally found to be between  $\lambda_s/4$  and  $\lambda_s/2$ . For the first overtone mode, the corresponding length range is  $4.8 \text{ mm} < l < 9.6 \text{ mm}$ , and  $l = 8.5 \text{ mm}$  was selected. For the fundamental mode, the optimal length falls between 30 mm and 60 mm. However, such a length would require a bulky acoustic detection module to accommodate the spectrophone and thus complicate the optical alignment operations. For these reasons, tubes with a length of 9.5 mm have been employed, which are 1 mm longer than the tubes used for the first overtone mode in order to maintain the spectrophone size as compact as possible. A low QEPAS signal enhancement is thus expected for the fundamental mode. Therefore, this mode was chosen to detect the gas target with the highest concentration. For both antinodes, tubes having an ID = 1.36 mm were mounted, which was proved to be the optimum internal diameter in terms of the signal-to-noise enhancement factor with respect to the bare QTF. The gap between tubes and the QTF surface was set to  $150 \mu\text{m}$ . A schematic of the spectrophone is shown in **Figure 2.1**.

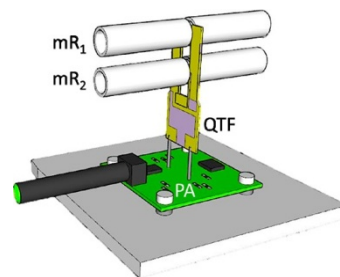


**Figure 2.1** Schematic of the spectrophone implemented. The QTF is coupled with two pairs of microresonators tubes aligned perpendicularly to the QTF. The first pair of tubes ( $mR_1$ ), each one 9.5 mm long, is located at the fundamental antinode point near the QTF

top, the second pair ( $mR_2$ ), each tube 8.5 mm long, is positioned 9.5 mm below the prongs top, at the second antinode point position of the QTF first overtone mode; the preamplifier (PA) board is shown on the bottom [108].

The vibrational properties of the QTF coupled with the microresonator tubes, namely the resonance frequency and the quality factor of both flexural modes were measured by electrically exciting the QTF. A sinusoidal voltage signal excites the QTF resulting in a piezoelectric charge displacement on its prongs via an inverse piezoelectric effect. Charges are collected by electrodes deposited on the QTF surface and the QTF current signal is converted into an output voltage by means of a transimpedance preamplifier. Finally, the output voltage is demodulated by a lock-in amplifier at the same frequency of the excitation signal. The resonance curves for the fundamental and first overtone mode of a bare QTF were fitted using a Lorentzian function to extract the resonance frequencies and the full width at half maximum (FWHM) values. The quality factor is calculated as  $Q = f/\text{fwhm}$ . In **Figure 2.2**, the QTF resonance curves of the fundamental and first overtone modes measured at 200 Torr are shown. The fundamental mode exhibits a resonance frequency of  $f_0 = 2871.05$  Hz and a quality factor of 6 680, while the overtone resonance mode occurs at  $f_1 = 17747.70$  Hz with a quality factor of 17 070. The first overtone mode exhibits a higher quality factor with respect to the fundamental one as already demonstrated in [106].

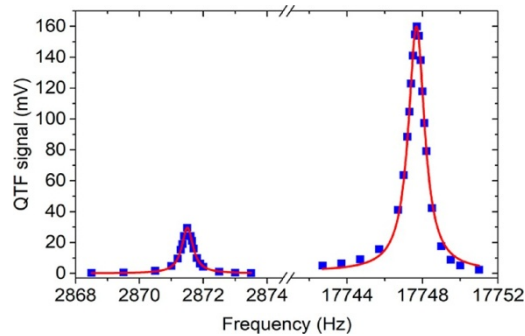


**Figure 2.2** Spectrophone resonance curves (blue squares) and related Lorentzian fits (red solid curves) of the fundamental and the first overtone modes at 200 Torr in air [108].

The fundamental mode will be used to monitor the water vapor concentration in air (whose concentration is expected to be in the percent-range), while the first overtone mode will be exploited to detect  $\text{CH}_4$  and  $\text{N}_2\text{O}$  trace gas concentration. The distance between the positions of the fundamental antinode and the second antinode of the first overtone mode is

~8 mm, allowing an easy alignment of the two laser beams through the microresonator tubes.

### 2.1.2 Architecture of dual-gas QEPAS sensor

The dual-gas spectrophone is enclosed in a gas cell, forming the acoustic detection module (ADM). The gas cell is equipped with a ZnSe window antireflection (AR)-coated in the range of 7–12  $\mu\text{m}$  on the front side and a N-BK7 window AR-coated in the 1–1.7  $\mu\text{m}$  range on the back side. Two connectors are used as a gas inlet and a gas outlet. The ADM was implemented in the QEPAS sensor setup depicted in **Figure 2.3**.

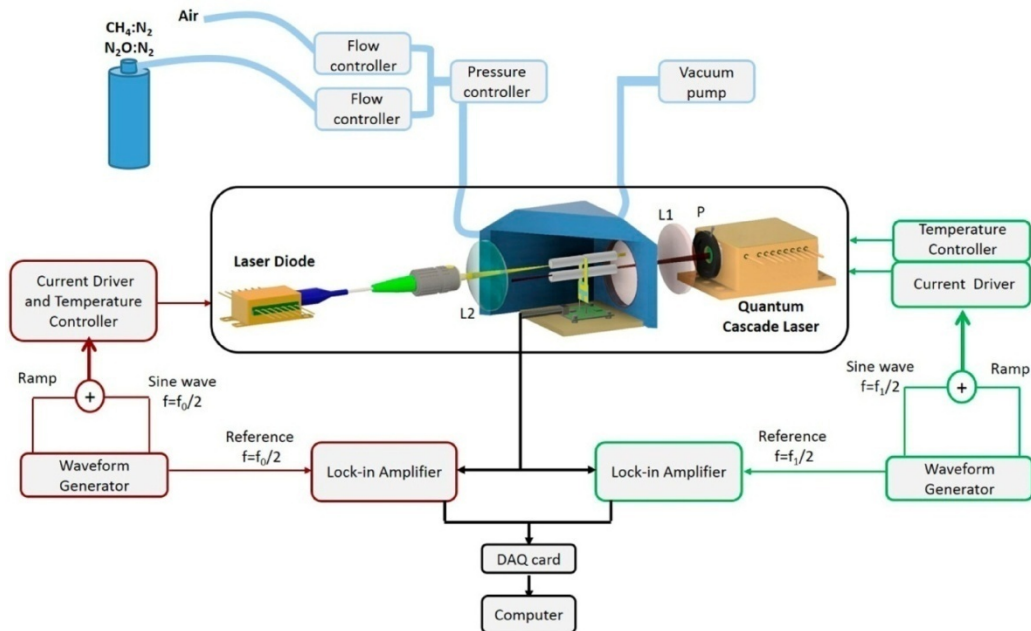


**Figure 2.3** Schematic of the dual-gas QEPAS sensor. P, pinhole; L1, AR-coated Zn–Se lens; L2, AR-coated N-BK7 lens; DAQ, Data Acquisition Board [108].

Two lasers were used as excitation sources. A DFB-QCL emitting at 7.73  $\mu\text{m}$  was used to alternately target methane and nitrous oxide absorption peaks exciting the first overtone QTF mode. The beam was then focused through the microresonator tubes located at the lower antinode point of the overtone mode by means of a 7–12  $\mu\text{m}$  AR-coated Zn–Se lens having a focal length of 75 mm. A pinhole was used as a spatial filter to cut the laser beam tails and prevent that the incident light hits the QTF prongs or the microresonator tubes and generates a background photothermal noise. A laser diode emitting at 1.392  $\mu\text{m}$  was used to target water vapor. A 1.05 - 1.7  $\mu\text{m}$  AR-coated N-BK7 lens having a focal length of 75 mm was used to focus the diode laser beam between the QTF prongs and through the tubes

located at to the antinode point of the fundamental mode. The beam waists of the QCL and the diode laser measured on the QTF plane have a diameter of 0.28 mm and 0.24 mm, respectively, well below the prong spacing of the QTF (0.7 mm). The portion of optical power transmitted through the microresonator tubes and between the prongs was 97.5% and 99.2% for the QCL and the diode laser, respectively. QEPAS signals were detected using the wavelength modulation technique with 2f-detection and the two lasers were independently modulated. A sinusoidal dither was applied to the current driving the diode laser at the half of the fundamental mode frequency  $f_0/2 = 1435.52$  Hz, while the current injected into the QCL was modulated at the half of the first overtone mode frequency,  $f_1/2 = 8873.85$  Hz. The QTF signal was converted into a voltage signal using a transimpedance preamplifier; and then was simultaneously demodulated at the fundamental and first overtone frequencies using two lock-in amplifiers. The integration time was set at 100 ms for both lock-in amplifiers. The demodulated signals were recorded and analyzed on a personal computer by using a multichannel data acquisition card from National Instruments. A gas line system was assembled to manage flow rates, pressures and compositions of the gas mixtures to be analyzed. One Y- ended gas line branch was connected to the gas cylinders containing certified concentrations of gas targets: 10 000 ppm of CH<sub>4</sub> in N<sub>2</sub> and 10 000 ppm of N<sub>2</sub>O in N<sub>2</sub>. The other gas line branch was connected to a valve allowing laboratory air to enter the line. Since the water vapor concentration in the laboratory environment can vary, a Nafion humidifier was inserted just before the ADM (not shown in **Figure 2.3**) to keep the water concentration in the ADM fixed to 1.6%. The pressure inside the ADM was fixed at 200 Torr and the flow set at 25 sccm by means of a pressure controller, a valve system and a vacuum diaphragm pump.

### 2.1.3 Simultaneous QEPAS detection of CH<sub>4</sub> and H<sub>2</sub>O

As a first step, the QEPAS sensor was tested for detection of methane and water vapor in a gas mixture, independently. The QCL and diode laser were alternatively switched on to excite the targeted CH<sub>4</sub> and H<sub>2</sub>O absorption lines, respectively. A preliminary study showed that the CH<sub>4</sub> QEPAS signal is maximized at a gas pressure of 200 Torr. The HITRAN database [78] was used to simulate the absorption cross-section of pure methane at 200 Torr in the QCL tunability range from 1298 cm<sup>-1</sup> to 1297.4 cm<sup>-1</sup>. The simulation result is depicted in **Figure 2.4(a)**.

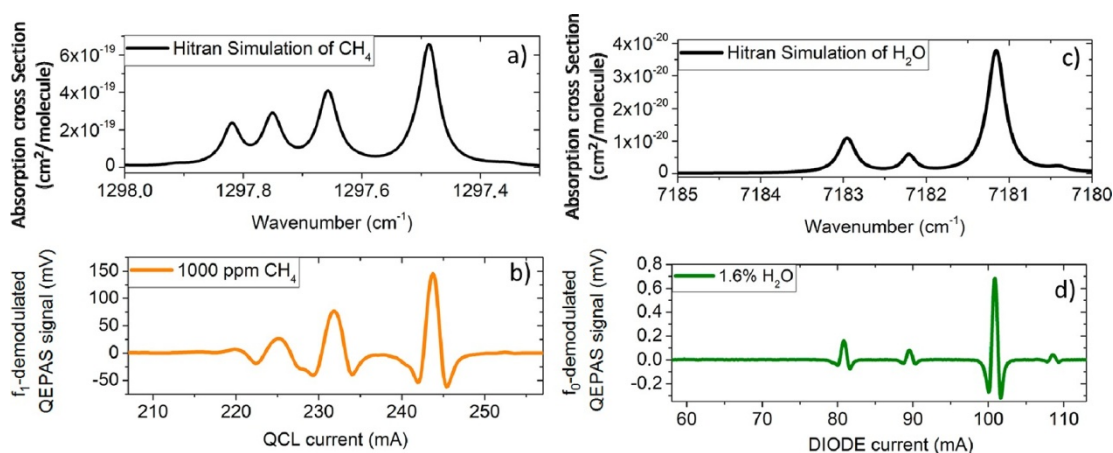


**Figure 2.4** (a) Hitran simulation of the pure methane absorption cross-section at 200 Torr; (b) QEPAS spectral scan of 1000 ppm of CH<sub>4</sub> at 200 Torr measured by demodulating the QTF signal at the overtone mode frequency; (c) Hitran simulation of the pure water vapor absorption cross-section at 200 Torr; (d) QEPAS spectral scan of 1.6% of H<sub>2</sub>O at 200 Torr measured by demodulating the QTF signal at the fundamental mode frequency [108].

The strongest absorption peak of methane falls at  $1297.47\text{ cm}^{-1}$  with a line strength of  $3.9 \cdot 10^{-20}\text{ cm/molecule}$ . No visible water lines fall in the investigated QCL emission spectral range. **Figure 2.4(b)** shows the corresponding QEPAS spectral scan acquired for a mixture of 1000 ppm of CH<sub>4</sub> with 1.6% of water vapor at 200 Torr. The QCL temperature was set to  $12.5\text{ }^{\circ}\text{C}$  and the injected current was scanned in the range 207–257 mA applying a 2 MHz ramp to the current driver. The QEPAS signal was demodulated at  $f_1$  for methane detection. The amplitude of the QEPAS signal related to the selected line (targeted at a laser current of  $I_{\text{QCL}} = 243.7\text{ mA}$ ) was optimized by varying the laser modulation depth. The highest CH<sub>4</sub> signal of 146 mV was observed at a modulation depth of 35 mV. The other features composing the QEPAS spectrum of **Figure 2.4(b)**, like the ones peaked at 224.8 mA and 231.8 mA, correspond to methane absorption lines with weaker linestrengths as confirmed by a HITRAN database simulation. The QCL was then turned off and the diode laser was used to excite the water vapor absorption line. **Figure 2.4(c)** shows the simulated absorption cross-section of pure water at 200 Torr in the 7180–7185  $\text{cm}^{-1}$  range, obtained using the HITRAN database [78]. Within the current dynamic range of the diode, the strongest absorption peak of H<sub>2</sub>O falls at  $7181.16\text{ cm}^{-1}$  with a linestrength of  $1.4 \cdot 10^{-20}\text{ cm/molecule}$ . **Figure 2.4(d)** shows the QEPAS spectral scan for a mixture of 1000 ppm of CH<sub>4</sub> with 1.6% of water vapor, at 200 Torr. These measurements were obtained by setting the temperature of the laser diode to  $25\text{ }^{\circ}\text{C}$  and scanning the laser

current in the range 50 - 115 mA, by applying a 2 mHz ramp to the current driver. The diode modulation amplitude was set to 12 mV and the QEPAS signal was demodulated at  $f_0$ . The selected H<sub>2</sub>O line shows a peak value of 0.68 mV. The QEPAS absorption features at 80.7 mA, 89.5 mA and 108.6 mA correspond to water vapor absorption lines with weaker linestrengths. The optical power focused inside the ADM was 128.0 mW at the QCL current set to target the selected CH<sub>4</sub> absorption line and 6.2 mW for the diode laser current set to hit the strongest H<sub>2</sub>O line absorption line. It is mandatory to verify that the QEPAS signal demodulated at  $f_0$  is not influenced by the first overtone mode vibration and that the QEPAS signal demodulated at  $f_1$  is not affected by the fundamental mode vibration. Therefore, a preliminary test was conducted to investigate the QTF response while simultaneously exciting the fundamental and first overtone vibrational modes. **Figure 2.5(a)** shows the QTF signal demodulated at  $f_1$  when the QCL excites the first overtone mode of the QTF (orange squares) and when both the QTF vibrational modes are simultaneously excited by the two laser sources (blue circles).

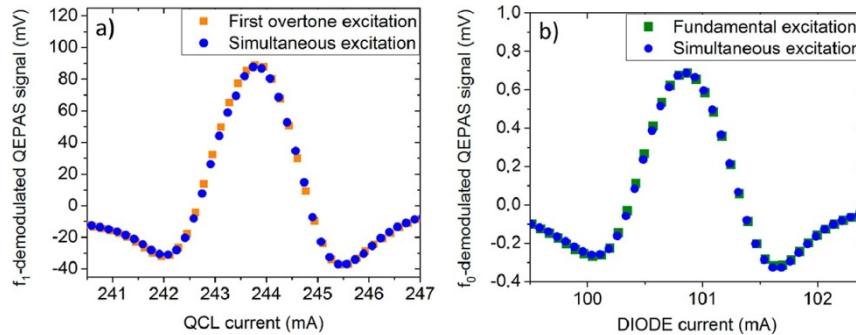


**Figure 2.5 (a)** QEPAS spectral scan of the methane absorption line at  $1297.47 \text{ cm}^{-1}$  detected at the first overtone mode when only the first overtone mode is excited (orange squares) or both the fundamental and the first overtone modes are excited (blue circles). **(b)** QEPAS spectral scan of the water vapor absorption line at  $7181.16 \text{ cm}^{-1}$  detected at the fundamental mode when only the fundamental mode is excited (green squares) or both the fundamental and first overtone modes are excited (blue circles) [108].

The QCL and the diode laser currents were tuned to detect the selected CH<sub>4</sub> and H<sub>2</sub>O absorption lines falling at  $1297.47 \text{ cm}^{-1}$  and  $7181.16 \text{ cm}^{-1}$ , respectively, in a mixture containing 600 ppm of CH<sub>4</sub> and 1.6% of water vapor. Similarly, **Figure 2.5(b)** shows the QTF signal demodulated at  $f_0$  when only the fundamental vibrational mode is excited using the diode laser (green squares) and when both the lasers operate (blue circles). The perfect

overlap between the curves in both figures indicates that there is no cross-talking between the QTF fundamental mode and first overtone mode operations, even in the presence of the two microresonator tubes placed at the antinode points. This allows the excitation of the two vibrational modes simultaneously, acquisition of the QTF signal and independent demodulation at the two resonance frequencies to identify the contribution due to each gas species and retrieve both gas concentrations. The calibration of the sensor for methane detection was performed acquiring spectral scans of mixtures of CH<sub>4</sub> in laboratory air with different gas target concentrations, ranging from 50 to 1000 ppm. In all generated mixtures, the water vapor concentration was fixed to 1.6% by using the Nafion humidifier. The sensor was used in the dual-gas detection mode in order to measure the CH<sub>4</sub> concentration and simultaneously monitor the water vapor level. **Figure 2.6(a)** shows the QEPAS signal acquired for methane at seven different concentrations and the correlated water QEPAS signal (see **Figure 2.6(b)**).

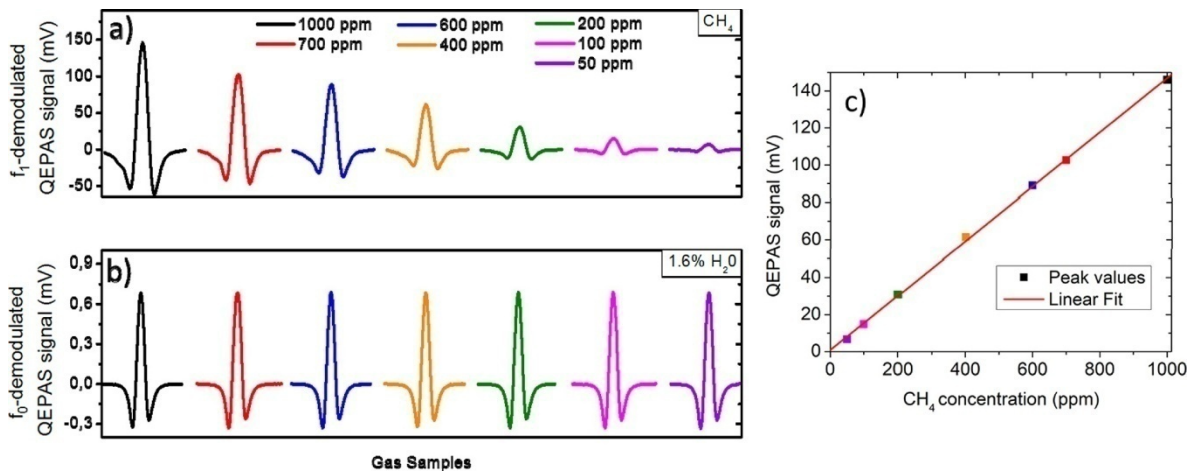


**Figure 2.6 (a)** Spectral scans of the methane absorption line at  $1297.47\text{ cm}^{-1}$  for different CH<sub>4</sub> concentrations in humidified air with 1.6% water vapor. **(b)** Corresponding spectral scans of the water absorption line at  $7181.16\text{ cm}^{-1}$  for CH<sub>4</sub> each dilution, confirming that the H<sub>2</sub>O concentration was kept constant. Simultaneous spectral scans are represented by the same curve color. **(c)** Peak values for each CH<sub>4</sub> concentration (square symbols) and the corresponding best linear fit (red line) [108].

The CH<sub>4</sub> peak values were extracted for each spectral scan and plotted as a function of the concentration in **Figure 2.6(c)**. A linear fit of the experimental data points was performed to obtain the sensor calibration curve for methane. The squared-R value of 0.999 confirms the linearity of the QEPAS signal with the methane concentration, with a slope of 0.146

mV/ppm and an intercept of 0.85 mV. For each dilution, the water vapor level has been monitored by scanning the H<sub>2</sub>O absorption line with the diode laser. The H<sub>2</sub>O QEPAS peak signals extracted from **Figure 2.6(b)** show a peak value fluctuation < 0.25% value, demonstrating the capability of the Nafion humidifier to efficiently fix the water concentration in the gas line. For CH<sub>4</sub>, a 1 $\sigma$ -noise level of 2.7  $\mu$ V was estimated at 100 ms lock-in integration time corresponding to a minimum detection limit (MDL) of 18 part-per-billion (ppb), while for H<sub>2</sub>O with a 100 ms integration time we obtained a 1 $\sigma$  noise of 1.0  $\mu$ V corresponding to an MDL of 20 ppm.

#### 2.1.4 Simultaneous QEPAS detection of N<sub>2</sub>O and H<sub>2</sub>O

The realized QEPAS sensor allows also the simultaneous detection of water vapor and nitrous oxide, since the QCL emission spectral range covers absorption lines of N<sub>2</sub>O. With the QCL temperature set to 12.5 °C and the QCL current scanned in the range of 152–287 mA, several N<sub>2</sub>O absorption lines can be targeted. The highest intensity line falls at 1297.05 cm<sup>-1</sup> with a line strength of 1.7·10<sup>-19</sup> cm/molecule. The QCL modulation amplitude and the gas pressure maximizing the N<sub>2</sub>O QEPAS signal were found to be 130 mV and 200 Torr, respectively. For water vapor detection, the diode laser working conditions remain the same as before. **Figure 2.7(a)** shows the QTF signal demodulated at f<sub>1</sub> for a mixture of 400 ppm of N<sub>2</sub>O and 1.6% H<sub>2</sub>O in air.

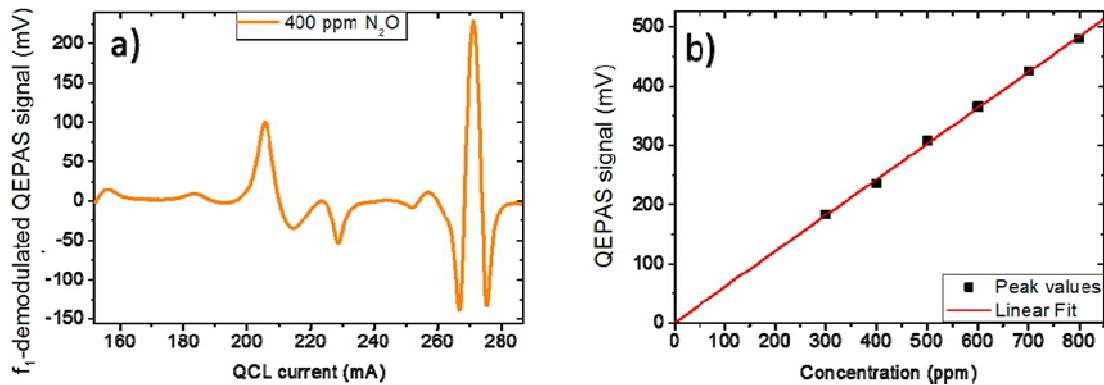


**Figure 2.7 (a)** Nitrous oxide spectral scan detected at f<sub>1</sub> exciting the first overtone vibrational mode of the QTF with the quantum cascade laser for a mixture of 400 ppm of nitrous oxide and 1.6% of water in air at 200 Torr. **(b)** Peak values for each N<sub>2</sub>O concentration (square symbols) and the corresponding best linear fit (red line) [108].

The selected  $\text{N}_2\text{O}$  absorption line is excited at a QCL current of  $I_{\text{QCL}} = 271.1$  mA and shows a peak value of 227 mV. The sensor was calibrated for  $\text{N}_2\text{O}$  detection in the range of 300–800 ppm starting from a 10 000-ppm certified concentration of  $\text{N}_2\text{O}:\text{N}_2$ . The QEPAS peak value scales linearly with  $\text{N}_2\text{O}$  concentration in the selected range with a slope of 0.60 mV/ppm, an intercept of 0.51 mV and a squared-R value of 0.997, as shown in **Figure 2.7(b)**. A  $1\sigma$ -noise level of 2.7  $\mu\text{V}$  at an integration time of 100 ms corresponds to an MDL of 5 ppb for  $\text{N}_2\text{O}$  detection. Furthermore, an analysis of the stability of the dual-gas sensor was performed by acquiring the QEPAS signal of  $\text{N}_2\text{O}$  and  $\text{H}_2\text{O}$  vapor for 20 min. This analysis is usually performed by fixing the laser current to correspond to the gas absorption peak, while the gas keeps flowing in the gas line. To avoid QEPAS signal fluctuations due to the possible laser sources instabilities and drifts, we applied two fast voltage ramps to the QCL and diode laser in order to scan the selected  $\text{N}_2\text{O}$  and  $\text{H}_2\text{O}$  absorption lines, respectively.

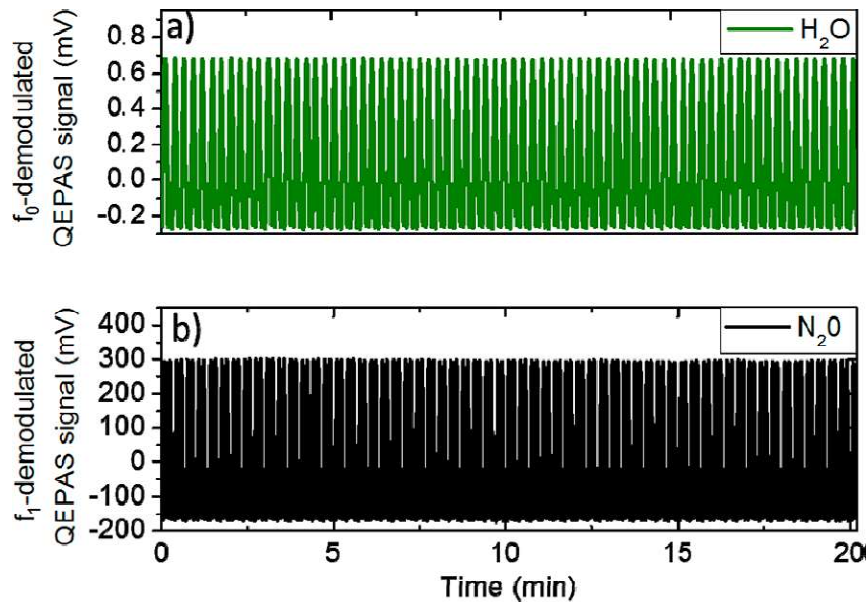


**Figure 2.8** Simultaneous QEPAS spectral scans for a mixture of 600 ppm of nitrous oxide in humidified air. **(a)**  $\text{H}_2\text{O}$  vapor signal detected at  $f_0$  applying a narrow ramp to the diode laser current centered on the water vapor line at  $7181.16\text{ cm}^{-1}$ . **(b)**  $\text{N}_2\text{O}$  signal detected at  $f_1$  applying a narrow ramp to the QCL current centered on the  $\text{N}_2\text{O}$  absorption line at  $1297.05\text{ cm}^{-1}$  [108].

The results are shown in **Figure 2.8**. The peak-to-peak amplitude  $V_{\text{ramp}}$  and frequency  $f$  ramp of the ramps applied to the diode laser and to the QCL were 15 mV and 30mHz, and

60 mV and 50 mHz, respectively. The  $f_{\text{ramp}}$  values were selected to provide a fast absorption line scan and avoid down-sampling reconstruction. As clearly visible in **Figure 2.8**, both the H<sub>2</sub>O and N<sub>2</sub>O peak signal values remain nearly constant with fluctuations lower than 0.9%, demonstrating the time stability of the dual gas QEPAS sensor.

## 2.2 QEPAS sensor for CH<sub>4</sub> environmental monitoring

Environmental monitoring of methane is crucial, because of its effect on global warming and climate change. A CH<sub>4</sub> sensor must guarantee (i) high sensitivity in the sub-ppm range, (ii) high selectivity to discriminate the CH<sub>4</sub> signal from other gas components in the atmosphere, in particular water vapor, and (iii) fast response time to track any variation in concentration. QEPAS sensors are capable to fulfill these requirements. The simultaneous detection of water vapor and methane employing two optical sources in a QEPAS sensor was demonstrated in [108]. Even though the high accuracy obtained, this two lasers configuration requires both higher electrical power absorption and higher space occupancy than typical QEPAS sensors. In this section, the use of an electronic hygrometer to complement QEPAS sensing is discussed as a solution to address the abovementioned issues.

### 2.2.1 QEPAS apparatus for CH<sub>4</sub> environmental monitoring

A schematic of the experimental apparatus used in this work is shown in **Figure 2.9** and consists of a combination of two sensors: a QEPAS-based sensor for the detection of CH<sub>4</sub> and H<sub>2</sub>O and a temperature and humidity sensor for monitoring the H<sub>2</sub>O concentration in air.

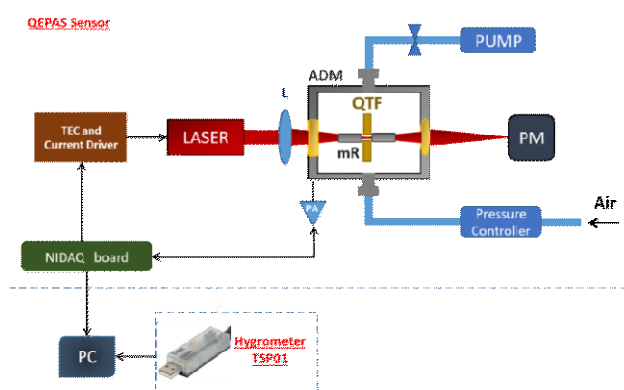


**Figure 2.9** Schematic of the sensor setup for methane and water vapor detection including a quartz-enhanced photoacoustic spectroscopy (QEPAS) module and a hygrometer. ADM, acoustic detection module; QTF, quartz tuning fork; mR, microresonators; L, focusing lens; PM, power meter; PA, preamplifier; NIDAQ board, National Instruments data acquisition board; PC, personal computer [109].

The QEPAS sensor for the detection of CH<sub>4</sub> and H<sub>2</sub>O is shown in the upper part of **Figure 2.9**. The light source was an interband cascade laser (ICL) emitting at 3.345 μm, capable of targeting two nearby CH<sub>4</sub> and H<sub>2</sub>O absorption lines. The laser beam was focused into an acoustic detection module (ADM) using lens with 40 mm focal length. The ADM contained a custom quartz tuning fork with fundamental resonance frequency  $f_0 = 12456.9$  Hz at 200 Torr. The QTF was acoustically coupled with two 12.4 mm long tubes with internal diameter of 1.6 mm to amplify the acoustic wave and enhance the QEPAS signal [91]. The laser beam was refocused on the sensitive element of a power meter set behind the ADM. The ICL current and temperature were controlled using a Benchtop Laser Diode/TEC Controller (Model ITC4002–Thorlabs, Newton, MA, USA). At the laser operating temperature of 25 °C, the optical power measured by the power meter was 12.5 mW. QEPAS measurements were performed using wavelength modulation with 2f-detection; a sinusoidal modulation was applied to the laser current at half of the QTF resonance frequency, and the QTF response was detected at  $f_0$  using a digital lock-in amplifier. QEPAS spectral scans were obtained by sweeping the laser current by a 4.4 mHz ramp. A National Instrument data acquisition board together with a dedicated LabVIEW-based software was used to feed the modulation and ramp to the ICL current driver and to acquire and demodulate the QTF signal. The pressure and flow of the sample gas inside the ADM were controlled and fixed using a system composed of a pressure controller, a needle valve, and a pump. The temperature and relative humidity of the air in laboratory environment close to the QEPAS sensor were also monitored using the hygrometer (model TSP01–Thorlabs, Newton, MA, USA) with the dimensions of a USB stick. TSP01 was directly connected to the computer.

### 2.2.3 Measurements of CH<sub>4</sub> and H<sub>2</sub>O in Air

**Figure 2.10** shows comparison between the absorption cross section of standard air at 200 Torr simulated using the HITRAN database [78] (**Figure 2.10(a)**) and a representative QEPAS scan of the laboratory air (**Figure 2.10(b)**).

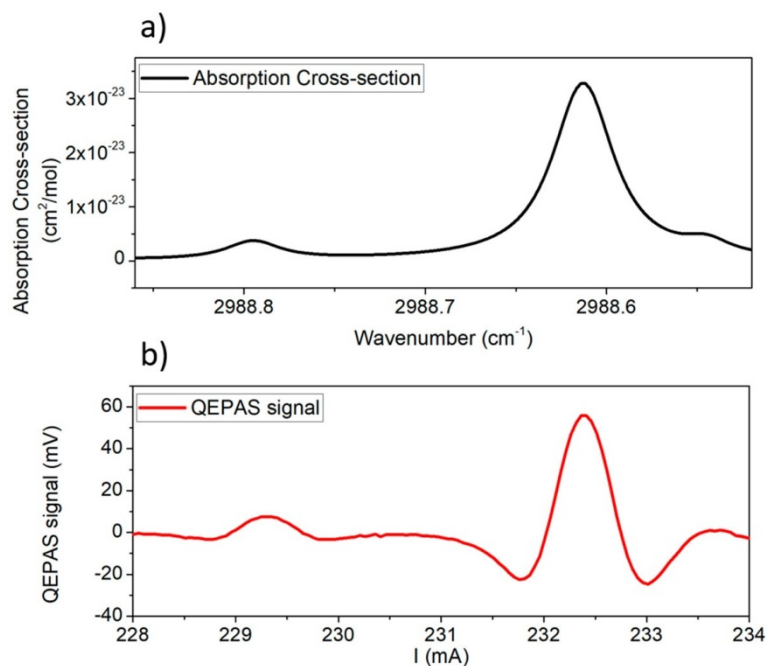


**Figure 2.10 (a)** Absorption spectrum of standard air simulated with HITRAN database at 200 Torr and room temperature; **(b)** QEPAS spectral scan of laboratory ambient air at 200 Torr [109].

From comparison, the highest peak at 232.35 mA clearly corresponds to the water absorption line, while the lower peak at 229.25 mA corresponds to the methane line. A preliminary calibration of the QEPAS sensor for the detection of CH<sub>4</sub> in dry N<sub>2</sub> was performed. The sensor was calibrated by acquiring the QEPAS signal of the CH<sub>4</sub> absorption line at 2988.8 cm<sup>-1</sup> for different concentrations of CH<sub>4</sub>. The mixtures were obtained starting from a certified concentration of 45 ppm of CH<sub>4</sub>, which was diluted in pure N<sub>2</sub> by means of a gas mixer. By linearly fitting the peak values as a function of the CH<sub>4</sub> concentration, the calibration curve  $y = (1.07 \text{ mV/ppm}) \cdot x$  was obtained with an  $R^2 = 0.999$ , confirming the linearity of the sensor response with respect to the CH<sub>4</sub> concentration. A minimum detection limit of ~180 ppb was achieved for a  $1\sigma$  noise of 0.20 mV at 200 ms integration time. An Allan variance analysis [110] of the hygrometer TSP01 signal was performed to study the long-term stability of the absolute humidity

measurement. Given a set of  $M$  time-series data acquired with an integration time  $\tau$ , its Allan variance  $\sigma_y^2(\tau)$  is defined as

$$\sigma_y^2(\tau) = \frac{1}{M} \sum_{k=1}^M \frac{1}{2} (y_{k+1} - y_k)^2 \quad \text{Eq. 2.1}$$

where  $y_k$  is the  $k_{th}$ -data averaged over an integration time  $\tau$ ,  $y_{k+1} - y_k$  is the difference between adjacent values of  $y_k$ , and  $M$  is the total number of data. To estimate how  $\sigma_y^2(\tau)$  changes with the integration time, a LabVIEW-based code was implemented. Starting from the set of  $M$  data acquired at an integration time  $\tau_0$  and assuming that there is no dead time between adjacent measurements, the software averages the values for  $y_1$  and  $y_2$  and obtains a new  $y_1$  value averaged over  $2\tau_0$ . Subsequently, this routine averages values for  $y_3$  and  $y_4$  and changes them as a new value  $y_2$  averaged over  $2\tau_0$  and finally applies **Eq. 2.1** to determine  $\sigma_y^2(2\tau_0)$ . The software repeats this process for other integer multiples  $m$  of  $\tau_0$  and at the end of the processing, it generates values  $\sigma_y^2(m\tau_0)$  as a function of  $(m\tau_0)$  [110]. The TSP01 sensor was closed in a climate chamber to fix the temperature and the relative humidity of surrounding air at 27 °C and 40%, respectively. The TSP01 signal was acquired for  $\sim 4$  h with an integration time of 2 s. The absolute humidity is the total mass of water vapor present in a certain volume or mass of air. It gives a measurement of the concentration of water vapor in air. The relative humidity is the ratio between the amount of water vapor in air and the amount of water vapor that would saturate the air at the same temperature and pressure. The H<sub>2</sub>O QEPAS signal is a measurement of the absolute humidity, TSP01 measures the relative humidity and the temperature of air. Both temperature (T) and relative humidity (RH) values were used to calculate the absolute humidity (AH) of the air sample, in ppm using the following equations [111], [112]:

$$AH = 10^6 \cdot \frac{P_w}{P - P_w}, P_w = P_{ws} \cdot \frac{RH}{100}, P_{ws} = 6.11 \cdot \exp\left(\frac{17.7 \cdot T}{T + 243.57^\circ C}\right) \quad \text{Eq. 2.2}$$

where  $P$  is the ambient pressure (760 Torr),  $P_w$  is the water vapor pressure, and  $P_{ws}$  is the saturated water vapor pressure. In **Figure 2.11**, the Allan deviation of the absolute humidity signal (calculated with **Eq. 2.2**) using the relative humidity and the temperature measured by TSP01) is shown as a function of the signal integration time.

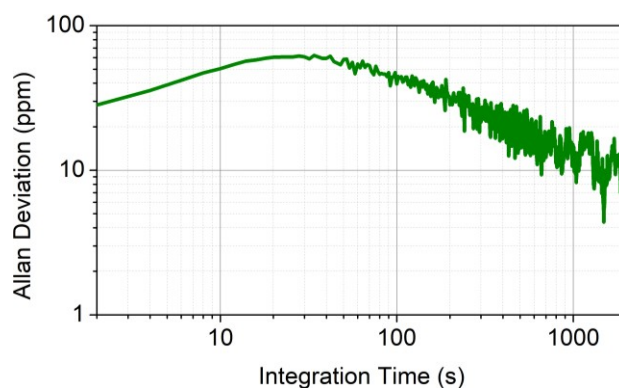


**Figure 2.11** Allan deviation in ppm of the absolute humidity calculated using **Eq. 2.2** [109].

The Allan deviation slightly increased from 2 to 20 s and then followed the  $t^{1/2}$  dependence expected, where the dominant noise source was the flicker noise. The accuracy of temperature and relative humidity measurements were 0.5 °C and 2%, respectively, as reported in the datasheet of the instrument. The precision of TSP01, evaluated experimentally with prolonged measurements of T and RH at fixed condition, was 0.01 °C for temperature and 0.1% for relative humidity. These values determined an accuracy and a precision on the calculated absolute humidity of ~350 and ~30 ppm, respectively, estimated using the error propagation for **Eq. 2.2**.

An investigation of the long-term stability of the methane peak values was performed when no water vapor was in the gas line. With this aim, a 10 h long measurement of fixed 45 ppm CH<sub>4</sub> concentration in dry N<sub>2</sub> was carried out. The measurements were performed by acquiring QEPAS spectral scans of the CH<sub>4</sub> absorption line with a 200 ms integration time and by extracting the peak value from each scan. Similarly, an 8 h long measurement of fixed concentration of H<sub>2</sub>O was performed to test the long-term stability of the H<sub>2</sub>O QEPAS peak values. A PermSelect humidifier was inserted in the gas line upstream the ADM to keep water concentration fixed to 1.6%. The CH<sub>4</sub> and the H<sub>2</sub>O QEPAS peak values are reported in **Figure 2.12** as a function of time.

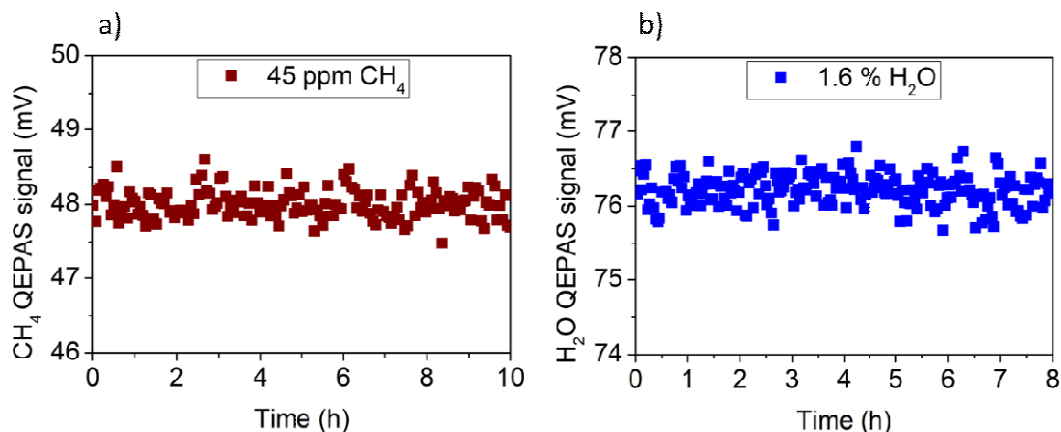


**Figure 2.12 (a)** Methane QEPAS peak signal as a function of time when a gas mixture of 45 ppm of dry  $\text{CH}_4$  in  $\text{N}_2$  was flowing in the sensor; **(b)**  $\text{H}_2\text{O}$  QEPAS peak signal as a function of time when water concentration in the gas line was fixed to 1.6% using a PermSelect humidifier [109].

Both the  $\text{CH}_4$  and  $\text{H}_2\text{O}$  QEPAS signals had no appreciable drifts during 10 h of continuous measurement. The  $1\sigma$  value of fluctuations was 0.20 mV for  $\text{CH}_4$  and 0.22 mV for  $\text{H}_2\text{O}$ , confirming the long-term stability of the sensor when both gases are detected separately. Once the sensor was calibrated, the  $\text{CH}_4$  and  $\text{H}_2\text{O}$  concentrations in laboratory ambient air were continuously monitored for 62 h over a weekend. The  $\text{CH}_4$  signal was measured using the QEPAS sensor, while the  $\text{H}_2\text{O}$  signal was acquired using both the QEPAS sensor and the hygrometer TSP01. ICL wavelength shifts can affect the QEPAS measurement. This is expected when the laser line is fixed to the  $\text{CH}_4$  absorption peak without a line-locking feedback system. To avoid this issue, QEPAS spectral scans were acquired by setting the temperature of the ICL to 25 °C and scanning the laser current in the range 228–234 mA, to detect both  $\text{CH}_4$  and  $\text{H}_2\text{O}$  (see **Figure 2.10(b)**) absorption lines. The pressure and the flow of the sample air flushed through the ADM were set to 200 Torr and 25 standard cubic centimeter per minute (sccm), respectively. For each spectral scan, the QEPAS peak signals of  $\text{H}_2\text{O}$  and  $\text{CH}_4$  absorption features were extracted and are plotted as a function of time in **Figure 2.13(a)-(b)**, respectively. The time interval between two consecutive peaks of the same gas species was 3.8 min. Simultaneously, the TSP01 sensor was placed close to the QEPAS sensor to acquire the temperature and the relative humidity of the laboratory ambient air. The temperature and relative humidity excursion intervals recorded during 62 h of sensor operation were 24 - 28 °C and 32 - 44%, respectively. The absolute humidity is plotted in **Figure 2.13(c)** as a function of time.

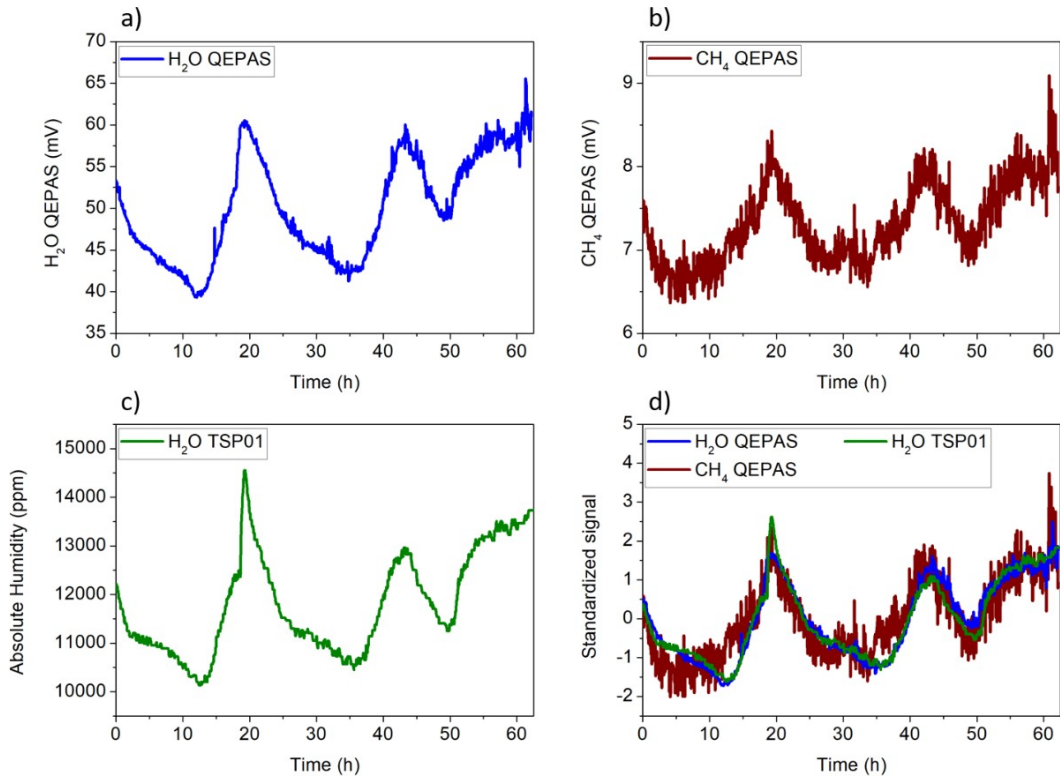


**Figure 2.13** QEPAS peak signal vs. time for **(a)** water vapor and **(b)** methane; **(c)** absolute humidity calculated from the temperature and relative humidity detected with TSP01 and using **Eq. 2.2**; **(d)** CH<sub>4</sub> QEPAS, H<sub>2</sub>O QEPAS, and absolute humidity signals standardized with respect to their mean and standard deviation values [109].

**Figure 2.13(d)** reports the standardized CH<sub>4</sub> QEPAS, H<sub>2</sub>O QEPAS, and the absolute humidity signals, overlapped on the same x-axis; each standardized signal was obtained by subtracting from the original signal its mean and dividing the difference by the standard deviation. The three signals exhibited the same trend as a function of time. Thus, the QEPAS sensor and the electronic hygrometer detected the same water vapor variations in ambient air, which in turn affected the CH<sub>4</sub> signal. Shifts of QTF resonance frequency as well as variations in the Q factor can affect QEPAS measurements. Indeed, the resonance frequency of the QTF determines the modulation frequency applied to the laser current, while the QEPAS signal is proportional to the Q factor itself. At the beginning and at the end of the 62 h long series of measurements, the QTF resonance curve was acquired, and no appreciable shifts in the frequency or sensible variations of the Q factor were measured.

As a first step, the absolute humidity values measured by TSP01 can be used to calibrate the QEPAS sensor for water vapor detection. In **Figure 2.14**, the H<sub>2</sub>O QEPAS signal is

plotted as a function of the absolute humidity (blue squares). The deviations of the H<sub>2</sub>O QEPAS signals with respect to hygrometer measurements can be mainly ascribed to a different precision of the two acquisition techniques and to the fact that the QTF is located in the gas cell, while the hygrometer is placed in the outside environment. The most immediate technique for smoothing signals consisting of equidistant points is the moving average. With a fixed subset size, the first element of the moving average is obtained by taking the average of the initial fixed subset of the number series. Then, the subset is modified by excluding the first datum of the series and including the next value in the subset. A LabVIEW-based software was implemented to perform a moving average and at the same time establish the optimized size of subsets. Starting from datasets with two points, a linear fit was performed on the obtained “smoothed” signal, and the R<sup>2</sup> value was extracted. Then, the subset size was increased, and R<sup>2</sup> values were plotted as a function of the subset size. R<sup>2</sup> value rapidly rose as the subset size increased until a plateau value of 0.99 was reached. This condition was obtained when the subset size was 20. **Figure 2.14** shows the averaged dataset when the subset size was 20 (green circles) and the best linear fit (red line), which returned a slope of  $k_1 = 5.9 \mu\text{V/ppm}$  and a negligible intercept. This curve can be used as a calibration curve to convert the H<sub>2</sub>O QEPAS signal into water vapor concentration.

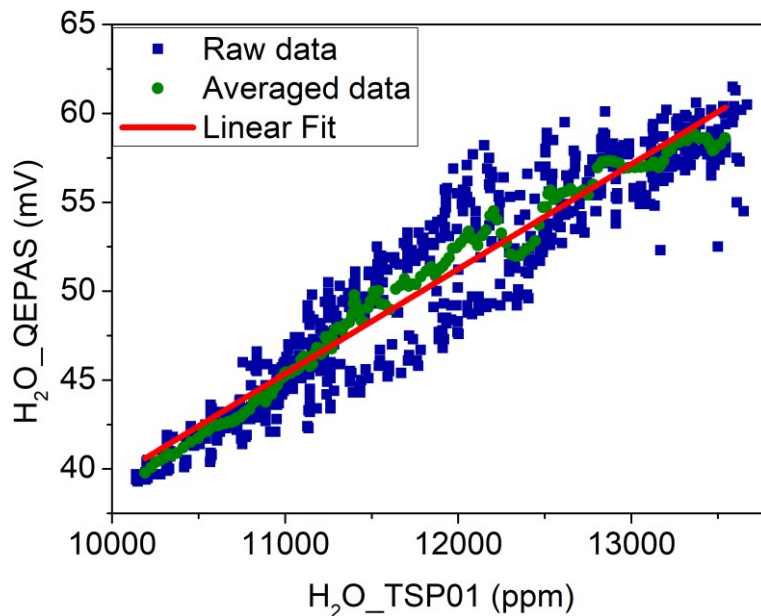


**Figure 2.14** H<sub>2</sub>O QEPAS signal plotted as a function of the absolute humidity (blue squares). Averaged dataset obtained with a moving average on 20 points (green circles); linear fit performed on the averaged dataset (red solid line) [109].

**Figure 2.13(d)** shows the influence of H<sub>2</sub>O variations on the CH<sub>4</sub> QEPAS signal due to water vapor acting as a relaxation promoter for methane. As the laboratory was closed without people inside for the entire duration of the measurement, the CH<sub>4</sub> concentration can be assumed to be constant with Gaussian-distributed fluctuations. At atmospheric concentrations level, the CH<sub>4</sub> QEPAS signal varies linearly with absolute humidity, as demonstrated in previous studies [113]. Thus, the CH<sub>4</sub> QEPAS signal is plotted as a function of the absolute humidity in **Figure 2.15** (black squares).

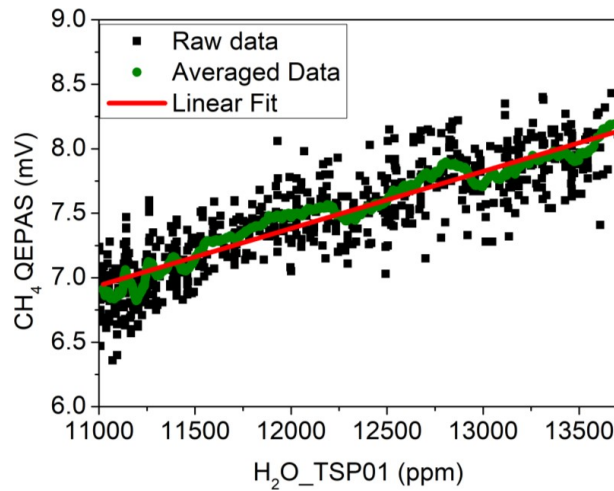


**Figure 2.15** CH<sub>4</sub> QEPAS signal in standard laboratory air plotted as a function of the absolute humidity of the air measured with the TSP01 sensor (black squares). Dataset obtained with a moving average on 25 points (green circles); linear fit performed on the averaged dataset (red solid line) [109].

A moving average was implemented on the dataset with subset size of 25 (green circles). The corresponding calibration curve (red line) is the linear fit to averaged dataset, resulting in a slope of  $m_1 = 0.4 \mu\text{V/ppm}$ , an intercept of  $q_1 = 1.95 \text{ mV}$ , and a  $R^2$  of 0.98. This calibration curve was used to compensate the influence of the H<sub>2</sub>O concentration in air on the CH<sub>4</sub> signal using the following equation:

$$\overline{CH_4}(mV) = CH_{4\text{ QEPAS}}(mV) - m_1 \left( \frac{mV}{ppm} \right) \cdot H_{2O_{TSP01}}(ppm) \quad \text{Eq. 2.3}$$

where  $\overline{CH_4}$  is the signal obtained with water compensation,  $CH_{4\text{ QEPAS}}$  is the measured CH<sub>4</sub> QEPAS signal, and  $H_{2O_{TSP01}}$  is the absolute humidity measured with the hygrometer.

**Figure 2.16** shows the comparison between the CH<sub>4</sub> concentration detected by the QEPAS sensor without (**Figure 2.16(a)**) and with (**Figure 2.16(b)**) water compensation.

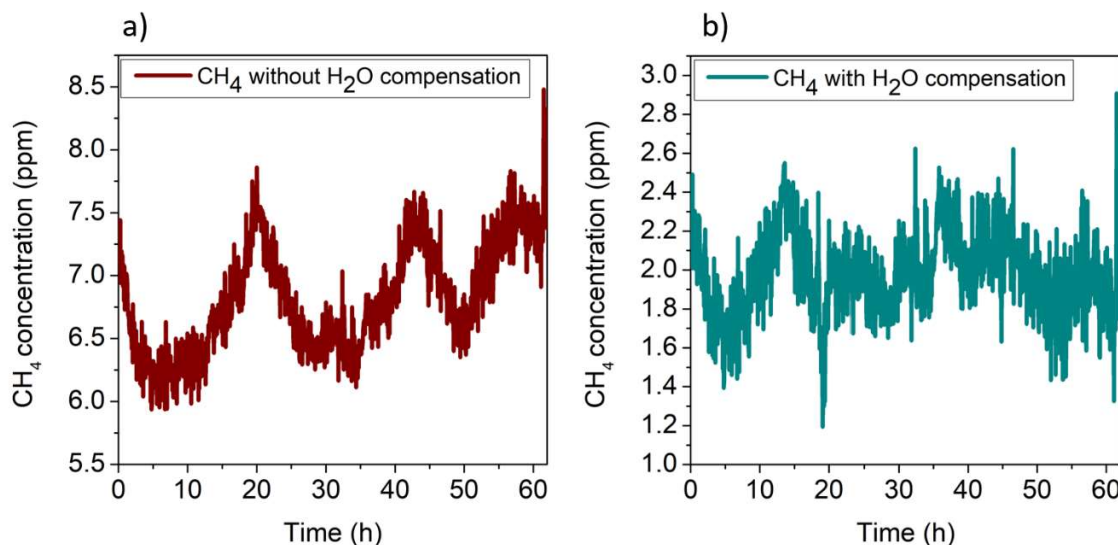


**Figure 2.16 (a)** QEPAS signal of methane in air without water compensation; **(b)** methane QEPAS signal after water compensation using the absolute humidity recorded by the hygrometer [109].

In both cases, the calibration curve of CH<sub>4</sub> in N<sub>2</sub> ( $y = 1.07 \text{ mV/ppm } x$ ) was used to convert the y-axis from mV to ppm. It is worth noting that a mean value of CH<sub>4</sub> concentration of 6.82 ppm with a standard deviation ( $1\sigma$ ) of 0.44 ppm was estimated without water compensation (**Figure 2.16(a)**), which does not represent a reliable measurement of the atmospheric CH<sub>4</sub> concentration. Conversely, the use of the electronic humidity sensor allowed correct calibration of the CH<sub>4</sub> signal, resulting in a mean concentration value of  $1.95 \pm 0.25$  ppm, significantly lower than the concentration estimated without water compensation and a noise comparable with that of the CH<sub>4</sub> sensor calibrated using the CH<sub>4</sub> – N<sub>2</sub> mixtures. For comparison, the H<sub>2</sub>O QEPAS signal was used for the correction of CH<sub>4</sub> QEPAS measurement instead of TSP01. The results are shown in **Figure 2.17**.

The corrected CH<sub>4</sub> signal showed a trend similar to those obtained when TSP01 was used for CH<sub>4</sub> signal compensation (see **Figure 2.16(b)**). A standard deviation of 0.27 ppm was measured, comparable with the 0.25 ppm value obtained using TSP01. As the use of the H<sub>2</sub>O QEPAS signal as methane signal compensation does not add any improvement, it was demonstrated that the use of the hygrometer is a valid alternative when the laser spectral range does not cover a H<sub>2</sub>O absorption line.

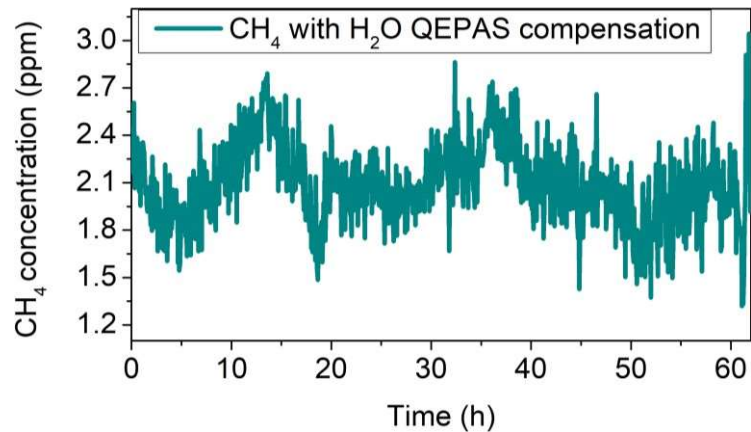


**Figure 2.17** Methane QEPAS signal after water compensation using the H<sub>2</sub>O QEPAS signal [109].

To verify the repeatability of the measurement, a second set of data was acquired for 48 h (the next weekend), and the same analysis was performed on this new dataset. **Figure 2.18** shows the CH<sub>4</sub> QEPAS signal (red line), the H<sub>2</sub>O QEPAS signal (blue line), and the H<sub>2</sub>O signal measured by the electronic hygrometer (green line) standardized to their mean and standard deviation values. Again, the influence of water on CH<sub>4</sub> signal is clearly visible.

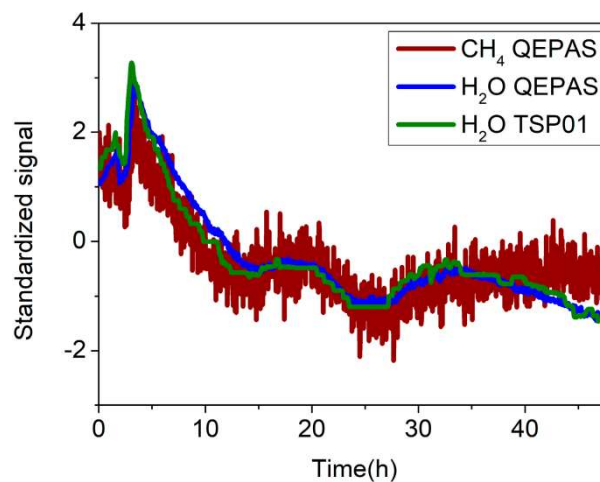


**Figure 2.18** Standardized signals of CH<sub>4</sub> (red line) and H<sub>2</sub>O (blue line) in laboratory air detected with the QEPAS sensor. Standardized absolute humidity detected with the TSP01 hygrometer (green line). Standardization was accomplished with respect to their mean and standard deviation values [109].

As for the first dataset, the H<sub>2</sub>O and CH<sub>4</sub> QEPAS signals as a function of the absolute humidity were averaged and linearly fitted; a slope of  $m_2 = 0.4 \mu\text{V/ppm}$  was extracted,

matching the value of  $m_1$ , thus demonstrating the repeatability of the measurements. The  $\text{CH}_4$  QEPAS signals were corrected using the linear fit with slope  $m_2$  as calibration curve. The results without and with water calibration are shown in **Figure 2.19(a)-(b)**, respectively, where the y-axis has been converted in ppm using the calibration curve of  $\text{CH}_4$  in  $\text{N}_2$ . A mean concentration value of methane in atmosphere of  $1.76 \pm 0.2$  ppm was extracted, comparable with the previous estimation.

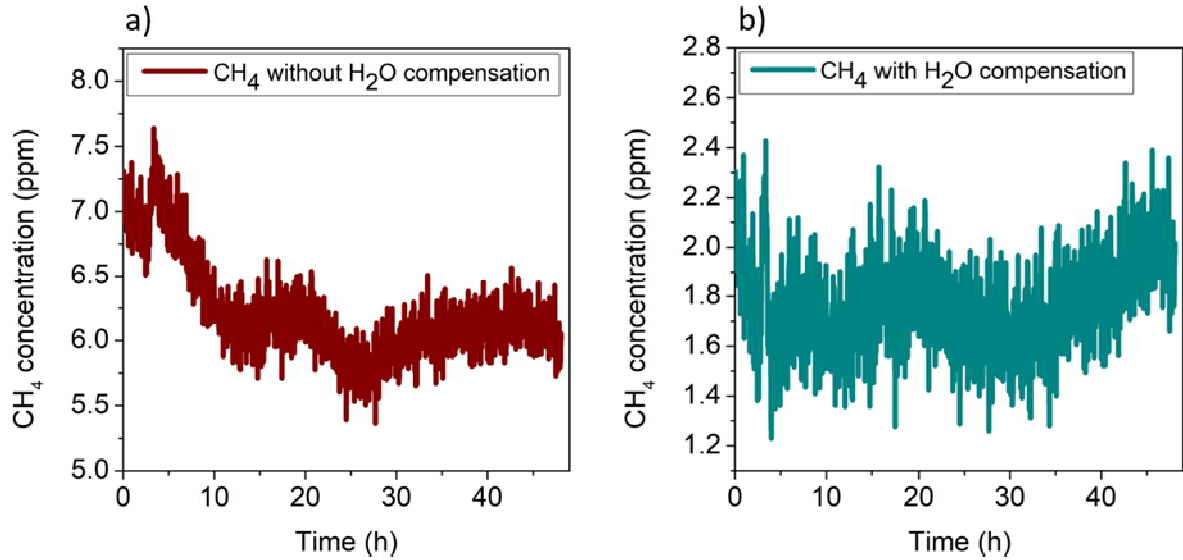


**Figure 2.19** (a) QEPAS signal of the methane in laboratory air without water compensation; (b) methane QEPAS signal after the compensation with the absolute humidity recorded by the hygrometer [109].

Although its sensitivity as well as response time is worse than  $\text{H}_2\text{O}$  QEPAS detection, a hygrometer can be successfully used to compensate the  $\text{CH}_4$  QEPAS signal for a reliable detection in the atmosphere. Therefore, this approach represents a valid solution that can be easily extended for detection of all gas species with the QEPAS technique without the use of an additional laser source to target water vapor.

### 2.3 Leak detector

Leak detectors employing gas traces as leakage markers are the most sensitive devices available on the market [114] - [116]. The gas should have the following properties [117]: it should give an unambiguous signal, it should be chemically and physically inert, non-explosive and cheap, easily removable from the system by pumping, with very low content in air and it should not contaminate the system. Tracer gas leak detectors can be operated

in two configurations [117]: the vacuum method and the positive pressure method, or sniffer technique. In the vacuum method, commonly used to search leaks at vacuum vessels, the system to be tested is continuously evacuated: if the tracer gas penetrates from the outside into the system, it is pumped through a leak detector where its concentration is measured. In the sniffer method, usually applied for pressurized systems, the device to be investigated is pressurized with the tracer gas. The leak positions of the test object are traced with a sniffer tip. Mass Spectrometers (MS) as leak detectors are the most sensitive instruments for stating leak presence in vacuum systems. MS for leak detection usually employs helium as tracer gas since it is unequivocally detectable with a MS; He has relative great mass distance from neighbor molecules, enabling high sensitivity and selectivity; it is present in normal air in a concentration of only 5 ppm; its small mass and atom volume assures good supply of gas through a leak; it is non-toxic and non-explosive; it is quite economical and chemically inert [115]. Because of high space occupancy of MSs and the depletion of helium supplies [118], innovative solutions to realize leak detectors are needed. Sulfur hexafluoride ( $\text{SF}_6$ ) is an alternative tracer gas to be employed in leak detectors [115]. In [86], a QEPAS sensor capable to detect part-per-trillion (ppt) level of  $\text{SF}_6$  is described, thus suggesting that QEPAS technology is employable for leak detection applications. In this section, a  $\text{SF}_6$  QEPAS sensor aimed to characterized leakages in mechanical components is illustrated.

### **2.3.1 $\text{SF}_6$ QEPAS sensor architecture**

Leakage detection of mechanical components requires the development of a compact and a robust sensor to be implemented in a test station. The typical apparatus of a QEPAS sensor [14] was engineered to fit in a compact  $15 \times 30 \times 35 \text{ cm}^3$  shoe-box sized sensor, shown in **Figure 2.20**.



**Figure 2.20** QEPAS sensor for the detection of SF<sub>6</sub>. All the components of a typical QEPAS sensor [14] fit inside the box.

The mechanical structure in **Figure 2.21** contains the components aimed to align the laser source and the ADM. This structure strongly improves the robustness of the optical components alignment.

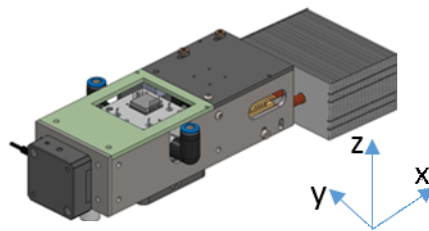


**Figure 2.21** Prototype of the mechanical structure containing the laser source, the focusing lens, the ADM and the power meter.

The laser source employed is a DFB QCL mounted in a HHL housing. It emits at a central wavelength of 10.54  $\mu\text{m}$ , where the strongest absorption lines of the SF<sub>6</sub> with linestrength of  $1.5 \cdot 10^{20}$  cm/mol are present [78]. The beam is focused into the ADM using a ZnSe BiConvex E3 coated lens of focal length 40 mm. The ADM consists of a QTF having prong length 9.4 mm, thickness 0.5 mm, spacing 0.8 mm, and fundamental frequency of 12 456,4 Hz at 100Torr [91]. It is coupled with a pair of microresonator tubes having length 12.4 mm and internal diameter 1.51 mm to enhance the sensitivity of the sensor. The laser current and temperature are controlled using an OEM laser driver and a miniature temperature controller (MTD1020T Miniature Temperature controller), shown in **Figure**

2.22. Its evaluation board (MTDEVAL1) is used to perform an oscillation test and set the correct PID parameters.

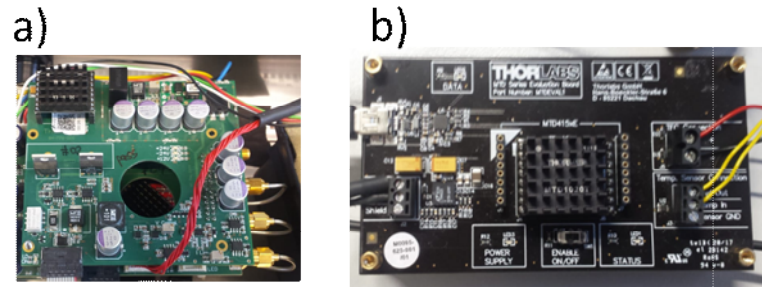


**Figure 2.22 (a)** OEM laser driver board; **(b)** Evaluation board used for setting the PID parameters of the temperature controller.

The RedPitaya STEMLab 125-14 board both generates signals for QTF characterization and laser modulation and acquire the QEPAS signal. A LabVIEW-based subroutine demodulate the QTF signal, thus replacing the lock-in amplifier. The gas line consists of a diaphragm pump, a pressure controller, a flow meter and a needle valve. A LabVIEW-based software controls every component of this compact QEPAS sensor.

### 2.3.2 SF<sub>6</sub> calibration

**Figure 2.23** shows a comparison between the absorption cross-section of the SF<sub>6</sub> at 100 Torr simulated using the HITRAN database [78] and the QEPAS scan measured for 20 ppm of SF<sub>6</sub> diluted in N<sub>2</sub>. The laser operating temperature was set to 30°C and the current was swept in the range 817 – 845 mA. The amplitude modulation was set to 13 mV.

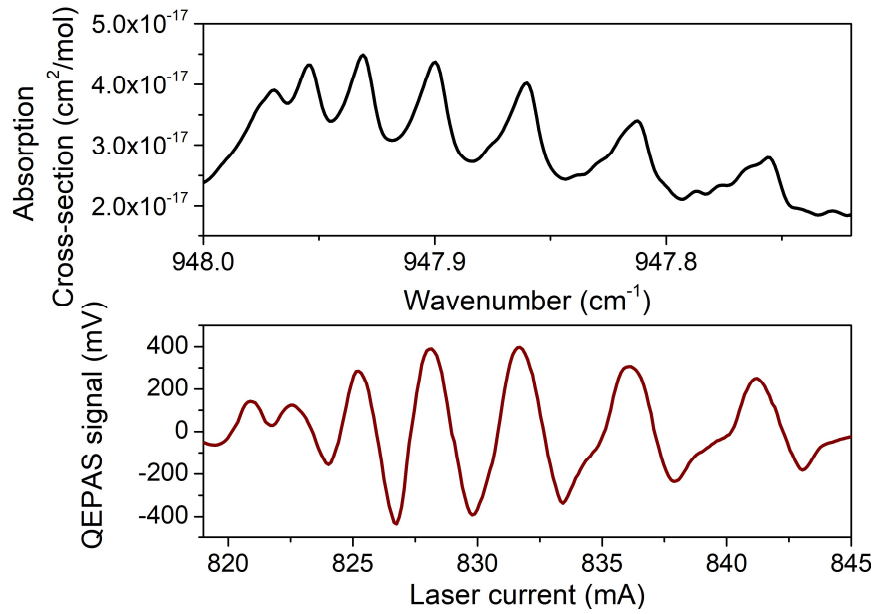


**Figure 2.23** Comparison of (a) QEPAS spectral scan measured for 20 ppm of  $\text{SF}_6$  at 100 Torr and (b) Hitran simulation of the absorption cross-section for pure  $\text{SF}_6$  at 100 Torr

The sensor was calibrated by diluting a certified 20 ppm  $\text{SF}_6:\text{N}_2$  cylinder and acquiring the QEPAS signal of the  $\text{SF}_6$  absorption line peaked at  $947.86 \text{ cm}^{-1}$ . The corresponding laser current and power are 831.7 mA and 34.9 mW, respectively.

**Figure 2.24(a)** shows the QEPAS spectral scans measured for  $\text{SF}_6$  concentrations in the 2 - 20 ppm range. The QEPAS peak values for the selected line were extracted from each spectral scan in **Figure 2.24(a)** and plotted as a function of the  $\text{SF}_6$  concentration in **Figure 2.24(b)**.

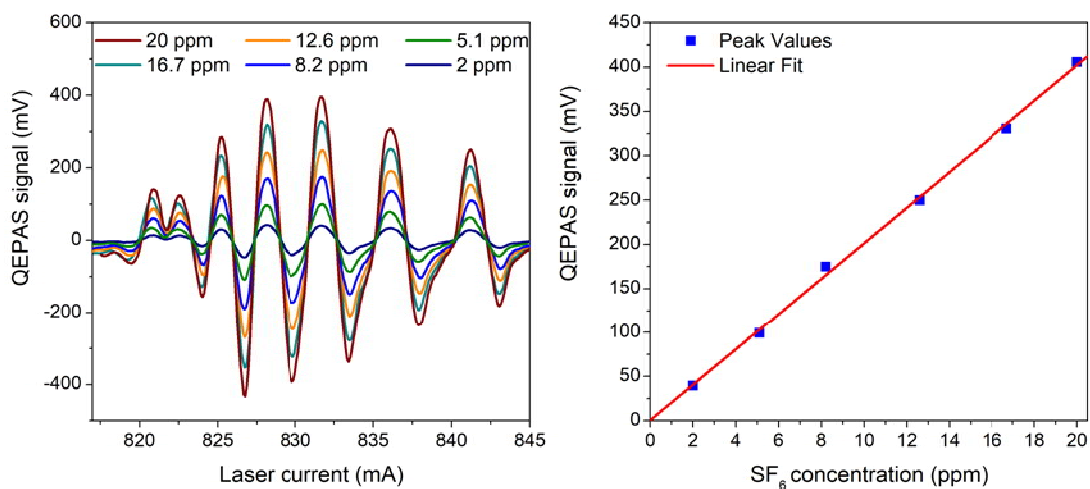


**Figure 2.24** QEPAS spectral scans (a) measured for 2 - 20 ppm SF<sub>6</sub>:N<sub>2</sub> and QEPAS peak values (b) measured for each SF<sub>6</sub> concentration (blue squares) with the corresponding best linear fit (red line).

The linear fit of the experimental data points in **Figure 2.24(b)** yields a slope of  $a = 20.08$  mV/ppm and an intercept of  $b = 0.43$  mV. The R-squared value equals 0.997, which verifies the linearity of the QEPAS sensor. For a measured  $1\sigma$ -noise level of 0.48 mV and a peak value of 405.72 mV, a SNR of 845 was estimated for the 20 ppm of SF<sub>6</sub>, corresponding to a MDL of 23 ppb at 8 ms integration time.

### 2.3.3 SF<sub>6</sub> QEPAS sensor for leak detection

A leak test station was designed and realized, by implementing the previously described QEPAS based SF<sub>6</sub> sensor system in a sniffer configuration previously described. This station is intended to detect and quantify leaks in the 3D printed vacuum chamber shown in **Figure 2.25**. These mechanical components realized in 3D printed technology could replace commercially available ADM [14], gaining the benefits of ease of fabrication and lightness.



**Figure 2.25** Example of 3D printed vacuum chamber.

**Figure 2.26(a)** shows the schematic diagram of the QEPAS leak-test station, including a 1% SF<sub>6</sub>:N<sub>2</sub> cylinder, a pressure meter and a test chamber containing the component under test (CUT). A picture of the test chamber is shown in **Figure 2.26(b)**. Two different 3D printed chambers were tested, differing in the fabrication layer height of 0.2 (CUT 1) and 0.1 (CUT 2) mm.

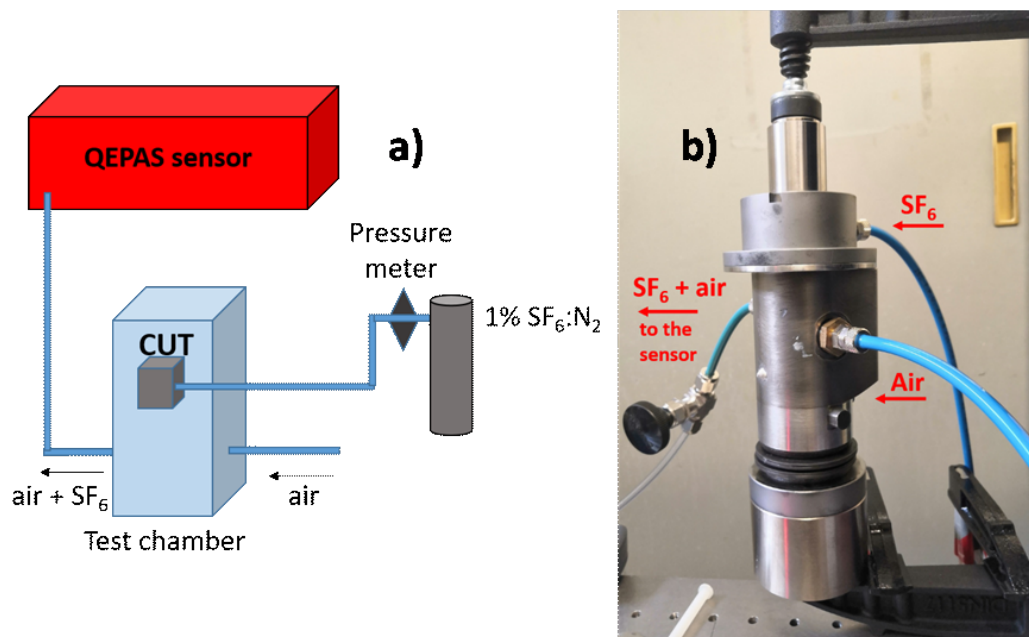


**Figure 2.26 (a)** Diagram of the leak-test station. CUT: component under test; **(b)** Picture of the test chamber, consisting of a SF<sub>6</sub> inlet port connected to the component under test, and of an inlet and outlet ports for the carrier gas.

In order to perform the leak measurement, the 3D printed component was inserted into the test chamber. Laboratory air was used as carrier gas, since the selected SF<sub>6</sub> absorption line is far from possible H<sub>2</sub>O absorption features which could cause interference effects; moreover, it was demonstrated that the presence of H<sub>2</sub>O in the gas mixtures does not modify the spectra of the SF<sub>6</sub> compared to the ones obtained for SF<sub>6</sub>:N<sub>2</sub> mixtures [86]. Laboratory air was passed through the test chamber at a flow rate of 0.90 mbar·l/s, while an over pressure of 1% SF<sub>6</sub>:N<sub>2</sub> was applied to the test component. Due to the differential pressure ( $\Delta P$ ) between the test chamber, at atmospheric pressure, and the SF<sub>6</sub>:N<sub>2</sub> mixture, leaks of the components will bring SF<sub>6</sub> molecules in the test chamber,. Thus, the gas sample coming out from the test chamber contains a SF<sub>6</sub> concentration, which depends on the leak intensity. The pressure controller inside the box allows the gas mixture to pass through the ADM at a fixed pressure of 100 Torr. This allows the measurement of SF<sub>6</sub> concentration using the QEPAS sensor, scanning across the SF<sub>6</sub> absorption line used for the calibration of the QEPAS sensor.

The pressure meter placed before the test chamber allows the measurement of the overpressure applied to the component.  $\Delta P$  was varied in the 0.2 bar - 3 bar range.

The resulting leak flow  $F_L$  corresponding to each  $\Delta P$  can be calculated from the following expression:

$$F_L = \frac{F_C \cdot (S - b)}{a \cdot C_{SF_6} - (S - b)} \quad \text{Eq. 2.4}$$

where  $F_C$  is the gas carrier flow (0.90mbar·l/s),  $S$  is the QEPAS peak signal recorded for each  $\Delta P$  considered, and  $C_{SF_6}$  is the certified concentration of SF<sub>6</sub> in N<sub>2</sub> used as leak tracer ( $C_{SF_6} = 1\%$  in our experiments). The test station response time, mainly depending on the flow rate and the length of the gas line connecting the test chamber to the ADM, was observed to be less than 10 sec.

The extracted leak fluxes as a function of the selected differential pressures for CUT 1 and CUT 2 are reported in **Figure 2.27**.

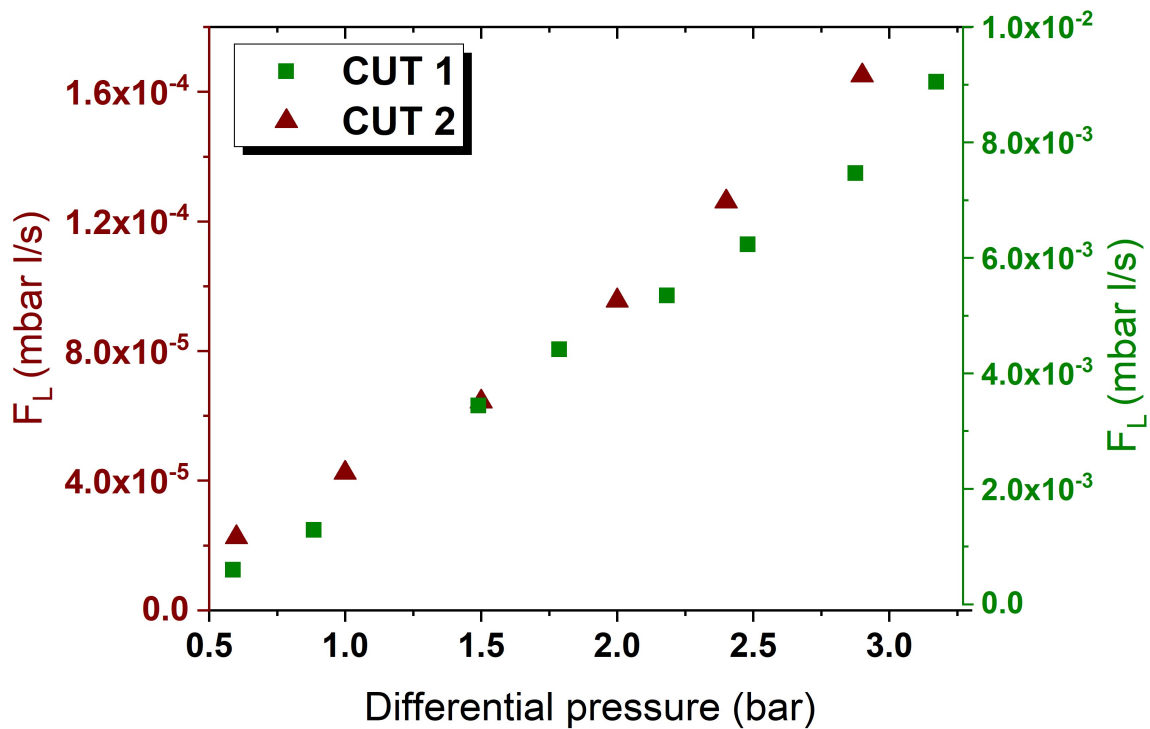


**Figure 2.27** Leak flows measured as a function of differential pressure  $\Delta P$  using the QEPAS sensors for CUT 1 (green squares) and CUT 2 (red triangles).

As shown in **Table 2.1**, in the same differential pressure range, the leak rate of the chamber CUT 2 are one order of magnitude lower than the leak rate of the chamber CUT 1. Therefore, it can be deduced that the smaller fabrication layer height of 0.1 mm of CUT

2 compared to the 0.2 mm height of CUT 1 improves the layer adhesion, resulting in a more tightened component.

**Table 2.1** Comparison of the leak rate of the two components under test.

	<b>F<sub>L</sub> @ ΔP=0.6 bar</b>	<b>F<sub>L</sub> @ ΔP=2.9 bar</b>
<b>CUT 1</b>	$6.57 \cdot 10^{-4}$	$7,46 \cdot 10^{-3}$
<b>CUT 2</b>	$2.25 \cdot 10^{-5}$	$1.65 \cdot 10^{-4}$

**Eq. 2.4** can be used to estimate the minimum detectable leak in these experimental conditions, starting from the QEPAS sensor noise-equivalent concentration of 23 ppb at 8 ms integration time; this results in a leak of  $\sim 2.25 \cdot 10^{-7}$  mbar· l/s. Further improvements of the minimum detectable leak could be obtained using pure SF<sub>6</sub> as leak test gas or reducing the air flux. However, the reduction of the carrier gas flux leads to an increase of the time needed for the SF<sub>6</sub> leak trace to reach the QEPAS sensor, causing an increase of the sensor response time.

## Chapter 3: Multi-gas detection

The detection of multiple gas in mixture is crucial in a wide variety of applications, from petrochemical to medicine [119]-[121]. Optical multi-gas sensing applications require either a wide tuning range of the exciting laser source or the employment of multiple sources. The spectral response of optical components can strongly affect the performance of the final sensor. Due to the wavelength independence responsivity of the QTF [14], QEPAS is perfectly suitable for these applications. Indeed, the piezoelectric transducers response depends only on the sound waves intensity and not on the wavelength of the exciting laser used.

In this chapter, numerous strategies to detect via QEPAS multiple gas components within complex matrices are illustrated.

Firstly, QEPAS sensors capable of detecting non-interfering absorbers are presented. Multiple and single laser sources are employed. In the first reported sensor, two laser diodes were employed to detect methane and ethane. These two hydrocarbons represent reliable markers for the identification and tracking of pollution sources, such as leakages from oil and gas pipelines and wildland fires [122].

Measurement of  $^{13}\text{CH}_4$ ,  $^{12}\text{CH}_4$  isotopic ratio helps in identifying the thermogenic or biogenic origin of natural gases, their sources and history [123]. In this chapter, a QEPAS sensor to detect methane isotopes sensor employing a quantum cascade laser is presented. The non-overlapping absorption features related to the two isotopologues fall within the dynamic range of the QCL.

In many other situations, gas fingerprints overlap within the dynamic range of the laser source, thus complicating the discrimination of the gas components in mixtures. Detection of the light alkanes such as methane (C1), ethane (C2) and propane (C3) in the gas phase, is crucial in the oil and gas industry to efficiently predict production outputs, estimate reserves and assess raw material quality of source rocks and reservoirs [8]. In this chapter, a QEPAS prototype employing an interband cascade laser (ICL) emitting at a central wavelength of 3345 nm is described. The tuning range of the laser source allowed covering a spectral window in which the absorption features of C1, C2 and C3 overlap. In this context, multilinear regression (MLR) proved to accurately detect their concentration in

mixture. The same approach was adopted to detect methane and nitrous oxide with an innovative laser source, consisting in an array of 32 quantum cascade lasers. The emission wavelengths of the 32 QCLs allowed the spectral coverage of  $150\text{ cm}^{-1}$ , with the possibility to study the overlap of the broadband absorptions of  $\text{CH}_4$  and  $\text{N}_2\text{O}$ , in the range  $1190\text{-}1340\text{ cm}^{-1}$ .

As a further improvement with respect to MLR approach, partial least square regression (PLSR) was implemented for the analysis of QEPAS spectra. In particular, the PLSR capability of identifying the cross-correlations among the measurements datasets allows the analysis to filter out the effect of the gas matrix variations on the detection of single components, by reducing the system to a new set of independent, non correlated, latent variables. The PLSR approach was adopted in QEPAS sensor devoted to methane/ethane detection at high concentrations and it was proved to extract concentration values with higher accuracy with respect to MLR method.

### **3.1 Trace gas detection of non-interfering absorbers**

As long as the target molecules exhibit well separated absorption features and their overall concentration in the mixture does not exceed the thousands of ppm, the realization of multiple gas traces sensors based on an easy detection scheme and relatively simple analysis of the QEPAS signals is possible. In this section, independent detection of different analytes will be described.

#### **3.1.1 Fiber-Coupled QEPAS sensor for $\text{CH}_4$ and $\text{C}_2\text{H}_6$ monitoring**

The first multiple gas detection approach employs multiple laser sources, one for each target gas. Switching between them, the qualitative and quantitative detection of the gas species in a mixture can be accomplished. In this paragraph, a methane and ethane QEPAS sensor employing two laser diodes is described. The light sources were fiber-coupled and collimated through the prongs of a T-shaped QTF [91]. This two lasers configuration allowed multiple gas detection, keeping compactness and robustness of the final QEPAS sensor.

### 3.1.1.1 Fiber-Based Quartz-Enhanced Photoacoustic Sensor Architecture

The architecture of the fiber-based QEPAS system designed for methane and ethane detection is depicted in **Figure 3.1**. Two near-IR distributed feedback (DFB) butterfly-packaged laser diodes were chosen as light sources. A laser diode (LD1) emitting around 1653.7 nm with an optical power of 12 mW (AOI DFB-1653-BF-12-CW-F2-H2-N127, AOI, Sugar Land, TX, USA) was chosen to target a merged methane triplet (P1) centered at  $6046.94\text{ cm}^{-1}$  with an overall cross-section of  $\sim 1 \cdot 10^{-20}\text{ cm}^2/\text{mol}$  at atmospheric pressure [78]. A laser diode (LD2) emitting around 1684 nm with an optical power of 8.5 mW (Eblana EP1684-0-DM-B06-FA, Eblana Photonics Ltd., Dublin, Ireland) targeted: (i) a six line merging structure (P2) of methane with an overall cross-section of  $7 \cdot 10^{-21}\text{ cm}^2/\text{mol}$  at atmospheric pressure located at  $5938.12\text{ cm}^{-1}$  [78]; (ii) several ethane absorption bands related to the overtones transition of the C-H stretching [124], [125], with the strongest peak (P3) being at  $5937.3\text{ cm}^{-1}$  [126]. Two compact laser diode drivers (Thorlabs CLD1015, Thorlabs, Newton, NJ, USA) controlled both the temperature and the laser sources' current. A custom-made Thorlabs fiber combiner (Thorlabs Canada ULC, Boulevard Montpellier Saint-Laurent, QC, Canada) was employed to couple the beams of the two lasers. Transmission efficiency of more than 92% was measured for both channels of the fiber coupler. The combiner was connected to the fiber port mounted on the ADM (see **Figure 3.1**), and the output beam was collimated through the tubes of the spectrophone composed of a custom T-shaped QTF having resonance frequency  $f_0$  of 12458.7 Hz and a dual-tube resonator system consisting of two 12.4 mm long tubes with an inner diameter of 1.6 mm. This spectrophone configuration provides both the highest signal to noise ratio enhancement with respect to the bare QTF ( $60\times$ ) [91] and allows an easy alignment of the laser beam through the QTF prongs spaced 0.8 mm apart. An optical power meter was employed for laser beam alignment purposes. About 99% of the incident radiation was measured passing through the spectrophone. The piezocurrent generated by the QTF was transduced into a voltage signal by means of a transimpedance amplifier. The 2f-detection wavelength modulation (WM) QEPAS technique was used by modulating the laser current with a frequency of  $f_0/2$  and acquiring the  $f_0$ -oscillating component of the spectrophone signal output. The analog outputs of a NI PCIe-6363 DAQ card (National Instruments, Austin, TX, USA) were used to provide the  $f_0/2$  modulation to the laser drivers (outputs AO1 and AO2) and the reference signal to a Perkin Elmer 7265 (Perkin

Elmer, Waltham, MA, USA) lock-in amplifier (output AO0). The QTF transduced signal was demodulated with an integration time set to 100 ms for all the measurements, if not stated otherwise. The signal was then acquired using the DAQ card, with an acquisition time of 300 ms. With the aim of developing a sensor suitable for real-time monitoring, measurements were performed by shining both lasers simultaneously through the ADM, to avoid any warm-up and temperature stability-related downtime. A LabVIEW (National Instruments, Austin, TX, USA) subroutine was developed to drive the two diode lasers and allow C1-C2 sequential monitoring. During a first 250 s-long time window (W1), the LD1 wavelength was modulated at  $f_0/2$  (sine waveform) and scanned across its full dynamic range (sawtooth waveform), from the threshold current of 30 mA to the maximum current of 160 mA, with a frequency of 4 mHz, while no current modulation was enabled on AO2. Once the LD1 sweep in time window W1 was complete, AO1 modulation was disabled and the LD2 wavelength was swept in the following 250 s-long time window W2, by modulating the injection current at  $f_0/2$  and scanning it from the threshold current of 20 mA to the maximum current of 120 mA, with a frequency of 4 mHz. The gas handling system was realized as follows: 1% C1:N<sub>2</sub>, 1% C2:N<sub>2</sub> and pure N<sub>2</sub> cylinders (Nippon Gases Italia, Modugno, Italy) were connected to an MCQ Instruments Gas Blender GB-103 (MCQ Instruments, Rome, Italy) to produce the desired gas sample mixtures. The gas sample passed through an MKS Type 649 (MKS Instruments Inc., Andover, MA, USA) pressure controller/flow meter, the ADM, a needle valve, and finally, a vacuum pump. A pressure controller, a needle valve and a pump allowed fixing and monitoring both gas pressure and flow inside the ADM.

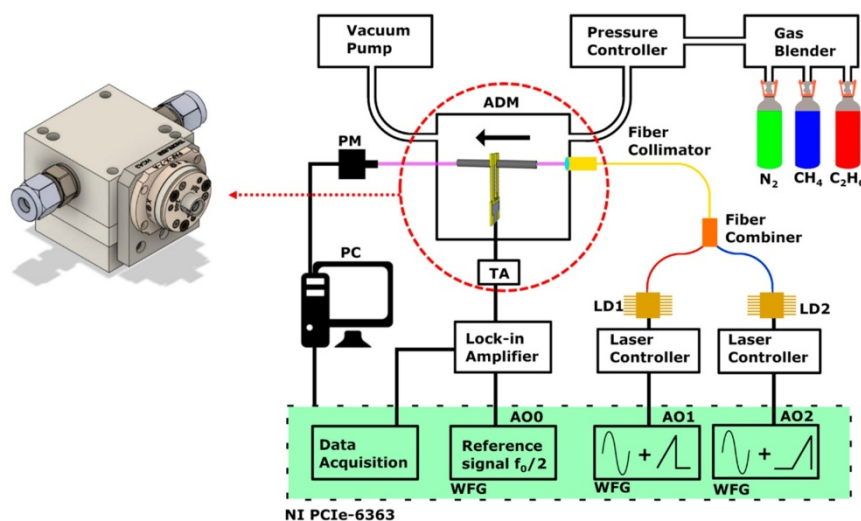


**Figure 3.1** Schematic of the experimental apparatus: ADM - acoustic detection module, LD1 - laser diode 1, LD2 - laser diode 2, TA - transimpedance amplifier, PM - power meter, PC - personal computer, WFG - waveform generator. The black arrow indicates the gas flow through the ADM. A detailed design of the fiber-coupled ADM is also shown [127].

### 3.1.1.2 Results and Discussion

All the experimental investigation and analysis presented in this work refer to spectra acquired in both time windows, W1 and W2. The TEC temperature was set to 25 °C for LD1 and 16 °C for LD2. The multiple C1 transitions composing P1 and P2 and simulated using the HITRAN database in **Figure 3.2(a)**, merge at 760 Torr in the W1-W2 QEPAS spectrum shown in **Figure 3.2(b)**, consisting of two well-separated second derivatives of a Lorentzian profile. The methane QEPAS signals displayed in **Figure 3.2(b)** were acquired by flushing a 0.1% methane – 99.9% nitrogen mixture through the sensor and employing a laser modulation depth of 110 mVpp for LD1 and 150 mVpp for LD2, which were identified as the values maximizing C1 signals.

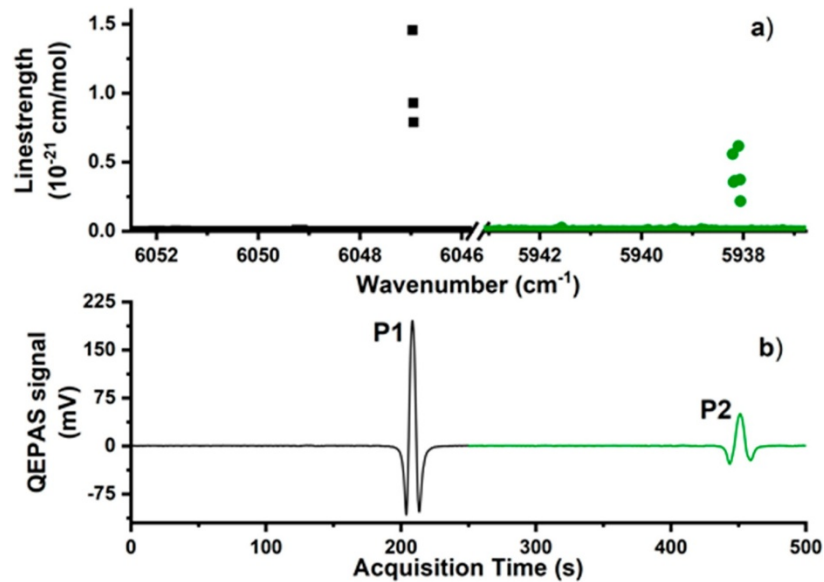


**Figure 3.2 (a)** Linestrength of methane absorption lines in the spectral ranges swept by LD1 (black dots) and LD2 (green dots). **(b)** 2f-QEPAS signal for a mixture containing 0.1% methane and 99.9% nitrogen obtained by scanning along the full dynamic range of LD1 (black curve) and LD2 (green curve). The QEPAS signals of the C1 peaks in LD1 range and LD2 range were 196.25 and 50.49 mV, respectively [127].

The P1 and P2 peak values were measured to be 196.25 and 50.49 mV, respectively. The noise level was calculated as the standard deviation of the acquired QEPAS signal, while pure nitrogen was flushing through the ADM. Noise levels of 145 and 150  $\mu\text{V}$  were respectively measured in the LD1 and LD2 ranges. The main contributions to the noise levels are represented by (i) the thermal noise of the QTF; (ii) the electrical noise of the whole system; (iii) the photothermal signal arising from the laser beam tails hitting the spectrophone; and (iv) slow oscillations of mechanical components. For a 0.1% C1 in  $\text{N}_2$  mixture, no background absorption with respect to the ground noise recorded in pure  $\text{N}_2$  was detected in LD1 and LD2 laser ranges. Ethane QEPAS spectrum in **Figure 3.3** was obtained by flushing a 1% ethane–99% nitrogen gas mixture through the ADM.

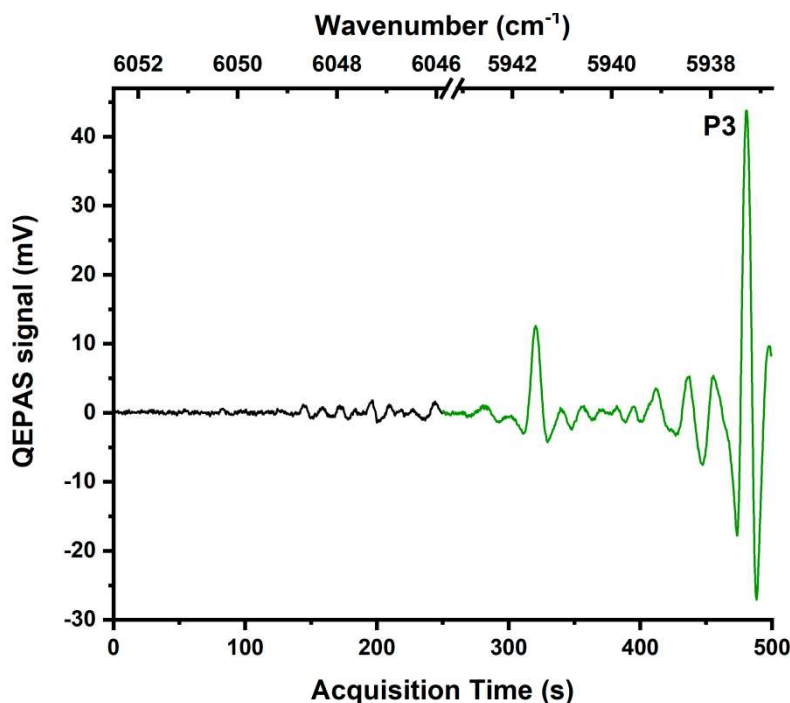


**Figure 3.3** 2f-QEPAS signal for a mixture containing 1% ethane and 99% nitrogen. The black curve was obtained by sweeping the full dynamic range of LD1, and the green curve was obtained by sweeping the full dynamic range of LD2 [127].

The tuning range covered by the two DFB lasers allowed targeting several ethane absorptions features. The QEPAS spectrum acquired in the LD1 range can be divided into two distinguishable regions. The first one from 0 to 140 s ( $6052.5 - 6049 \text{ cm}^{-1}$ ) is characterized by a standard deviation comparable to the noise floor. A standard deviation of  $650 \mu\text{V}$  characterizes the second one from 140 to 250 s ( $6049 - 6046 \text{ cm}^{-1}$ ) with a non-resolved absorption background. Much stronger QEPAS signals are observed in the

spectral range covered by LD2, with the strongest peak (P3) falling at 480 s ( $5937.3 \text{ cm}^{-1}$ ). The sensor performances for methane and ethane detection in mixtures are displayed in Figures 3.4 – 3.7. In Figure 3.4(a) a portion of the W1 2f-QEPAS spectra acquired for six different mixtures, simulating a 1% contamination of a pure nitrogen matrix with different C1–C2 combined concentrations, are shown.

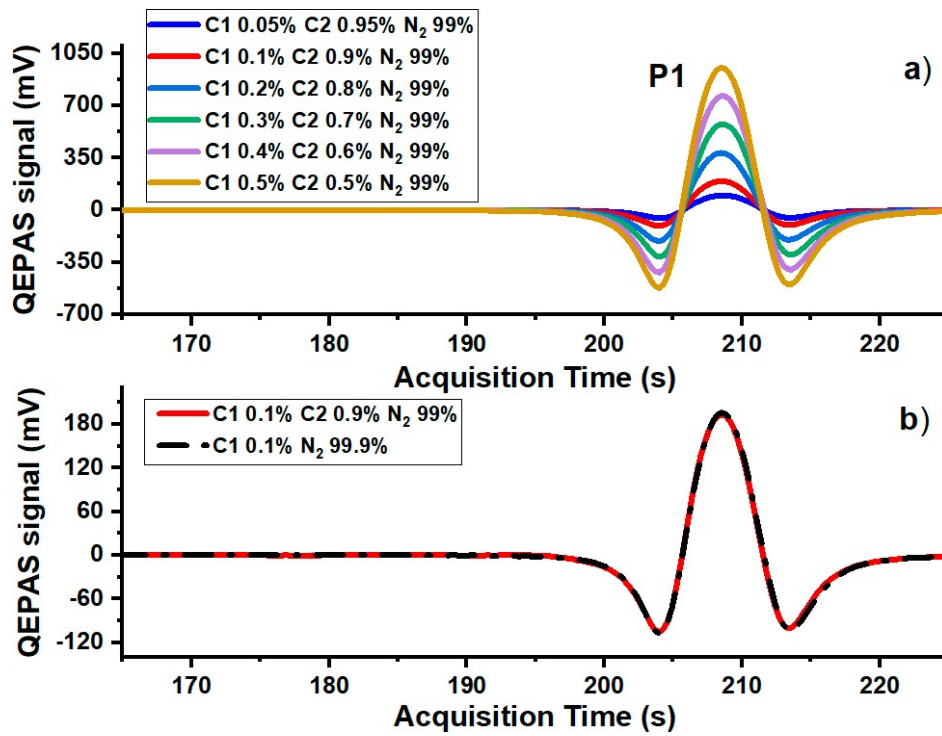


**Figure 3.4 (a)** P1 QEPAS signals measured in the LD1 emission range nearby P1 for six mixtures of C1, C2 and N<sub>2</sub>. **(b)** Comparison of LD1 0.1% methane QEPAS signals between mixtures containing 99.9% nitrogen, and 99% nitrogen and 0.9% ethane [127].

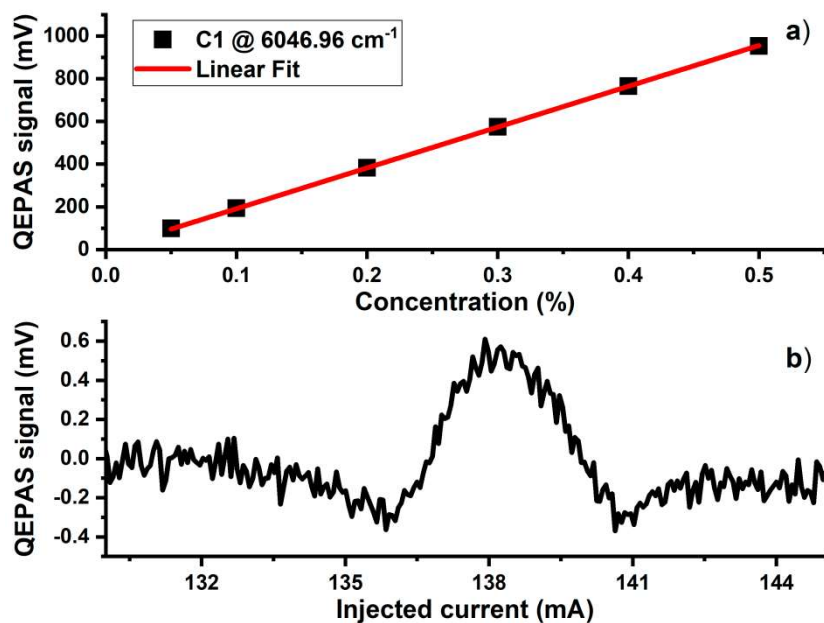


**Figure 3.5 (a)** Linearity of the 2f methane peak signal in the concentration range 0.05–0.5% in mixtures containing both C<sub>2</sub> and N<sub>2</sub>. The uncertainty of the measured data points lies within the size of the depicted data point symbols. **(b)** 2f C<sub>1</sub> QEPAS signal in the LD1 range measured for a standard-air mixture containing 1.9 ppm of methane [127].

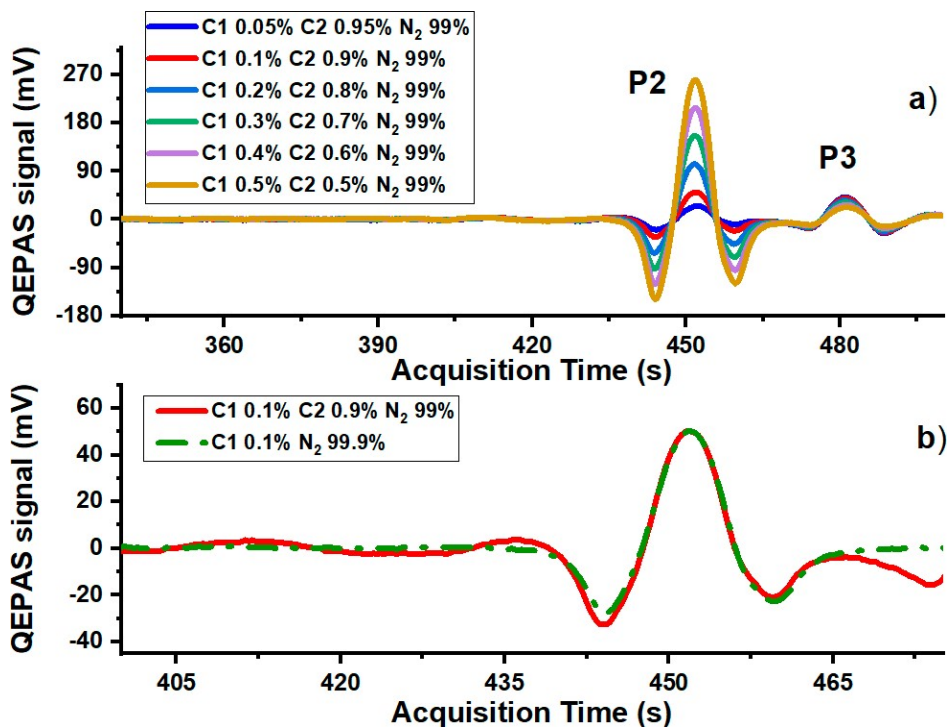


**Figure 3.6 (a)** 2f-signals in the LD2 range measured for six mixtures of C<sub>1</sub>, C<sub>2</sub> and N<sub>2</sub>. **(b)** Comparison of 0.1% of LD2 methane QEPAS signals between mixtures containing 99.9% nitrogen, and 99% nitrogen and 0.9% of ethane [127].

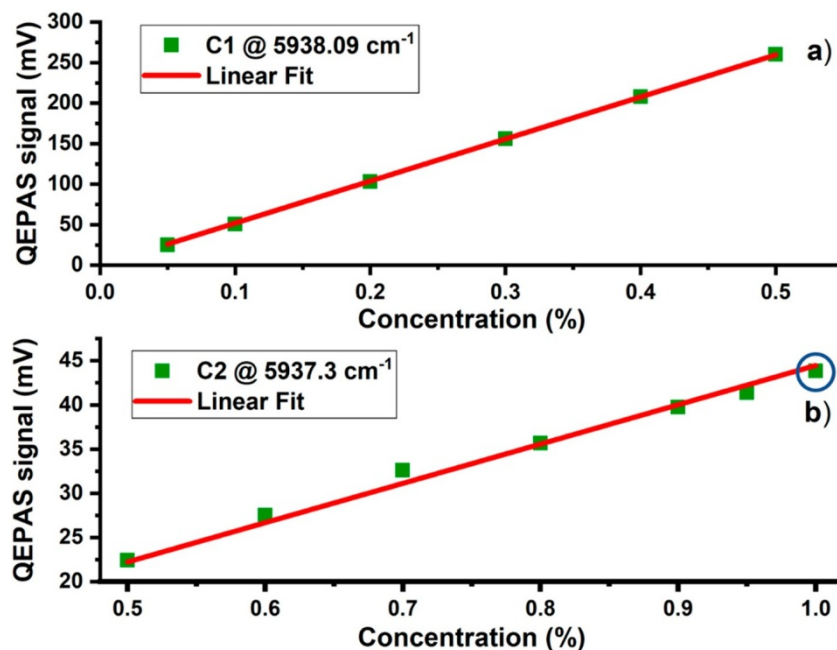


**Figure 3.7 (a)** Linearity of the 2f methane peak signal in the concentration range 0.05–0.5% in mixtures with C2 and N<sub>2</sub>. **(b)** Linearity of the 2f ethane peak signal in the concentration range 0.5–1% in mixtures with C1 and N<sub>2</sub>. The uncertainty of the measured data points lies within the size of the depicted data point symbols [127].

**Figure 3.4(b)** shows the comparison between the P1 QEPAS spectra measured for a mixture of 0.1% of C1 in a matrix of pure N<sub>2</sub>, and a mixture with a C1 concentration fixed at 0.1%, while C2 concentration is at 0.9% and the rest is N<sub>2</sub>. It is clearly visible that the presence of 0.9% of C2 does not influence the intensity or the shape of P1, neither in terms of absorption interference nor in terms of energy relaxation as a collisional promoter. This experimental evidence is confirmed by the perfect linearity of the peak value of P1 versus the C1 concentration (**Figure 3.5(a)**) extracted from the 2f-QEPAS spectra shown in **Figure 3.4(a)**. The slope of the calibration curve, obtained by interpolating the data in **Figure 3.5(a)** with a linear fit, is 1910 mV/%. The minimum detection limit (MDL) that can be reached at 100 ms of integration time is 0.76 ppm, more than two times lower than the natural C1 concentration in standard air (~1.9 ppm). This sensitivity, together with the absence of interference effects from ethane, justify the use of LD1 for continuous monitoring of the environmental CH<sub>4</sub> concentration. The measurement of ambient methane in a standard air matrix is shown in **Figure 3.5(b)**. In order to enhance the natural C1 QEPAS peak for this measurement, an integration time of 2 s and an acquisition time of 6 s were chosen.

The QEPAS spectrum shown in **Figure 3.5(b)** was obtained at atmospheric pressure. Compared to the expected value of  $\sim 0.36$  mV calculated from the pure  $N_2$  matrix calibration shown in **Figure 3.5(a)**, the  $\sim 0.5$  mV peak value measured in standard air was slightly higher. This could be related to the effects of water vapor and  $O_2$  in the air matrix on methane relaxation dynamics. Acoustic wave generation relies on the transfer rate at which vibrational energy of the excited target gas molecules is converted into the kinetic energy of the surrounding molecules (V-T relaxation). This process is characterized by a relaxation time  $\tau$ , which depends on the composition of the mixture according to the formula [128]:

$$\frac{1}{\tau_M} = \sum_i C_i \cdot \frac{1}{\tau_{M-M_i}} \quad \text{Eq. 3.1}$$

where  $1/\tau_M$  is the relaxation rate of an excited state of a molecule  $M$ ,  $1/\tau_{M-M_i}$  is the relaxation rate corresponding to collisions with the  $i$ -th molecule in the gas mixture and  $C_i$  is the concentration of the  $i$ -th molecule. The radiation-to-sound conversion efficiency of a molecule depends on the product  $2\pi f\tau$ , where  $f$  is the frequency of the generated acoustic wave ( $f = f_0$  in our case). If this product is much lower than 1 while each component's concentration varies, the mixture composition does not affect the QEPAS signal of the target molecule [128]. Nitrogen, water vapor and oxygen are the main air components. Methane QEPAS signal was proven to depend on water vapor concentration variations when the absolute humidity varied in the range of 1.2–1.6% [113], [109], when targeting absorption transition lines in the mid-IR wavelength range at 3.3  $\mu\text{m}$ . This experimental evidence indicates that a C1 QEPAS signal compensation with respect to the mixture's absolute humidity is required.

In the near-IR, the configurations of the energy levels and the relaxation rates of each energy transfer were investigated in many different studies [85], [128]. For the transitions involved in the experiment presented here, at a working pressure of 760 Torr, the relaxation rates of the excited C1 energy levels through the collisional partners are listed in **Table 3.1**:

**Table 3.1** V–T relaxation rates of the  $n$ th  $\nu_4$   $CH_4^*$  excited vibrational state with the main collisional partners in standard air at a working pressure of 1 atm [127].

Reaction	$1/\tau_{M-M_i} (s^{-1})$	Reference
$CH_4^*(nv_4) + CH_4 \rightarrow CH_4^*[(n-1)v_4] + CH_4$	$8 \cdot 10^5$	[128]
$CH_4^*(nv_4) + N_2 \rightarrow CH_4^*[(n-1)v_4] + N_2$	$8 \cdot 10^4$	[128]
$CH_4^*(nv_4) + O_2 \rightarrow CH_4^*[(n-1)v_4] + O_2$	$1.3 \cdot 10^5$	[128]
$CH_4^*(nv_4) + H_2O \rightarrow CH_4^*[(n-1)v_4] + H_2O$	$8.2 \cdot 10^7$	[85]

Considering a sample of standard air composed of 1.9 ppm of methane, 20.9 % oxygen, 1.86 % water and the remaining part of nitrogen, the relaxation rate of C1 is in the  $10^7 s^{-1}$  order of magnitude. The order of magnitude of the product  $2\pi f\tau$  is in the  $10^{-3}$  scale. The dominant contribution on the  $CH_4$  relaxation rate in standard air is the V-T relaxation of methane on water vapor. Even if the concentrations of the other components change, the methane relaxation rate does not change. Calculations using **Eq. 3.1** indicate that the water vapor influence on the methane relaxation rate saturates at  $H_2O$  concentrations over 0.6%. Thereby, in the typical water vapor concentration range of standard air (between 0.6% and 3% [78]), no variations of the C1 QEPAS signal are expected when targeting transitions at  $1.654 \mu m$ . This implies that the radiation-to-sound conversion efficiency will not change. Therefore, the methane QEPAS signal in this wavelength range at atmospheric pressure is not expected depending on water vapor or oxygen variations around the atmospheric concentration or on other components in standard air. All these assumptions avoid the necessity of C1 signal compensation.

This kind of sensor architecture could be implemented for applications like sensing on drone. For example, while LD1 can guide the drone along the concentration gradients, LD2 can be used to measure both C1 and C2 in an air sample once the pollution source has been identified, to characterize the source through the C2/C1 ratio. **Figure 3.6(a)** shows the QEPAS spectra in a portion of the LD2 dynamic range for the same mixtures investigated in the LD1 range (see **Figure 3.4(a)**). P2 and P3 features are well-resolved in the 2f-QEPAS scans even for unbalanced mixtures (e.g., 0.05% C1-0.95% C2-99%  $N_2$ ). Additionally, in W2 the C1 exhibits no absorption background, but the C2 broadband absorption slightly influences the P2 peak profile. Indeed, as shown in **Figure 3.6(b)**, a small difference between the spectra related to the 0.1% C1—99.9%  $N_2$  (green dash dots) and 0.1% C1-0.9% C2-99%  $N_2$  (red line) mixtures can be appreciated just for the negative lobes. This means that the C1 concentration measurements extracted from the peak values are not affected even in a mixture with a C2 concentration almost one order of magnitude

larger than C1, which is still an unlikely situation in real life. Despite different ethane concentrations in the mixtures, the calibration with respect to P2 reflects a perfect linearity between the measured peak signal and the C1 concentration (**Figure 3.7(a)**).

This further experimental evidence confirms that ethane does not influence the methane QEPAS signal in this wavelength range. The slope obtained from the linear fit was 520 mV/%. The sensitivity reached at 100 ms integration time was 2.9 ppm. The lower sensitivity of P2 with respect to P1 extends the overall detectable methane concentration range to higher values, without signal saturation. In this configuration, higher C1 concentrations can be detected with LD2 in the immediate vicinity of the pollution source/leakage. Combining both LD1 (W1) and LD2 (W2), this QEPAS sensor can detect methane concentrations ranging from ppb to few percent. The calibration of the 5937.3  $\text{cm}^{-1}$  ethane peak P3 is shown in **Figure 3.7(b)**. The 1% ethane peak value, highlighted with a blue circle in **Figure 3.7(b)**, corresponds to the peak value of **Figure 3.3**, without methane in the mixture. The linearity shown in **Figure 3.7(b)** demonstrates that presence of methane does not influence the ethane QEPAS signal in the mixture. The slope retrieved from the linear fit of the C2 calibration is 44 mV/%. Considering the 150  $\mu\text{V}$  noise level, the ethane sensitivity at 100 ms of integration time is 34 ppm.

### 3.1.2 Detection of methane isotopes

In laser spectroscopy, high precision isotopic ratio measurements with individual ro-vibrational lines require a spectral separation at a given pressure, which is large enough to avoid absorption interference. In the case of methane isotopes, both  $^{12}\text{CH}_4$  and  $^{13}\text{CH}_4$  are spherical rotors that show similar vibrational–rotational line patterns, shifted by 10  $\text{cm}^{-1}$  due to the C mass difference [129]. Therefore, the location of the strongest  $^{13}\text{CH}_4$  isotopic lines will be relatively close to those of the parent  $^{12}\text{CH}_4$  species. For  $^{13}\text{CH}_4/^{12}\text{CH}_4$  features having comparable line-strengths, the isotopic ratio measurement is affected by the large dynamic range expected for the different isotopic abundances ( $\sim 1/100$ ). In order to compensate the absorption cross-sections, the most suited target consists of a pair of  $^{13}\text{CH}_4$  -  $^{12}\text{CH}_4$  lines in which the  $^{13}\text{C}$  isotope transition has an oscillator strength approximately two order of magnitude higher with respect to the  $^{12}\text{C}$  transition. Attention must be also given regarding the possible large dependence that a ratio in intensity has on the temperature through ground-state energies and broadening coefficients.

In this paragraph, a QEPAS sensor employing a single quantum cascade laser (QCL) capable to detect two methane isotopes is described. Considering the laser tuning range, the pair of absorption features that better fulfill the requirements listed above is composed of two lines at  $1296.12\text{ cm}^{-1}$  and  $1296.03\text{ cm}^{-1}$  for  $^{12}\text{CH}_4$  and  $^{13}\text{CH}_4$ , respectively, characterized by a temperature coefficient of the cross-section ratio of  $-6.7\%/^{\circ}\text{C}$ .

### 3.1.2.1 Methane isotopes QEPAS sensor

The experimental apparatus employed to detect methane isotopes is shown in **Figure 3.8**.

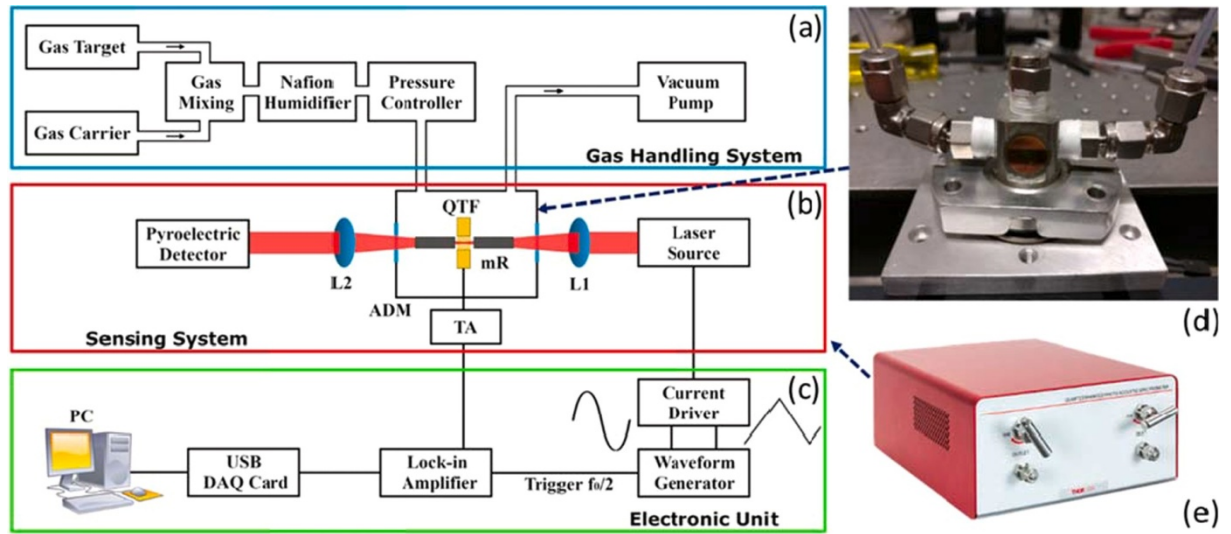


**Figure 3.8** Schematic of the experimental apparatus divided in three main building blocks: **(a)** a gas handling system including a 3 channels MCQ Instrument Gas Blender 1003, **(b)** a sensing system and **(c)** an electronic unit. **(d)** is a picture of the ADM: acoustic detection module including the QTF and the acoustic micro-resonator tubes (mR). L1 and L2 are AR-coated ZnSe lenses, TA is the transimpedance amplifier. The sensing system has been embedded into a shoe box sized case (sizes  $30\text{ cm} \times 10\text{ cm} \times 20\text{ cm}$ ) shown in the picture **(e)** [130].

The laser source selected for this investigation is a distributed-feedback QCL produced by Corning and emitting at  $7.73\text{ }\mu\text{m}$ , in the middle of the absorption bands of the C-H bond bending [78]. Since the QCL beam waist at the focal point has a FWHM of  $\sim 300\text{ }\mu\text{m}$ , a custom T-shaped QTF with a prong spacing of  $0.8\text{ mm}$  was used. The resonance properties of the custom QTF were investigated in detail in [91]. The measured resonance frequency is  $12461.22\text{ kHz}$  with a quality factor of 42000 at 50 Torr. The custom QTF was acoustically coupled with a pair of micro-resonator tubes in an ON-BEAM configuration

and housed in a gas cell. In the lower panel of **Figure 3.9** are plotted the absorption cross-sections for  $^{12}\text{CH}_4$  and  $^{13}\text{CH}_4$ , simulated at 50 Torr by using the HITRAN database [78].

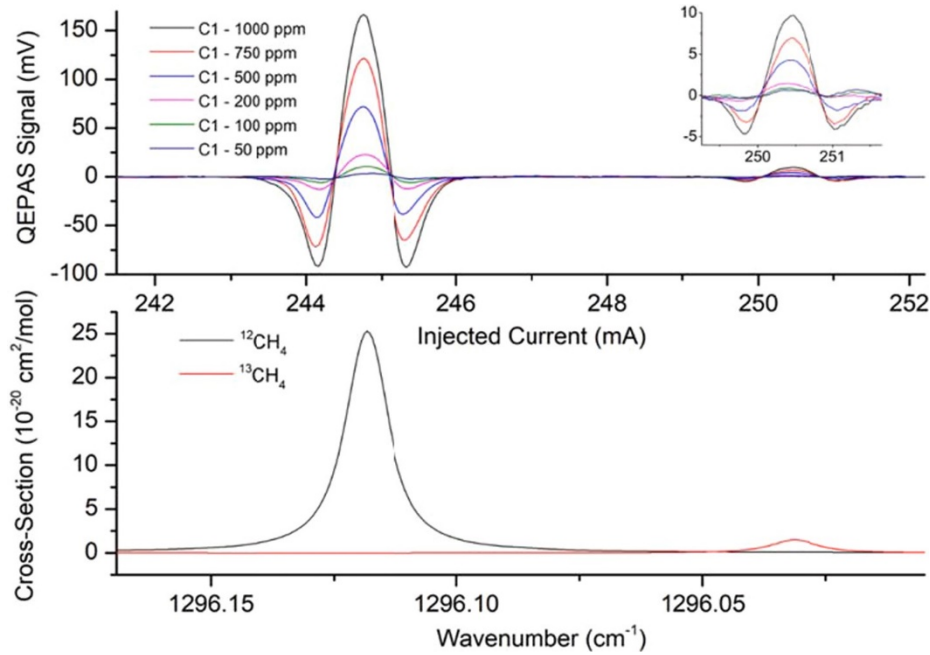


**Figure 3.9** Lower panel: absorption cross-section for  $^{12}\text{CH}_4$  (black line) and  $^{13}\text{CH}_4$  (red line) absorption features at 50 Torr; Upper panel: 2f-QEPAS signal recorded for standard methane at concentration levels varying from 1000 ppm down to 50 ppm in pure  $\text{N}_2$  at a pressure of 50 Torr. The QCL injected current scan in the upper panel corresponds to the wavelength tuning reported in the lower panel (1296–1296.15  $\text{cm}^{-1}$ ). In the inset a zoom on the  $^{13}\text{C}$  peak is shown [130].

The absorption cross-section takes into account the natural abundance of each isotope ( $\sim 98.82\%$   $^{12}\text{CH}_4$ ,  $1.11\%$   $^{13}\text{CH}_4$ ). The cross-section ratio at 20 °C is  $\sigma_{13}/\sigma_{12} \sim 0.06$ , with a temperature coefficient of  $-6.7\%/^{\circ}\text{C}$ , which represents a negligible correction with respect to the gas temperature variations expected during the experiment. As shown in the lower panel of **Figure 3.9**, at 50 Torr the spectral separation between the two lines is more than 7 times larger than their full width half maximum ( $\sim 0.012 \text{ cm}^{-1}$ ), so that no overlap occurs between the two Lorentzian-like absorption profiles. In order to verify the validity of all the assumptions made and demonstrate the sensor capability in detecting methane isotopes, a gas sample of standard methane was analyzed. In the upper panel of **Figure 3.18**, the QEPAS spectra acquired at 50 Torr for different standard methane concentrations (from 50 ppm to 1000 ppm) in  $\text{N}_2$  are displayed. The 242.6 mA – 252.6 mA QCL injected

current scan corresponds to a wavenumber tuning from  $1296 \text{ cm}^{-1}$  to  $1296.15 \text{ cm}^{-1}$ . The modulation depth was set at 7.5 mV. As shown in the upper panel of **Figure 3.18**, the two features related to the isotope  $^{12}\text{CH}_4$  and  $^{13}\text{CH}_4$  are perfectly distinguishable. The 1000-ppm mixture of standard methane was then diluted with  $\text{N}_2$  down to 50 ppm. We verified that there is a perfect linearity of the 2f-QEPAS signal peaks versus the methane concentration for both isotopes  $^{12}\text{CH}_4$  and  $^{13}\text{CH}_4$  (see upper panel in **Figure 3.9**).

For all the concentrations, the ratio between the QEPAS peak signals  $S_{13}/S_{12}$  was verified to be  $\sim 0.06$ . This result is in excellent agreement with the cross-section ratio simulated by the HITRAN database for a standard abundance ratio and consistent with the proportionality between the QEPAS signal and the absorption coefficient expressed by **Eq. 1.1 [78]**. The standard deviation of the noise level is 0.1 mV, while the  $^{13}\text{CH}_4$ -QEPAS signal peak for a concentration of 11 ppm resulted  $\sim 10$  mV. This corresponds to a minimum detection limit of  $\sim 110$  ppb achievable at 0.1 s of lock-in integration time. In the same way, the  $^{12}\text{CH}_4$  minimum detection limit at the same operating conditions was 600 ppb. The sensor capability in measuring variation of the  $^{13}\text{C}/^{12}\text{C}$  abundance ratio can be calculated starting from the deviation  $\delta^{13}\text{C}$  of  $^{13}\text{C}/^{12}\text{C}$  in the sample with respect to a standard ratio:

$$\delta^{13}\text{C} = \left[ \frac{\left(\frac{^{13}\text{C}}{^{12}\text{C}}\right)_{\text{sample}}}{\left(\frac{^{13}\text{C}}{^{12}\text{C}}\right)_{\text{standard}}} - 1 \right] \times 100 \% \quad \text{Eq. 3.2}$$

The  $\delta^{13}\text{C}$  variations  $\Delta\delta^{13}\text{C}$ , calculated from **Eq. 3.2** through the propagation of error, for a mixture of 1000 ppm of methane in  $\text{N}_2$  results proportional to signal fluctuations and inversely proportional to the  $S_{12}$  peak signal. Considering that the  $1-\sigma$  fluctuations of  $S_{12}$  and  $S_{13}$  peak signals were measured as low as of 0.1 mV, at 0.1 sec of integration time  $\Delta\delta^{13}\text{C}$  is calculated slightly below 10%.

In **Table 3.2** is reported a comparison among the preliminary results obtained with our QEPAS sensor, targeting a pair of  $^{12}\text{CH}_4$ ,  $^{13}\text{CH}_4$  absorption lines at  $\sim 7.73 \mu\text{m}$ , and the performance of a couple of well-established and field proven methane isotope analyzers. As it can be noticed, the essential requirement for providing valuable and reliable methane

isotopic ratio deviations is the capability to sense  $\delta^{13}\text{C}$  variation with a precision of 1‰ or lower in a detection range as wide as possible.

**Table 3.2** Performance comparison among the most representative optical sensors for methane  $\delta^{13}\text{C}$  ratio determination [130].

	CRDS PICARRO G2132-i [131]		OA-ICOS LOS GATOS Methane Carbon Isotope Analyzer [132]		QEPAS Spectrometer	
	$^{12}\text{CH}_4$	$^{13}\text{CH}_4$	$^{12}\text{CH}_4$	$^{13}\text{CH}_4$	$^{12}\text{CH}_4$	$^{13}\text{CH}_4$
<b>Precision</b>	50 ppb @ 30 s	10 ppb @ 30 s	< 0.2‰ @ 300 s	< 0.2‰ @ 300 s	600 ppb @ 0.1 s	110 ppb @ 0.1 s
<b>Precision <math>\delta^{13}\text{C}</math></b>	< 0.4‰ @ 1 h		< 1‰ @ 300 s		< 10 ‰ @ 0.1 s	
<b>Range</b>	10–100 ppm	10–100 ppm	1 ppm-100%	1 ppm-100%	50–1000 ppm	50–1000 ppm

For a methane gas mixture in the percent concentration scale, typical of natural gas samples, and at an integration time in the order of magnitude of tens of seconds, the  $\Delta\delta^{13}\text{C}$  for the QEPAS spectrometer is expected to reach a value well below the 1‰ as well. Further improvements in precision can be achieved by implementing differential measurements with two ADMs, also combined with a modulation cancellation approach [59].

## 3.2 Trace gas detection of overlapping absorbers

Simple molecules (< 5 atoms) absorption lines are usually isolated and without significant background. In more complex molecules, a high density of vibrational states and line broadening often reflect structured absorption bands over a wide spectral region [133]. In such cases, their detection in mixture is not trivial. In this section, several strategies aimed to detect complex gas components in mixture are discussed.

### 3.2.1 $\text{CH}_4$ , $\text{C}_2\text{H}_6$ and $\text{C}_3\text{H}_8$ detection using a QEPAS sensor and an ICL

In this paragraph, the detection strategy aimed at quantifying the concentration of three hydrocarbons in mixture is described. The target gases are methane (C1), ethane (C2) and

propane (C3). These two last species are complex molecules. The absorption features of the three components overlap in the tuning range of the selected ICL.

### 3.2.1.1 Selection of C1 and C2 spectral range for QEPAS operation

As a first step, it was identified the spectral region that can be covered with a single ICL source, containing well resolved  $\text{CH}_4$  and  $\text{C}_2\text{H}_6$  absorption features and characterized by absorption cross-sections in the  $10^{-18}$  ( $\text{cm}^2/\text{mol}$ ) range.

In **Figure 3.10**  $\text{CH}_4$  and  $\text{C}_2\text{H}_6$  absorption cross-sections and related linestrengths are plotted in the range  $2984\text{-}2992\text{ cm}^{-1}$  using data from the HITRAN database [78].

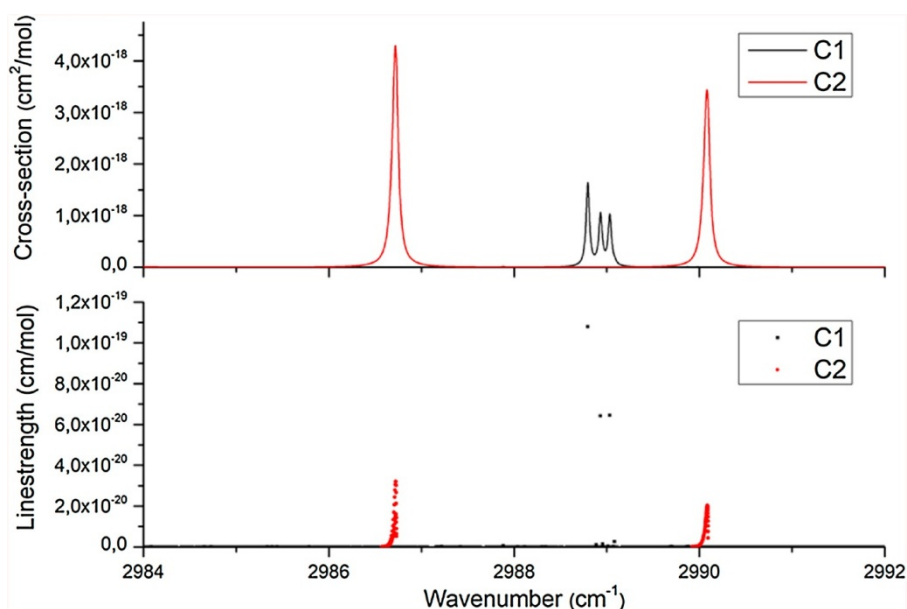


**Figure 3.10** Top panel: absorption cross-sections at 50 Torr pressure for methane (black curve) and ethane (red curve) in the range  $2984\text{-}2992\text{ cm}^{-1}$  simulated using the Hitran database [78]. Bottom panel: C1 (black dots) and C2 (red dots) corresponding linestrengths [134].

These spectra were simulated for pure  $\text{CH}_4$  and  $\text{C}_2\text{H}_6$  at 50 Torr. At this pressure, the absorption line broadening due to collisions is low enough to allow distinguishing the fine structure of the absorption bands. Within a spectral range of  $3.5\text{ cm}^{-1}$  there are two Lorentzian-like absorption lines of  $\text{C}_2\text{H}_6$ , composed by several lines marked in red dots, as shown in the lower panel of **Figure 3.10**, and in the middle three partially merged lines of  $\text{CH}_4$ . Even though the line strength of a single  $\text{CH}_4$  transition is higher with respect to the two  $\text{C}_2\text{H}_6$  transitions, the collisional broadening at a pressure of 50 Torr or higher gives

rise to two isolated  $C_2H_6$  absorption features with a cross-section larger than the three-fold  $CH_4$  structures. The spectral separation between the  $CH_4$  three-lines structure and the two  $C_2H_6$  lines guarantees a non-interfering detection of both species.

### 3.2.1.2 QEPAS sensor configuration

The identification of target lines represented in **Figure 3.10** led to a specific ICL design commercialized by Nanoplus, with a central emission wavelength of 3345 nm ( $2989\text{ cm}^{-1}$ ). The ICL current dynamic range is  $I = 15 - 70\text{ mA}$  and the optimal operating temperature range is from  $T = 5\text{ }^\circ\text{C}$  to  $T = 15\text{ }^\circ\text{C}$ . The ICL is mounted in a standard TO66 package equipped with a collimating lens (see **Figure 3.11**).

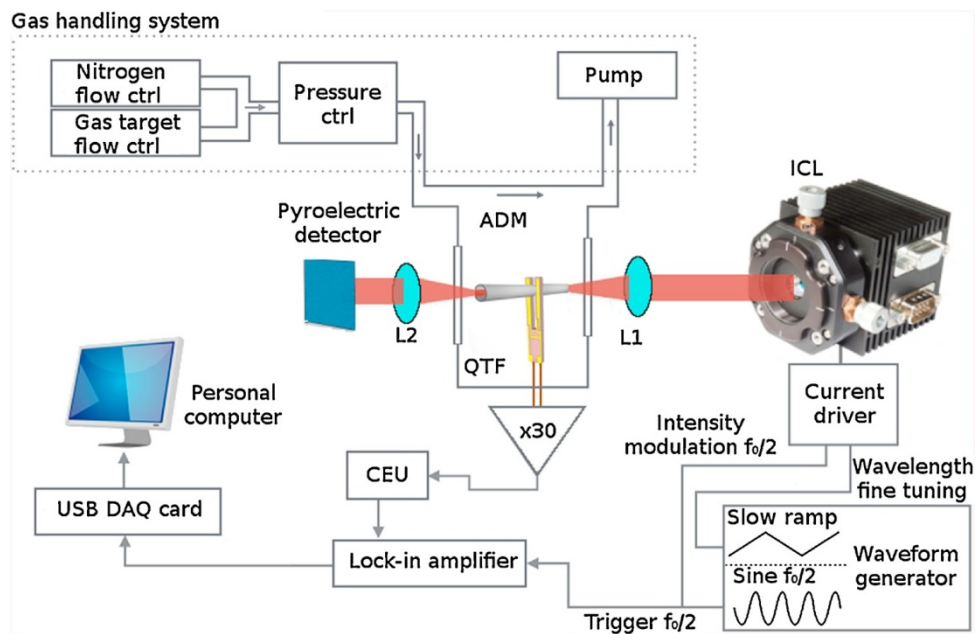


**Figure 3.11** Schematic of the experimental apparatus. CEU - control-electronic-unit; ADM - acoustic detection module; L1, L2 –ZnSe lenses; ICL – intercascade laser [134].

The beam emerging from the lens has a nearly perfect Gaussian power distribution with a diameter of 3 mm. A maximum power of  $\sim 11\text{ mW}$  was measured at  $T = 5\text{ }^\circ\text{C}$  and  $I = 70\text{ mA}$  with an electric power consumption of  $0.273\text{ W}$ . The high quality of the laser beam allowed operation with a standard  $32\text{ kHz}$  QTF (prong spacing of  $0.3\text{ mm}$  and length of  $3\text{ mm}$ ) mounted in an on-beam double tube configuration, constituting the spectrophone of the QEPAS sensor system. The acoustic detection module (ADM) consists of a cylindrical chamber with gas-in and gas-out connectors and two optical ZnSe windows. The spectrophone is positioned inside the ADM. The employed spectrophone shows a quality

factor of  $Q = 2100$  at atmospheric pressure and a resonance frequency for the QTF fundamental flexural in-plane mode of  $f_0 = 32\,741.5$  Hz.

The collimated light exiting the ICL is focused by a ZnSe lens (L1) through the ADM; L1 has a focal length of 7.5 cm and a transmittivity of 95% at 3345 nm. A gas line connects the ADM to the pump on the outlet side and to a pressure controller located at the inlet side. The pressure controller maintains the downstream pressure of the targeted gas mixture into the ADM. The mixtures are generated by flow controllers and a constant water concentration of 1.7% was provided by a Nafion humidifier inserted on one of the gas lines. The light exiting from the ADM is re-collimated using a ZnSe lens (L2) and collected by a VIGO detector (model PVI-3TE-3.4) with a detectivity of  $7.0 \cdot 10^{11}$   $\text{cm} \cdot \text{Hz}^{1/2} \cdot \text{W}^{-1}$ , current responsivity  $\geq 0.8$   $\text{A} \cdot \text{W}^{-1}$  and time constant  $< 200$  ns was used for monitoring the laser power and for alignment purpose. The piezoelectric current generated by the photoacoustic excitation is converted into a voltage signal and amplified by a factor 30 using a transimpedance amplifier (with a feedback resistor of 10 M $\Omega$ ) and then sent to the Control Electronics Unit (CEU). The CEU is used to determine the main QTF parameters: the electrical resistance  $R$ , the quality factor  $Q$ , and the resonance frequency  $f_0$ . It is also used to transfer the signal coming from the transimpedance amplifier to a lock-in amplifier. The output analog signal from the lock-in amplifier is then digitalized by a National Instruments DAQ card (USB 6008) connected to a personal computer. LabVIEW-based software acquires the temporal evolution of the QEPAS signal and the response of the pyroelectric detector. All measurements were performed by using an integration time of 100 ms and acquisition time of 300 ms.

### 3.2.1.3 Sensor calibration for methane detection

We investigated the full ICL dynamic range to retrieve the most convenient experimental conditions for C1-C2 detection in the current scan mode. A mixture of 1000 ppm of  $\text{CH}_4:\text{N}_2$  and a mixture of 1000 ppm of  $\text{C}_2\text{H}_6:\text{N}_2$  were analyzed. 2f-wavelength modulation (WM) was employed as the detection scheme since it is characterized by a background-free signal [105]. The ICL injected current  $I$  was modulated at half of the resonance frequency  $f_0/2$  and the QEPAS signal was demodulated at the resonance frequency  $f_0$  (2f-signal). Usually, the current sinusoidal excitation and the QEPAS signal are out of phase. For this reason, the demodulation of the QEPAS signal occurs at a detection phase  $\phi_i$  maximizing the demodulated signal amplitude. The main results from this investigation

showed that by operating at an ICL temperature of 15 °C, the laser emission wavelength is resonant with the C<sub>2</sub>H<sub>6</sub> absorption line located at 2986.25 cm<sup>-1</sup> (C2) at a laser current of I = 65.5 mA, while to target the strongest CH<sub>4</sub> absorption line peak at 2988.8 cm<sup>-1</sup> (C1) and for the C<sub>2</sub>H<sub>6</sub> line located at 2990.1 cm<sup>-1</sup> (C2) the injected current must be set at I = 48 mA and I = 35 mA, respectively. Thus, all three transitions C2 can be excited by keeping the laser operating temperature fixed at 15 °C and exploiting the ICL current dynamic range. Once the ICL operating conditions to target the selected CH<sub>4</sub> and C<sub>2</sub>H<sub>6</sub> absorption lines were identified, the full sensor calibration procedure was performed. The QEPAS response to the excitation of C1 at different pressures was recorded. The data reported in **Figure 3.12(a)** correspond to the 2f-QEPAS peak signals obtained by operating in the wavelength modulation configuration and optimizing the modulation depth for each different operating pressure.

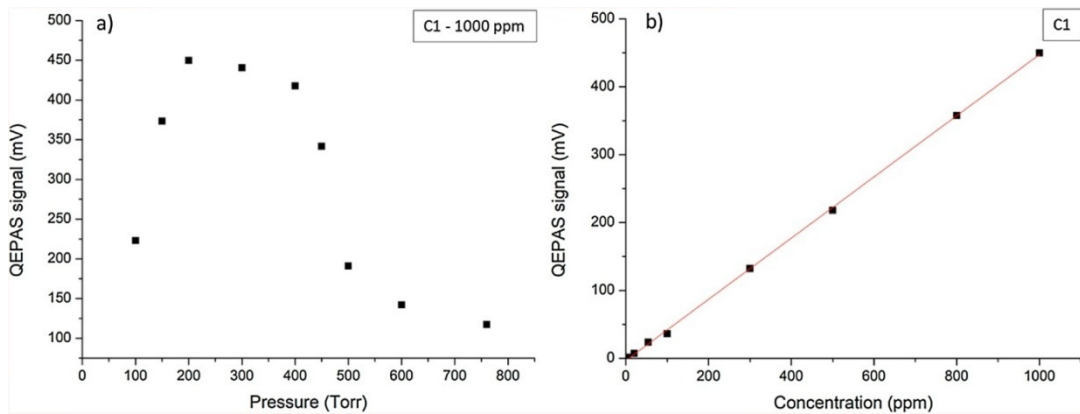


**Figure 3.12 (a)** 2f-signal peak values related to C1 at their optimum modulation depth for different pressures ranging from 100 Torr to atmospheric pressure; **(b)** linearity of the 2f-signal peak values obtained at 200 Torr over a range of C1 concentrations from 4 ppm to 1000 ppm in pure N<sub>2</sub> [134].

For methane, the strongest response to photoacoustic excitation was achieved at a gas pressure of 200 Torr and a modulation amplitude of 130 mV peak-to-peak (Vp-p). The detection phase  $\phi_1$  maximizing the QEPAS signal related to C1 excitation was 99.91°. These operating parameters were used for all the following C1 measurements. Once determined the best operating conditions in terms of gas pressure and modulation depth, the 2f-signal peak signals at different C1 concentrations were recorded. Different CH<sub>4</sub> concentrations in the range 4-1000 ppm were generated, starting from a certified 1000 ppm CH<sub>4</sub> in N<sub>2</sub> mixture and using pure N<sub>2</sub> as diluting gas. By keeping fix the total flow of the

mixture at 50 sccm, the uncertainty of the CH<sub>4</sub> concentration was estimated from the nominal values of the accuracy of the two mass flow meters, one dedicated to the methane and the other one to pure nitrogen. The error estimated for the minimum concentration level of 4 ppm of CH<sub>4</sub> is  $\pm 1.6$  ppm. The data reported in **Figure 3.12(b)** demonstrate a good linearity for the CH<sub>4</sub> sensor over a wide range of concentrations from 4 ppm to 1000 ppm. A linearity coefficient of 0.46 mV/ppm was derived from the linear fit and a negligible intercept with 1- $\sigma$  noise fluctuations of 0.073 mV.

In **Figure 3.13(a)** and **(b)** are shown two representative acquisitions of CH<sub>4</sub> signal for 1000 ppm and 4 ppm, respectively.

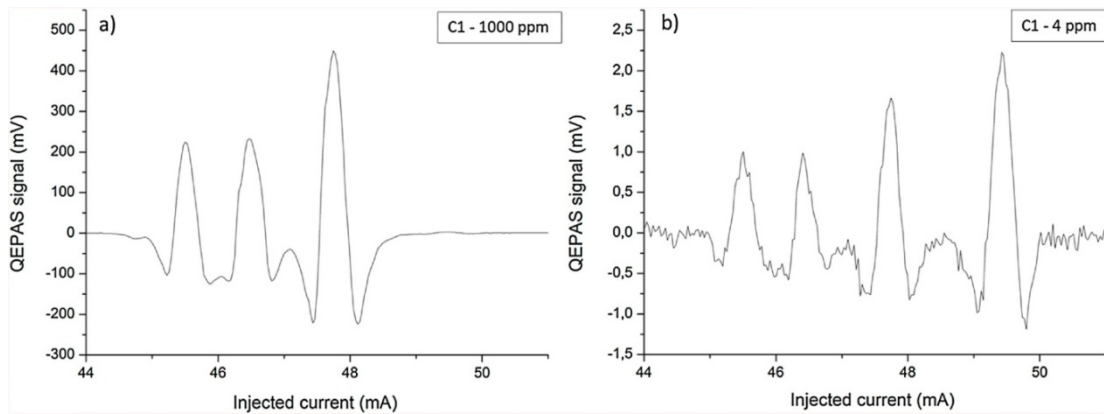


**Figure 3.13 (a)** 2f-signal corresponding to a humidified mixture of 1000 ppm-C1:N<sub>2</sub>; **(b)** 2f-signal corresponding to a humidified mixture of 4 ppm-C1:N<sub>2</sub> [134].

In **Figure 3.13(b)** it is clearly visible that a water absorption line falling at  $2988.61 \text{ cm}^{-1}$  [78], corresponding to at a laser injected current  $I = 49.5 \text{ mA}$ , with a line strength of  $1.1 \cdot 10^{-22} \text{ cm/mol}$ , gives rise to a 2f-signal with a peak value of  $\sim 2.25 \text{ mV}$ . This signal is barely visible in **Figure 3.13(a)** due to the much higher CH<sub>4</sub> concentration. A very good correspondence between the absorption features listed in the Hitran database [78] and the 2f-QEPAS signal structures due to methane absorption was found. The background signal not involving gas absorption lines has comparable 1- $\sigma$  noise fluctuations at different CH<sub>4</sub> concentrations. Allan deviation analysis [110] shows that for a 1 s integration time the detection limit for methane is  $\sim 90 \text{ ppb}$ . This is a value well below the sensitivity needed for a sensor aimed at hydrocarbon detection at a well site, where C1 concentrations are expected to be generally well above the ppm scale.

### 3.2.1.4 Sensor calibration for ethane detection

Interesting results were observed when the sensor was calibrated for ethane detection. Line C2 was targeted for determining the sensitivity of the sensor with respect to  $C_2H_6$ . The calibration procedure for  $C_2H_6$  is similar to the one illustrated in the previous section and the QEPAS response at different working pressures was investigated at a  $C_2H_6$  concentration of 100 ppm. The optimum gas mixture pressure, located at 300 Torr, provides a QEPAS signal only  $\sim 1.3$  times higher with respect to the value recorded at the atmospheric pressure (**Figure 3.14(a)**), differently from methane where at 1atm the QEPAS signal decreased by  $\sim 70\%$  with respect to the maximum signal recorded at 200 Torr. This means that the  $C_2H_6$  sensor works efficiently also at atmospheric pressure which is advantageous for in-situ applications.

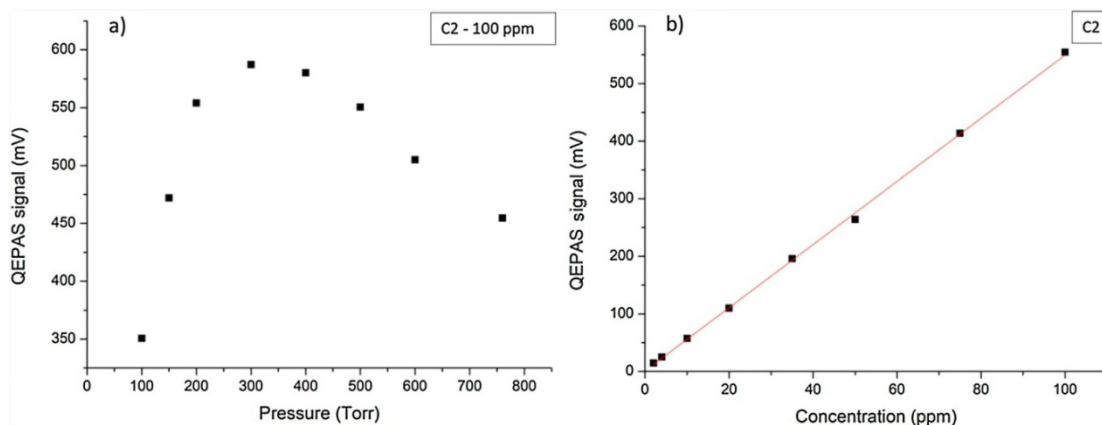


**Figure 3.14 (a)** 2f-signal peak values related to C2 at optimum modulation depths for different pressures, from 100 Torr to atmospheric pressure; **(b)** linearity of the 2f-signal peak values obtained at 200 Torr for a range of C2 concentrations from 2 ppm to 100 ppm in pure  $N_2$  [134].

It was observed that 200 Torr is the optimum working pressure for methane and the pressure controller has proven to have the smallest fluctuations at this pressure. Moreover, since the QEPAS signal at 200 Torr from  $v_2^{C_2}$  is  $\sim 4\%$  smaller with respect to the highest signal recorded at 300 Torr (see **Figure 3.14(a)**), a pressure of 200 Torr was chosen for performing the measurements for both  $CH_4$  and  $C_2H_6$ . For  $C_2H_6$  the optimum modulation depth results  $V_{p-p} = 130$  mV and detection phase  $\phi_2 = 166.15^\circ$ . The  $C_2H_6$ -calibration curve is shown in **Figure 3.14(b)** and the linearity of the QEPAS response was demonstrated from 100 ppm down to 2 ppm, with a linearity coefficient of 5.54 mV/ppm

and a negligible intercept. Different from methane, ethane shows a broadband background absorption signal due to the presence of several absorption features with a small linestrength in the ICL operation spectral range. This can easily be noticed by comparing the signal at 1000 ppm for methane (see **Figure 3.13(a)**) with the signal at 100 ppm for ethane (see **Figure 3.15(a)**).

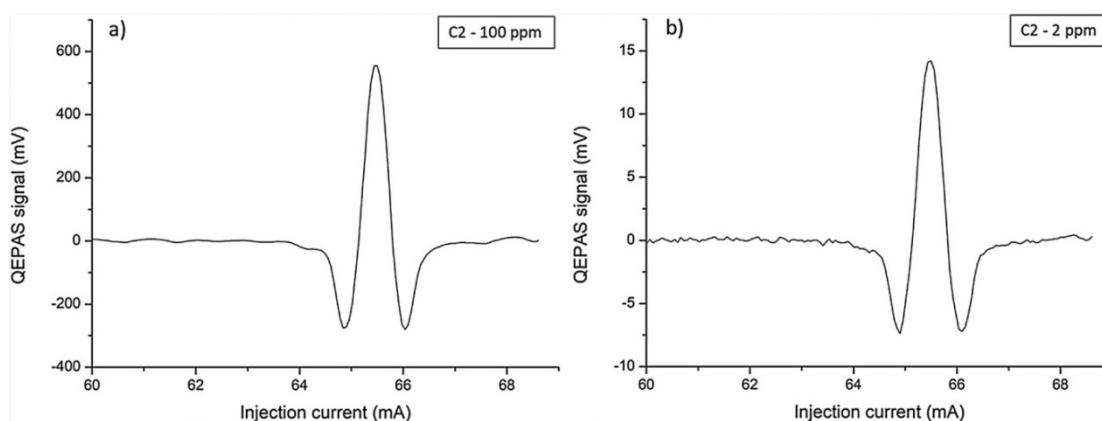


**Figure 3.15 (a)** 2f-signal corresponding to a humidified mixture of 100 ppm-C<sub>2</sub>:N<sub>2</sub>; **(b)** 2f-signal corresponding to a humidified mixture of 2 ppm-C<sub>2</sub>:N<sub>2</sub> [134].

By comparing **Figure 3.15(a)** and **(b)**, it can be noticed that the broadband background absorption levels off as the ethane concentration decreases. At 200 Torr and 2 ppm ethane concentration, the 1- $\sigma$  signal value calculated far from the C<sub>2</sub> 2f-peak is 0.14 mV, only about two times the noise level measured for a 1000 ppm CH<sub>4</sub>:N<sub>2</sub> mixture. Allan deviation analysis [110] shows that for a 1 s integration time the detection limit for ethane is  $\sim 7$  ppb. This represents a record for the QEPAS technique and opens the way to the implementation of QEPAS sensors for exploration and identification of ethane reservoirs, an application of strong interest for petrochemical and plastic industries.

### 3.2.1.5 Sensor performance and analysis of C<sub>1</sub>/C<sub>2</sub> mixture

Considering the previous results, an unbalanced wet mixture containing 990 ppm CH<sub>4</sub>, 10 ppm C<sub>2</sub>H<sub>6</sub>:N<sub>2</sub> was used to perform the first test of a fast C<sub>1</sub>/C<sub>2</sub> detection scan. In the upper panel of **Figure 3.16**, the QEPAS signal acquired for an ICL current span from 20 mA to 70 mA at T = 15 °C is displayed.

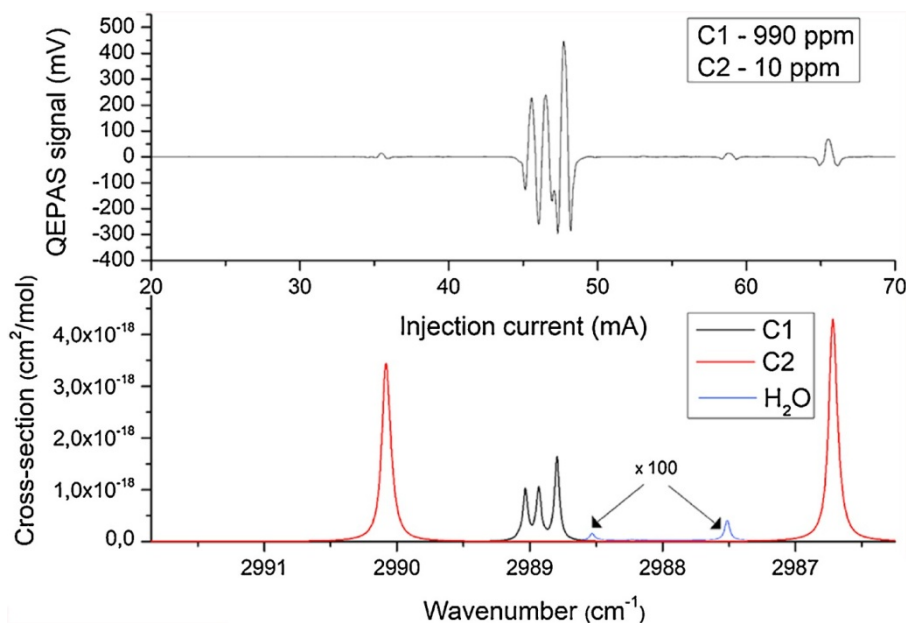


**Figure 3.16** Top panel: QEPAS 2f-signal for a humidified mixture of 990 ppm-C1 and 10 ppm-C2:N<sub>2</sub> with an adjusted detection phase of  $\nu_3^{C1}(\phi_1)$  and  $\nu_2^{C2}(\phi_2)$ . Bottom panel: absorption cross-section for C1 and C2 obtained using the Hitran database [78]. Two weak H<sub>2</sub>O absorption features are also shown (blue curve) by multiplying the related cross-sections by a factor of 100 [134].

The working pressure was fixed at 200 Torr and the modulation amplitude at 130 mVp-p. The second derivative profile of ethane absorption features  $\nu_1^{C2}$ ,  $\nu_2^{C2}$  and the second derivative shape of the three-lines structure from methane are clearly visible. The spectral separation is coherent with the absorption cross-section graph for both CH<sub>4</sub> and C<sub>2</sub>H<sub>6</sub> simulated using the Hitran database and shown in the lower panel of **Figure 3.16**. In order to maximize the QEPAS response of the CH<sub>4</sub> and C<sub>2</sub>H<sub>6</sub> lines, the optimal detection phases identified for each gas were used during the current scan in the proximity of the related absorption features. A  $\nu_3^{C1}$  2f-signal peak of 455 mV and a C2 2f-signal peak of 63 mV were obtained as expected from the sensor calibration. Furthermore, the full spectral scan over the ICL dynamic range showed the presence of barely visible water line at I = 59 mA, different from the one previously observed at I = 49.5 mA.

The detection scheme is versatile, because in one single current scan CH<sub>4</sub> and C<sub>2</sub>H<sub>6</sub> can be independently detected at sub-ppm scale and can also deal with unbalanced mixtures in which the methane concentration is two orders of magnitude or even higher in

concentration with respect to ethane. More interesting is a comparison between two or more broadband absorber molecules that can be found in downhole mixture compositions.

### 3.2.1.6 Propane detection and analysis of broadband absorbers spectra

Since propane absorption lines in the 2–4  $\mu\text{m}$  range are not listed in the Hitran database, the PNNL database [135] was taken as reference to analyze the QEPAS measurements obtained for a mixture of 1000 ppm of  $\text{C}_3\text{H}_8:\text{N}_2$ . In **Figure 3.17** the absorption cross-section of  $\text{C}_3\text{H}_8$  in the spectral range 2850–3100 nm is shown.

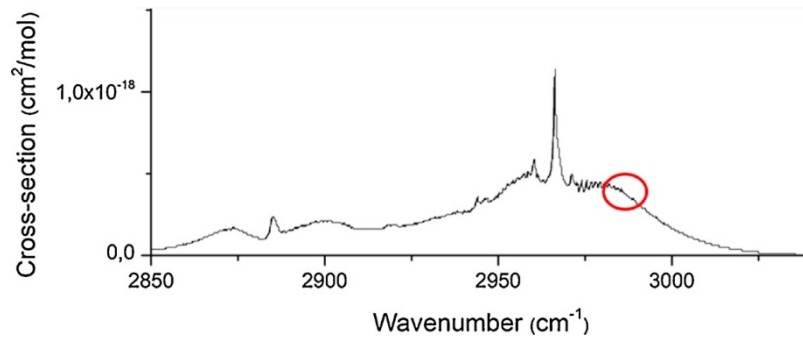


**Figure 3.17** Cross-section of propane in the range 2850 nm–3100 nm, using PNNL database [135]. The red circle highlights the spectral range corresponding to the ICL tuning range [134].

The  $\text{C}_3\text{H}_8$  absorption cross-sections in the ICL tuning range (see the red circle in **Figure 3.17**) are almost five times lower in linestrength than  $\nu_2^{\text{C}2}$  ( $1.26 \cdot 10^{-18}$  cm/mol) at atmospheric pressure. Nevertheless, the lack of sharp Lorentzian-like features like  $\nu_2^{\text{C}2}$  or  $\nu_3^{\text{C}1}$  leads to a photoacoustic excitation intensity in a wavelength modulation configuration that is low. In order to increase the  $\text{C}_3\text{H}_8$  WM QEPAS signal, all the measurements were carried out at atmospheric pressure, where multiple absorption lines merge to build a spectrum composed of well-separated bands. The lock-in phase maximizing the  $\text{C}_3\text{H}_8$  QEPAS signal was  $\phi_3 = 107.25^\circ$ . In **Figure 3.18**, the QEPAS spectra related to the  $\text{C}_3\text{H}_8$  absorption bands spectra measured at atmospheric pressure and for different  $\text{C}_3\text{H}_8$  dry concentrations, ranging from 1000 ppm to 200 ppm in pure  $\text{N}_2$ , are plotted.

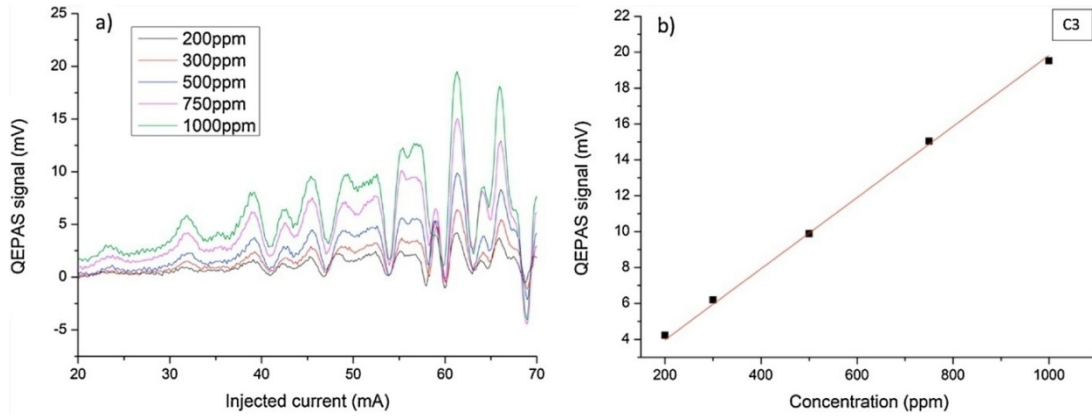


**Figure 3.18** (a) 2f-QEPAS spectra measured for different C3 concentrations from 1000 ppm to 200 ppm in pure N<sub>2</sub> at atmospheric pressure and using a modulation depth  $V_{p-p} = 300$  mV, in the laser current range 20–70 mA; (b) linear fit (red line) of the 2f-signal peak values (black square dots) related to the absorption feature falling at  $I = 61.3$  m for a range of C3 concentrations from 1000 ppm to 200 ppm [134].

These spectra were obtained by scanning the laser injected current from 20 mA to 70 mA at  $T = 15$  °C and employing a modulation depth of 300 mVpp. **Figure 3.18(b)** demonstrates the linearity of photoacoustic response as a function of the C<sub>3</sub>H<sub>8</sub> concentration, extracted for the peak of the QEPAS spectrum C3 located at  $I = 61.3$  mA. The linearity coefficient is 0.0191 mV/ppm. The detection limit, extracted via an Allan deviation analysis of the QEPAS C3 peak signals, results in  $< 3$  ppm for a 1 s integration time. It was verified that each peak of the C<sub>3</sub>H<sub>8</sub> spectrum exhibits a linear QEPAS response with C3 concentrations, as observed in **Figure 3.18(a)**. The QEPAS signal measured for a pure N<sub>2</sub> mixture is flat within the ICL current dynamic range and comparable with the noise level. A flat background noise and QEPAS signal scaling linearly with the gas target concentration are mandatory requirements to compare C<sub>2</sub>H<sub>6</sub> and C<sub>3</sub>H<sub>8</sub> backgrounds. The QEPAS signal  $Y(\lambda)$  acquired for a mixture of  $n$  gases (C<sub>2</sub>H<sub>6</sub> and C<sub>3</sub>H<sub>8</sub>) for a given wavelength spectrum can be assumed to be the sum of the QEPAS signals related to the individual gases:

$$Y(\lambda) = \sum_{i=0}^n A_i X(\lambda)_i = A_2 X(\lambda)_{C_2} + A_3 X(\lambda)_{C_3} \quad \text{Eq. 3.3}$$

where  $Y(\lambda)$  is the acquired QEPAS signal (in mV),  $A_i$  is the concentration of the  $i$ -th gas (in ppm) and  $X(\lambda)_i$  the related QEPAS spectrum, in mV/ppm unit [136]. If the operating

temperature is set to 15 °C, the laser emission wavelength is related to the drive current. In order to discriminate both contributions in C2-C3 mixtures, an injected current range from 35 to 60 mA was selected, in which range no strong C<sub>2</sub>H<sub>6</sub> features are present and both C<sub>2</sub>H<sub>6</sub> and C<sub>3</sub>H<sub>8</sub> absorption broadband backgrounds can be easily compared (see **Figure 3.19(a)**). The detection phase used for these measurements is the one maximizing the C3 QEPAS signal, i.e.,  $\phi_3 = 107.25^\circ$ : in this way we also slightly reduced the intensity of the C2 background signal. However, it was verified that the C2 background signal detected at  $\phi_3$  is still linear as function of C2 concentrations. The reference QEPAS spectra used for the fitting procedure using **Eq. 3.3** are the C<sub>2</sub>H<sub>6</sub> and C<sub>3</sub>H<sub>8</sub> signals recorded at 1000 ppm in pure N<sub>2</sub> concentration, therefore **Eq. 3.3** becomes:

$$Y = aX_{1000ppm}^{C2} + bX_{1000ppm}^{C3} \quad \text{Eq. 3.4}$$

where a and b are the fraction of 1000 ppm of the reference spectra. The first validation test of this multi-gas detection approach was made using dry mixtures composed of: i) C2-500 ppm, C3-500 ppm in pure N<sub>2</sub> (mix#1); ii) C2-800 ppm, C3-200 ppm in pure N<sub>2</sub> (mix#2); iii) C2-200 ppm, C3-800 ppm in pure N<sub>2</sub> (mix#3). In **Figure 3.19(b)–(d)** the QEPAS spectra and the related fits for all the three gas mixtures are shown. The calculated concentration values are listed in **Table 3.3**. In brackets the 95% confidence interval uncertainties are reported.

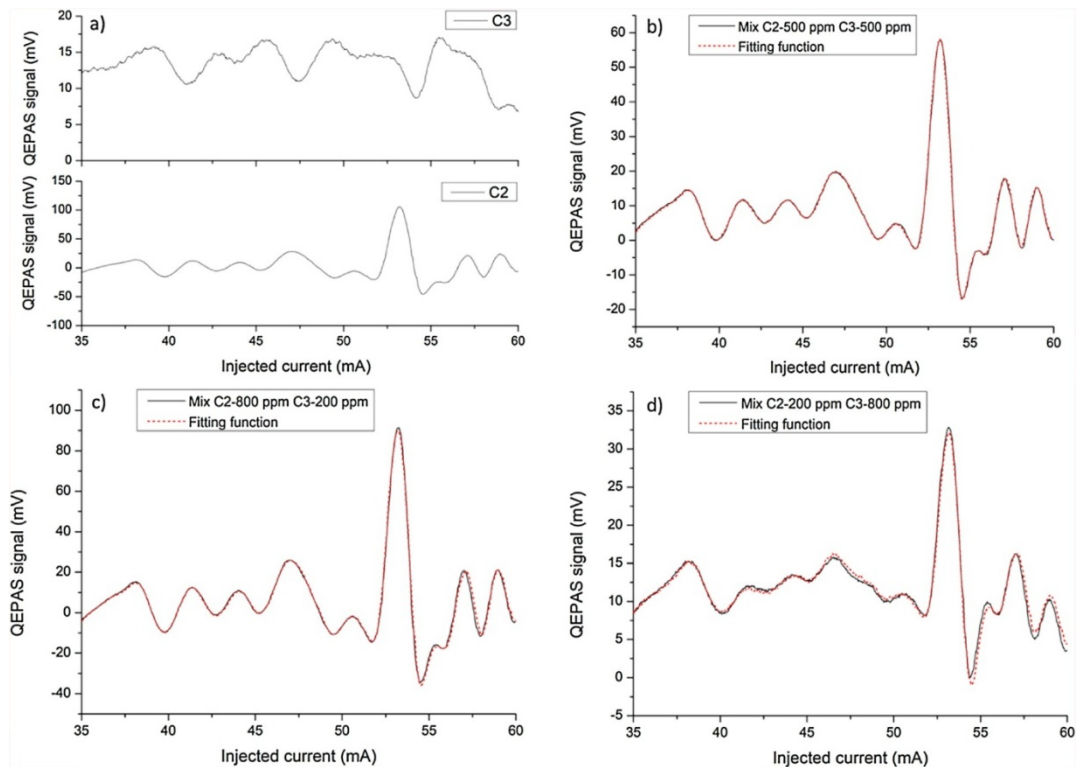


**Figure 3.19** (a) Top panel: 2f-signal for 1000 ppm-C<sub>3</sub>:N<sub>2</sub> acquired in the laser injected current range 35–60 mA. Bottom panel: 2f-signal for 1000 ppm-C<sub>2</sub>:N<sub>2</sub>; (b) 2f-signal for a dry mixture containing 500 ppm of C<sub>2</sub> and 500 ppm of C<sub>3</sub>, in pure N<sub>2</sub>; (c) 2f-signal for a dry mixture containing 800 ppm of C<sub>2</sub> and 200 ppm of C<sub>3</sub> in pure N<sub>2</sub>; (d) 2f-signal for a dry mixture containing 200 ppm of C<sub>2</sub> and 800 ppm of C<sub>3</sub> in pure N<sub>2</sub> [134].

**Table 3.3** Actual and calculated C<sub>2</sub>H<sub>6</sub> and C<sub>3</sub>H<sub>8</sub> concentration for the investigated gas mixtures [134].

Mixture	Actual C <sub>2</sub> H <sub>6</sub> concentration (ppm)	Actual C <sub>3</sub> H <sub>8</sub> concentration (ppm)	Calculated C <sub>2</sub> H <sub>6</sub> concentration (ppm)	Calculated C <sub>3</sub> H <sub>8</sub> concentration (ppm)
1	500	500	487.02 (±1.4)	520.00 (±2.5)
2	800	200	828.98 (±3.8)	208.01 (±6.8)
3	200	800	199.98 (±1.7)	831.47 (±2.9)

The differences between the fitting parameters, i.e. the calculated C<sub>2</sub>H<sub>6</sub> and C<sub>3</sub>H<sub>8</sub> concentrations, and the nominal concentrations expected remains below 5% and are mainly due to uncertainties in the certified gases flows used for producing the mixtures (especially for flows as low as 8 sccm, as used in our experiments). The obtained results successfully demonstrate the feasibility to perform photoacoustic C<sub>2</sub>/C<sub>3</sub> gas detection by fitting the QEPAS spectra measured for the gas mixtures. Among different valid approaches such as multivariate analysis or machine learning, a fitting procedure based on a linear combination of reference spectra still represents the most straightforward strategy. Since in the investigated spectral range, C<sub>1</sub> is characterized by well isolated absorption peaks and no background, we successfully determined CH<sub>4</sub>, C<sub>2</sub>H<sub>6</sub> and C<sub>3</sub>H<sub>8</sub> concentrations in humidified and dry gas mixtures respectively, using pure nitrogen as gas carrier.

### 3.2.2 Broadband detection of CH<sub>4</sub> and N<sub>2</sub>O using a DFB QCL array

Apart from specific cases in which two or more absorption lines can be covered within their dynamic current range [134], DFB lasers do not represent the optimal choice for multi-gas detection. Quantum cascade lasers (QCLs) in external-cavity configuration (EC-QCLs) are commonly employed to cover wide mid-infrared spectral ranges and have been exploited for the detection of several greenhouse and harmful gases [137]. For broadband gas detection (over a ~40 cm<sup>-1</sup> wide spectral range), EC-QCLs have been employed [33].

Compared to DFB laser sources, EC-QCLs are bulky and suffer from grating mechanical instability which generates alignment and laser instability-related noise signals [138]. An alternative and more compact broadband emission laser source can be realized by using an array of DFB QCLs monolithically grown on a single semiconductor chip, combining the compactness of a single chip, the wide tunability range of an array of devices and the pulse-to-pulse stability, spectral purity, and tuning reproducibility of DFB-QCLs [139]. This innovative laser source is employed in the QEPAS sensor, aimed to detect methane and nitrous oxide, described in the following paragraph.

### 3.2.2.1 Laser source spectral characterization and beam profile analysis

The employed laser source consists in a monolithic array of 32 individually addressable distributed-feedback quantum cascade lasers grown on a single semiconductor chip and operated in pulsed mode, as described in [138] - [140]. Thermoelectric cooler and laser pulser boards are embedded in a single unit controlled by a LabVIEW-based software. As a first step, the spectral emission of the employed laser source was analyzed by using a Fourier-transform interferometer (FTIR-Nicolet 6700) with a spectral resolution of  $0.125 \text{ cm}^{-1}$  in a rapid-scan mode. In **Figure 3.20(a)** the normalized emission spectra of the devices composing the monolithic QCL array are reported for a TEC temperature of  $25 \text{ }^\circ\text{C}$ , a drive voltage properly set for each device in order to ensure the highest optical power output ( $18.0 - 20.0 \text{ V}$ ), a repetition frequency of  $33 \text{ kHz}$  and a pulse-width of  $300 \text{ ns}$  resulting in a duty cycle of  $1 \%$ .

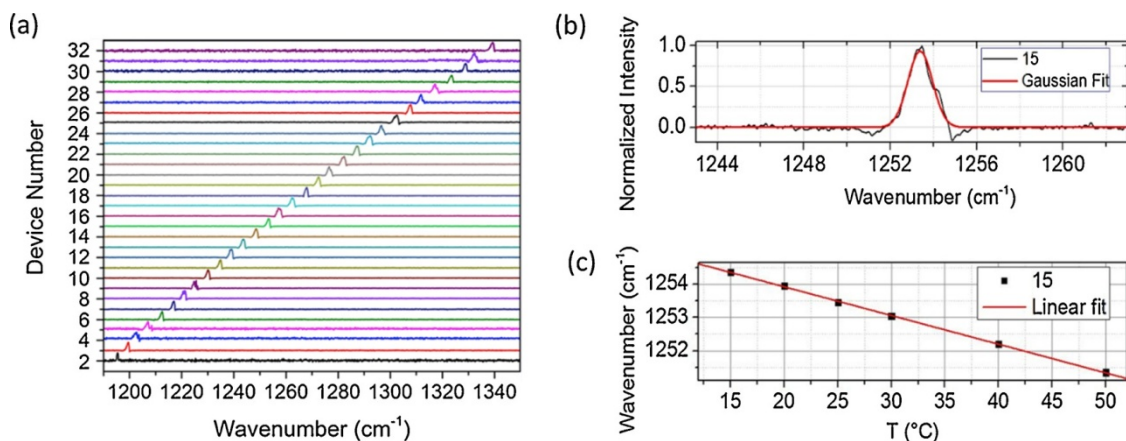


**Figure 3.20 (a)** QCL array FTIR normalized intensity spectra for a  $25 \text{ }^\circ\text{C}$  operating temperature, a  $33 \text{ kHz}$  repetition frequency, a  $300 \text{ ns}$  pulse-width and a driving voltage maximizing the devices optical power; **(b)** Gaussian fit (red solid line) of the normalized

emission spectrum (black solid line) and (c) linear fit (red solid line) of temperature tuning of the peak emission wavelength (black dots) for the DFB-QCL number 15 [141].

The overall emission spectrum of the QCL array covers a range  $150\text{ cm}^{-1}$  wide from  $1190\text{ cm}^{-1}$  to  $1340\text{ cm}^{-1}$ . Each device in the array shows a single-mode output, whose peak emission wavenumber and linewidth were determined by fitting the spectrum with a Gaussian curve. As a representative, the FTIR measured spectrum of the QCL number 15 is reported at a driving voltage of 18 V in **Figure 3.20(b)** together with its best Gaussian fit. The emission peak occurs at  $1253.4\text{ cm}^{-1}$  with a linewidth of  $1.3\text{ cm}^{-1}$ . By repeating the measurements and the fit procedure for all the QCLs, a spectral spacing between adjacent devices lower than  $5\text{ cm}^{-1}$  was measured, while the linewidths ranged between  $1.1\text{ cm}^{-1}$  and  $1.5\text{ cm}^{-1}$ . Narrower spectral lines (down to  $< 0.2\text{ cm}^{-1}$ ) can be obtained by reducing the pulse durations. However, this also leads to a reduction of the average power if the repetition rate is kept constant to match the resonance of the quartz tuning fork. Since the QEPAS signal is proportional to laser average power, this is not advantageous. Mode hop-free tuning of the lasers' optical frequency with the operating temperature was also verified in the  $15\text{ }^{\circ}\text{C}$ – $50\text{ }^{\circ}\text{C}$  range. The temperature-tuning coefficient was calculated by linearly fitting the peak wavenumber as a function of the operating temperature. The optical frequency temperature tuning of the device number 15 is reported in **Figure 3.20(c)** together with the best linear fit. A tuning coefficient of  $-0.09\text{ cm}^{-1}/^{\circ}\text{C}$  was measured for all the devices in the array, resulting in an overall tuning of each QCL optical frequency of  $3.15\text{ cm}^{-1}$  within the investigated temperature range. Next, the spatial quality of the QCL beams was investigated. The beams exiting the QCL array package were collected by a ZnSe focusing lens having a 25.4 mm diameter, a 50 mm focal length and an anti-reflection (AR) coating in the  $7\text{--}12\text{ }\mu\text{m}$  spectral range. The beam profile of each device was acquired in the lens focal plane by a pyroelectric camera (Ophir Spiricon Pyrocam III-C) composed of an array of  $124 \times 124$   $100\text{ }\mu\text{m}$ -side square pixels. Devices from number 1 to number 19 shown on the camera a secondary spot,  $\sim 1\text{ mm}$  distant from the fundamental one, caused by stray light in the laser package. An updated design is currently being engineered to mitigate this issue. As representative, the three-dimensional far field image of the device number 15 is shown in **Figure 3.21(a)**.

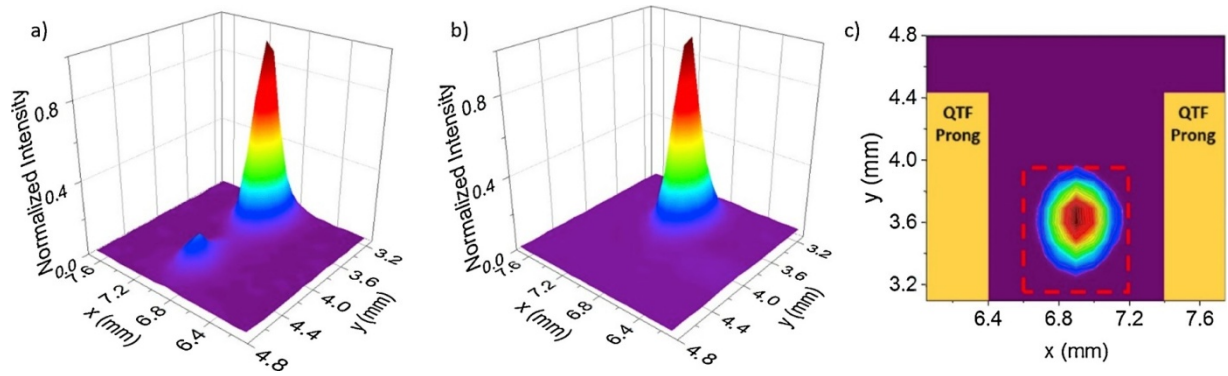


**Figure 3.21** (a) QCL number 15 focused 3D beam profile. (b) Same QCL beam profile filtered by a 2-mm pinhole. (c) QCL number 15 2D spatially filtered beam profile. The two yellow areas represent the positions of the QTF prongs, spaced by 1-mm. The array overall illuminated area is highlighted with a red dashed line. All dimensions are represented in scale [141].

The secondary spot is 6 times less intense and appears  $900\ \mu\text{m}$  far from the highest peak. In an on-beam QEPAS configuration, the laser source beam must be focused between the QTF prongs. When light hits the QTF prongs a background optical noise is generated. Therefore, multimode and/or poor spatial quality beams drastically affect the ultimate detection sensitivity of a QEPAS sensor. With the QCL array employed in this work, a spatial filter was used to suppress all secondary spots. Although hollow-core waveguides (HCWs) have been demonstrated to act as efficient low-loss single mode delivery spatial filters in the mid-infrared spectral range, the observed shifts of the focused beams when switching from one device to another do not permit the use of an HCW, since realignments become necessary when switching the QCLs [142], [143]. Instead, a 2 mm-diameter pinhole was positioned between the laser source and the focusing lens, allowing all the secondary spots to be cut off while preserving the fundamental mode Gaussian shape and intensity, as shown in **Figure 3.21(b)** for device 15. Once the secondary spots are removed, beam radii of  $260\text{--}300\ \mu\text{m}$  in the x-direction and of  $290\text{--}340\ \mu\text{m}$  in the y-direction were measured in the lens focal plane by fitting all beam profiles with a Gaussian function in both directions. By considering also shifts in position of all primary spots, an overall illuminated area of  $600 \times 800\ \mu\text{m}^2$  was identified, represented by a dashed line-rectangle in **Figure 3.21(c)**. Hence, a 1 mm-prong spacing custom QTF (labeled as QTF#4 in [70]) was selected to reduce as much as possible the possibility that beam tails hit the QTF.

### 3.2.2.2 Experimental setup

The architecture of the broadband detection QEPAS sensor is depicted in **Figure 3.22**.

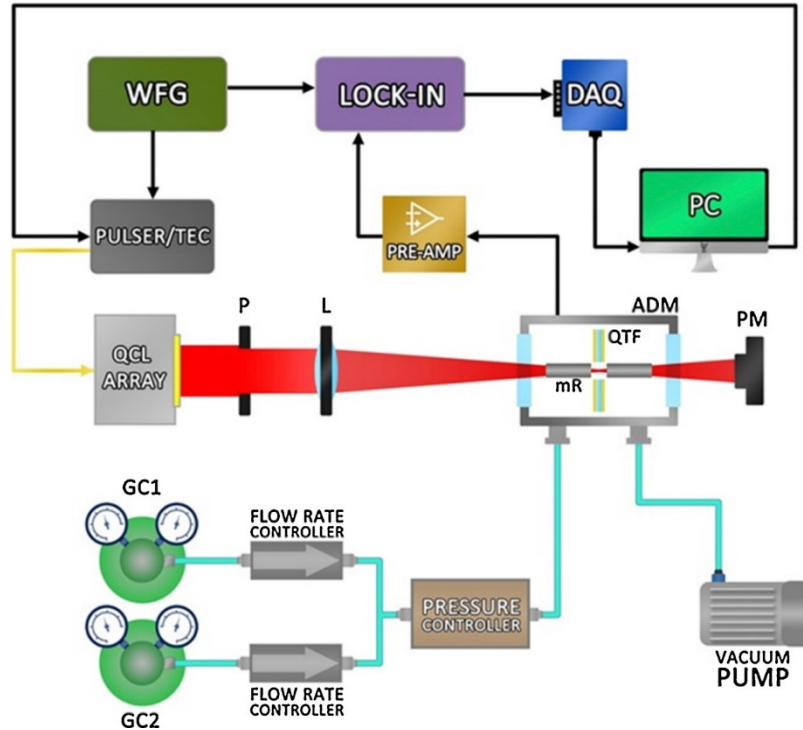


**Figure 3.22** Schematic of the experimental apparatus. WFG – wave- form generator; DAQ – data acquisition board; TEC – temperature controller; PRE-AMP – Preamplifier; PC – personal computer; QCL ARRAY – quantum cascade laser array; P – pinhole; L – focusing lens; ADM - acoustic detection module; QTF – quartz tuning fork; mR – micro-resonator tubes; PM – power-meter; GC1, GC2 – gas cylinders [141].

As discussed in the previous section, the laser beam is spatially filtered by a pinhole and then focused through the acoustic detection module (ADM) by means of the ZnSe focusing lens. The ADM is composed of a gas cell, equipped with two ZnSe windows for the laser input and output, a pair of connectors for gas inlet and outlet and a QTF acoustically coupled with two 1.52 mm-internal diameter and 5.3 mm-long micro-resonator tubes in an on-beam configuration. A power meter is set behind the ADM for optical power measurement and monitoring. At atmospheric pressure, the spectrophone composed of a QTF and microresonator tubes exhibits a first overtone flexural mode resonance curve peaked at  $f = 25\,390.63$  Hz with a full-width half-maximum value of 2.41 Hz, resulting in a quality factor of 10 530. The laser pulser is externally triggered by a waveform generator to set the pulse repetition rate at  $f$ . For all QEPAS measurements, a 300 ns pulse-width was

used, resulting in a 0.75 % duty cycle, while the QCL driving voltage was set to the value ensuring the highest optical power for each device. The QTF current signal is converted into a voltage signal by a 10 M $\Omega$  feedback resistor pre-amplifier and then demodulated by a lock-in amplifier at the frequency  $f$  with a 100 ms integration time. The demodulated signal is digitized by a DAQ card and acquired by a LabVIEW-based software with a sampling time of 300 ms.

The target gas flows from the gas cylinder GC1 through the ADM by using a vacuum pump. The gas flow rate and pressure in the ADM are set by controllers at 30 sccm and 760 Torr, respectively. A hygrometer (not shown in figure) was placed in-line to monitor the absence of humidity in the line and check any presence of undesired water vapor. Gas mixtures with a second gas species contained in the gas cylinder GC2 are obtained by appropriate setting the rate parameter of the flow controllers mounted on the two branches of the Y-shaped gas line.

### 3.2.2.3 Methane broadband detection

Within the emission wavelength range of the employed DFB-QCL array, methane exhibits an uneven absorption spectrum composed of several lines differing both in line-strength and in wavenumber spacing. QEPAS measurements were performed by switching the QCLs in sequence while keeping the devices operating temperature fixed at 25 °C (fixed temperature acquisition mode-FTAM). All measurements were performed by using the lock-in phase  $\varphi = 57.3^\circ$ , maximizing the demodulated signal amplitude of the methane peaks. The QCL output power varies for each device. For this reason, a preliminary measurement of the array optical power was performed as a function of light wavenumber, by recording the output power while switching the devices in sequence. The obtained curve was then normalized to 1 with respect to the highest value. This curve will be referred hereafter as FTAM optical power calibration curve. QEPAS signals obtained for a certified concentration of 1000 ppm of CH<sub>4</sub>:N<sub>2</sub> in GC1 were normalized to the FTAM optical power calibration curve. The resulting QEPAS spectrum is shown in **Figure 3.23** (black squares).

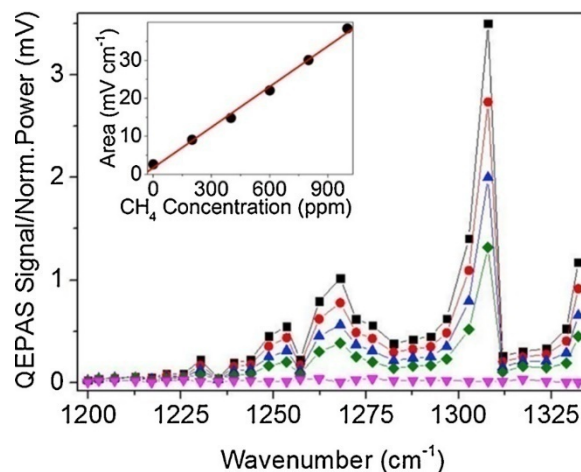


**Figure 3.23** 1000 ppm (black squares), 800 ppm (red dots), 600 ppm (blue triangles) and 400 ppm (green diamonds) CH<sub>4</sub>:N<sub>2</sub> and pure N<sub>2</sub> (pink triangles) FTAM QEPAS signal normalized to the optical power calibration curve. Solid lines are visual guides. Inset: Area underneath the QEPAS spectrum in mV·cm<sup>-1</sup> units measured for each CH<sub>4</sub>:N<sub>2</sub> concentration (black dots) and corresponding best linear fit (red line) [141].

The FTAM QEPAS spectrum reproduces the highest intensity peak at 1306.10 cm<sup>-1</sup> as well as several side features. For each device, a 1 $\sigma$  noise level of  $\sim 2$   $\mu$ V was estimated when pure N<sub>2</sub> is flowing in the ADM. This suggests that the background optical noise related to light- induced photothermal effects on QTF prongs does not change when switching between different devices. Therefore, the selected QEPAS sensor architecture, i.e. the use of the pinhole together with a 1mm - prong spacing QTF, allows the QEPAS sensor alignment conditions to be preserved while switching among the devices.

The QEPAS sensor linear responsivity with the methane concentration was verified in the 200–1000 ppm range, by diluting the 1000 ppm CH<sub>4</sub>:N<sub>2</sub> certified concentration with pure nitrogen. The measurements obtained in fast acquisition mode for 400, 600, 800 and 1000 ppm CH<sub>4</sub> concentrations are shown in **Figure 3.23**, together with the spectra recorded when pure N<sub>2</sub> was flowing in the ADM. The area underneath the spectra was calculated using the rectangles approximation and plotted as a function of the CH<sub>4</sub> concentration in the inset of **Figure 3.23**. A slope of 0.036 mV·cm<sup>-1</sup>/ppm was extracted by linearly fitting the data points in the graph. The fit exhibits an intercept of 1.74 mV·cm<sup>-1</sup>, comparable with the area of 2.6 mV·cm<sup>-1</sup> measured underneath the pure nitrogen QEPAS spectrum. For the lowest concentration, i.e. 200 ppm CH<sub>4</sub>:N<sub>2</sub>, an area of 7.87 mV·cm<sup>-1</sup> was calculated. The

standard deviation  $\sigma_{\text{Area}}$  of the area underneath the QEPAS spectrum can be obtained by using the propagation of uncertainty law:

$$\sigma_A = \sqrt{\sum_i \left[ \left( \frac{\partial A}{\partial x_i} \right)^2 \sigma_{x_i}^2 + \left( \frac{\partial A}{\partial S_i} \right)^2 \sigma_{S_i}^2 \right]} \quad \text{Eq. 3.5}$$

where  $x_i$  and  $S_i$  are the  $i$ -th rectangle base and height. The parameter  $x_i$  is the FTIR error, while  $S_i$  is the  $1\sigma$  noise of the QEPAS signal. The QEPAS signal for each QCL exhibits a  $1\sigma$  noise level of  $\sim 2 \mu\text{V}$ . By neglecting the FTIR error contribution,  $\sigma_{\text{Area}}$  is proportional to  $1\sigma$  and the extracted value is  $0.05 \text{ mV}\cdot\text{cm}^{-1}$ . The sensor minimum detection limit (MDL) can be defined as the methane concentration corresponding to an area under the spectrum equal to  $\sigma_{\text{Area}}$ . Based on these considerations, an MDL of 1.27 ppm was estimated.  $1\sigma$  noise of the QEPAS signal can be further reduced by integrating the signal over longer times. An Allan-Werle deviation analysis was performed to calculate  $1\sigma$  noise as a function of the signal integration time [110]. For a 10 s lock-in integration time, the methane MDL was estimated to improve down to 200 ppb,  $\sim 9$  times lower than the methane concentration in atmosphere [144].

The methane spectrum was also measured by employing a higher-resolution acquisition mode which consists in tuning the operating temperature of each QCL within the 15 – 50 °C range, in steps of 3 °C, corresponding to a spectral resolution of  $0.27 \text{ cm}^{-1}$ , and driving the devices one by one, in sequence (temperature tuning acquisition mode-TTAM). A preliminary measurement of the TTAM optical power calibration curve was performed. QEPAS signals obtained for a certified concentration of 1000 ppm of  $\text{CH}_4:\text{N}_2$  in GC1 were normalized to the TTAM optical power calibration curve. The resulting QEPAS spectrum is shown in **Figure 3.24** (black dots) together with a simulation of the absorption spectrum of 1000 ppm of  $\text{CH}_4:\text{N}_2$  obtained by using the HITRAN database [78].

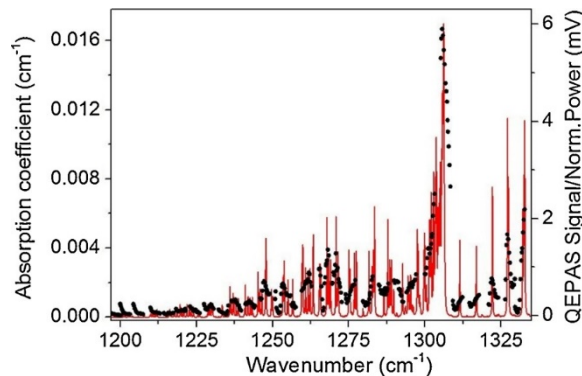


**Figure 3.24** Comparison between the 1000 ppm CH<sub>4</sub>:N<sub>2</sub> TTAM QEPAS signals normalized to the optical power calibration curve (black dots, right y-axis), and the absorption spectrum simulated by using the HITRAN database (red solid lines, left y-axis) [141].

QEPAS measurements well reconstruct the highest intensity peak centered at 1306.10 cm<sup>-1</sup>. Compared to **Figure 3.23**, five equally spaced absorption features on the right side of the highest peak are now distinguishable and well reconstructed. However, the large QCLs emission linewidth, combined with the ~5 cm<sup>-1</sup> spacing and the 1 – 4 cm<sup>-1</sup> width of the methane absorption peaks, results in a QEPAS spectrum less sharp than the simulated absorption coefficient spectrum, for all the five absorption features. On the left side, the absorption features are so spectrally dense that it is hard to distinguish among them. Narrower emission linewidth (attainable with shorter laser current pulse-widths) would allow a better reconstruction of the absorption features, but the reduction of the average optical power would negatively affect the ultimate detection sensitivity of the sensor. In this mode, the spectrum acquisition time is 14 times longer, but the resolution step decreases from 4–5 cm<sup>-1</sup>, depending on the optical frequency difference between adjacent devices, to 0.3 cm<sup>-1</sup>, thus allowing a more accurate peaks reconstruction.

#### 3.2.2.4 Methane/nitrous oxide mixtures broadband detection

The results and the sensitivities obtained so far demonstrate that the DFB-QCL array-based QEPAS sensor can be considered as a valid tool for broadband detection of one single gas species in nitrogen. A further investigation is needed to demonstrate the feasibility of broadband multi-gas detection, particularly in the case of overlapping absorption features belonging to different gas species. This is the case for nitrous oxide and methane. The absorption spectrum of N<sub>2</sub>O has been reported in [139], where FTAM and TTAM QEPAS measurements well mimic the simulated spectrum of the P- and R-branches. These two nearly-Gaussian envelope bands overlap with uneven absorption features of CH<sub>4</sub> [78], within the array emission spectral range. For this experiment, three different N<sub>2</sub>O/CH<sub>4</sub> mixtures in N<sub>2</sub> were used. A concentration of 1020 ppm of N<sub>2</sub>O:N<sub>2</sub> in GC2 was mixed with three concentrations of CH<sub>4</sub>:N<sub>2</sub> in GC1, containing 1900 ppm, 1000 ppm and 300 ppm of methane, in order to obtain three gas mixtures composed of a fixed concentration of 510 ppm of N<sub>2</sub>O and a concentration of 150 ppm, 500 ppm and 950 ppm of CH<sub>4</sub> in N<sub>2</sub>, respectively. Keeping the concentration of one gas species constant, it is possible to

investigate how the presence of the second gas species ( $\text{CH}_4$ ) can affect the overall spectrum profile.

FTAM QEPAS measurements were performed, using a lock-in phase  $\phi$  fixed at  $57.31^\circ$ . Reference spectra measured for 510 ppm of  $\text{N}_2\text{O}:\text{N}_2$ ,  $R(\nu)_{\text{N}_2\text{O}}$ , and 1000 ppm of  $\text{CH}_4:\text{N}_2$ ,  $R(\nu)_{\text{CH}_4}$ , are shown in **Figure 3.25(a)** and **(b)**, respectively, while the QEPAS spectra obtained for the three different mixtures are plotted in **Figure 3.25(c)**. All spectra are normalized to the optical power calibration curve.

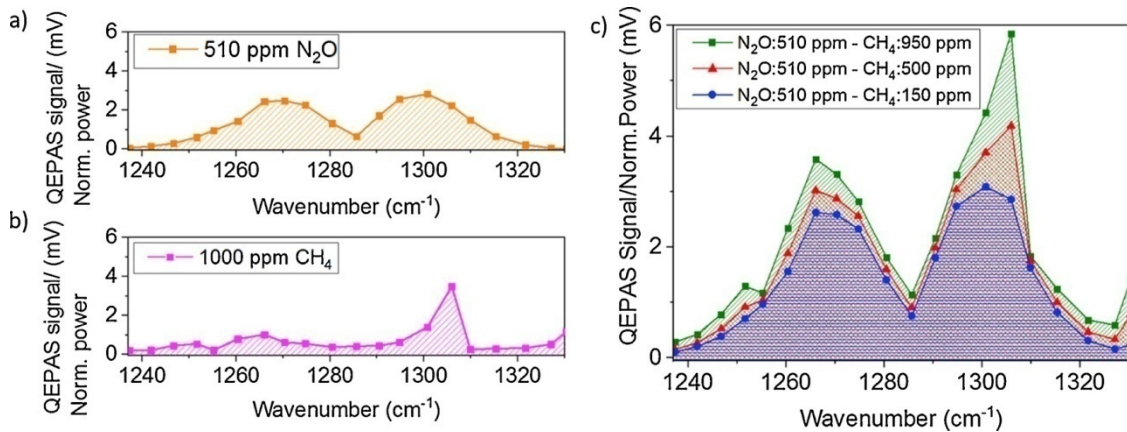


**Figure 3.25 (a)** 510 ppm  $\text{N}_2\text{O}:\text{N}_2$  and **(b)** 1000 ppm  $\text{CH}_4:\text{N}_2$  FTAM reference spectra; **(c)** FTAM QEPAS signal normalized to the optical power calibration curve for three dry mixtures containing 510 ppm of  $\text{N}_2\text{O}$  and 150 ppm of  $\text{CH}_4$  (blue dots), 500 ppm of  $\text{CH}_4$  (red triangles) and 950 ppm of  $\text{CH}_4$  (green squares), respectively [141].

The presence of methane in all three mixtures clearly affects the smooth envelope of the two  $\text{N}_2\text{O}$  nearly-Gaussian absorption bands, whose QEPAS reference spectrum  $R(\nu)_{\text{N}_2\text{O}}$  in **Figure 3.25(a)** is consistent with the measurements presented in [139]. By considering  $R(\nu)_{\text{CH}_4}$ , three spectral features centered at  $1266.04 \text{ cm}^{-1}$ ,  $1306.10 \text{ cm}^{-1}$  and  $1330.35 \text{ cm}^{-1}$  are clearly distinguishable. As the methane concentration increases, the presence of these bands become clearer in the mixture spectrum. In addition, in the mixture  $\text{N}_2\text{O}:\text{510 ppm}-\text{CH}_4:\text{950 ppm}$ , a fourth spectral feature addressable to the methane contribution arises at  $1251.60 \text{ cm}^{-1}$ . Besides this qualitative analysis, a quantitative estimation of the amount of the two gas species in the mixture can be obtained by supposing the  $i$ -th mixture spectrum,  $M_i(\nu)$ , as the linear combination of the two reference spectra  $R(\nu)_{\text{N}_2\text{O}}$  and  $R(\nu)_{\text{CH}_4}$ . MATLAB-based software was developed to retrieve the  $\text{N}_2\text{O}$  and  $\text{CH}_4$  concentrations in all

three mixtures. The results obtained for the three gas mixtures, together with related standard errors, are summarized in **Table 3.4**.

**Table 3.4** Nominal and calculated N<sub>2</sub>O and CH<sub>4</sub> concentration for the three investigated gas mixtures analyzed with FTAM QEPAS [141].

Mixture	Nominal N <sub>2</sub> O concentration (ppm)	Nominal CH <sub>4</sub> concentration (ppm)	Calculated N <sub>2</sub> O concentration (ppm)	Calculated CH <sub>4</sub> concentration (ppm)
1	510	150	503.1 (± 3.5)	159.8 (± 9.9)
2	510	500	510.9 (± 4.7)	504.8 (± 13.2)
3	510	950	516.5 (± 6.6)	947.6 (± 18.6)

The discrepancy between the calculated and the nominal concentration for methane decreases at higher CH<sub>4</sub> concentrations as well as the relative standard errors, considering its increasing contribution on the QEPAS spectrum. The discrepancy between the calculated and the nominal concentrations is below 5 % for both gases, except for methane in mixture 1, where the discrepancy is ~ 6.5 %. The relative standard error of the calculated concentrations is lower than 3 % for the two gases in all the mixtures, except for the relative standard error of 6.2 % estimated for methane in mixture 1, where absorption features of methane are hardly recognizable. The obtained results prove the robustness of the QEPAS technique for a fast broadband detection of gas mixtures. However, the capability of the sensor to recognize the influence of methane absorption features on the two N<sub>2</sub>O absorption bands is expected to improve as the acquisition spectral resolution is increased. Therefore, measurements were repeated in the TTAM configuration. The reference spectra and the three mixtures spectra are shown in **Figure 3.26**.

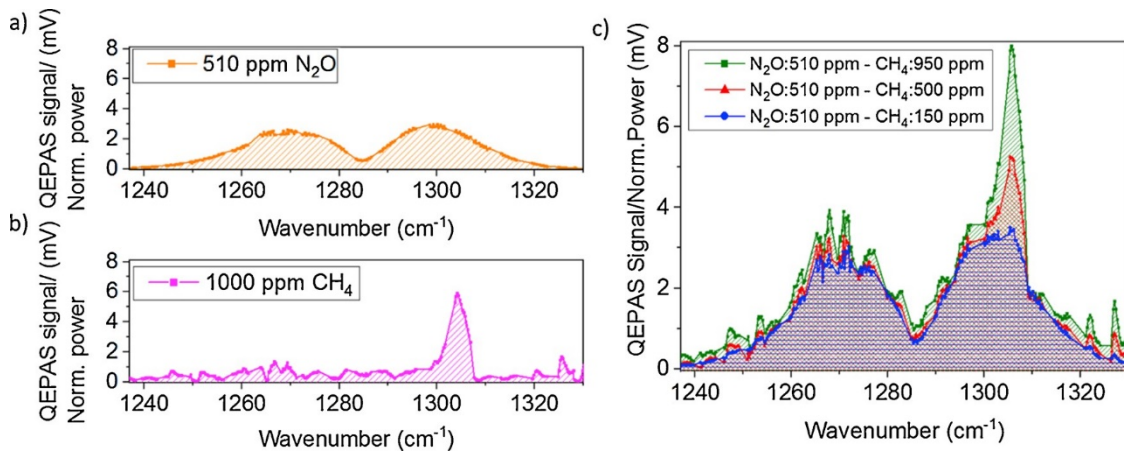


**Figure 3.26 (a)** 510 ppm N<sub>2</sub>O:N<sub>2</sub> and **(b)** 1000 ppm CH<sub>4</sub>:N<sub>2</sub> TTAM QEPAS reference spectra; **(c)** TTAM QEPAS signal normalized to the optical power calibration curve for three dry mixtures containing 510 ppm of N<sub>2</sub>O and 150 ppm of CH<sub>4</sub> (blue dots), 500 ppm of CH<sub>4</sub> (red triangles) and 950 ppm of CH<sub>4</sub> (green squares), respectively [141].

The spectra in **Figure 3.26(c)** clearly show the different contributions of the two gaseous components in the mixtures, with several methane peaks becoming visible from the N<sub>2</sub>O P- and R-branches, even at the lowest CH<sub>4</sub> concentration. The N<sub>2</sub>O and CH<sub>4</sub> concentrations in the three mixtures were also calculated by using the MATLAB-based software and the results are reported in **Table 3.5**.

**Table 3.5** Nominal and calculated N<sub>2</sub>O and CH<sub>4</sub> concentration for the three investigated gas mixtures analyzed in TTAM [141].

Mixture	Nominal N <sub>2</sub> O concentration (ppm)	Nominal CH <sub>4</sub> concentration (ppm)	Calculated N <sub>2</sub> O concentration (ppm)	Calculated CH <sub>4</sub> concentration (ppm)
1	510	150	520.9 (± 1.8)	157.4 (± 4.6)
2	510	500	504.6 (± 2.9)	484.5 (± 7.2)
3	510	950	509.8 (± 3.9)	954.8 (± 9.7)

The discrepancy between the nominal and the calculated concentration of nitrous oxide and methane is lower than 5 % for all the mixtures. Moreover, the relative standard errors of the concentrations improved of a factor ~2 compared to the values reported in **Table 3.4**. Compared to FTAM, TTAM measurements provide spectra with more recognizable absorption structures that can be associated to the single gas components in the mixture. Ultimately, the fitting procedure allows N<sub>2</sub>O and CH<sub>4</sub> concentrations to be retrieved with a comparable level of accuracy for both acquisition modes and a higher precision is obtained in the case of operating in TTAM.

### 3.2.3 PLSR as a tool to retrieve gas concentrations in mixtures detected using QEPAS

Multilinear regression (MLR) methods employed in previous paragraph show a high statistical significance when there is no collinearity among the predictor variables. When two or more variables in a multiple regression model are correlated (multicollinearity), they cannot independently predict the value of the dependent variable, leading to a decrease in the statistical significance of the prediction. Therefore, when dealing with

complex systems made of correlated data [145], which is the case for spectroscopic analysis of overlapping absorption features of different components in a gas mixture, these requirements cannot be guaranteed, and the use of an MLR approach can result in a lack of precision and accuracy [146], [147]. In [134] and [141], merged absorption features using QEPAS-based sensors and analyzed using MLR were detected. In both cases, the regression technique results in calculating values with large confidence intervals. This suggests empowering all the laser based spectroscopic techniques with a more sophisticated analysis tool whenever strongly overlapping gas species must be analyzed in a mixture. Partial Least Squares Regression (PLSR) is an excellent candidate to overcome these limitations, because extends the MLR approach to deal with a large number of strongly correlated and noisy experimental data [146], [147]. In this paragraph, MLR and PLSR are compared as tools to identify gas components in a mixture with strongly overlapping absorption features over the full spectral dynamic range of QCL sources employed in QEPAS sensors. A two-gas mixture composed of carbon monoxide (CO) and nitrous oxide (N<sub>2</sub>O) and a three-gas mixture of acetylene (C<sub>2</sub>H<sub>2</sub>), methane (CH<sub>4</sub>), and nitrous oxide have been analyzed. Both mixtures are diluted in nitrogen (N<sub>2</sub>). Absolute concentrations of gas components in the mixtures were estimated starting from single-gas reference spectra.

### 3.2.3.1 Partial Least-Squares Regression

The multiple regression equation in matrix form is as follows:

$$Y = X \times B + E \quad \text{Eq. 3.6}$$

where  $X$  is the  $n \times m$  matrix of independent variables (matrix of experimental spectra),  $Y$  the  $n \times k$  matrix of the predicted values of the variables (matrix of physical parameters to be estimated, i.e., the gas component concentrations),  $B$  is the  $m \times k$  matrix of the regression coefficients, and  $E$  is the  $n \times k$  errors matrix, assumed to be uncorrelated and with the same variance. PLSR is based on the assumption that the investigated system is influenced by a set of factors called latent variables (LVs) [146]. The prediction is achieved by extracting LVs having the best predictive power from the predictors [147]. From a geometrical point of view, this procedure is equal to a projection of the  $X$ -variables into a new space, representative of the latent variables. The strength of the PLSR method compared to other multivariate analysis (MVA) techniques (i.e., multiple linear regression,

ridge regression etc.) is in the stability of predictors. Since the uncertainty of the estimated parameters is the dominant factor in the variability of predictors, it is crucial to keep the number of variables as low as possible. In this way, PLSR gives the minimum number of necessary variables [148], [149]. This technique can be used for both modeling the underlying relationship between physical or chemical parameters and performing predictive analysis on a sample with unknown properties requiring evaluation. The latter condition assumes a machine learning-like approach, where the experimental data set  $X$  is split into a training-set  $X_{tr}$ , associated with a known  $Y_{tr}$ , and a test-set  $X_{test}$ , with  $Y_{test}$  to be evaluated. With the aim of evaluating the concentrations of chemical species in a multi-gas mixture, the training-data set will be developed starting from single-gas spectra used as reference spectra to calibrate the model and analyze the gas mixtures spectra. The PLSR analysis is performed on the training-set to calculate the regression coefficients matrix  $B$ , used in turn to evaluate the  $Y_{test}$  matrix via the matrix product:  $Y_{test} = X_{test} \times B$ . The regression matrix  $B$  provides information about the correlation between the experimental data set and the concentration of the corresponding gas, since a high absolute value of the regression coefficient highlights a significant influence of the experimental point on the gas concentration [147]. To perform PLSR, a MATLAB code has been developed using MATLAB built-in Simple Partial Least Squares (SIMPLS) algorithm to perform the regression [150], [151]. In contrast with MLR, where the error on calibration is calculated as the error on the regression coefficients, the evaluation of the PLSR calibration error is not straightforward. A reliable tool for the estimating calibration errors is the 10-fold cross-validation (CV) [152]. This procedure returns the root mean squared error of calibration (RMSECV,  $\epsilon$ ) based on the algorithm performance in the training step, which is known a priori without any information about the test data set. Therefore, RMSECV is based on the predictive ability of the PLS algorithm rather than on the quality of the measurements under test. For these reasons, the estimation of CV-RMSEP will be considered in the following discussion as the error associated with the PLS prediction of gas concentrations in the analyzed mixtures [153] - [155]. Root mean squared error of prediction (RMSEP) will be also evaluated comparing the expected concentrations and the retrieved values, for each analyte [156].

### 3.2.3.2 Experimental section

Absorption spectra of gas mixtures were acquired by using the QEPAS setup depicted in **Figure 3.27**.

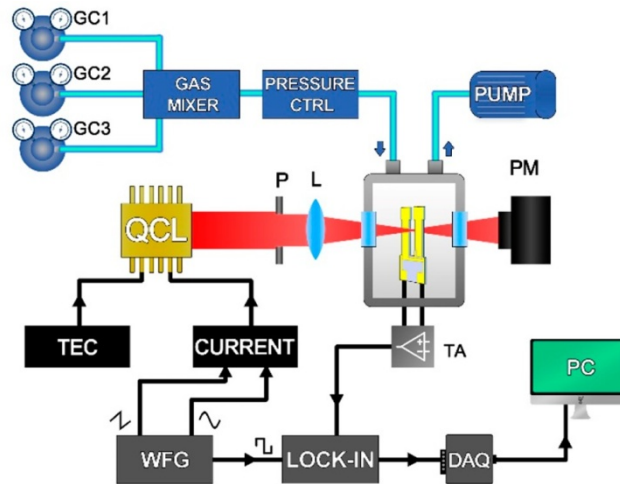


**Figure 3.27** QEPAS sensor for multi-gas detection. QCL, quantum cascade laser; P, pinhole; L, lens; QTF, quartz tuning fork; ADM, acoustic detection module; PM, power meter; TA, transimpedance amplifier; TEC, thermo-electric cooler; WFG, waveform generator; DAQ, digital acquisition card; PC, personal computer; GC, gas cylinder; and PRESSURE CTRL, pressure controller [157].

An AdTech QCL with a central emission wavelength at 4.61  $\mu\text{m}$  and a Corning QCL with a central emission wavelength at 7.72  $\mu\text{m}$  were used to detect  $\text{N}_2\text{O}$  and  $\text{CO}$  in a two-gas mixture and  $\text{C}_2\text{H}_2$ ,  $\text{CH}_4$ , and  $\text{N}_2\text{O}$  in a three-gas mixture, respectively. For both mixtures, the absorption features can be detected by varying the laser injection current within its dynamic range, at a fixed operating temperature. The setup allowed an easy interchange of QCL sources. The laser beams were first spatially filtered by using a pinhole and then focused within an acoustic detection module (ADM) by means of a lens with focal length  $f = 75$  mm.

The ADM (Thorlabs ADM01) consisted of a gas cell, equipped with two windows (Thorlabs WW01050-E1 with 2 – 5  $\mu\text{m}$  AR coating and Thorlabs WW71050-E3 with 7–12  $\mu\text{m}$  AR coating), a pair of connectors for gas inlet and outlet and a custom T-shaped quartz tuning fork with a resonance frequency of  $f_0 = 12458$  Hz and a quality factor of 12 500 at atmospheric pressure [91]. A power meter was set behind the ADM for alignment

purpose. All measurements were performed at atmospheric pressure ( $P = 760$  Torr) and room temperature ( $T = 25$  °C). The piezoelectric current generated by the QTF was collected and transduced into a voltage signal by a transimpedance amplifier with a feedback resistor  $R_{fb} = 10$  M $\Omega$ . The voltage signal was sent to an EG&G model 7265 lock-in amplifier, set with a time constant of 100 ms. Both QCLs were polarized using an Arroyo 5300 current driver. An Arroyo 4300 thermo-electric cooler (TEC) was used to stabilize the operating temperature. QCL emission frequencies were tuned by sweeping the laser injection current with a 2 mHz triangular ramp and were simultaneously modulated by a sinusoidal waveform with frequency  $f_0/2$ . The lock-in demodulated the QTF voltage signal at  $f_0$ : in this way the sensor was operated in  $2f$  based wavelength modulation. Both the sweep and the modulation were provided by a Tektronix AFG3102 waveform generator, which also supplied the reference signal for the lock-in amplifier at  $f_0/2$ . The demodulated output signal was then sent to a DAQ card (National Instrument 6002) and stored on a PC using a LabVIEW-based software. All the measurements were performed in a continuous gas flow of 30 sccm. Four cylinders with certified concentrations of the single gas targets (1000 ppm of CO in N<sub>2</sub>, 1000 ppm of N<sub>2</sub>O in N<sub>2</sub>, 1000 ppm of C<sub>2</sub>H<sub>2</sub> in N<sub>2</sub>, and 1% of CH<sub>4</sub> in N<sub>2</sub>) and one cylinder of pure N<sub>2</sub> were used to generate different gas mixtures. A gas mixer (MCQ Instrument Gas Blender 1003) was used to manage gas flows for up to 3 different input gas lines at the same time, with  $1\sigma$  single-channel accuracy of  $\sim 1\%$  provided by the instrument datasheet. The pressure inside the gas line was fixed and monitored by an MKS Pressure Controller Type 649.

### 3.2.3.3 Two-Gas Mixture Detection

HITRAN database [78] was used to simulate the absorption cross section of 1000 ppm of CO in N<sub>2</sub> and 1000 ppm of N<sub>2</sub>O in N<sub>2</sub>, at atmospheric pressure and room temperature over the whole spectral dynamic range of the AdTech QCL (2188.8–2191.2 cm<sup>-1</sup>). The results of the simulation are shown in **Figure 3.28(a)**.

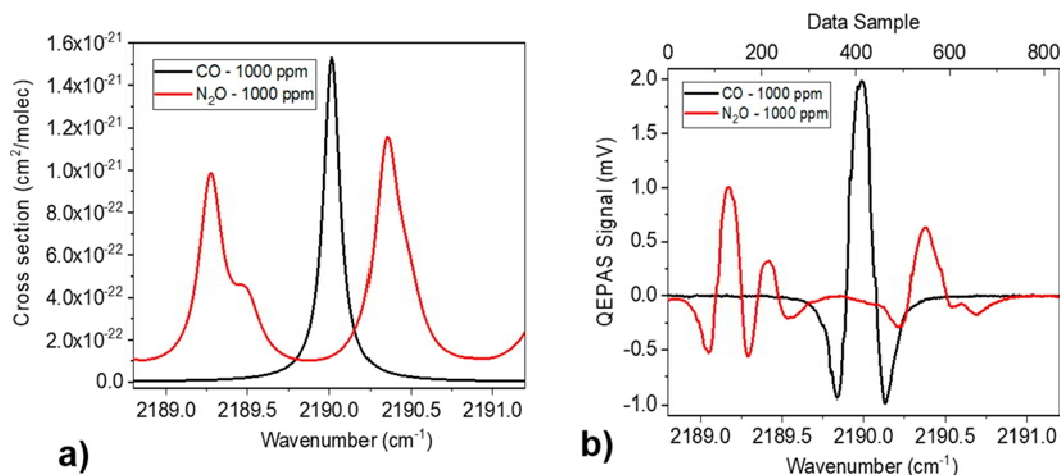


**Figure 3.28** (a) HITRAN simulation of absorption cross section spectrum and (b) QEPAS scan of 1000 ppm of CO in N<sub>2</sub> (black curve) and 1000 ppm of N<sub>2</sub>O in N<sub>2</sub> (red curve) [157].

The CO exhibits a Lorentzian-like absorption feature peaked at 2190.02 cm<sup>-1</sup> while the N<sub>2</sub>O shows two partially merged absorption features with peaks at 2189.35 and 2189.4 cm<sup>-1</sup> and a well-isolated Lorentzian-like absorption feature at 2190.35 cm<sup>-1</sup>. As a first step, the single-gas reference spectra were acquired by analyzing gas mixture coming directly from the gas cylinders, without the use of the mixer. Hence, the reference spectra are referred to certified concentrations. To scan the spectral range reported in **Figure 3.28(a)**, the AdTech QCL operating temperature was set at 15 °C, and the injection current was tuned from 230 mA to 310 mA. The maximum optical power measured at the injected current of 310 mA (corresponding to 2188.8 cm<sup>-1</sup>) was 75 mW. The QEPAS signal was collected with a lock-in amplifier demodulation phase  $\phi_1 = -132.17^\circ$ , corresponding to the phase value maximizing the CO peak signal. The QEPAS scan referred to the positive slope of the triangular ramp is reported in **Figure 3.28(b)**. In order to enlarge the data statistics, both positive and negative ramp slopes were considered in the PLSR algorithm. With a signal acquisition time of 300 ms, a single spectrum consisted in 1666 data-points. To ensure the reproducibility of the measurements, the reference data are collected every time a new set of mixtures spectra is acquired. In this way, the consistency of the operative conditions is guaranteed.

The CO reference spectrum shows a single absorption feature with a signal intensity of ~2 mV, corresponding to the isolated absorption peak at 2190.02 cm<sup>-1</sup> in **Figure 3.28(a)**. From left to right, the N<sub>2</sub>O reference spectrum shows three features with peak intensities of ~1, ~0.3, and ~0.6 mV. The first two peaks are clearly due to the partially merged

absorption features at  $2189.35\text{ cm}^{-1}$  and at  $2189.4\text{ cm}^{-1}$ , while the third peak is associated with the isolated absorption line peaked at  $2190.35\text{ cm}^{-1}$ . The  $1\sigma$ -noise level measured far from the absorption features is  $\sim 3\text{ }\mu\text{V}$  for both spectra, resulting in a Signal-to-Noise Ratio (SNR) of 660 and 330 for CO and N<sub>2</sub>O, respectively. The measured noise level is comparable to the calculate thermal noise value of  $2.6\text{ }\mu\text{V}$ , which affects the resonator in the employed configuration [110].

Starting from the certified concentrations of 1000 ppm of N<sub>2</sub>O in N<sub>2</sub> and 1000 ppm of CO in N<sub>2</sub>, the following mixtures of N<sub>2</sub>O–CO were generated by using the gas blender: 250–750 ppm, 500–500, and 750–250 ppm, in N<sub>2</sub>. All QEPAS measurements were performed by setting the lock-in phase to  $\phi_1$ . The acquired QEPAS spectra scans are reported in **Figure 3.29**.

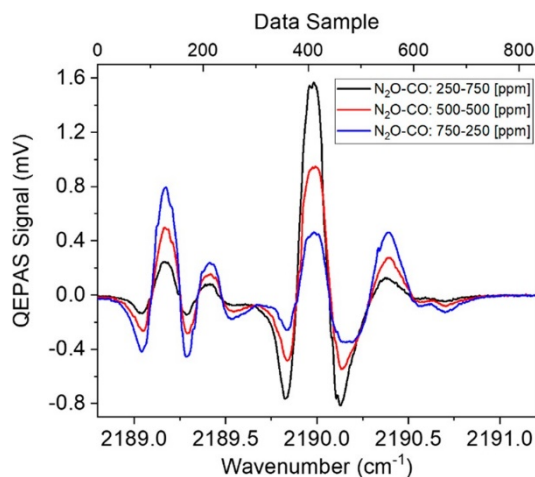


**Figure 3.29** QEPAS scan acquired for three mixtures containing 250 ppm of N<sub>2</sub>O and 750 ppm of CO (black curve), 500 ppm of N<sub>2</sub>O and 500 ppm of CO (red curve), and 750 ppm of N<sub>2</sub>O and 250 ppm of CO (blue curve), respectively, in N<sub>2</sub> [157].

All absorption features of N<sub>2</sub>O and CO are clearly distinguishable. Spectral overlap is only limited to the superposition of the right-side negative lobe of the CO absorption feature with the left-side negative lobe of the N<sub>2</sub>O absorption feature peaked at  $2190.35\text{ cm}^{-1}$ .

### 3.2.3.4 Two-Gas Mixture PLS Model Calibration and Test

Data analysis starts from the configuration of the training data set for PLS model calibration. MATLAB-based algorithm projects the training data set on a number of PLS factors, i.e., the number of latent variables, equal to two, representing the components of

the gas mixtures. However, larger data sets correspond to lower calibration errors. Unlike MLR, PLSR allows the employment of simulated data to perform the regression [158], [159]. Hence, the experimental data set was enriched by simulated spectra calculated as linear combinations of the actual reference spectra [160]. Actual reference spectra were combined using 10 coefficients, from 0 to 0.9 at step of 0.1, properly chosen according to the concentration range expected in mixtures under investigation. The simulation process resulted in  $10^{\text{PLS-factors}} = 100$  simulated spectra. This enlargement of the experimental data set represents one of the main advantages of PLSR compared to MLR. In contrast to MLR, PLSR allows for the addition of input noise fluctuations on the simulated spectra to consider the non-negligible fluctuations affecting the reference spectra. A reliable distribution of the input noise fluctuations must match the distribution of the QEPAS signal fluctuations around its mean value, namely the peak value. The experimental distribution has been retrieved by repeatedly scanning over the QEPAS absorption peaks. For both target gases, a Gaussian noise distribution with a  $1\sigma$ -noise fluctuation of  $\sim 3\%$  around the mean value was obtained. Hence, a white Gaussian noise was superimposed to the simulated reference spectra. With these conditions, the X- training data set is a  $100 \times 1666$  matrix (100 different simulated reference spectra, each one composed of 1666 data samples) while the Y-training data set is a  $100 \times 2$  matrix with the related gas concentrations. A preliminary analysis on the whole data set showed that modeling the system with 2 PLS factors explains more than 99% of  $Y_{tr}$  variance, confirming the validity of the theoretical assumptions about physical relevance of PLS factors. Then, the PLSR algorithm is used to calculate regression coefficients (matrix B). In **Table 3.6**, the results of the PLSR applied to the three gas mixtures are reported, together with MLR results and their associated calibration errors  $\varepsilon$ .

**Table 3.6** PLSR and MLR Results (Concentrations and Calibration Errors) for Each Component of Dual-Gas Mixtures. The nominal concentrations are also reported together with the accuracy determined from the gas mixer datasheet [157].

Mixture	Nominal concentration (ppm)		PLSR estimation (ppm)		MLR estimation (ppm)	
	N <sub>2</sub> O	CO	N <sub>2</sub> O	CO	N <sub>2</sub> O	CO
1	250 ( $\eta=\pm 10$ )	750 ( $\eta=\pm 10$ )	240 ( $\varepsilon=\pm 1.5$ )	779 ( $\varepsilon=\pm 2.0$ )	240 ( $\varepsilon=\pm 7.6$ )	779 ( $\varepsilon=\pm 4.5$ )
2	500 ( $\eta=\pm 10$ )	500 ( $\eta=\pm 10$ )	478 ( $\varepsilon=\pm 1.5$ )	499 ( $\varepsilon=\pm 2.0$ )	477 ( $\varepsilon=\pm 4.4$ )	499 ( $\varepsilon=\pm 2.6$ )

<b>3</b>	750 ( $\eta=\pm 10$ )	250 ( $\eta=\pm 10$ )	770 ( $\varepsilon=\pm 1.5$ )	251 ( $\varepsilon=\pm 2.0$ )	770 ( $\varepsilon=\pm 5.2$ )	251 ( $\varepsilon=\pm 3.1$ )
----------	--------------------------	--------------------------	----------------------------------	----------------------------------	----------------------------------	----------------------------------

The nominal concentrations of the mixture components are also reported with an accuracy of  $\eta = \pm 10$  ppm, calculated by considering the gas mixer flow accuracy of 1% starting from the certified gas cylinder concentrations. Considering this instrumental limitation, we used the cross-validation error  $\varepsilon$  as main indicator for quantifying the robustness of the regression model employed, i.e., PLSR and MLR.

The results show that PLSR and MLR predict the same concentration values in gas mixtures, while the RMSECV estimated by PLSR is up to 3 times lower than the MLR estimation. The estimated values of gas concentrations are within the  $2\sigma$  interval determined by the accuracy of the gas mixer. The PLSR-RMSEP are equal to 18 and 17 ppm, while the MLR-RMSEP are equal to 19 and 17 ppm, for  $N_2O$  and CO, respectively. Due to the instrumental limitation, it is not possible to compare the collected results with the reference standard concentration values in the gas line. However, the stability of the algorithms results, which is strictly connected to the regression precision, can be verified by performing the analysis on repeated measurements. As expected from the theoretical background [147], the PLSR results are less affected by experimental data fluctuations. This means that bias effects in concentrations estimation can be removed in a validation step to be performed before moving the sensor outside the laboratory.

The influence of the input noise fluctuations added to the simulated spectra on the calibration error has been evaluated. PLSR analysis was performed by varying the input  $1\sigma$ -noise fluctuation to evaluate the effect both on the retrieved concentrations and on the associated errors  $\varepsilon$ . Negligible variations in the estimated concentration values ( $<1$  ppm) were calculated for fluctuations up to 50%. Whereas the  $\varepsilon$  values are strongly dependent from input noise fluctuations. **Figure 3.30** shows the total RMSECV, calculated as the square root of the sum of the squared  $\varepsilon$  of the single gases divided by the number of gases, as a function of input  $1\sigma$ -noise fluctuations. Equation  $y = (0.617 \pm 0.004) \cdot x + (-0.14 \pm 0.07)$  with  $R^2 = 0.999$  is the best fit for the data in **Figure 3.30**.

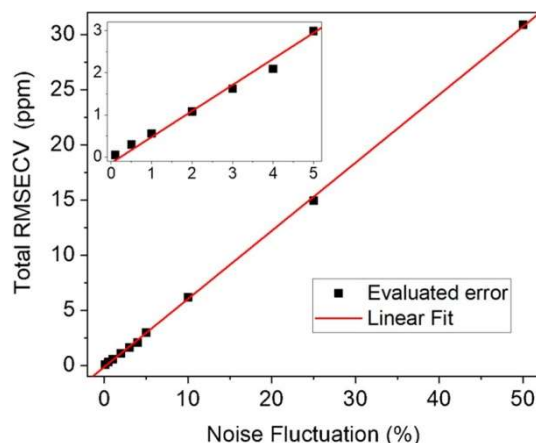


**Figure 3.30** Total RMSECV as a function of the  $1\sigma$ -noise fluctuation added to simulated spectra in training data set (black squares) and the best linear fit (red line). Inset: zoom in the range 0–5% of noise fluctuations, as typical values in spectroscopic experiments [157].

### 3.2.3.5 Three-Gas Mixture Detection

Gas mixtures with three components having a strong spectral overlap were tested to get a benchmark on the efficiency of PLSR in analyzing QEPAS- based absorption features. With this aim,  $C_2H_2$ ,  $CH_4$ , and  $N_2O$  were selected. **Figure 3.31(a)** shows HITRAN database simulations [78] at atmospheric pressure and room temperature of the listed gases absorption cross-section within the emission spectral range of the Corning QCL operated at 30 °C, when varying the injection current from 200 to 270 mA ( $1295.5\text{ cm}^{-1}$ -  $1296.5\text{ cm}^{-1}$ ).

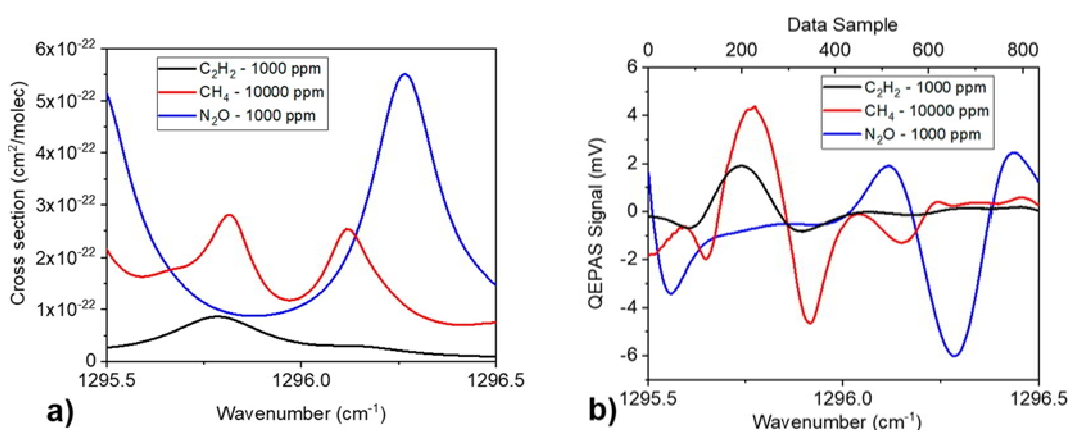


**Figure 3.31 (a)** HITRAN simulation of the absorption cross section spectrum and **(b)** QEPAS scan of 1000 ppm of  $C_2H_2$  in  $N_2$  (black curve), 10 000 ppm of  $CH_4$  in  $N_2$  (red curve), and 1000 ppm of  $N_2O$  in  $N_2$  (blue curve) [157].

The cross-sections are scaled on the certified concentrations in gas cylinders: 1000 ppm for C<sub>2</sub>H<sub>2</sub>, 1000 ppm for N<sub>2</sub>O, and 10 000 ppm for CH<sub>4</sub>, in N<sub>2</sub>. C<sub>2</sub>H<sub>2</sub> has a strong absorption features peaked at 1295.78 cm<sup>-1</sup> and a weak one at 1296.16 cm<sup>-1</sup>; CH<sub>4</sub> has two absorption lines falling at 1295.81 and 1296.12 cm<sup>-1</sup>; and N<sub>2</sub>O shows a single absorption line peaked at 1296.27 cm<sup>-1</sup>. The maximum optical power detected at the injected current of 270 mA is 112 mW. To build the training data set, the single-gas reference spectra for the three target gases were acquired directly from the gas cylinders. The lock-in amplifier demodulation phase was fixed at  $\phi_2 = -136.75^\circ$ , corresponding to the phase maximizing the C<sub>2</sub>H<sub>2</sub> peak signal. This choice allowed the enhancement of the C<sub>2</sub>H<sub>2</sub> spectral feature, showing the weakest absorption coefficient. The three QEPAS spectral scans obtained by sweeping the QCL injection current are reported in **Figure 3.31(b)**. As for the two-gas mixtures, the reference data are collected every time a new set of mixtures spectra is acquired, in order to ensure the consistency of the operative conditions. The C<sub>2</sub>H<sub>2</sub> reference spectrum shows a characteristic line-shape of the second derivative of Lorentzian profile, with a signal intensity of  $\sim 1.9$  mV. Due to the choice of lock-in demodulation phase, the spectral characteristics of N<sub>2</sub>O have the same line-shape of C<sub>2</sub>H<sub>2</sub> but inverted. The QEPAS CH<sub>4</sub> reference spectrum has a pronounced absorption peak of  $\sim 4.3$  mV, corresponding to the strongest absorption peak at 1295.81 cm<sup>-1</sup>, while the absorption feature at 1296.12 cm<sup>-1</sup> is also recognizable but inverted in shape due to a difference in signal phase with the peak at 1295.81 cm<sup>-1</sup>. On the left side of the graph, CH<sub>4</sub> and C<sub>2</sub>H<sub>2</sub> strongly overlap; on the right side, the N<sub>2</sub>O absorption feature is weakly disturbed by the other two gases. The measured 1 $\sigma$ -noise is  $\sim 4$   $\mu$ V for all three gases, comparable with the QTF thermal noise and resulting in an SNR of 470, 1150, and 1500 for C<sub>2</sub>H<sub>2</sub>, CH<sub>4</sub>, and N<sub>2</sub>O, respectively. Starting from the certified concentrations, five mixtures of C<sub>2</sub>H<sub>2</sub>-CH<sub>4</sub>-N<sub>2</sub>O, with a fixed concentration of 3000 ppm of CH<sub>4</sub> have been generated, as reported in the legend of **Figure 3.32**. All the QEPAS measurements were performed by setting the lock-in phase to  $\phi_2$ . The acquired QEPAS spectra scans are reported in **Figure 3.32**.

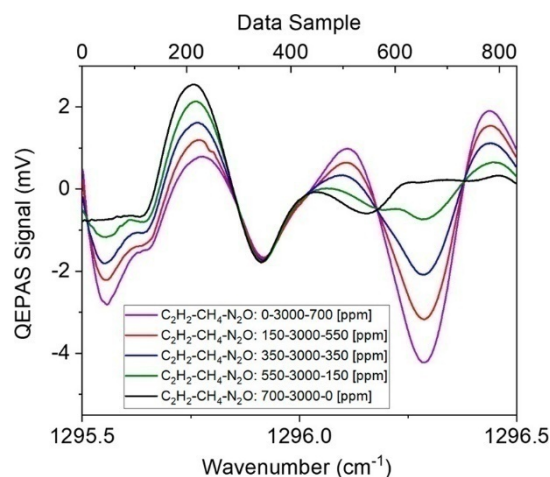


**Figure 3.32** QEPAS scan for five mixtures containing 0 ppm of C<sub>2</sub>H<sub>2</sub>, 3000 ppm of CH<sub>4</sub> and 700 ppm of N<sub>2</sub>O (purple curve), 150 ppm of C<sub>2</sub>H<sub>2</sub>, 3000 ppm of CH<sub>4</sub> and 550 ppm of N<sub>2</sub>O (green curve), 350 ppm of C<sub>2</sub>H<sub>2</sub>, 3000 ppm of CH<sub>4</sub> and 350 ppm of N<sub>2</sub>O (blue curve), 550 ppm of C<sub>2</sub>H<sub>2</sub>, 3000 ppm of CH<sub>4</sub> and 150 ppm of N<sub>2</sub>O (red curve), 700 ppm of C<sub>2</sub>H<sub>2</sub>, 3000 ppm of CH<sub>4</sub>, and 0 ppm of N<sub>2</sub>O (black curve) [157].

As expected, the strong absorption feature of N<sub>2</sub>O is well recognizable at 1296.27 cm<sup>-1</sup> (650 data sample). The CH<sub>4</sub> and C<sub>2</sub>H<sub>2</sub> absorption features are completely overlapped in the wavenumber range from 1295.65 to 1295.91 cm<sup>-1</sup>, while deformations of the spectra induced by the increasing amount of acetylene can be observed in the 1295.50 cm<sup>-1</sup>–1295.65 cm<sup>-1</sup> sample range.

### 3.2.3.6 Three-Gas Mixture PLS Analysis

The PLSR has been performed by projecting the training data set on three PLS factors, representing the number of gas components in the mixtures. As for the two-gas mixture, a 1000 × 1666 matrix X<sub>tr</sub>, has been obtained by simulating 10<sup>PLS-factors</sup> = 1000 spectra with a superimposed Gaussian noise. The Y training data set is a 1000 × 3 matrix with the associated gas concentrations. Preliminary analysis on the whole data set shows that modeling the system with 3 PLS factors explains more than 99% of Y<sub>tr</sub> variance. The PLSR is therefore performed, and the regression coefficients matrix B is calculated. As for the two-gas mixture analysis, variations lower than 1 ppm in the estimated concentration values were calculated for input 1σ-noise fluctuations up to 50%. The analysis of the Total RMSECV as a function of Gaussian noise fluctuation showed a linear trend with a best fit

equation  $y = (4.65 \pm 0.04) \cdot x + (-0.61 \pm 0.64)$  and  $R^2 = 0.999$ . In **Table 3.6**, the PLSR results for the five mixtures shown in **Figure 3.32** and related MLR results are reported.

**Table 3.7** PLSR and MLR Results (Concentrations and Calibration Errors) for Each Component of the Analyzed Three-Gas Mixtures. The nominal concentrations are also reported together with the accuracy determined by the gas mixer datasheet [157].

Mix	Nominal concentration (ppm)			PLSR concentration (ppm)			MLR concentration (ppm)		
	C <sub>2</sub> H <sub>2</sub>	CH <sub>4</sub>	N <sub>2</sub> O	C <sub>2</sub> H <sub>2</sub>	CH <sub>4</sub>	N <sub>2</sub> O	C <sub>2</sub> H <sub>2</sub>	CH <sub>4</sub>	N <sub>2</sub> O
1	0 $\eta = \pm 10$	3000 $\eta = \pm 100$	700 $\eta = \pm 10$	44 $\epsilon = \pm 1.9$	2832 $\epsilon = \pm 7.5$	711 $\epsilon = \pm 0.5$	55 $\epsilon = \pm 7.1$	2795 $\epsilon = \pm 25.1$	709 $\epsilon = \pm 1.2$
2	150 $\eta = \pm 10$	3000 $\eta = \pm 100$	550 $\eta = \pm 10$	163 $\epsilon = \pm 1.9$	2934 $\epsilon = \pm 7.5$	540 $\epsilon = \pm 0.5$	171 $\epsilon = \pm 7.8$	2909 $\epsilon = \pm 27.6$	538 $\epsilon = \pm 1.4$
3	350 $\eta = \pm 10$	3000 $\eta = \pm 100$	350 $\eta = \pm 10$	378 $\epsilon = \pm 1.9$	2863 $\epsilon = \pm 7.5$	361 $\epsilon = \pm 0.5$	378 $\epsilon = \pm 9.5$	2863 $\epsilon = \pm 33.5$	361 $\epsilon = \pm 1.7$
4	550 $\eta = \pm 10$	3000 $\eta = \pm 100$	150 $\eta = \pm 10$	506 $\epsilon = \pm 1.9$	3060 $\epsilon = \pm 7.5$	145 $\epsilon = \pm 0.5$	495 $\epsilon = \pm 9.7$	3099 $\epsilon = \pm 34.2$	147 $\epsilon = \pm 1.7$
5	700 $\eta = \pm 10$	3000 $\eta = \pm 100$	0 $\eta = \pm 10$	720 $\epsilon = \pm 1.9$	2908 $\epsilon = \pm 7.5$	-4 $\epsilon = \pm 0.5$	714 $\epsilon = \pm 9.7$	2927 $\epsilon = \pm 34.3$	-3 $\epsilon = \pm 1.7$

In contrast to the two-gas mixtures analysis, PLSR and MLR predict different concentration values. The estimated values of gas concentrations are within the  $2\sigma$  interval determined by the accuracy of the gas mixer, with few exceptions for C<sub>2</sub>H<sub>2</sub>. This can be ascribed to the difficulties of both methods in the identification of the C<sub>2</sub>H<sub>2</sub> contribution, due to the strong overlap with the CH<sub>4</sub> absorption line, as supported by the highest relative error measured for C<sub>2</sub>H<sub>2</sub> in all mixtures. With three-gas mixtures with strongly overlapped features, calibration error by PLSR is significantly lower than MLR, up to a factor of  $\sim 5$ . The calculated PLSR-RMSEP are equal to 32, 113, and 9 ppm, while the MLR-RMSEP are equal to 39, 130, and 9 ppm for C<sub>2</sub>H<sub>2</sub>, CH<sub>4</sub>, and N<sub>2</sub>O, respectively. In mixture 1 with no C<sub>2</sub>H<sub>2</sub>, both PLSR and MLR predict the presence of C<sub>2</sub>H<sub>2</sub>, with a concentration of 44 and 55 ppm, respectively. A lower accuracy for the MLR can be explained considering that the algorithm is forced to search for all the gas components set as reference spectra. Therefore, a higher bias in regression is expected, reducing the accuracy of the prediction. However, as reported for the two-gas mixtures, even with three-gas mixtures, the PLSR results were verified to be more stable to repeated measurements compared to MLR ones. The evidence of the bias influence can be observed repeating the analysis excluding the C<sub>2</sub>H<sub>2</sub> reference spectrum from the training data set. The retrieved concentrations thus become 2958 and 710 ppm for CH<sub>4</sub> and N<sub>2</sub>O, respectively, and a decrease in calibration

error is obtained, with  $\varepsilon_{\text{CH}_4} = 4.2$  ppm and  $\varepsilon_{\text{N}_2\text{O}} = 0.4$  ppm. In the mixture with no  $\text{N}_2\text{O}$ , both methods predict a negative value for  $\text{N}_2\text{O}$  concentration: this is obviously not possible and must be intended as a zero concentration. However, with respect to  $\text{C}_2\text{H}_2$  estimation in the mixture with no  $\text{C}_2\text{H}_2$ , both algorithms are more accurate in the prediction because the  $\text{N}_2\text{O}$  absorption feature is well-defined within all mixture spectra.

These kinds of false-positive results may occur when dealing with missing components, as well as false-negative results may occur when one of the target analytes generates a negligible QEPAS signal. For real-field applications, regression algorithms are trained on analyte concentrations similar to the ones expected in the sample to test. In this case, a threshold concentration can be set to discern the effective presence of a chemical species, based on the expected sample composition.

### 3.2.3.7 Overlap Parameter Estimation

The results obtained for the two-gas mixtures showed that, when dealing with weakly overlapping spectral features, the PLSR and the MLR return the same values, but the PLSR calibration error estimation can be up to 3 times lower than that of the MLR. When analyzing spectra originated by strongly overlapping absorbing features, PLSR predicts different gas concentrations with respect to MLR, with a lower calibration error up to a factor of 5. To quantify the overlap between absorption features, a parameter should be introduced. Considering the Lorentzian-like line-shape (see **Figures 3.28(a)** and **3.29(a)**), the overlap parameter  $Z$  between two absorption features labeled as 1 and 2 can be defined as follows:

$$Z = \begin{cases} 1 - \frac{|x_1 - x_2|}{w_{n,1} + w_{n,2}} & |x_1 - x_2| \leq w_{n,1} + w_{n,2} \\ 0 & |x_1 - x_2| > w_{n,1} + w_{n,2} \end{cases} \quad \text{Eq. 3.7}$$

where  $x_i$  is the peak wavenumber, and  $w_{n,i}$  is the normalized Lorentzian width defined as the ratio between the full-width half-maximum of the Lorentzian curve  $w_i$  and the peak value  $A_i$ . The overlap parameter tends to 0 when the distance between the absorption peaks tends to  $w_{n,1} + w_{n,2}$ , while  $Z$  is equal to 1 when  $x_1 = x_2$ . For features whose peaks distance is greater than  $w_{n,1} + w_{n,2}$ ,  $Z$  is negative and overlap effects are negligible. The overlap parameters (in %) calculated for adjacent absorption peaks in the three-gas mixture are  $Z_{\text{CO-N}_2\text{O}} = 7.3\%$ ,  $Z_{\text{CH}_4\text{-N}_2\text{O}} = 79.8\%$ , and  $Z_{\text{C}_2\text{H}_2\text{-CH}_4} = 97.4\%$ . With overlap as high as 97%,

PLSR is able to identify both contributions with a precision significantly higher than that of the standard MLR.

### 3.3 High concentration QEPAS measurements

There is a wide range of applications where the bulk composition of the gas matrix can change. A similar scenario can be found in natural gas analysis, when the concentrations of each component are normally measured in the percent scale [119]. In these applications, the accurate quantification of both bulk matrix component and gas traces in the mixture is fundamental. In percentage range, thus high absorption coefficients, Lambert-Beer law cannot be considered linear [9], [10]. Furthermore, high variations of the bulk composition of a gas mixture influence the mechanical properties (i.e. resonance frequency and quality factor QTF and microresonator tubes amplification) of the spectrophone [14]. Finally, relaxation dynamics of target gas molecules strongly depends on the mixture composition when components concentration can reach percentage range [128]. Because of all these reasons, QEPAS signal of a component in a high-varying mixture depends on its concentration and on the concentration of the other components in mixture. In this section, a QEPAS sensor aimed at high concentration detection of methane and ethane is described.

#### 3.3.1 CH<sub>4</sub> and C<sub>2</sub>H<sub>6</sub> high concentration detection

The tuning range of the ICL employed in [134] is well-suited to detect methane (C1) and ethane (C2) in a QEPAS sensor architecture. A Nanoplus ICL emitting at a central wavelength of 3345 nm and operating at 27.5 °C was mounted in the same compact QEPAS sensor configuration described in the section 2.3.1 of this thesis. Since the high sensitivity obtained in [134], electronic components were optimized to avoid saturation of signals. 760 Torr was employed as working pressure. The range of concentration of C1 and C2 were 7 - 10 % and 0.2 -0.5 %, respectively. These ranges simulate a 1:10 dilution in nitrogen (N<sub>2</sub>) of natural gas-like mixtures [119]. An example of gas mixtures QEPAS spectra is reported in **Figure 3.33(a)**. Two partially merged C1 absorption features can be observed corresponding to a laser injected current  $I_{\text{laser}} = 52$  mA and  $I_{\text{laser}} = 54$  mA, while two well-separated C2 absorption features can be observed at  $I_{\text{laser}} = 43$  mA and  $I_{\text{laser}} = 69$  mA. Significant variations of the C1 peak signal were observed changing the samples composition. As an example, the QEPAS peak values for a fixed concentration of C1 with varying C2 is reported in **Figure 3.33(b)**.

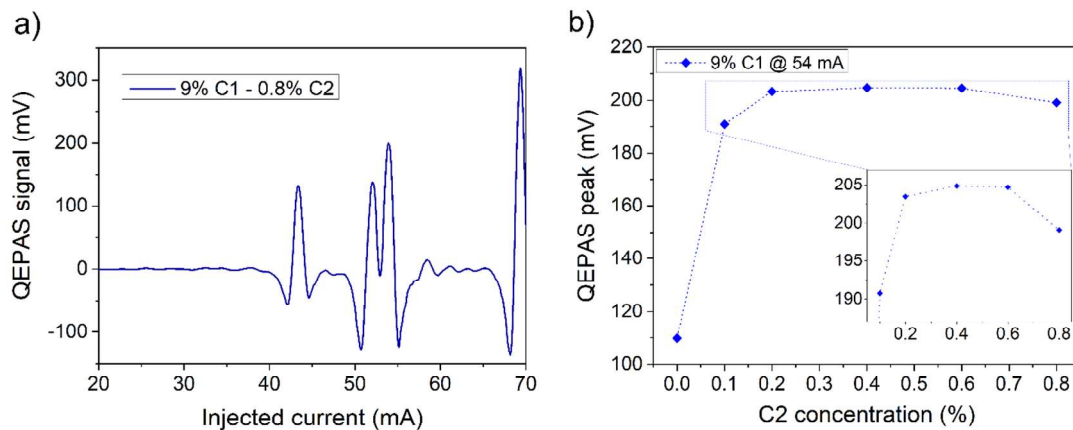


**Figure 3.33 (a)** QEPAS spectrum of the mixture composed by 9% C1, 0.8% C2 and N<sub>2</sub>. **(b)** QEPAS peak signals of a fixed 9% C1 concentration with varying C2 in nitrogen.

C1 peak signals are significantly higher when C2 is introduced in the gas matrix compared to the one acquired in pure nitrogen matrix. Moreover, C1 peak values vs C2 concentration changes does not show a monotonic trend. The sharp signal increase of C1 signal, from the one obtained in pure N<sub>2</sub> and the one recorded when 1000 ppm of C2 are added to the mixture, is due to the modification of the density of energy levels available for V-T relaxation. Once reached a C1 signal plateau from 2000 ppm to 6000 ppm of C2, the signal starts decreasing because of the quality factor deterioration and the sound speed variation. In order to analyze the acquired QEPAS mixtures spectra and retrieve the analytes concentrations, PLSR analysis was used. This statistical method has proven its potential with highly overlapped QEPAS spectra [157] and it is well-known in different spectroscopic fields for being able to deal with matrix effects [161], [162]. The PLSR was set using a machine learning approach, with a calibration step and a test step. The measurements' dataset was split assigning 36 spectra to the calibration set and 4 spectra to the test set, whose components concentrations were unknown to the regression algorithm. The test measurements were selected among those characterized by a composition similar to natural gas samples from real-field applications (C1 > 7%, C2 ≈ 0.2% - 0.8%). The number of PLS components to be used for the analysis was determined by means of a validation step using a 10-fold cross-validation method. The optimal number of components was evaluated using the root mean squared error of cross-validation (RMSECV) as selecting parameter and was found equal to three. Following this preliminary step, the calibration of the PLS algorithm was performed and the regression coefficients matrix was calculated. Using this calibration model, the concentrations of the

hydrocarbons in the test set were predicted and compared to the expected ones, as shown in **Figure 3.34(a)-(b)** for C1 and C2, respectively. In **Table 3.8** are reported the retrieved concentrations.

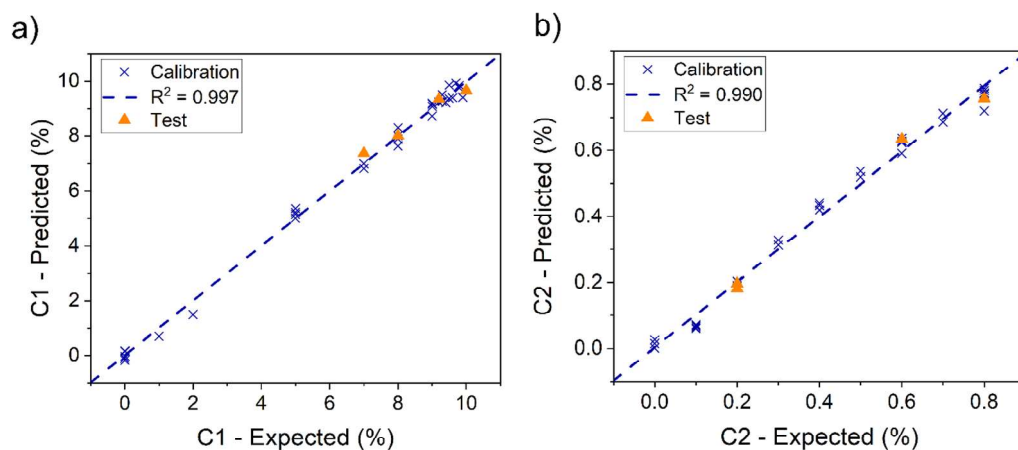


**Figure 3.34** Plot of predicted concentrations versus expected concentrations of **(a)** C1 and **(b)** C2. Both the test set (orange triangles) and the calibration set (blue crosses) are shown, alongside with the linear fit of the latter ones (dashed line).

**Table 3.8** Comparison between expected concentrations and PLSR-predicted concentrations, in test set.

Mix	Expected (%)		Predicted (%)	
	C1	C2	C1	C2
#1	7.0	0.20	7.4	0.20
#2	8.0	0.60	8.0	0.63
#3	9.2	0.80	9.3	0.76
#4	10.0	0.20	9.7	0.18

The calibration data of both chemical species were linearly fitted and the returned determination coefficient  $R^2$  was equal to 0.997 for C1 and 0.990 for C2. The root-mean square error of calibration (RMSEC) was used to evaluate the PLSR model and was equal to 0.23% and 0.029% for C1 and C2, respectively. The root-mean-square error of prediction (RMSEP) for the test samples was used to verify the prediction capabilities of the PLSR models and was equal to 0.26% and 0.028% for C1 and C2, respectively. The collected results show the ability of the employed statistical method to retrieve the samples

compositions with a good accuracy, leveling out or at least reducing the impact of gas matrix variation on photoacoustic generation and detection.

## Chapter 4: Integration of QEPAS sensors

QEPAS sensors beam delivery system still relies on free-space optics and optical fibers. These components are subject to misalignments. The solution proposed in section 2.3.1 strongly improved the robustness of QEPAS sensors, but it is bulky. In this chapter, the modeling of a semi-integrated version of QEPAS sensor is proposed. In this configuration, the QTF is excited by means of the evanescent wave leaking out from an integrated waveguide, improving the alignment robustness and the sensor compactness. An integrated optical resonator coupled with the waveguide has been designed and modeled to increase the optical power interacting with the gas target to generate the acoustic wave.

### 4.1 Modeling and Design of a Semi-Integrated QEPAS Sensor

One of the main issues with QEPAS based sensor systems is the required focusing of the laser excitation beam between the QTF prongs. The laser beam must not hit the prongs to avoid the arising of large undesirable non-zero background. This limits the sensor detection sensitivity [14]. Moreover, for those applications in which sensors must work in challenging environments like downhole analysis of natural gas or early fire detection empowered by the drone technology, the further miniaturization step requires a different level of integration of the opto-acoustic components [127], [130]. Exploiting the enhancement of light provided by resonant cavities together with a mechanical microresonator, semi-integrated QEPAS sensor performances can be comparable with those obtained in state-of-art QEPAS sensor. The integration of a laser source on Silicon chips is today possible thanks to bonding processes [163]. Therefore, the possibility of integrating all the optical components of a QEPAS system on a Silicon chip, apart from the QTF, could represent a promising alternative. Due to some limitations of integrated waveguides, such as a small confinement factor on cladding [164], it is not easy to achieve performances comparable to the state-of-art QEPAS. Thus, a feasibility study on semi-integrated versions of QEPAS setups will be presented in this section and supported by numerical simulation in COMSOL Multiphysics.

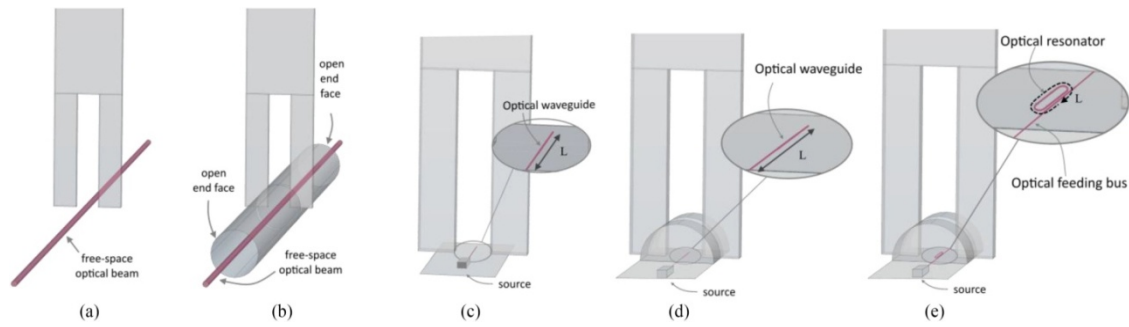


**Figure 4.1** Different configurations of QEPAS setups analyzed in this work. FS-QEPAS **(a)** is a simple QEPAS configuration without any mechanical resonator. MR-QEPAS **(b)** is a free space configuration with a mechanical resonator. SI-QEPAS **(c)** is a semi-integrated version of QEPAS without mechanical resonators. MRSI-QEPAS **(d)** is a semi-integrated version of QEPAS with a mechanical resonator. OMRSI-QEPAS **(e)** is a semi-integrated version of QEPAS with a mechanical resonator and an optical resonator (fed by an optical bus) [165].

Five different configurations, schematically depicted in **Figure 4.1**, will be investigated and compared:

- FS-QEPAS (Free Space QEPAS): standard configuration without mechanical resonators
- MR-QEPAS (Mechanical Resonator QEPAS): a free space configuration using a mechanical microresonator to enhance the pressure signal (state-of-art)
- SI-QEPAS (Semi-Integrated QEPAS): semi-integrated version without mechanical resonators
- MRSI-QEPAS: (Mechanical Resonator, Semi-Integrated QEPAS): semi-integrated version with a mechanical resonator
- OMRSI-QEPAS: (Optical and Mechanical Resonators, Semi- Integrated QEPAS): semi-integrated version with a mechanical resonator and an optical resonator

#### 4.1.1 Modeling and Design of a Semi-Integrated QEPAS Sensor

In photoacoustic spectroscopy, as well as in QEPAS, the signal  $S$  obtained from the acoustic-electrical transducer, i.e. the microphone or the tuning fork, is proportional to the

absorption coefficient  $\alpha$  of the gas sample, the radiation-to-sound conversion efficiency  $\varepsilon$ , the QTF quality factor  $Q$  and the optical power  $P$  available from the laser source [14]:

$$S \approx \alpha Q P \varepsilon \quad \text{Eq. 4.1}$$

In order to design a semi-integrated version of the QEPAS sensor with performances comparable with the standard QEPAS systems, we initially try to model the sound wave generated by photoacoustic effect starting from the fraction of optical power interacting with the target gas. The light absorbed by the gas is converted into a heat source ( $H$ ) proportional to the absorbed optical intensity  $I$  [166]

$$H(\vec{r}, t) = \alpha I(\vec{r}, t) \quad \text{Eq. 4.2}$$

where  $\alpha$  is the power absorption coefficient per unit length. The generated heat  $H$  and the consequent energy relaxation gives rise to acoustic waves. The Helmholtz equation in the harmonic regime can be written as follows [167]:

$$\left( \nabla^2 + \frac{\omega^2}{v^2} \right) p(\vec{r}, \omega) = -\frac{\gamma - 1}{v^2} j \omega H(\vec{r}, \omega) \quad \text{Eq. 4.3}$$

where  $p$  is the local pressure,  $v$  is the local speed of sound,  $\gamma$  is the ratio between the specific heat at constant volume ( $C_V$ ) and the specific heat at constant pressure ( $C_P$ ) and  $\omega$  is the angular frequency of the laser excitation. The solutions of the wave equations are determined by the boundary conditions. In particular, the solution  $p$  can be expressed as an expansion over the modes  $p_j$  with amplitudes  $A_j$  [167]:

$$p(\vec{r}, \omega) = \sum p_i(\vec{r}) A_i(\omega) \quad \text{Eq. 4.4}$$

It can be found that under rigid-walls boundary conditions (good approximation for the boundary condition of microresonators) [167]:

$$A_i(\omega) = \frac{-j\omega^2 [(\gamma - 1)/V_c] \int p_i^* H dV}{\omega_i \left( 1 - \frac{\omega^2}{\omega_i^2} - j \frac{\omega}{\omega_i Q_i} \right)} \quad \text{Eq. 4.5}$$

where  $\omega_j$  is the resonance angular frequency of the  $j$ -th mechanical resonant mode,  $Q_j$  is the quality factor of the  $j$ -th mode,  $V_c$  is the volume defined by the boundary conditions. By approximating  $H$  as a two-dimensional Dirac-delta input for the Helmholtz equation (possible if the linear dimensions of the cross-section of the beam are much smaller than

the acoustic wavelength) and by considering  $z$  the direction of propagation of the light beam we obtain:

$$H(\vec{r}, t) = \alpha P_{gas} \delta(x, y) \quad \text{Eq. 4.6}$$

with  $P_{gas}$  the fraction of the optical power interacting with the target gas. Thus, Eq. 4.5 becomes:

$$A_i(\omega) = \frac{-j\omega^2 \left[ \frac{(\gamma-1)}{S_C} \right] p_i^*(0,0,z) \alpha P_{gas}}{\omega_i \left( 1 - \frac{\omega^2}{\omega_i^2} - j \frac{\omega}{\omega_i Q_i} \right)} \quad \text{Eq. 4.7}$$

with  $S_C$  the area of the cross section delimited by the boundary conditions. Using Eq. 4.4:

$$p(\vec{r}, \omega) = \sum p_i A_i = \alpha P_{gas} \sum \frac{-j\omega^2 \left[ \frac{(\gamma-1)}{S_C} \right] p_i^*(0,0,z)}{\omega_i \left( 1 - \frac{\omega^2}{\omega_i^2} - j \frac{\omega}{\omega_i Q_i} \right)} p_i(\vec{r}) \quad \text{Eq. 4.8}$$

So, we obtained that the amplitude of the pressure, and thus the QTF signal is proportional to the optical power interacting with the target gas ( $P_{gas}$ ).

In free space, all the power of the laser interacts with air, whereas in integrated optical devices, the light is guided into a medium, thus, only a small fraction of the power propagates outside the guide as an evanescent wave and interacts with the gas. The air confinement factor ( $\Gamma_{gas}$ ) is defined as the fraction of the power propagating in air ( $P_{gas}$ ) divided by the total power propagating through the waveguide ( $P_P$ ):

$$\Gamma_{gas} = \frac{\int_{gas} S_z d\bar{S}}{\int_{total} S_z d\bar{S}} = \frac{P_{gas}}{P_P} \quad \text{Eq. 4.9}$$

with  $S_z$  the Poynting vector along the direction of propagation  $z$ .

It means that with the same amount of power consumption and under the same boundary conditions, the pressure amplitude  $p$  of the sound wave, photoacoustically generated by the evanescent wave in waveguide-based structure, is  $\Gamma_{gas}$  times lower than the wavefront pressure generated in free space.

**Figure 4.2(b)** shows  $\Gamma_{gas}$  as a function of the width  $W$  of a Silicon waveguide (for a standard waveguide height of 500 nm) for a propagating radiation with a wavelength  $\lambda = 3345$  nm, useful for detecting methane and ethane in the mid-IR region [134]. As it can be

seen, the maximum achievable confinement factor is around 18% for this kind of strip waveguides (**Figure 4.2(b)**).

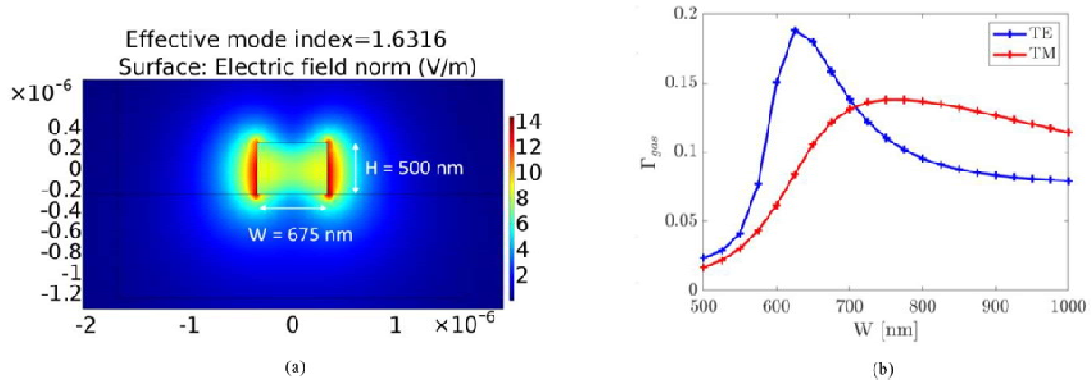


**Figure 4.2** Light mode in waveguide-based structure for a waveguide width  $W = 600 \text{ nm}$  and height  $H = 500 \text{ nm}$  (a) and Confinement Factor  $\Gamma_{\text{gas}}$  for different values of the widths of the waveguide (with  $H = 500 \text{ nm}$ ) for TE and TM modes (b) [165].

We considered that the dominant source of loss for this waveguide is due to the bulk loss in  $\text{SiO}_2$  (10 dB/cm at a wavelength of  $3.345 \mu\text{m}$  [168]). Consequently, the optimal waveguide design for this application is a trade-off between the fraction of evanescent power in air ( $\Gamma_{\text{gas}}$ ) and the total loss of the waveguide. We chose a width of 675 nm, for which the fraction of power in  $\text{SiO}_2$  is 27%, meaning a total propagation loss of 2.7 dB/cm (propagation loss in Silicon is negligible). **Figure 4.2(a)** shows the designed waveguide (500 nm x 675 nm) and the chosen mode (TE) that will be used for all the integrated configurations in the next sections.

#### 4.1.2 Performance comparison: FS-QEPAS vs SI-QEPAS

The key idea of this paper is to demonstrate that a semi-integrated configuration of a QEPAS setup can potentially replace the standard free-space configuration making the space occupation much lower and eliminating any optical alignment issue. As a first step, we simulated the photoacoustic generation when a free-space laser beam propagates between the prongs of a bare QTF (FS-QEPAS, **Figure 4.1(a)**), which represents a non-interactive element in the following analysis. Then, we compared the FS-QEPAS model with a similar structure exploiting an integrated waveguide on a Silicon chip (SI-QEPAS, **Figure 4.1(c)**). We performed the fully mechanical simulations by implementing the Helmholtz equation (**Eq. 4.3**) on the “Pressure Acoustic, Frequency Domain” module of

COMSOL Multiphysics, with the heat source  $H$  obtained by combining **Eq. 4.6** and **Eq. 4.9**. The wavelength selected is resonant with an optical transition related to the C-H bond stretching of methane at  $2989\text{ cm}^{-1}$  ( $3345\text{ nm}$ ) and having an absorption coefficient of  $\alpha\ 12\text{ cm}^{-1}$  at a pressure of 1 atm and a temperature of 296 K [78].

The QTF selected as a reference to model the non-interacting probe in our design is a tuning fork having a resonance frequency of 15.8 kHz, a prong thickness of  $250\ \mu\text{m}$ , a prong spacing of  $800\ \mu\text{m}$  and thus slightly different from the one investigated in [94], which has an enlarged prong spacing of 1.5 mm. The other dimensions of the QTF have no influence on the simulations because the prong internal surfaces were treated as hard wall boundary conditions. We used an implementation of Helmholtz equation in COMSOL Multiphysics to simulate the pressure signal generated from a heat source located between the free ends of the QTF. In fact, the QTF is aligned so that the light beam propagates perpendicular to the QTF plane and exactly centered between the top of the prongs, where the vibrational antinode is theoretically expected [10]. In the FS-QEPAS case, the light beam has been simulated with an equivalent  $100\ \mu\text{m}$  radius uniform power beam, whereas in the SI-QEPAS case, the light propagates into a waveguide on the surface of an integrated chip (TE mode of a  $675\text{ nm} \times 500\text{ nm}$  Silicon strip waveguide in **Figure 4.2(a)**) and has been simulated with an equivalent  $0.5\ \mu\text{m}$ -radius uniform beam with equivalent power equal to  $P_P\Gamma_{\text{gas}}$ . The length of the waveguide has been varied between  $400\ \mu\text{m}$  and 1 mm. For these lengths, the propagation losses due to  $\text{SiO}_2$  have not been accounted into simulation, because negligible. In both cases a total input power  $P_P = 1\text{ mW}$  was considered. **Figure 4.3(a)** shows the pressure signal in static conditions (for non-vibrating prongs) for a waveguide length  $L$  of 1 mm.

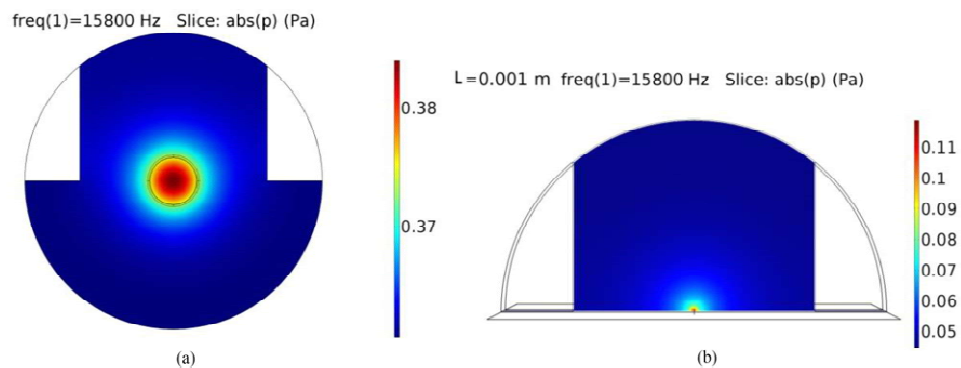


**Figure 4.3** Acoustic pressure field, with optical power of 1mW without resonators in FS-QEPAS configuration **(a)** and SI-QEPAS configuration **(b)** [165].

It is easy to appreciate that for the SI-QEPAS configuration, the pressure signal in the proximity of the prongs is almost one order of magnitude lower than in FS-QEPAS case.

### 4.1.3 Performances comparison with microresonators: MR-QEPAS vs MRSI-QEPAS

The employment of acoustic resonator tubes has been widely exploited in literature and in sensor prototypes to increase the SNR of the piezoelectric signal. In the on-beam configuration, a pair of tubes are aligned perpendicular to the QTF plane, with the tube axes at the same height of the fundamental vibration mode antinode and at a distance from the QTF typically of several tens of micron [19]. Thus, when the modulated laser radiation propagates through the dual tube system, a standing sound wave is photoacoustically generated, with its pressure peak occurring at the vibrational antinode between the prongs. The schematic of the dual tube on-beam configuration, here referred as MR-QEPAS, is shown in **Figure 4.1(b)**. acting as a micromechanical resonator enhancing the pressure of the photoacoustic sound wave. This is the most used QEPAS configuration [19]. The MR-QEPAS simulated for this investigation is composed of a cylindrical microresonator open at its end faces. The distance between the internal edges of the tubes was set to 310  $\mu\text{m}$  to accommodate a QTF for sensing the pressure variations. Each tube is 10.3 mm long, with an inner diameter of 1.27 mm. These tube dimensions demonstrated to provide the highest SNR when acoustically coupled with a 15 kHz custom QTF [94].

The MR-QEPAS was then compared to a SI-QEPAS configuration in which a closed micromechanical resonator was added in order to obtain a further enhancement of the pressure in the proximity of the QTF prongs. The micromechanical resonator is made up of a closed semi-cylinder with a central gap where the QTF is located. If the laser radiation is delivered through the micro mechanical resonator by means of a feeding bus, the light can be coupled again to the waveguide so that the  $\Gamma_{\text{gas}}$  portion of the input power can interact with the target gas over a length L (**Figure 4.1(d)**, MRSI-QEPAS). The size of the gap at the center of the microresonator is the same as in the MR-QEPAS). The inner diameter of the semicylindrical resonator is 1.27 mm and the total microresonator length is 2 mm. We simulated and compared the pressure signal per input power obtained at the base of the QTF prongs between the MR-QEPAS and the semi-integrated version MRSI-QEPAS. The light beams were simulated as indicated in the previous paragraph. The colormaps in

**Figure 4.4(a)** and **(b)** show the pressure signal for input power of 1 mW on the central cross-section for both the configurations (with  $L = 1\text{mm}$  in the MRSI-QEPAS case).

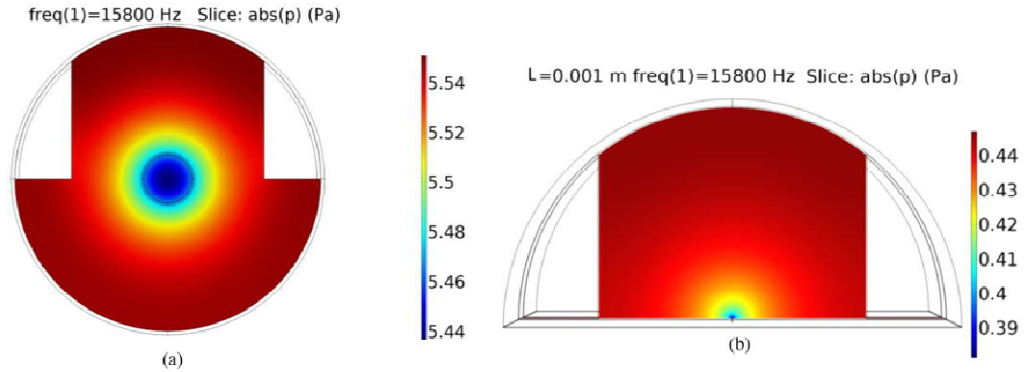


**Figure 4.4** Acoustic pressure field, with optical power of 1mW without resonators in the MRQEPAS configuration **(a)** and MRSI-QEPAS configuration **(b)** [165].

In the case of MRSI-QEPAS, since the system is closed, all the optical power absorbed should be converted into a pressure signal. Through an energetic approach it is possible to find the dependence of the pressure signal on the length of the absorption path in the MRSI-QEPAS (approximation of closed system). In particular, when considering an optical mode propagating in an integrated waveguide, the fraction ( $P_{abs,int}$ ) of the total power propagating in the waveguide ( $P_p$ ) that has been absorbed by the target gas over a length  $L$  (in the hypothesis of small absorption) is [169]:

$$P_{abs,int} \approx P_p \Gamma_{gas} \alpha L. \quad \text{Eq. 4.10}$$

Consequently, in MRSI-QEPAS we expect  $p$  to be proportional to the length of absorption  $L$ . The simulation results confirm that the pressure amplitude per input power varies linearly with the absorption length. As it is possible to see in **Figure 4.5**, the pressure signal obtained in MRSI-QEPAS is one order of magnitude lower than in the MR-QEPAS.

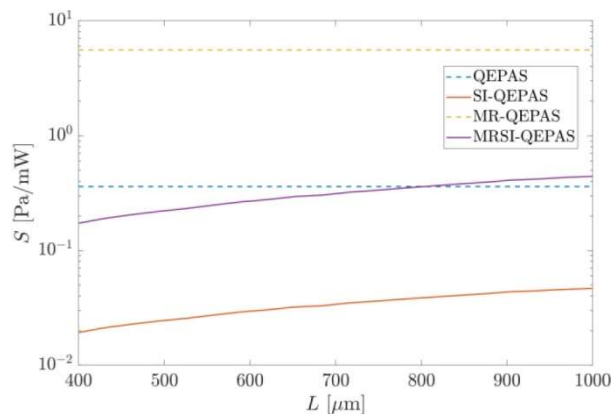


**Figure 4.5** Pressure signal per input power (S) as a function of the length of the waveguide in the SI-QEPAS and MRSI-QEPAS compared to the pressure signal per input power in QEPAS and MR-QEPAS [165].

However, the guidance of the laser light can be further and more effectively exploited by implementing an optical resonant cavity to be directly coupled with the waveguide modeled and simulated in SI-QEPAS and MRSI-QEPAS configurations.

#### 4.1.4 Optical resonant enhancement: OMRSI-QEPAS

The results of the previous paragraphs showed that the integrated solutions (SI-QEPAS and MRSI-QEPAS) produce a pressure signal one order of magnitude lower than the corresponding free space configurations (QEPAS and MR-QEPAS).

In order to achieve better performances in terms of signal amplitude with a semi-integrated setup, we propose to implement an optical-resonant-cavity architecture in the MRSI-QEPAS, with the aim of increasing the optical power interacting with the gas target starting from the same input power simulated in the previous configurations. The modification to the MRSI-QEPAS setup is shown in **Figure 4.1(e)**. It is possible to see that an optical resonator is fed by an optical bus. The racetrack resonator is designed to have a total length  $L$  and a gap between the two long-side waveguide of  $80 \mu\text{m}$  (bend radius of  $40 \mu\text{m}$ ).

It is easy to demonstrate that the enhancement factor  $E_F$ , calculated as the ratio between the power circulating into a section of the cavity ( $P_{cav}$ ) (modulated at the resonance frequency of the tuning fork) and the input power within the feeding bus ( $P_P$ ) is [170]:

$$E_F = \frac{P_{cav}}{P_P} = \frac{e^{-\alpha_{wg}L}k^2}{\left(1 - e^{-\frac{\alpha_{wg}}{2}L\sqrt{1-k^2}}\right)^2} \approx \frac{4k^2}{\left(\alpha_{wg}L + k^2\right)^2} \quad \text{Eq. 4.11}$$

with  $\kappa^2$  the non-dimensional power coupling efficiency between a feeding waveguide and the resonator.

In order to estimate the enhancement factor, we considered the propagation loss already estimated (2.7 dB/cm) and bend losses. We estimated the bend losses by evaluating the superposition of the optical mode in the straight waveguide and in the bent waveguide (equal to 99.6%, with a curvature radius of  $40 \mu\text{m}$ ).

$$BL = -4_{interfaces} 10\log_{10}(0.9966) = 0.013 \text{ dB} \quad \text{Eq. 4.12}$$

We obtained a bend loss around 0.013 dB per roundtrip (0.013dB/L, with L the length of the resonator). So,  $\alpha_{wg} = 2.7 \text{ dB/cm} + 0.013 \text{ dB/L}$ . The parameters of the final designed resonator are summarized in **Table 4.1**.

**Table 4.1** Parameters of the optical resonator [165].

Parameter	Symbol	Value
Cavity length	L	1000.63 $\mu\text{m}$
Order of resonance	m	488
Resonance wavelength	$\lambda_0$	3.34555 $\mu\text{m}$
Q-factor	Q	19749
Finesse	F	40.5
Free spectral range (FSR)	FSR	6.86 nm

**Figure 4.6** shows the enhancement factor as a function of the coupling efficiency and the length L of the resonator.

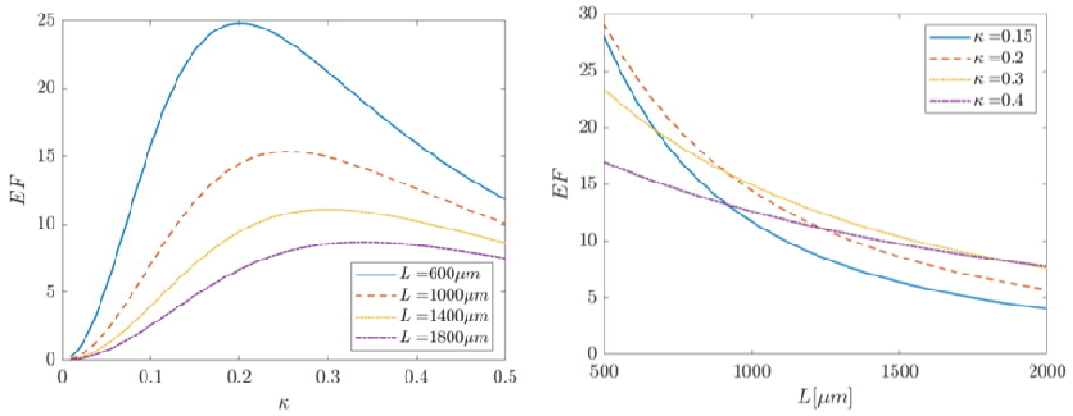


**Figure 4.6** Enhancement factor as a function of  $\kappa$  for different values of L(a) and enhancement factor as a function of L for different values of  $\kappa$ , with estimated loss  $\alpha_{wg} = 0.69 \text{ dB/cm}$  [165].

By properly designing the distance  $d_{gap}$  between the feeding bus and the resonator, the power coupling efficiency  $\kappa^2$  can be calculated and engineered through the following expression (valid for straight couplers) [171]:

$$k^2 = \sin^2 \left( \frac{\pi L_{cp} \Delta n(d_{gap})}{\lambda} \right) \quad \text{Eq. 4.13}$$

Here  $\Delta n(d_{gap})$  is the difference between the effective indices of the even and the odd modes in the coupling region, where the evanescent coupling between feeding bus and resonator takes place.  $L_{cp}$  is the length of the coupling region and  $\lambda$  is the wavelength of input light. **Figure 4.7(a)** shows the pressure amplitude at a central cross section obtained for an optical resonator with a length of  $L = 1$  mm in an OMRSI-QEPAS configuration. **Figure 4.7(b)** shows the performance of the OMRSI-QEPAS as a function of  $L$  at different values of  $\kappa$ , compared with the pressure value obtained with MR-QEPAS.

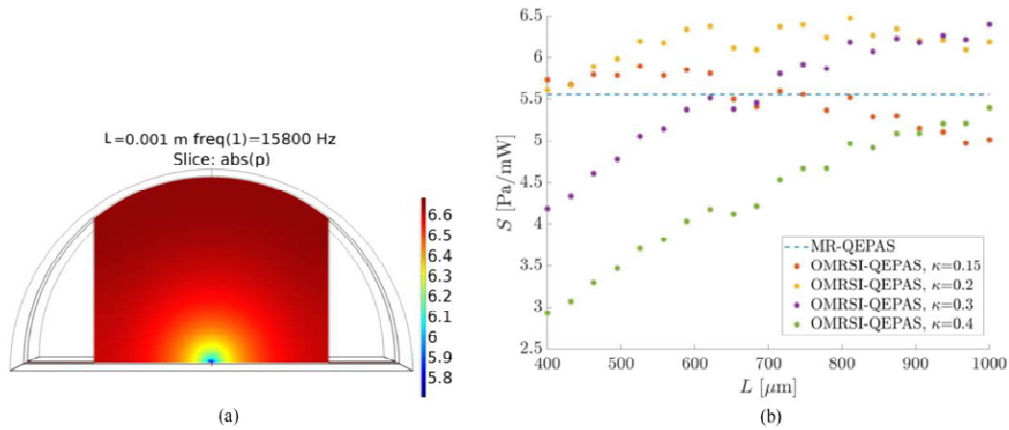


**Fig. 4.7** Pressure signal per input power ( $S$ ) over a central cross section in OMRSI-QEPAS **(a)** and Pressure signal per input power ( $S$ ) as a function of the length of the waveguide in OMRSI-QEPAS, compared with MR-QEPAS **(b)** [165].

As it can be easily argued from the figure, in an OMRSI-QEPAS configuration comparable or higher-pressure values for the sound wavefront can be achieved with respect to a standard MR-QEPAS approach. **Table 4.2** summarizes the peak pressure signals obtained for each simulated configuration.

**Table 4.2** Comparison of signal amplitude for different configurations [165].

Configuration	Peak pressure (Pa)
SI-QEPAS (1-mm source)	0.047
FS-QEPAS	0.361
MRSI-QEPAS (1-mm source)	0.443
MR-QEPAS	5.55
OMRSI-QEPAS (1-mm source, $k = 0.3$ )	6.396

The obtained results demonstrate that an integrated configuration of QEPAS (in particular the OMRSI-QEPAS) can exceed the performances of the state-of-art QEPAS

configurations. The use of optical enhancement can overcome the problem of a low air confinement factor thanks to the use of optical resonators.

**Figure 4.8** shows the final configuration of the OMRSI-QEPAS setup.

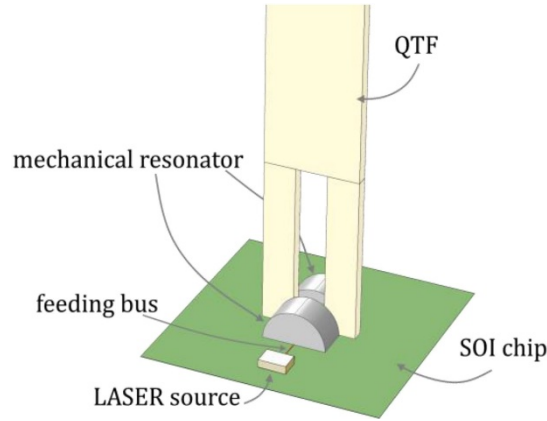


**Figure 4.8** Final configuration of the OMRSI-QEPAS setup [165].

Thanks to the possibility of bonding an external laser to a SOI chip, it is possible to feed the optical resonator through a feeding optical bus entering the mechanical resonator. The laser source should be placed sufficiently distant from the mechanical resonator and the QTF to guarantee an effective heat dissipation/cooling and avoid that temperature gradients in the gas affect the photoacoustic generation and response.

As for the fabrication process, the initial step would be to etch the waveguides and the resonator on a standard Si/SiO<sub>2</sub> chip (500 nm of Silicon layer). Then, the external laser would be bonded upon the SOI chip, which can be mounted inside an HHL-like package. As for the mechanical resonator, the simplest approach would be to mechanically bond it to the SOI chip. Finally, the QTF would be connected from the base to the upper enclosure of the packaging and then coupled with the ring resonator upside down. We want to underline that the approach we propose can be extended to other platforms different from Si/SiO<sub>2</sub> (for example on InP platform) where it can be possible to monolithically grow the laser upon the chip.

## Conclusions and perspectives

The aim of this thesis was the improvement and implementation of state-of-art Quartz Enhanced Photoacoustic Spectroscopy (QEPAS) for gas sensing in real world applications. The main merits of the QEPAS sensors consists in high compactness and robustness, high sensitivity, wide concentration detection range (from ppt to %), real-time and in-situ operations and possibility to perform multiple gas simultaneous detection. All these characteristics, together with the design and the optimization of custom Quartz Tuning Forks (QTFs) for gas sensing applications, pave the way to the commercialization of QEPAS sensors. The design of a voltage front-end amplifier demonstrates a further enhancement of QEPAS sensors performance, in terms of SNR. The study, modeling and measurements of the mechanical and resonance properties of QTFs provided the design rules for optimizing the resonator characteristics with respect to the requirements of the final application. These results triggered the interest in studying and modeling the electrical properties of these innovative transducers. These new studies will bring to the design of an Application Specific Integrated Circuit (ASIC), capable of reaching further better QEPAS sensor performances.

Thanks to the use of custom QTFs and their capability of being excited at the first two flexural modes, two laser sources were focused at the fundamental and overtone mode antinodes of a 2.8 kHz custom resonator. This sensor demonstrates the possibility of simultaneously detecting methane or nitrous oxide and water vapor in a mixture, without any interference between the two vibrational modes. The monitoring of water vapor and other gas traces is fundamental in air quality monitoring. In this perspective, the second QEPAS sensor presented in this thesis work was designed for methane trace gas detection employing an interband cascade laser, a 12kHz T-shaped QTF and an electronic hygrometer for signal compensation. The same QTF was used in the SF<sub>6</sub> QEPAS sensor, designed for testing the sealing of mechanical components.

Several solutions demonstrated the possibility to detect multiple gas species in mixture. Two laser diodes were employed to independently detect methane and ethane gas traces, methane isotopes were independently detected using a QCL and a T-shaped QTF operated at low pressure. A single interband cascade laser was employed for detecting methane, ethane and propane, which exhibit overlapping absorption features within the ICL tuning range. The possibility of performing multigas detection by using only one laser source is

crucial for minimizing the overall cost of the sensors, the space occupation and the power consumptions. Multigas detection was also achieved using an innovative array of QCLs. The tuning range of this device allowed methane and nitrous oxide to be detected. Higher accuracy of the detected concentration can be achieved employing PLSR to analyze QEPAS signals of gas mixtures containing two or more components. The same method was demonstrated to be effective when employed to retrieve concentrations of a mixture composed of methane and ethane at high concentrations. Starting from these results, state-of-art Artificial Intelligence (AI) algorithm will be compared to the PLSR method to improve the detection accuracy of QEPAS sensors.

Finally, a Semi-Integrated version of a QEPAS sensor is proposed. This configuration aims at improving robustness and compactness of the final sensor. This solution open the way at the integration on the same wafer of both light guiding systems and read-out electronics.

## Bibliography

- [1] Earth System Research Laboratory. Global Monitoring Division. Available online: [https://esrl.noaa.gov/gmd/ccgg/trends\\_ch4](https://esrl.noaa.gov/gmd/ccgg/trends_ch4) (accessed on **21 March 2021**).
- [2] J. Seinfeld, S. Pandis, Atmospheric Chemistry and Physics: From Air Pollution to Climate Change. *John Wiley & Sons*, **2006**.
- [3] C.W. Moore, B. Zielinska, G. Pétron, R.B. Jackson, *Environ. Sci. Technol.*, **2014**, 48, 8349–8359.
- [4] D.T. Allen, V.M. Torres, J. Thomas, D.W. Sullivan, M. Harrison, A. Hendler, S.C. Herndon, C.E. Kolb, M.P. Fraser, A.D. Hill, B. K. Lamb, J. Miskimins, R. F. Sawyer, J. H. Seinfeld, *Proc. Natl. Acad. Sci. USA*, **2013**, 110, 17768–17773.
- [5] J. Aali, H. Rahimpour-Bonab, M. Reza Kamali, *J. Petrol. Sci. Eng.*, **2006**, 50 (3–4) 161.
- [6] Department of Health and Human Services, NIOSH *Pocket Guide to Chemical Hazards*, National Institute for Occupational Safety and Health, **2007**.
- [7] Toxicological Review of Hydrogen Sulfide, US Environmental Protection Agency, *Support of Summary Information on the Integrated Risk Information System (IRIS)*, **2003**.
- [8] J.G. Speight, The Chemistry and Technology of Petroleum, CRC Press, **2014**, Boca Raton.
- [9] J. Hodgkinson, R. P. Tatam, *Meas. Sci. Technol.*, **2013**, 24, 012004.
- [10] P. Patimisco, G. Scamarcio, F. K. Tittel, V. Spagnolo, *Sensors*, **2014**, 14, 6165.
- [11] G. Eranna, B. C. Joshi, D. P. Runthala, R. P. Gupta, *Crit. Rev. Solid State Mater. Sci.*, **2004** 29, 111–188.
- [12] D. Kohl, *J. Phys. D: Appl. Phys*, **2001**, 34, R125–R149.
- [13] C. Wang, L. Yin, L. Zhang, D. Xiang, R. Gao, *Sensors*, **2010**, 10, 2088–2106.
- [14] P. Patimisco, A. Sampaolo, L Dong, F. K. Tittel, Vincenzo Spagnolo, *Applied Physics Reviews*, **2018**, 5, 011106.
- [15] A. Elia, P.M. Lugarà, C. Di Franco, V. Spagnolo, *Sensors*, **2009**, 9, 9616-9628.
- [16] W. H. Flygare, *Acc. Chem. Res.*, **1968**, 1, 4, 121–127.
- [17] A. A. Kosterev; Yu. A. Bakhirkin; R. F. Curl; F. K. Tittel; *Opt. Lett.*, **2002**, 27, 1902-1904.

- [18] A. A. Kosterev, F. K. Tittel, D. Serebryakov, A. Malinovsky, A. Morozov; *Rev. Sci. Instrum.*, **2005**, 76, 043105.
- [19] L. Dong, A. A. Kosterev, D. Thomazy, F. K. Tittel, *Appl. Phys. B*, **2010**, 100, 627–635.
- [20] M. Jahjah, S. Belahsene, L. Nahle, M. Fischer, J. Koeth, Y. Rouillard, A. Vicet, *Opt. Lett.*, **2012**, 37, 2502–2504.
- [21] V. Spagnolo, P. Patimisco, S. Borri, G. Scamarcio, B. E. Bernacki, J. Kriesel, *Opt. Lett.*, **2012**, 37, 4461–4463.
- [22] T. N. Ba, M. Triki, G. Desbrosses, A. Vicet, *Rev. Sci. Instrum.*, **2015**, 86, 023111.
- [23] K. Liu, X. Guo, H. Yi, W. Chen, W. Zhang, X. Gao, *Opt. Lett.*, **2009**, 34, 1594–1596.
- [24] S. Böttger, M. Köhring, U. Willer, W. Schade, *Appl. Phys. B*, **2013**, 113, 227–232.
- [25] J. P. Waclawek, H. Moser, B. Lendl, *Opt. Express*, **2016**, 24, 6559–6571.
- [26] M. Lassen, L. Lamard, Y. Feng, A. Peremans, J. C. Petersen, *Opt. Lett.*, **2016**, 41, 4118–4121.
- [27] H. Yi, K. Liu, W. Chen, T. Tan, L. Wang, X. Gao, *Opt. Lett.*, **2011**, 36, 481–483.
- [28] K. Liu, H. Yi, A. A. Kosterev, W. Chen, L. Dong, L. Wang, T. Tan, W. Zhang, F. K. Tittel, X. Gao, *Rev. Sci. Instrum.*, **2010**, 81, 103103.
- [29] Z. Wang, Q. Wang, J. Y. L. Ching, J. C. Y. Wu, G. Zhang, W. Ren, *Sens. Actuators, B*, **2017**, 246, 710–715.
- [30] V. Spagnolo, A. A. Kosterev, L. Dong, R. Lewicki, F. K. Tittel, *Appl. Phys. B*, **2010**, 100, 125–130.
- [31] L. Dong, V. Spagnolo, R. Lewicki, F. K. Tittel, *Opt. Express*, **2011**, 19, 24037–24045.
- [32] [https://www.thorlabs.com/newgrouppage9.cfm?objectgroup\\_id=11241](https://www.thorlabs.com/newgrouppage9.cfm?objectgroup_id=11241) (accessed on 21 March 2021).
- [33] R. Lewicki, G. Wysocki, A. A. Kosterev, F. K. Tittel, *Opt. Express*, **2007**, 15, 7357–7366.
- [34] A. A. Kosterev, P. R. Buerki, L. Dong, M. Reed, T. Day, F. K. Tittel, *Appl. Phys. B*, **2010**, 100, 173–180.
- [35] P. Patimisco, A. Sampaolo, Y. Bidaux, A. Bismuto, M. Schott, J. Jiang, A. Muller, J. Faist, F. K. Tittel, V. Spagnolo, *Opt. Express*, **2016**, 24, 25943–25954.
- [36] P. Patimisco, V. Spagnolo, M. S. Vitiello, A. Tredicucci, G. Scamarcio, C. M.

- Bledt, J. A. Harrington, *Appl. Phys. B*, **2012**, 108, 255–260.
- [37] P. Patimisco, V. Spagnolo, M. S. Vitiello, A. Tredicucci, G. Scamarcio, C. M. Bledt, J. A. Harrington, *Sensors*, **2013**, 13, 1329–1340.
- [38] A. Sampaolo, P. Patimisco, J. M. Kriesel, F. K. Tittel, G. Scamarcio, and V. Spagnolo, *Opt. Express*, **2015**, 23, 195–204.
- [39] P. Patimisco, A. Sampaolo, L. Mihai, M. Giglio, J. Kriesel, D. Sporea, G. Scamarcio, F. K. Tittel, V. Spagnolo, *Sensors*, **2016**, 16, 533.
- [40] N. Hô, M. C. Phillips, H. Qiao, P. J. Allen, K. Krishnaswami, B. J. Riley, T. L. Myers, N. C. Anheier, *Opt. Lett.*, **2006**, 31, 1860–1862.
- [41] C. Tsay, Y. Zha, C. B. Arnold, *Opt. Express*, **2010**, 18, 26744–26753.
- [42] C. Caillaud, G. Renversez, L. Brilland, D. Mechin, L. Calvez, J.-L. Adam, J. Troles, *Materials*, **2014**, 7(9), 6120–6129.
- [43] V. Spagnolo, P. Patimisco, S. Borri, G. Scamarcio, B. E. Bernacki, J. Kriesel, *Appl. Phys. B*, **2013**, 112, 25–33.
- [44] M. Siciliani de Cumis, S. Viciani, S. Borri, P. Patimisco, A. Sampaolo, G. Scamarcio, P. De Natale, F. D’Amato, V. Spagnolo, *Opt. Express*, **2014**, 22(23), 28222–28231.
- [45] M. Köhring, U. Willer, S. Böttger, A. Pohlkötter, W. Schade, *IEEE J. Sel. Top. Quantum Electron.*, **2012**, 18, 1566–1572.
- [46] Y. Ma, G. Yu, J. Zhang, X. Yu, R. Sun, *J. Opt.*, **2015**, 17, 055401.
- [47] Y. Cao, W. Jin, L. H. Ho, Z. Liu, *Opt. Lett.*, **2012**, 37, 214–216.
- [48] Z. Li, Z. Wang, C. Wang, W. Ren, *Appl. Phys. B*, **2016**, 122, 147.
- [49] Z. Li, Z. Wang, Y. Qi, W. Jin, W. Ren, *Sens. Actuators, B*, **2017**, 248, 1023–1028.
- [50] S. Borri, P. Patimisco, I. Galli, D. Mazzotti, G. Giusfredi, N. Akikusa, M. Yamanishi, G. Scamarcio, P. De Natale, V. Spagnolo, *Appl. Phys. Lett.*, **2014**, 104, 091114.
- [51] P. Patimisco, S. Borri, I. Galli, D. Mazzotti, G. Giusfredi, N. Akikusa, M. Yamanishi, G. Scamarcio, P. De Natale, V. Spagnolo, *Analyst*, **2015**, 140, 736–743.
- [52] J. Wojtas, A. Gluszek, A. Hudzikowski, F. K. Tittel, *Sensors*, **2017**, 17, 513.
- [53] P. Patimisco, A. Sampaolo, F. K. Tittel, V. Spagnolo, *Sens. Actuators, A*, **2017**, 267, 70–75.
- [54] N. Petra, J. Zweck, A. A. Kosterev, S. E. Minkoff, D. Thomazy, *Appl. Phys. B*,

- 2009, 94, 673–680.
- [55] H. Wu, L. Dong, W. Ren, W. Yin, W. Ma, L. Zhang, S. Jia, F. K. Tittel, *Sens. Actuators, B*, **2015**, 206, 364–370.
- [56] L. Dong, H. Wu, H. Zheng, Y. Liu, X. Liu, W. Jiang, L. Zhang, W. Ma, W. Ren, W. Yin, S. Jia, F. K. Tittel, *Opt. Lett.*, **2014**, 39, 2479–2482.
- [57] V. Spagnolo, L. Dong, A. A. Kosterev, D. Thomazy, J. Doty, F. K. Tittel, *Opt. Lett.*, **2011**, 36, 460–462.
- [58] V. Spagnolo, L. Dong, A. A. Kosterev, D. Thomazy, J. Doty, F. K. Tittel, *Appl. Phys. B*, **2011**, 103, 735–742.
- [59] V. Spagnolo, L. Dong, A. A. Kosterev, F. K. Tittel, *Opt. Express*, **2012**, 20, 3401–3407.
- [60] Y. Ma, X. Yu, G. Yu, X. Li, J. Zhang, D. Chen, R. Sun, F. K. Tittel, *Appl. Phys. Lett.*, **2015**, 107, 021106.
- [61] H. Zheng, X. Yin, L. Dong, H. Wu, X. Liu, W. Ma, L. Zhang, W. Yin, S. Jia, *J. Spectrosc.*, **2015**, 218413.
- [62] W. Griffith, *J. Appl. Phys.*, **1950**, 21, 1319.
- [63] A. A. Kosterev, Y. A. Bakhirkin, R. F. Curl, F. K. Tittel, *Appl. Phys. B*, **2005**, 80, 133.
- [64] J. Li, W. Chen, B. Yu, *Appl. Spectrosc. Rev.*, **2011**, 46, 440–471.
- [65] F. R. Blom, S. Bouwstra, M. Elwenspoek, J. H. J. Fluitman, *J. Vac. Sci. Technol. B*, **1992**, 10, 19.
- [66] P. Patimisco, A. Sampaolo, L. Dong, M. Giglio, G. Scamarcio, F. K. Tittel, V. Spagnolo, *Sens. Actuators, B*, **2016**, 227, 539–546.
- [67] M. Hirata, K. Kokubun, M. Ono, K. Nakayama, *J. Vac. Sci. Technol. A*, **1985**, 3, 1742.
- [68] M. Christen, *Sens. Actuators*, **1983**, 4, 555–554.
- [69] W. Zhang, K. Turner, *Sens. Actuators, A*, **2007**, 134, 594–599.
- [70] P. Patimisco, A. Sampaolo, H. Zheng, L. Dong, F. K. Tittel, V. Spagnolo, *Adv. Phys. X*, **2016**, 2, 169–187.
- [71] X. Yin, L. Dong, H. Zheng, X. Liu, H. Wu, Y. Yang, W. Ma, L. Zhang, W. Yin, L. Xiao, S. Jia, *Sensors*, **2016**, 16, 162.
- [72] M. Mordmüller, M. Köhring, W. Schade, U. Willer, *Appl. Phys. B*, **2015**, 119, 111–118.

- [73] J. M. Friedt, É. Carry, *Am. J. Phys.*, **2007**, 75, 415.
- [74] A. Sampaolo, P. Patimisco, L. Dong, A. Geras, G. Scamarcio, T. Starecki, F. K. Tittel, V. Spagnolo, *Appl. Phys. Lett.*, **2015**, 107, 231102.
- [75] H. Hosaka, K. Itao, S. Kuroda, *Sens. Actuators, A*, **1995**, 49, 87–95.
- [76] R. R. Archer, N. H. Cook, S. H. Crandall, N. C. Dahl, F. A. McClintock, E. Rabinowicz, G. S. Reichenbach, *An Introduction to the Mechanics of Solids*, McGraw-Hill, New York, **1959**.
- [77] Z. Hao, A. Erbil, F. Ayazi, *Sens. Actuators, A*, **2003**, 109, 156.
- [78] L. S. Rothman, I. E. Gordon, Y. Babikov, A. Barbe, D. Chris Benner, P. F. Bernath, M. Birk, L. Bizzocchi, V. Boudon, L. R. Brown, A. Campargue, K. Chance, E. A. Cohen, L. H. Coudert, V. M. Devi, B. J. Drouin, A. Fayt, J. M. Flaud, R. R. Gamache, J. J. Harrison, J. M. Hartmann, C. Hill, J. T. Hodges, D. Jacquemart, A. Jolly, J. Lamouroux, R. J. Le Roy, G. Li, D. A. Long, O. M. Lyulin, C. J. Mackie, S. T. Massie, S. Mikhailenko, H. S. P. Muller, O. V. Naumenko, A. V. Nikitin, J. Orphal, V. Perevalov, A. Perrin, E. R. Polovtseva, C. Richard, M. A. H. Smith, E. Starikova, K. Sung, S. Tashkun, J. Tennyson, G. C. Toon, V. G. Tyuterev, G. Wagner, *J. Quant. Spectrosc. Radiat. Transf.*, **2013**, 130, 4–50.
- [79] H. Zheng, L. Dong, A. Sampaolo, H. Wu, P. Patimisco, X. Yin, W. Ma, L. Zhang, W. Yin, V. Spagnolo, S. Jia, F. K. Tittel, *Opt. Lett.*, **2016**, 41, 978–981.
- [80] S. Borri, P. Patimisco, A. Sampaolo, H. E. Beere, D. A. Ritchie, M. S. Vitiello, G. Scamarcio, V. Spagnolo, *Appl. Phys. Lett.*, **2013**, 103, 021105.
- [81] H. Zheng, L. Dong, A. Sampaolo, P. Patimisco, W. Ma, L. Zhang, W. Yin, L. Xiao, V. Spagnolo, S. Jia, F. K. Tittel, *Appl. Phys. Lett.*, **2016**, 109, 111103.
- [82] H. Zheng, L. Dong, P. Patimisco, H. Wu, A. Sampaolo, X. Yin, S. Li, W. Ma, L. Zhang, W. Yin, L. Xiao, V. Spagnolo, S. Jia, F. K. Tittel, *Appl. Phys. Lett.*, **2017**, 110, 021110.
- [83] H. Wu, X. Yin, L. Dong, K. Pei, A. Sampaolo, P. Patimisco, H. Zheng, W. Ma, L. Zhang, W. Yin, L. Xiao, V. Spagnolo, S. Jia, F. K. Tittel, *Appl. Phys. Lett.*, **2017**, 110, 121104.
- [84] Y. Ma, R. Lewicki, M. Razeghi, F. K. Tittel, *Opt. Express*, **2013**, 21, 1008–1019.
- [85] A.A. Kosterev, Y.A. Bakhirkin, F.K. Tittel, S. McWhorter, B. Ashcraft, *Appl. Phys. B Lasers Opt.*, **2008**, 92, 103–109.
- [86] V. Spagnolo, P. Patimisco, S. Borri, G. Scamarcio, B. E. Bernacki, J. Kriesel, *Opt.*

- Letters*, **2012**, 37, 21, 4461-4463.
- [87] A.A. Kosterev, Y.A. Bakhirkin, F.K. Tittel, *Appl. Phys. B Lasers Opt.*, **2005**, 80, 133–138.
- [88] S. Dello Russo, A. Sampaolo, P. Patimisco, G. Menduni, M. Giglio, C. Hoelzl, V.M.N. Passaro, H. Wu, L. Dong, V. Spagnolo, *Photoacoustics*, **2021**, 21, 100227.
- [89] P. Repond, M.W. Sigrist, *Appl. Opt.*, **1996**, 35, 4065.
- [90] G. Wysocki, A. A. Kosterev, F. K. Tittel, *Appl. Phys. B*, **2006**, 85, 301.
- [91] P. Patimisco, A. Sampaolo, M. Giglio, S. Dello Russo, V. Mackowiak, H. Rossmadl, A. Cable, F.K. Tittel, V. Spagnolo, *Opt. Express*, **2019**, 27, 1401–1415.
- [92] N. Ogawa, F. Kaneko, *Eur. J. Phys.*, **2013**, 34, 1159–1165.
- [93] H. Levine, J. Schwinger, *Phys. Rev.*, **1948**, 73, 383–406.
- [94] S. Dello Russo, M. Giglio, A. Sampaolo, P. Patimisco, G. Menduni, H. Wu, L. Dong, V.M.N. Passaro, V. Spagnolo, *Sensors*, **2019**, 19(19):4109.
- [95] P. Patimisco, A. Sampaolo, V. Mackowiak, H. Rossmadl, A. Cable, F.K. Tittel, V. Spagnolo, *IEEE T. Ultrason. Ferr.*, **2018**, 65, 1951–1957.
- [96] A. A. Kosterev, T. S. Mosely, F. K. Tittel, *Appl. Phys. B*, **2006**, 85, 295.
- [97] Y. Ma, Y. He, L. Zhang, X. Yu, J. Zhang, R. Sun, F. K. Tittel, *Appl. Phys. Lett.*, **2017**, 110, 031107.
- [98] M. Giglio, G. Menduni, P. Patimisco, A. Sampaolo, A. Elefante, V.M.N. Passaro, V. Spagnolo, *Phys. Status Solidi A*, **2019**, 216: 1800552.
- [99] D. M. Photiadis, D. J. Goldstein, J. M. Willey, *J. Appl. Phys.*, **2016**, 119, 064503.
- [100] Y.S. Shmaliy, *IEEE Trans. Ultrason. Ferroelectr. Freq. Control*, **2004**, 51, 25–32.
- [101] W. Liu, C. Tsai, T. Han, T. Wu, *IEEE Microw. Wirel. Compon. Lett.*, **2008**, 18, 248–250.
- [102] S. Wang, P. Kong, F.C. Lee, *IEEE Trans. Power Electron.*, **2007**, 22, 1410–1416.
- [103] R. Pallas-Areny, J.G. Webster, *IEEE Trans. Instrum. Meas.*, **1991**, 40, 669–676.
- [104] G. Menduni, A. Sampaolo, P. Patimisco, M. Giglio, S. Dello Russo, A. Zifarelli, A. Elefante, P.Z. Wiczorek, T. Starecki, V.M.N. Passaro, F.K. Tittel, V. Spagnolo, *Appl. Sci.*, **2020**, 10, 2947.
- [105] P. Patimisco, A. Sampaolo, Y. Bidaux, A. Bismuto, M. Schott, J. Jiang, A. Muller, J. Faist, F.K. Tittel, V. Spagnolo, *Opt. Exp.*, **2016**, 24, 25943–25954.

- [106] F.K. Tittel, A. Sampaolo, P. Patimisco, L. Dong, A. Geras, T. Starecki, V. Spagnolo, *Opt. Express*, **2016**, 24, A682–A692.
- [107] M. Giglio, A. Elefante, P. Patimisco, A. Sampaolo, F. Sgobba, H. Rossmadl, V. Mackowiak, H. Wu, F. K. Tittel, L. Dong, V. Spagnolo, *Opt. Express*, **2019**, 27, 4271–4280.
- [108] A. Elefante, M. Giglio, A. Sampaolo, G. Menduni, P. Patimisco, V.M.N. Passaro, H. Wu, H. Rossmadl, V. Mackowiak, A. Cable, F. K. Tittel, L. Dong, V. Spagnolo, *Anal. Chem.*, **2019**, 91, 20, 12866–12873.
- [109] A. Elefante, G. Menduni, H. Rossmadl, V. Mackowiak, M. Giglio, A. Sampaolo, P. Patimisco, V.M.N. Passaro, V. Spagnolo, *Sensors*, **2020**, 20, 2935.
- [110] M. Giglio, P. Patimisco, A. Sampaolo, G. Scamarcio, F.K. Tittel, V. Spagnolo, *IEEE Trans. Ultrason. Ferroelectr. Freq. Control*, **2016**, 63, 555–560.
- [111] D. Bolton, *Mon. Weather Rev.*, **1980**, 108, 1046–1053.
- [112] J.M. Wallace, P.V. Hobbs, *Atmospheric Science: An Introductory Survey*, **2006**, Elsevier: Amsterdam, The Netherlands, Volume 92.
- [113] H. Wu, L. Dong, X. Yin, A. Sampaolo, P. Patimisco, W. Ma, L. Zhang, W. Yin, L. Xiao, V. Spagnolo, S. Jia, *Sensors and Actuators B: Chemical*, **2019**, 297, 126753.
- [114] A. Sampaolo, P. Patimisco, M. Giglio, L. Chieco, G. Scamarcio, F. K. Tittel, V. Spagnolo, *Opt. Express*, **2016**, 24, 14, 15872.
- [115] [https://www.leyboldproducts.com/media/pdf/90/c7/87/Fundamentals\\_of\\_Leak\\_Detection\\_EN.pdf](https://www.leyboldproducts.com/media/pdf/90/c7/87/Fundamentals_of_Leak_Detection_EN.pdf) (accessed on **21 March 2021**).
- [116] S. Costello, M. P. Y. Desmulliez and S. McCracken, *IEEE Transactions on Components, Packaging and Manufacturing Technology*, **2012**, 2, 3, 430-438.
- [117] K. Zapfe, *Leak detection*, CERN, Accelerators and Storage Rings, **2007**.
- [118] C. Witchalls, *New Scientist*, **2010**, 207, 2773, 29.
- [119] M.H. Saberi, A.R. Rabbani, *J. Nat. Gas Sci. Eng.*, **2015**, 26, 558–569.
- [120] J. Pereira, P. Porto-Figueira, C. Cavaco, K. Taunk, S. Rapole, R. Dhakne, H. Nagarajaram, J.S. Câmara, *Metabolites.*, **2015**, 5, 3–55.
- [121] C.B. Schmidt Dubeux, E.L. La Rovere, *Cities.*, **2007**, 24, 353–364.
- [122] C.W. Moore, B. Zielinska, G. Pétron, R.B. Jackson, *Environ. Sci. Technol.*, **2014**, 48, 8349–8359.
- [123] F.S. Kinnaman, D.L. Valentine, S.C. Tyler, *Geochim. Cosmochim. Ac.*, **2007**, 71,

271–283.

- [124] M. Hepp, M. Herman, *Mol. Phys.*, **2000**, 98, 57–61.
- [125] L. G. Smith, *J. Chem. Phys.*, **1949**, 17, 139–167.
- [126] X. Tian, Y. Cao, J. Chen, K. Liu, G. Wang, T. Tan, J. Mei, W. Chen, X. Gao, *Sensors*, **2019**, 19, 820.
- [127] G. Menduni, F. Sgobba, S. Dello Russo, A. C. Ranieri, A. Sampaolo, P. Patimisco, M. Giglio, V. M. N. Passaro, S. Csutak, D. Assante, E. Ranieri, E. Geoffrion, V. Spagnolo, *Molecules*, **2020**, 25, 5607.
- [128] S. Schilt, J.-P. Besson, L. Thévenaz, *Appl. Phys. B Lasers Opt.*, **2006**, 82, 319–328.
- [129] F. Kinnaman, D. Valentine, S. Tyler, *Geochim. Cosmochim. Ac.*, **2007**, 71:271–83.
- [130] A. Sampaolo, G. Menduni, P. Patimisco, M. Giglio, V.M.N. Passaro, L. Dong, H. Wu, F. K. Tittel, V. Spagnolo, *Fuel*, **2020**, 277, 118118, 0016-2361.
- [131] [https://www.picarro.com/g2132\\_i\\_isotope\\_analyzer](https://www.picarro.com/g2132_i_isotope_analyzer) (accessed on **21 March 2021**).
- [132] <https://www.lgrinc.com/analyzers/isotope/methane-carbon-isotope-analyzer> (accessed on **21 March 2021**).
- [133] F. Merkt, M. Quack, *Molecular Quantum Mechanics and Molecular Spectra, Molecular Symmetry, and Interaction of Matter with Radiation*, **2011**.
- [134] A. Sampaolo, S. Csutak, P. Patimisco, M. Giglio, G. Menduni, V. Passaro, F. K. Tittel, M. Deffenbaugh, V. Spagnolo, *Sensors and Actuators B: Chemical*, **2019**, 282, 952-960.
- [135] PNNL database. Available online: <http://vpl.astro.washington.edu/spectra/> (accessed on **21 March 2021**).
- [136] I.T. Sorokina, K.L. Vodopyanov, *Solid-State Mid-Infrared Laser Sources*, Springer-Verlag, Berlin Heidelberg, **2003**.
- [137] G.N. Rao, A. Karpf, *Appl. Opt.*, **2011**, 50, A100.
- [138] D. Weidmann, G. Wysocki, *Opt. Express*, **2009**, 17, 248.
- [139] M. Giglio, P. Patimisco, A. Sampaolo, A. Zifarelli, R. Blanchard, C. Pfluegl, M.F. Witinski, D. Vakhshoori, F.K. Tittel, V. Spagnolo, *Appl. Phys. Lett.*, **2018**, 113, 171101.
- [140] B.G. Lee, J. Kansky, A.K. Goyal, C. Pflügl, L. Diehl, M.A. Belkin, A. Sanchez,

- F. Capasso, *Opt. Express*, **2009**, 17, 16216.
- [141] M. Giglio, A. Zifarelli, A. Sampaolo, G. Menduni, A. Elefante, R. Blanchard, C. Pfluegl, M. F. Witinski, D. Vakhshoori, H. Wu, V. M.N. Passaro, P. Patimisco, F. K. Tittel, L. Dong, V. Spagnolo, *Photoacoustics*, **2020**, 17, 100159, 2213-5979.
- [142] M. Giglio, P. Patimisco, A. Sampaolo, J.M. Kriesel, F.K. Tittel, V. Spagnolo, *Opt. Eng.*, **2017**, 57, 011004.
- [143] P. Patimisco, A. Sampaolo, L. Mihai, M. Giglio, J. Kriesel, D. Sporea, G. Scamarcio, F.K. Tittel, V. Spagnolo, *Sensors*, **2016**, 16, 533.
- [144] <https://www.methanelevels.org/> (accessed on **21 March 2021**).
- [145] G. Bollinger, D. A. Belsley, E. Kuh, R. E. Welsch, *Regression Diagnostics: Identifying Influential Data and Sources of Collinearity: Wiley Series in Probability and Statistics, Wiley: New York*, **1981**, Vol. 18.
- [146] S. Wold, E. Johansson, M. Cocchi, *PLS: Partial Least Squares Projections to Latent Structures, 3D QSAR in Drug Design. In 3D QSAR in Drug Design, Vol. 1: Theory Methods and Applications, Drug Design, Theory, Methods, and Applications, Leiden*, pp 523–550, **1993**.
- [147] S. Wold, M. Sjöström, L. Eriksson, *Chemom. Intell. Lab. Syst.*, **2001**, 58 (2), 109–130.
- [148] A. J. Höskuldsson, *Chemom.*, **1988**, 2 (3), 211–228.
- [149] P. Geladi, B. R. Kowalski, *Anal. Chim. Acta*, **1986**, 185 (C), 1–17.
- [150] S. de Jong, *Chemom. Intell. Lab. Syst.*, **1993**, 18 (3), 251–263.
- [151] A. Lorber, L. E. Wangen, B. R. J. Kowalski, *Chemom.*, **1987**, 1 (1), 19–31.
- [152] J. Shao, *J. Am. Stat. Assoc.*, **1993**, 88 (422), 486.
- [153] R. Bro, Ó. Rinnan, N. M. Faber, *Chemom. Intell. Lab. Syst.*, **2005**, 75 (1), 69–76.
- [154] N. M. Faber, R. Bro, *Chemom. Intell. Lab. Syst.*, **2002**, 61 (1–2), 133–149.
- [155] I. N. Wakeling, J. J. Morris, *J. Chemom.*, **1993**, 7 (4), 291–304.
- [156] A. C. Olivieri, *Introduction to Multivariate Calibration: A Practical Approach*, Springer: Netherlands, **2018**.
- [157] A. Zifarelli, M. Giglio, G. Menduni, A. Sampaolo, P. Patimisco, V. M. N. Passaro, H. Wu, L. Dong, V. Spagnolo, *Analytical Chemistry*, **2020**, 92 (16), 11035-11043.
- [158] B.ør.-H. Mevik, V. H. Segtnan, T. J. Næs, *Chemom.*, **2004**, 18 (11), 498–507.
- [159] A. K. Conlin, E. B. Martin, A. J. Morris, *Chemom. Intell. Lab. Syst.*, **1998**, 44

- (1–2), 161–173.
- [160] Y. Saalberg, M. Wolff, *Sensors*, **2018**, 18 (5), 1562.
- [161] T. Takahashi, B. Thornton, *Spectrochim. Acta - Part B At. Spectrosc.*, **2017**, 138, 31–42.
- [162] Z.Q. Hao, C.M. Li, M. Shen, X.Y. Yang, K.H. Li, L.B. Guo, X.Y. Li, Y.F. Lu, X.Y. Zeng, *Opt. Express.*, **2015**, 23, 7795.
- [163] Z. Zhou, B. Yin, J. Michel, *Light: Sci. Appl.*, **2015**, 4, 11, e358–e358.
- [164] V. Passaro, C. Tullio, B. Troia, M. Notte, G. Giannoccaro, F. Leonardis, *Sensors*, **2012**, 12, 11, 15558–15598.
- [165] M. De Carlo, G. Menduni, A. Sampaolo, F. De Leonardis, V. Spagnolo, V. M. N. Passaro, *Journal of Lightwave Technology*, **2020**, 39, 646–653.
- [166] Y. Pao, *Optoacoustic Spectroscopy and Detection*. Ed. by Y. Pao. NY, San Francisco, London: Academic, XI, **1977**.
- [167] L. B. Kreuzer, *Amsterdam, Netherlands: Elsevier*, pp. 1–25, **1977**.
- [168] S. A. Miller, M. Yu, X. Ji, A. G. Griffith, J. Cardenas, A. L. Gaeta, M. Lipson, *Optica*, **2017**, 4, 707–712.
- [169] A. Mason, *Sensing Technology*, Berlin, Germany: Springer, **2016**.
- [170] D. Rabus, *Integrated Ring Resonators*, Berlin, Germany: Springer, **2007**.
- [171] H. Nishihara, M. Harupa, T. Suhara, *Optical Integrated Circuits*, NY, USA: McGraw-Hill, **1989**.

# List of publications

## Publications on international journal

1. Dello Russo, S., Sampaolo, A., Patimisco, P., **Menduni, G.**, Giglio, M., Hoelzl, C., Passaro, V.M.N., Wu, H., Dong, L., Spagnolo, V. Quartz-enhanced photoacoustic spectroscopy exploiting low-frequency tuning forks as a tool to measure the vibrational relaxation rate in gas species (2021) *Photoacoustics*, 21, 100227, 10.1016/j.pacs.2020.100227;
2. De Carlo, M., **Menduni, G.**, Sampaolo, A., De Leonardis, F., Spagnolo, V., Passaro, V.M.N. Modeling and Design of a Semi-Integrated QEPAS Sensor (2021) *Journal of Lightwave Technology*, 39 (2), 9222489, pp. 646-653, 10.1109/JLT.2020.3030682;
3. **Menduni, G.**, Sgobba, F., Russo, S.D., Ranieri, A.C., Sampaolo, A., Patimisco, P., Giglio, M., Passaro, V.M.M., Csutak, S., Assante, D., Ranieri, E., Geoffrion, E., Spagnolo, V. Fiber-coupled quartz-enhanced photoacoustic spectroscopy system for methane and ethane monitoring in the near-infrared spectral range (2020) *Molecules*, 25 (23), 5607, 10.3390/molecules25235607;
4. Sampaolo, A., **Menduni, G.**, Patimisco, P., Giglio, M., Passaro, V.M.N., Dong, L., Wu, H., Tittel, F.K., Spagnolo, V. Quartz-enhanced photoacoustic spectroscopy for hydrocarbon trace gas detection and petroleum exploration (2020) *Fuel*, 277, 118118, 10.1016/j.fuel.2020.118118;
5. Zifarelli, A., Giglio, M., **Menduni, G.**, Sampaolo, A., Patimisco, P., Passaro, V.M.N., Wu, H., Dong, L., Spagnolo, V. Partial Least-Squares Regression as a Tool to Retrieve Gas Concentrations in Mixtures Detected Using Quartz-Enhanced Photoacoustic Spectroscopy (2020) *Analytical Chemistry*, 92 (16), pp. 11035-11043, 10.1021/acs.analchem.0c00075;
6. Elefante, A., **Menduni, G.**, Rossmadl, H., Mackowiak, V., Giglio, M., Sampaolo, A., Patimisco, P., Passaro, V.M.N., Spagnolo, V. Environmental monitoring of methane with quartz-enhanced photoacoustic spectroscopy exploiting an electronic hygrometer to compensate the H<sub>2</sub>O influence on the sensor signal (2020) *Sensors (Switzerland)*, 20 (10), 2935, 10.3390/s20102935;
7. Sgobba, F., **Menduni, G.**, Russo, S.D., Sampaolo, A., Patimisco, P., Giglio, M.,

- Ranieri, E., Passaro, V.M.N., Tittel, F.K., Spagnolo, V. Quartz-enhanced photoacoustic detection of ethane in the near-IR exploiting a highly performant spectrophone (2020) *Applied Sciences* (Switzerland), 10 (7), 2447, 10.3390/app10072447;
8. **Menduni, G.**, Sampaolo, A., Patimisco, P., Giglio, M., Russo, S.D., Zifarelli, A., Elefante, A., Wiczorek, P.Z., Starecki, T., Passaro, V.M.N., Tittel, F.K., Spagnolo, V. Front-end amplifiers for tuning forks in quartz enhanced photoacoustic spectroscopy (2020) *Applied Sciences* (Switzerland), 10 (8), 2947, 10.3390/APP10082947;
  9. Giglio, M., Zifarelli, A., Sampaolo, A., **Menduni, G.**, Elefante, A., Blanchard, R., Pfluegl, C., Witinski, M.F., Vakhshoori, D., Wu, H., Passaro, V.M.N., Patimisco, P., Tittel, F.K., Dong, L., Spagnolo, V. Broadband detection of methane and nitrous oxide using a distributed-feedback quantum cascade laser array and quartz-enhanced photoacoustic sensing (2020) *Photoacoustics*, 17, 100159, 10.1016/j.pacs.2019.100159;
  10. Elefante, A., Giglio, M., Sampaolo, A., **Menduni, G.**, Patimisco, P., Passaro, V.M.N., Wu, H., Rossmadl, H., Mackowiak, V., Cable, A., Tittel, F.K., Dong, L., Spagnolo, V. Dual-Gas Quartz-Enhanced Photoacoustic Sensor for Simultaneous Detection of Methane/Nitrous Oxide and Water Vapor (2019) *Analytical Chemistry*, 91 (20), pp. 12866-12873, 10.1021/acs.analchem.9b02709;
  11. Russo, S.D., Giglio, M., Sampaolo, A., Patimisco, P., **Menduni, G.**, Wu, H., Dong, L., Passaro, V.M.N., Spagnolo, V. Acoustic coupling between resonator tubes in quartz-enhanced photoacoustic spectrophones employing a large prong spacing tuning fork (2019) *Sensors* (Switzerland), 19 (19), 4109, 10.3390/s19194109;
  12. Sampaolo, A., Csutak, S., Patimisco, P., Giglio, M., **Menduni, G.**, Passaro, V., Tittel, F.K., Deffenbaugh, M., Spagnolo, V. Methane, ethane and propane detection using a compact quartz enhanced photoacoustic sensor and a single interband cascade laser (2019) *Sensors and Actuators, B: Chemical*, 282, pp. 952-960, 10.1016/j.snb.2018.11.132;
  13. Giglio, M., **Menduni, G.**, Patimisco, P., Sampaolo, A., Elefante, A., Passaro, V.M.N., Spagnolo, V. Damping Mechanisms of Piezoelectric Quartz Tuning Forks Employed in Photoacoustic Spectroscopy for Trace Gas Sensing (2019) *Physica Status Solidi (A) Applications and Materials Science*, 216 (3), 1800552,

## Proceeding of international conferences

1. Passaro, V.M.N., De Carlo, M., De Leonardis, F., **Menduni, G.**, Lamberti, L., Perri, A.G. Parity-time and anti-parity-time-symmetry integrated optical gyroscopes: A perspective for high performance devices (2020) *International Conference on Transparent Optical Networks*, 2020-July, 9203305, 10.1109/ICTON51198.2020.9203305;
2. Sgobba, F., **Menduni, G.**, Sampaolo, A., Patimisco, P., Giglio, M., Elefante, A., Passaro, V., Tittel, F.K., Spagnolo, V. Fiber-coupled quartz-enhanced photoacoustic sensor for methane and ethane trace detection (2020) *Proceedings of SPIE - The International Society for Optical Engineering*, 11288, 112882D, 10.1117/12.2545782;
3. Dello Russo, S., Patimisco, P., Sampaolo, A., Giglio, M., **Menduni, G.**, Elefante, A., Passaro, V., Tittel, F.K., Spagnolo, V. Measurement of non-radiative gas molecules relaxation rates by using quartz-enhanced photoacoustic spectroscopy (2020) *Proceedings of SPIE - The International Society for Optical Engineering*, 11288, 112882C, 10.1117/12.2545774;
4. Zifarelli, A., Patimisco, P., Sampaolo, A., Giglio, M., **Menduni, G.**, Elefante, A., Passaro, V., Tittel, F.K., Spagnolo, V. Partial least squares regression as novel tool for gas mixtures analysis in quartz-enhanced photoacoustic spectroscopy (2020) *Proceedings of SPIE - The International Society for Optical Engineering*, 11288, 112882B, 10.1117/12.2545766;
5. Sampaolo, A., Patimisco, P., Giglio, M., **Menduni, G.**, Elefante, A., Passaro, V., Tittel, F.K., Spagnolo, V. Simultaneous dual gas QEPAS sensing of water and methane/nitrous oxide (2019) *Proceedings of SPIE - The International Society for Optical Engineering*, 10926, 109262L, 10.1117/12.2507922;
6. **Menduni, G.**, Sampaolo, A., Csutak, S., Patimisco, P., Giglio, M., Elefante, A., Passaro, V., Tittel, F.K., Deffenbaugh, M., Spagnolo, V. Quartz-enhanced photoacoustic sensors for detection of multiple hydrocarbon and methane isotopes (2019) *Proceedings of SPIE - The International Society for Optical Engineering*, 10926, 109260C, 10.1117/12.2507881;

7. Elefante, A., Patimisco, P., Sampaolo, A., Giglio, M., **Menduni, G.**, Rossmadl, H., Mackowiak, V., Passaro, V., Gross, B., Cable, A., Tittel, F.K., Spagnolo, V. Octupole electrode pattern for tuning forks vibrating at the first overtone mode in quartz-enhanced photoacoustic spectroscopy (2019) *Proceedings of SPIE - The International Society for Optical Engineering*, 10926, 109262K, 10.1117/12.2507909;
8. Patimisco, P., Sampaolo, A., Giglio, M., Dello Russo, S., Elefante, A., **Menduni, G.**, Passaro, V., Rossmadl, H., Mackowiak, V., Gross, B., Cable, A., Tittel, F.K., Spagnolo, V. New generation of tuning forks for quartz-enhanced photoacoustic spectroscopy (2019) *Proceedings of SPIE - The International Society for Optical Engineering*, 10926, 109260D, 10.1117/12.2507932;
9. Giglio, M., Patimisco, P., Sampaolo, A., Zifarelli, A., **Menduni, G.**, Elefante, A., Blanchard, R., Pfluegl, C., Witinski, M.F., Vakhshoori, D., Passaro, V., Tittel, F.K., Spagnolo, V. Quartz-enhanced photoacoustic spectroscopy employing a distributed feedback-quantum cascade laser array for nitrous oxide and methane broadband detection (2019) *Proceedings of SPIE - The International Society for Optical Engineering*, 10939, 109391Q, 10.1117/12.2507926;
10. Sampaolo, A., Csutak, S., Patimisco, P., Giglio, M., **Menduni, G.**, Passaro, V., Tittel, F.K., Deffenbaugh, M., Spagnolo, V. Interband cascade laser based quartz-enhanced photoacoustic sensor for multiple hydrocarbons detection (2018) *Proceedings of SPIE - The International Society for Optical Engineering*, 10540, 105400C, 10.1117/12.2288336.

La borsa di dottorato è stata cofinanziata con risorse del  
Programma Operativo Nazionale Ricerca e Innovazione 2014-2020 (CCI 2014IT16M2OP005),  
Fondo Sociale Europeo, Azione I.1 “Dottorati Innovativi con caratterizzazione Industriale”



UNIONE EUROPEA  
Fondo Sociale Europeo



*Ministero dell'Istruzione,  
dell'Università e della Ricerca*

